

# The Structure and Polarization Properties of the SiO Masers in the Extended Atmosphere of R Aquarii

David Allen Boboltz, Jr.

Dissertation submitted to the Faculty of the Virginia Polytechnic Institute and  
State University in partial fulfillment of the requirements for the degree of

Doctor of Philosophy  
in  
Physics

John H. Simonetti, Chair  
Philip J. Diamond  
Brian K. Dennison  
Lay Nam Chang  
John J. Broderick

June 13, 1997  
Blacksburg, Virginia

Keywords: Masers, Symbiotic Binaries, Circumstellar Matter, R Aquarii  
Copyright ©1997, David A. Boboltz, Jr.

# The Structure and Polarization Properties of the SiO Masers in the Extended Atmosphere of R Aquarii

David Allen Boboltz, Jr.

## ABSTRACT

Silicon monoxide (SiO) maser emission has been observed towards many late-type stars. The conditions necessary for the formation of SiO masers dictate that they be produced in a region which is inside the silicate dust formation point close to the surface of the star. Very Long Baseline Interferometry (VLBI) has shown that these masers do indeed lie close to the stellar surface at a distance of a few stellar radii. This extended atmosphere is a complex region dominated by stellar pulsations and permeated by circumstellar shocks.

This dissertation presents the results of a multi-epoch VLBI study of the  $v = 1, J = 1-0$ , 43-GHz SiO maser emission towards the symbiotic binary R Aquarii. Four epochs of full-polarization observations were recorded using the Very Long Baseline Array a facility the National Radio Astronomy Observatory. The first high-resolution images of the extended atmosphere of a Mira variable in a symbiotic binary have been produced.

The SiO masers towards R Aquarii have been found to exhibit a ring-like morphology  $\sim 31$  mas ( $\sim 6.8$  AU) in diameter. The emission changes significantly over a time period of  $\sim 1-2$  months with almost no similarity in structure on timescales  $\gtrsim 6$  months. An analysis of the four epochs of observations has provided the first direct evidence of SiO maser proper motions. These observations, taken as the Mira variable approached maximum light, show that over a 98-day period the masers have an average inward proper motion of  $\sim 1$  mas. This contraction of the maser shell implies an infall velocity of  $\sim 4$  km s $^{-1}$  for the SiO masers during this phase of the stellar pulsation cycle.

In addition to the total intensity images, maps of the linear and circular polarization morphology were also produced. These images show that the SiO masers

are significantly polarized, and that the polarization structure and intensity change on timescales as short as  $\sim 1$ -2 months. For three of the four epochs, a mean fractional circular polarization of  $\sim 4\%$  was determined implying a magnetic field strength  $B \sec \theta \approx 13$  G. For one of the four epochs, the mean fractional circular polarization was found to be  $\sim 14\%$  indicating a magnetic field strength  $B \sec \theta \approx 46$  G. The fractional linear polarization is fairly constant for all four epochs with mean values ranging from 20.8–25.0%, and peak values as high as  $\sim 83\%$  for isolated maser features. Maps of the linear polarization vectors show an orderly structure over large portions of the maser shell indicating a uniform magnetic field topology in these regions of the extended atmosphere of R Aquarii.

## ACKNOWLEDGMENTS

“Time has this funny plastic quality, and everything that goes around comes around. When you get on the bus, you think it won’t be taking you far — across town maybe, no further than that — and all at once, holy shit! You’re halfway across the next continent.”

*Stephen King, Four Past Midnight*

Approximately 7 years ago, I decided to give up a lucrative career in mechanical engineering to pursue a doctorate in radio astronomy. There are numerous people who have helped me achieve this goal. First of all, I would like to thank my advisor, Dr. John Simonetti, and Dr. Brian Dennison for getting me started in astronomy. I am grateful to the many friends I made at Virginia Tech who helped me get through the first couple of years of graduate school especially Dan Korwan, Hector Emanuel, Charles Moller, Calvin Doss, Mark Mattson, and Scott Massie.

Two years ago, Dr. Philip Diamond took a chance by allowing a graduate student with very little knowledge of Very Long Baseline Interferometry and even less knowledge of spectral line techniques to come and work with him; for this I am deeply indebted. As the fourth (and hopefully not the last) of the *Diamond-backs* I have had the pleasure to learn from one of the best in the spectral line VLBI business. This dissertation would never have happened without his guidance and encouragement.

I would like to thank the National Radio Astronomy Observatory for providing me with a pre-doctoral fellowship. I am grateful to Dr. Miller Goss and the entire staff at NRAO in Socorro, New Mexico for their assistance during my two year stay. I would especially like to thank Tony Beasley, Mark Claussen, Chris Depree, Ketan Desai (Diamond-back number two), all the coffee-time guys, and the numerous others who have made my time at NRAO a great experience. Special thanks go to Athol Kembball and Kevin Marvel (Diamond-back numbers one and three). Kevin was extremely helpful in getting me started processing VLBI spectral line data. Athol patiently answered all of my questions without ever kicking me out of his office. Both were a great help in the processing and interpretation of the data in this dissertation.

I would also like to thank my family for their support during my graduate school experience. My father, Dave Sr., whose hard work put me through my first four years at Virginia Tech and whose courage during some of the tough times in his life provided me with the inspiration to achieve my goals. To my sister, Renee, who won the “race”, thanks for your encouragement. To my in-laws, Betty and Norbert

Walecka, thank you for never doubting me and for never saying “When are you going to finish and get a real job?”.

Most of all, I would like to thank the two most important and influential people in my life; my wife Mary and my mother Florence. To my mom, who put the graduate school bug in my head, I wish you had made it to see the completion of my Ph.D. To my wife and my best friend Mary, I could never have gone the distance without your love and support. Thank you for putting your life on hold for seven long years while I chased a dream, I owe everything to you.

# Contents

<b>LIST OF TABLES</b>	<b>ix</b>
<b>LIST OF FIGURES</b>	<b>x</b>
<b>1 INTRODUCTION</b>	<b>1</b>
1.1 Astrophysical Masers . . . . .	1
1.1.1 History . . . . .	1
1.1.2 Maser Physics . . . . .	3
1.1.3 Circumstellar Masers . . . . .	7
1.2 Long-Period Variables and Symbiotic Binaries . . . . .	11
1.2.1 Mira Variables . . . . .	11
1.2.2 Symbiotic Binaries . . . . .	13
1.3 Very Long Baseline Interferometry . . . . .	15
1.3.1 Basic VLBI Theory . . . . .	15
1.3.2 Spectropolarimetry . . . . .	17
1.4 Dissertation Goals . . . . .	21
<b>2 REDUCTION OF VLBI SPECTROPOLARIMETRY DATA</b>	<b>24</b>
2.1 Introduction . . . . .	24
2.2 Response of the VLBI Array . . . . .	25
2.3 Data Reduction Path . . . . .	27
2.3.1 Loading and Editing the Data . . . . .	27

2.3.2	Parallactic Angle Correction . . . . .	29
2.3.3	Bandpass Calibration . . . . .	30
2.3.4	Doppler Velocity Correction . . . . .	31
2.3.5	Amplitude Calibration . . . . .	32
2.3.6	Phase Calibration . . . . .	34
2.3.7	Feed Calibration . . . . .	38
2.3.8	Imaging . . . . .	39
<b>3</b>	<b>VLBA OBSERVATIONS OF R AQUARI</b>	<b>41</b>
3.1	Introduction . . . . .	41
3.2	Epoch 1 . . . . .	43
3.2.1	Observations . . . . .	43
3.2.2	Calibration and Imaging . . . . .	44
3.3	Epoch 2 . . . . .	53
3.3.1	Observations . . . . .	53
3.3.2	Calibration and Imaging . . . . .	53
3.4	Epoch 3 . . . . .	63
3.4.1	Observations . . . . .	63
3.4.2	Calibration and Imaging . . . . .	63
3.5	Epoch 4 . . . . .	73
3.5.1	Observations . . . . .	73
3.5.2	Calibration and Imaging . . . . .	73
<b>4</b>	<b>R AQUARI: REVIEW OF SOURCE PROPERTIES</b>	<b>83</b>
4.1	Introduction . . . . .	83
4.2	History and General Properties of R Aquarii . . . . .	84
4.2.1	Identification as a Symbiotic Star . . . . .	84
4.2.2	The Nebulae Surrounding R Aquarii . . . . .	84
4.2.3	Distance to R Aquarii . . . . .	86

4.2.4	The Binary Orbit of R Aquarii . . . . .	88
4.3	The R Aquarii Radio/Optical/UV Jet . . . . .	90
4.4	Maser Emission Towards R Aquarii . . . . .	95
4.4.1	Single-Dish Observations . . . . .	95
4.4.2	Spectral Line Interferometry . . . . .	97
4.5	Models for R Aquarii . . . . .	98
<b>5</b>	<b>STRUCTURE AND DYNAMICS OF THE SiO MASERS</b>	<b>102</b>
5.1	Introduction . . . . .	102
5.2	Structure and Variability . . . . .	102
5.3	Locating SiO Maser Features . . . . .	105
5.3.1	Component Selection . . . . .	105
5.3.2	Error Estimation . . . . .	106
5.4	Proper Motions . . . . .	112
<b>6</b>	<b>POLARIZATION OF THE SiO MASERS</b>	<b>122</b>
6.1	Introduction . . . . .	122
6.2	Component Polarization Determination . . . . .	122
6.3	Circular Polarization . . . . .	130
6.4	Linear Polarization . . . . .	134
6.4.1	Fractional Linear Polarization . . . . .	134
6.4.2	Linear Polarization Position Angle . . . . .	137
6.5	The Magnetic Field of R Aqr . . . . .	144
<b>7</b>	<b>CONCLUSIONS</b>	<b>153</b>
7.1	Summary of Results . . . . .	153
7.2	Future Work . . . . .	159

<b>BIBLIOGRAPHY</b>	<b>161</b>
<b>APPENDICES</b>	<b>170</b>
<b>A TOTAL INTENSITY CHANNEL MAPS FOR R AQUARII</b>	<b>171</b>
<b>B COMPONENT LISTS FOR R AQUARII</b>	<b>196</b>

# List of Tables

1.1	Initial detections of various maser species . . . . .	2
1.2	VLBA antenna locations . . . . .	23
3.1	Coordinates of observed sources . . . . .	41
3.2	Epoch 2 R–L amplitude corrections . . . . .	54
3.3	Epoch 4 R–L amplitude corrections . . . . .	74
4.1	Measurements of the distance to R Aqr . . . . .	88
B.1	List of components for Epoch 1 . . . . .	197
B.2	List of components for Epoch 2 . . . . .	199
B.3	List of components for Epoch 3 . . . . .	201
B.4	List of components for Epoch 4 . . . . .	203

# List of Figures

1.1	VLBI signal path diagram . . . . .	18
1.2	VLBA antenna locations . . . . .	22
2.1	VLBI spectropolarimetry data reduction path . . . . .	28
3.1	Visual light curve for R Aqr . . . . .	42
3.2	Epoch 1 Stokes $I$ cross-power spectrum . . . . .	46
3.3	Epoch 1 integrated Stokes $I$ image . . . . .	47
3.4	Epoch 1 integrated Stokes $V$ image . . . . .	48
3.5	Epoch 1 integrated Stokes $Q$ image . . . . .	49
3.6	Epoch 1 integrated Stokes $U$ image . . . . .	50
3.7	Epoch 1 linear polarization image . . . . .	51
3.8	Epoch 1 velocity map . . . . .	52
3.9	Epoch 2 Stokes $I$ cross-power spectrum . . . . .	56
3.10	Epoch 2 integrated Stokes $I$ image . . . . .	57
3.11	Epoch 2 integrated Stokes $V$ image . . . . .	58
3.12	Epoch 2 integrated Stokes $Q$ image . . . . .	59
3.13	Epoch 2 integrated Stokes $U$ image . . . . .	60
3.14	Epoch 2 linear polarization image . . . . .	61
3.15	Epoch 2 velocity map . . . . .	62
3.16	Epoch 3 Stokes $I$ cross-power spectrum . . . . .	66
3.17	Epoch 3 integrated Stokes $I$ image . . . . .	67

3.18	Epoch 3 integrated Stokes $V$ image . . . . .	68
3.19	Epoch 3 integrated Stokes $Q$ image . . . . .	69
3.20	Epoch 3 integrated Stokes $U$ image . . . . .	70
3.21	Epoch 3 linear polarization image . . . . .	71
3.22	Epoch 3 velocity map . . . . .	72
3.23	Epoch 4 Stokes $I$ cross-power spectrum . . . . .	76
3.24	Epoch 4 integrated Stokes $I$ image . . . . .	77
3.25	Epoch 4 integrated Stokes $V$ image . . . . .	78
3.26	Epoch 4 integrated Stokes $Q$ image . . . . .	79
3.27	Epoch 4 integrated Stokes $U$ image . . . . .	80
3.28	Epoch 4 linear polarization image . . . . .	81
3.29	Epoch 4 velocity map . . . . .	82
4.1	Optical images of the R Aqr nebulae . . . . .	85
4.2	Radio image of the R Aqr nebulae . . . . .	87
4.3	Radio image of the R Aqr jet . . . . .	91
4.4	HST UV image of the R Aqr system . . . . .	93
4.5	Radio images of the inner R Aqr jet . . . . .	94
4.6	HST UV images showing the motion of the R Aqr jet . . . . .	96
5.1	Composite of total intensity images for Epochs 1–4 . . . . .	104
5.2	Epoch 1 component distribution . . . . .	107
5.3	Epoch 2 component distribution . . . . .	108
5.4	Epoch 3 component distribution . . . . .	109
5.5	Epoch 4 component distribution . . . . .	110
5.6	Rereferenced component positions Epochs 2, 3, and 4 . . . . .	114
5.7	Proper motion vectors Epoch 2 to Epoch 4 . . . . .	115
5.8	Proper motion vectors Epoch 2 to Epoch 4 with mean subtracted . . . . .	116
5.9	Pairwise component separations Epochs 2, 3, and 4 . . . . .	117

5.10	Pairwise separations for components >15 mas apart . . . . .	118
5.11	Circle fits to components common to Epochs 2, 3, and 4 . . . . .	119
6.1	Composite of linear polarization images for Epochs 1–4 . . . . .	123
6.2	Epoch 1 polarized component distribution . . . . .	126
6.3	Epoch 2 polarized component distribution . . . . .	127
6.4	Epoch 3 polarized component distribution . . . . .	128
6.5	Epoch 4 polarized component distribution . . . . .	129
6.6	Fractional circular polarization for R Aqr . . . . .	132
6.7	Absolute value of fractional circular polarization . . . . .	132
6.8	Fractional circular polarization vs. Stokes <i>I</i> Epochs 1–4 . . . . .	133
6.9	Fractional linear polarization for R Aqr . . . . .	135
6.10	Fractional linear polarization vs. Stokes <i>I</i> Epochs 1–4 . . . . .	136
6.11	Epoch 1 component linear polarization maps . . . . .	138
6.12	Epoch 2 component linear polarization maps . . . . .	139
6.13	Epoch 3 component linear polarization maps . . . . .	140
6.14	Epoch 4 component linear polarization maps . . . . .	141
6.15	Epoch 1 polarization as a function of position angle . . . . .	143
6.16	Epoch 2 polarization as a function of position angle . . . . .	144
6.17	Epoch 3 polarization as a function of position angle . . . . .	145
6.18	Epoch 4 polarization as a function of position angle . . . . .	146
6.19	Fractional linear vs. fractional circular polarization . . . . .	148
7.1	Diagram of the R Aqr system . . . . .	155
A.1	Epoch 1 Stokes <i>I</i> channel maps . . . . .	172
A.2	Epoch 2 Stokes <i>I</i> channel maps . . . . .	178
A.3	Epoch 3 Stokes <i>I</i> channel maps . . . . .	184
A.4	Epoch 4 Stokes <i>I</i> channel maps . . . . .	190

# Chapter 1

## INTRODUCTION

“Said I’m giving you a decision to make.  
Things to lose, things to take.”

*Violent Femmes, Add It Up*

### 1.1 Astrophysical Masers

#### 1.1.1 History

The first detection of maser emission from an astronomical source was made by Weaver et al. (1965) when they detected the 1665-MHz main line transition of the hydroxyl ion (OH) towards several interstellar H II regions. Weaver et al. found the ratio of the 1667-MHz/1665-MHz emission to be inconsistent with either optically thin or optically thick thermal emission, and named this new line of emission “mysterium”. Weinreb et al. (1965) observed the OH emission at 1665, 1667 and 1720 MHz towards the H II region W3 and found the 1667-MHz emission to have linear polarization as high as 37%. This led them to the conclusion that “mysterium” was actually anomalously excited OH emission. As one possible mechanism for the production of this highly polarized emission Weinreb et al. suggested the amplification of polarized background radiation through a *maser-type* population inversion.

For the next two years, searches performed at radio wavelengths detected no new molecules. However, in the period from 1968 to 1969, three new masers were discovered: NH<sub>3</sub>, H<sub>2</sub>CO, and H<sub>2</sub>O. These new molecules were detected towards cold dark clouds, regions conducive to molecule formation but invisible to earlier searches

conducted at 21 cm. Since that time, a number of new masing molecules have been detected. Some of these discoveries are listed in Table 1.1 below.

Table 1.1: Initial detections of various maser species.

Molecule	Common Name	Reference
OH		Weaver et al. (1965)
NH <sub>3</sub>	ammonia	Cheung et al. (1968)
H <sub>2</sub> CO	formaldehyde	Snyder and Buhl (1969)
H <sub>2</sub> O	water	Cheung et al. (1969)
CH <sub>3</sub> OH	methanol	Ball et al. (1970)
CH		Rydbeck, Ellder, and Irvine (1973) Turner and Zuckerman (1973)
SiO		Snyder and Buhl (1974)
HCN		Guilloteau, Omont, and Lucas (1987)

Masers are found in a wide variety of astronomical settings including: regions of active star-formation, the circumstellar shells of evolved stars, cometary halos, supernova remnants, and external galaxies. Due to their compact size and their intense brightness, astronomical masers provide an excellent tool for the study of processes unrelated to the actual maser action. One obvious use for masers is to use them as tracers of the structure, the velocity fields, and the magnetic fields towards astronomically interesting objects. Radio interferometers can measure the distribution of masers in position and velocity space yielding information on the morphology and the kinematics of the gas towards an object. Some masers (i.e. OH and SiO) are useful probes for determining the magnetic fields towards regions where these masers exist. Polarization observations of a masing molecule such as OH, coupled with the knowledge of OH maser theory, allow the determination of the magnetic fields influencing the maser emission.

Masers have been used to study the physical characteristics of both our own galaxy and external galaxies. Within our own galaxy they have been used to measure the galactic rotation curve and the galactic magnetic field. Since they provide strong point-like sources, masers have also been used to study the scattering properties of the interstellar medium. Three maser species OH, H<sub>2</sub>O, and H<sub>2</sub>CO have, thus far, been observed outside our own galaxy. Extragalactic OH maser emission was first identified towards the galaxy NGC 253 by Whiteoak and Gardener (1974). These masers were found to have isotropic luminosities between 10 and 100 times the strongest OH

masers in our own galaxy. Later, a new class of extragalactic masers was discovered by Baan, Wood, and Haschik (1982) in the galaxy IC 4553. Because of their enormous isotropic luminosity ( $\sim 10^3 L_{\odot}$ ) as compared with the average H II region ( $\sim 10^{-3} L_{\odot}$ ) these masers were dubbed *megamasers*. The initial discovery of extragalactic H<sub>2</sub>O maser emission was made when Chruchwell et al. (1977) detected the 22-GHz line towards the HII region IC 133 in the spiral galaxy M33. Similar detections have been made towards other nearby galaxies such as the Large and Small Magellanic clouds. These masers are thought to reside in the star-forming regions of these systems, similar to those in our own galaxy. A new class of extragalactic H<sub>2</sub>O masers was later discovered by Dos Santos and Lepine (1979) towards the edge-on spiral galaxy NGC 4945. Unlike the former class, these new masers are located near the nuclei of distant galaxies. Extragalactic masers provide useful probes of the cores of external galaxies, and most recently have furnished the most convincing evidence yet for the existence of massive black holes at their centers (Miyoshi et al. 1995).

Another useful property of maser emission is the fairly long lifetimes of individual maser spots. This property allows the observer to track the position and intensity of the masers over multiple epochs of observations. The motion of individual maser features across the plane of the sky (the *proper motion*) can be measured by observing the features at several different epochs. Proper motion measurements are an important means of determining distances to astronomical sources since they do not rely on assumptions of the physical properties of the source or the intervening medium. In addition, proper motions allow an observer to determine the kinematics in the vicinity of astronomical objects. Most importantly (for myself at least), the advent of Very Long Baseline Interferometry (VLBI) allows the measurement of maser proper motions to be performed within the timescale of a Ph.D. dissertation.

### 1.1.2 Maser Physics

A comprehensive treatment of maser radiation is contained in *Astronomical Masers* (Elitzur 1992). In this section I will outline some of the important physics involved in maser emission leaving out many of the details. The interested reader is referred to Elitzur (1992) for an in-depth study of maser emission.

Maser emission is the microwave equivalent of laser emission, and it is natural to begin the discussion with the equation governing the transfer of radiation and its interactions with matter. The full-blown equation of radiative transfer may be

written in terms of the frequency-dependent specific intensity  $I_\nu$  as

$$\begin{aligned} \frac{1}{c} \frac{dI_\nu}{dt} + \hat{k} \cdot \vec{\nabla} I_\nu &= \frac{\rho j_\nu}{4\pi} + \rho \kappa_\nu^{scatt} \oint \Phi(\hat{k}, \hat{k}') I_\nu(\hat{k}') d\Omega' \\ &\quad - \rho \kappa_\nu^{abs} I_\nu - \rho \kappa_\nu^{scatt} I_\nu. \end{aligned} \quad (1.1)$$

The first two terms on the right-hand side of the equation represent emission and scattering into the beam, respectively (sources of radiation). Absorptions and scattering out of the beam (sinks for radiation) are represented by the final two terms on the right-hand side of equation (1.1). If we make some reasonable assumptions such as:

1. no time dependent changes in the intensity (steady state);  $\frac{1}{c} \frac{dI_\nu}{dt} = 0$ ,
2. changes in the intensity only occur along the ray path;  $\hat{k} \cdot \vec{\nabla} I_\nu = \frac{dI_\nu}{dl}$ ,
3. no scattering into or out of the beam;  $\kappa_\nu^{scatt} = 0$ ,

then the equation of radiative transfer reduces to

$$\frac{dI_\nu}{dl} = \frac{\rho j_\nu}{4\pi} - \rho \kappa_\nu I_\nu. \quad (1.2)$$

Furthermore, if we define the optical depth,  $d\tau_\nu = \rho \kappa_\nu dl$ , and the source function,  $S_\nu = \rho j_\nu / 4\pi$  then the equation of radiative transfer can be written in the compact form

$$\frac{dI_\nu}{d\tau_\nu} + I_\nu = S_\nu. \quad (1.3)$$

The solution for equation (1.3), which governs the passage of radiation through the medium, is commonly called the *formal solution* and is written

$$I_\nu(\hat{k}, \tau_\nu) = I_\nu(\hat{k}, 0)e^{-\tau_\nu} + \int_0^{\tau_\nu} S_\nu(\hat{k}', \tau'_\nu) e^{-(\tau_\nu - \tau'_\nu)} d\tau'_\nu. \quad (1.4)$$

If one final assumption is made, namely, that the radiation is passing through a uniform slab of material  $S_\nu(\hat{k}', \tau'_\nu) = S_\nu(\hat{k}', 0)$ , then the formal solution becomes

$$I_\nu(\tau_\nu) = I_\nu(0)e^{-\tau_\nu} + S_\nu(1 - e^{-\tau_\nu}), \quad (1.5)$$

where  $I_\nu(0)$  is the radiation incident on some distribution of material and  $I_\nu(\tau_\nu)$  is the radiation emergent from the material.

There are still two quantities that are required to determine the emergent radiation field:  $\tau_\nu$  the frequency dependent optical depth, and  $S_\nu$  the frequency dependent source function. The goal of the majority of theoretical models for astrophysical maser emission is the determination of these two functions. This can be a complicated task since it involves solving the equations which govern the population of the numerous molecular sublevels. The solution of these *rate* equations is greatly simplified if we first consider a two-level system in which we include only spontaneous decays, absorptions, and stimulated emissions. These three transitions are characterized by the three Einstein coefficients  $A_{21}$ ,  $B_{12}$ , and  $B_{21}$  respectively. The relationships between the Einstein coefficients are

$$g_1 B_{12} = g_2 B_{21}, \quad (1.6)$$

and

$$A_{21} = \frac{2h\nu^3}{c^2} B_{21}, \quad (1.7)$$

where  $g_1$  and  $g_2$  are the statistical weights of the two levels. If the statistical weights are assumed equal and we solve the level population equations, then relationships can be determined for the optical depth

$$\tau_\nu = g_2 B_{21} (n_1 - n_2) \frac{h\nu}{4\pi} \phi(\nu) l, \quad (1.8)$$

and for the source function

$$\begin{aligned} S_\nu &= \frac{A_{21}}{B_{21}(n_1/n_2 - 1)} \\ &= \frac{2h\nu^3}{c^2} \frac{1}{(n_1/n_2 - 1)}. \end{aligned} \quad (1.9)$$

Here,  $n_1$  and  $n_2$  are the number densities of the two levels and  $\phi(\nu)$  is the line profile. When the particles have a Maxwellian velocity distribution, then the line profile becomes the Doppler profile

$$\phi(\nu) = \frac{1}{\sqrt{\pi} \Delta\nu_D} e^{-\left[\frac{\nu - \nu_0}{\Delta\nu_D}\right]^2}, \quad (1.10)$$

where  $\Delta\nu_D$  is the Doppler linewidth and  $\nu_0$  is the line center. Elitzur (1990) introduces the population difference  $\Delta n = (n_2 - n_1)$ , the total population  $n = (n_1 + n_2)$  and the inversion efficiency  $\eta = \Delta n/n$  and rewrites equations (1.8) and (1.9) as

$$\tau_\nu = -g_2 B_{21} \Delta n \frac{h\nu}{4\pi} \phi(\nu), \quad (1.11)$$

and

$$S_\nu = -\frac{2h\nu^3}{c^2} \left( \frac{1 + \eta}{\eta} \right). \quad (1.12)$$

From equations (1.5) and (1.11) we see that when there is a level population inversion ( $n_2 > n_1$ ;  $\Delta n > 0$ ) then exponential amplification of the radiation can occur and we get a maser. There are two limiting cases for the maser emission. The first is the optically thin regime where  $\tau_\nu \ll 1$  and

$$e^{-\tau_\nu} \approx 1 + |\tau_\nu|. \quad (1.13)$$

In this case equation (1.5) becomes

$$I_\nu(\tau_\nu) = I_\nu(0)(1 + |\tau_\nu|) + S_\nu|\tau_\nu|, \quad (1.14)$$

and the radiation undergoes linear amplification proportional to the path length of the masing gas. In the second regime (optically thick;  $\tau_\nu \gg 1$ ) the solution to the equation of radiative transfer is simply

$$I_\nu(\tau_\nu) = I_\nu(0)e^{|\tau_\nu|} + S_\nu(1 - e^{|\tau_\nu|}), \quad (1.15)$$

and the result is exponential amplification of the radiation with increasing path length.

This exponential amplification of the radiation can't continue indefinitely, and saturation is the culprit that puts a damper on the party. To incorporate saturation effects into the simple two-level system, some additional transition mechanisms must be incorporated. These mechanisms include: loss rates out of each level which we will assume equal ( $\Gamma_1 = \Gamma_2 = \Gamma$ ), pump rates that populate the levels ( $P_1$  and  $P_2$ ), and collision rates which cause transitions between levels which we also assume equal ( $C_{12} = C_{21} = C$ ). Combining the rate equations for the sublevels and again assuming equal statistical weights, an expression for the population difference can be written

$$\Delta n = \frac{\Delta p - An}{(\Gamma + A + 2C) \left[ \frac{2B_{21}J_\nu}{(\Gamma + A + 2C)} + 1 \right]}, \quad (1.16)$$

where  $J_\nu$  is the angle averaged intensity of the radiation and  $\Delta p$  is the difference in the pump rates weighted by their statistical weights. If we let  $\Delta n_0$  be the population difference in the absence of radiation

$$\Delta n_0 = \frac{\Delta p - An}{(\Gamma + A + 2C)}, \quad (1.17)$$

and define the angle averaged saturation intensity

$$J_s = \frac{(\Gamma + A + 2C)}{2B}, \quad (1.18)$$

then we get a simplified expression for the population difference

$$\Delta n = \Delta n_0 \left( \frac{1}{1 + J_\nu/J_s} \right). \quad (1.19)$$

From equations (1.17)–(1.19) we note some interesting physics. First, the populations of the system levels is dependent upon the intensity of the radiation. To compute the radiation from the maser we must solve a set of nonlinear coupled equations. Second, one should notice that as the intensity increases above the saturation intensity,  $J_s$ , the level population difference is approximated by

$$\Delta n \approx \Delta n_0 \frac{J_s}{J_\nu}. \quad (1.20)$$

As  $J_\nu$  is increased,  $\Delta n$  decreases, and from equation (1.11) the optical depth  $\tau_\nu \ll 1$ . This is equivalent to the optically thin regime where the maser is linearly amplified. Thus, as the maser saturates it switches from exponential to linear amplification. Finally, if the collision rate ( $C$ ) becomes large then both  $\Delta n_0$  and  $\Delta n$  go to zero and the maser effect is destroyed (the levels *thermalize*).

### 1.1.3 Circumstellar Masers

The extended envelopes of many evolved stars display one or more of the three “classical” masers: SiO, H<sub>2</sub>O, and OH. These three species exist at various distances from the central star with the SiO masers populating the stellar atmosphere, and the H<sub>2</sub>O and OH masers lying farther out in the cool stellar wind at distances of  $\lesssim 10^{15}$  cm and  $\gtrsim 10^{16}$  cm respectively. Aside from the observational evidence placing the masers in these regions, there are several theoretical arguments for why the three species exist at different distances from the star. These arguments are based on the relative abundances of the various masing molecules and the excitation temperature of the particular maser species.

In addition to being the first detected maser line, OH also has the distinction of being the first circumstellar maser to be discovered (Wilson and Barrett 1968). OH emitting stars are frequently referred to as *OH/IR stars*. These stars are closely related to the Mira variables discussed in § 1.2.1, and their name reflects the strong emission in the infrared (IR) produced by circumstellar dust and the obvious OH maser emission. OH/IR stars are divided into two classes: *Type I* which exhibit the

strongest maser emission in the 1665-MHz and 1667-MHz OH mainline transitions, and *Type II* in which the 1612-MHz OH satellite-line is the strongest source of emission. Various types of evolved stars can fall into the OH/IR classification including long-period (Mira) variables, semiregular variables, and M-supergiants. These evolved stars are usually oxygen rich with surface temperatures ranging from  $\sim 2000\text{--}3000$  K. Most are surrounded by dust shells and undergo mass loss from a stellar wind which blows the dust and molecular gas away from the star. Goldreich and Scoville (1976) developed a theoretical model of the circumstellar envelope of an OH/IR star and showed that the OH molecules are produced from the dissociation of  $\text{H}_2\text{O}$  molecules by the interstellar ultraviolet (UV) radiation field and by collisions with dust grains in the stellar wind.

Type II OH/IR stars are the most well-studied of the two types, and they have a distinct double-peak spectral profile indicative of an expanding shell of emission. The two peaks of emission are generally separated by  $20\text{--}50$  km s $^{-1}$  and tend to have similar shapes. The outside edges of the features are abrupt, while the inside edges have a gradual downward taper towards the center. The strong blue- and red-shifted peaks are usually seen as compact features in spectral line channel maps marking the front and back of the shell respectively. The weaker features in the region of the taper usually show a ring-shaped distribution in the channel maps. The first model of circumstellar OH maser emission from Type II OH/IR stars (Elitzur, Goldreich, and Scoville 1976) demonstrated that the OH masers are radiatively pumped by far-infrared ( $35$   $\mu\text{m}$ ) photons emitted by nearby dust grains. This radiative pumping mechanism is supported by the observations of (Harvey et al. 1974). Through long-term monitoring of the emission towards 14 OH/IR stars they showed that there is virtually no phase difference between the 1612-MHz OH and the infrared emission. This lack of a phase-lag between the two types of emission establishes radiation as the most likely pumping mechanism for Type II OH/IR stars.

The 1665 and 1667-MHz emission displayed by Type I OH/IR stars is generally much weaker than the 1612-MHz masers in Type II OH/IR stars. The spectral profiles of the OH emission in Type I stars do not exhibit the characteristic double-peak structure of the Type II OH/IR stars, and the emission is usually confined to a smaller velocity range in the spectra. As in the 1612-MHz masers, the mainline transitions are inverted by far-infrared radiation from the circumstellar dust. Unlike the satellite line, the mainline inversions are much less stable and increases in the density of OH can eliminate the inversion altogether (Elitzur 1978).

Circumstellar  $\text{H}_2\text{O}$  masers were first detected towards the M-supergiant VY Canis Majoris (VY CMa) by Knowles et al. (1969). Like OH masers, they were found to exist in the stellar winds of evolved stars. The spectra of the 22-GHz  $\text{H}_2\text{O}$  emission towards the majority of late-type stars do not resemble the double-peak profile of

1612-MHz OH masers. In stars that contain both OH and water masers, the H<sub>2</sub>O commonly has a smaller velocity range centered within the range of the 1612-MHz emission. This smaller velocity range is expected since the water masers lie closer to the star in an accelerating wind. Theoretical arguments place the water masers in a spherical layer with a range  $\sim 10^{14} - 10^{16}$  cm. The inner boundary is set by the dust formation region where the densities required to form the dust thermalize the H<sub>2</sub>O levels and destroy the inversion. The outer boundary is set by the point where water is photodissociated by the interstellar UV field. Images of the Mira variable W Hydrae (W Hya) (Reid and Menten 1990) confirm that the H<sub>2</sub>O masers can lie close to the star at a distance of  $3 \times 10^{14}$  cm ( $\sim 20$  AU).

Water masers in the envelopes of late-type stars can have significant variations on timescales of a few months making long-term monitoring programs difficult. Despite this variability, Engels, Schmid-Burgk, and Walmsley (1986) were able to find a delay of  $\sim 0.1-0.2$  in the phase of the H<sub>2</sub>O emission relative to the stellar IR emission. This phase-lag suggests that the water maser inversion is pumped by a mechanism other than radiation. Detailed modeling of circumstellar H<sub>2</sub>O maser emission (Deguchi 1977; Cooke and Elitzur 1985; Palma et al. 1988) demonstrated that a collisional pumping is the source of the inversion. As in the case of OH emission, H<sub>2</sub>O masers in the envelopes of late-type stars have been well-studied and the physical properties have, for the most part, been properly identified.

The first detection of SiO maser emission was made towards a star-forming region named Orion A (Snyder and Buhl 1974). This was a surprising observation since SiO maser activity is a relatively rare occurrence towards these regions. SiO masers are more often found in the circumstellar envelopes of evolved stars. Discoveries of circumstellar SiO masers quickly followed the initial detection in Orion A. These detections include: Thaddeus et al. (1974) who detected the  $v = 1, J = 1 - 0$ , 43.122-GHz SiO transition towards W Hya, and Buhl et al. (1974) who observed the  $v = 1$  and  $v = 2, J = 1 - 0$  transitions at 43.122 GHz and 42.821 GHz towards W Hya, VY CMa, *o* Ceti (Mira itself), and R Leonis (R Leo). These were followed by observations of the  $v = 1, J = 2 - 1$ , 86.243-GHz emission towards 12 late-type stars (Kaifu, Buhl, and Snyder 1975) and the  $v = 3, J = 1 - 0$  transition at 42.519 GHz towards W Hya and VX Sagittarii (VX Sgr) (Scalise and Lépine 1978).

The first theoretical papers on circumstellar SiO emission were based on the success of earlier models of circumstellar OH masers which suggested the masers are radiatively pumped and reside in the stellar wind region. Likewise, early models of SiO maser emission (Geballe and Townes 1974; Kwan and Scoville 1974; Deguchi and Iguchi 1976) were based on these presumptions. It was later pointed out by Cahn and Elitzur (1979) that radiative pumping does not have the efficiency required to produce the observed SiO maser luminosities. Calculations by Elitzur (1980) and Langer

and Watson (1984) showed that the densities in the stellar wind are not sufficient to produce the observed maser strengths especially for the higher transitions (i.e.  $v = 3$ ). Elitzur (1980) suggested that SiO is collisionally pumped and the masers reside in the clumpy atmosphere of the star rather than the smooth stellar wind. Elitzur used the results of the first VLBI observations of circumstellar SiO to support this claim. Observations using a single 75-km baseline from the Haystack Observatory 36.6-m antenna to the Five College Radio Astronomy Observatory (FCRAO) 13.7-m antenna by Moran et al. (1979) showed that the SiO masers towards VX Sgr and R Cassiopeiae (R Cas), indeed, lie close to the star at distances of  $5 R_*$  and  $1.3 R_*$  respectively. Additional VLBI observations made with the same baseline (Lane 1984; McIntosh et al. 1989) confirmed the finding that circumstellar SiO masers, in general, lie  $\sim 2-6 R_*$  from the center of the star.

Elitzur (1992) presents several additional arguments explaining why the the SiO masers must reside inside the formation point for the stellar wind. First, SiO masers occur in a wide range of late-type stars including some with relatively low mass-loss rates. The vibrational transitions for SiO must be optically thick requiring a dense medium, but only those winds from stars with high mass-loss rates have this required density. Thus, SiO masers must be produced in a region which can account for SiO masers towards stars with low mass-loss rates (e.g. the stellar atmosphere). A second argument involves the abundance of circumstellar silicon, and the formation of silicate dust. Greater than 90% of the silicon in the interstellar medium is incorporated into dust grains. The stellar wind forms outside the dust formation point where radiation pressure can drive the momentum coupled gas and dust grains outward. If 90% of the available Si is wrapped up in dust grains, then gaseous SiO must be nearly non-existent outside the dust formation point. Finally, Nyman and Olofsson (1986) find no apparent association between the properties of the expanding wind, and those of the SiO masers. This suggests the SiO masers reside in a region unrelated to that of the stellar wind.

Recent VLBI observations have verified that the SiO masers do lie within the dust formation point close to the star. Earlier VLBI experiments, mentioned above, involved only a single baseline and maps were produced using less accurate fringe-frequency mapping techniques. More recently, high-resolution synthesis images have been produced of late-type stars U Herculis (U Her), TX Camelopardalis (TX Cam) (Diamond et al. 1994), W Hya (Miyoshi et al. 1994), VX Sgr (Greenhill et al. 1995), and R Aquarii (R Aqr) (Boboltz, Diamond, and Kemball 1997 and this dissertation). These images demonstrate that the masers lie in ring-like structures a few stellar radii from the center of the star. In addition, the observed ring structures are suggestive of tangential amplification of the maser emission (Diamond et al. 1994).

The observations of W Hya by Miyoshi et al. (1994) showed that the pumping

mechanism for SiO masers is most likely collisional. Through VLBI observations of the  $v = 1$  and  $v = 2$ ,  $J = 1 - 0$  emission, they determined the maser spots to be coincident in both transitions. This places severe restrictions on the pumping mechanism and essentially rules out a radiative pumping scheme since the energy required to excite SiO to the  $v = 2$  level ( $T = 3570$  K) is twice that of the  $v = 1$  level ( $T = 1785$  K). One would not expect a radiative mechanism to be able to provide pumping for both levels at the same position in space. An additional argument involving light travel times can be made against radiative pumping as the source of maser emission. In a long-term study of eight evolved stars Nyman and Olofsson (1986) found a phase-lag of  $\sim 0.1$ – $0.2$  between the visual amplitude of the variable star and the associated circumstellar SiO emission. The time for light to travel the distance to the SiO maser shell is on the order of a few hours. The phase-lag seen by Nyman and Olofsson should not occur if the pumping scheme is radiative.

## 1.2 Long-Period Variables and Symbiotic Binaries

Since this dissertation is based on observations of the long-period variable (LPV) star in the symbiotic binary R Aquarii, it is helpful to briefly discuss the properties of both long-period variables and symbiotic stars. A more detailed discussion of the specific properties of R Aquarii is presented in Chapter 4.

### 1.2.1 Mira Variables

Long-period variables, often called Mira variables after the prototype  $\alpha$  Ceti, are slowly varying stars which exhibit large variations in visual magnitude. Mira was first observed by the Dutch astronomer David Fabricius in 1596 who mistook the star for a nova (Burnham 1978). Thus, the star was not observed again until years later when it was eventually found to be a variable. Mira variables are late-type stars, generally red giants and supergiants, which exist on the far right end of the giant branch of the Hertzsprung-Russell (H-R) diagram. This region of the diagram is also known as the asymptotic giant branch (AGB) and the stars that reside there are referred to as *AGB stars*. Not all AGB stars are Miras, although all Miras are AGB stars (Habing 1990).

AGB stars are objects which have burned all their central hydrogen and helium and are left with a degenerate carbon/oxygen core. Surrounding the degenerate core are a layer of helium and a huge shell of hydrogen. In the early AGB phase the thick shell of helium burns while the outer envelope of hydrogen remains inert. During this early phase, the luminosity of the star rises. In the latter AGB stages

burning takes place in both shells with the helium burned during thermal pulses or flashes and the hydrogen burned continuously in the outer shell. During this latter phase, the luminosity of the star continues to increase as the carbon/oxygen core grows (Weidemann and Schönberner 1990). Theoretically, the density in the core could increase until the carbon is ignited resulting in a Type I supernova event. However, the star is able to eject enough mass from the outer envelope in the form of a stellar wind and/or planetary nebula to prevent this from happening. The remaining degenerate core continues to rise in temperature until it is hot enough ( $\sim 30,000$  K) to ionize the surrounding ejecta which then appears as a planetary nebula (Weidemann and Schönberner 1990).

Stars classified as Mira variables generally have amplitude variations  $\gtrsim 2$  mag and periods  $\gtrsim 90$  days. Variable stars with periods  $< 90$  days nearly always show irregularities and are thus classified as semiregular variables (Hoffmeister, Richter, and Wenzel 1985). The majority of Mira variables have periods in the range of 200–400 days with a few exceeding 700 days. The absolute bolometric range for Miras is on the order of 1 magnitude although the variations at visual wavelengths for most Miras are quite large  $\sim 5$ – $6$  mag with some exceeding 9 mag (e.g.  $\chi$  Cygni). This is mainly due to huge opacity variations at optical wavelengths. Mira (*o* Ceti) itself has a magnitude range of  $\sim 6$  over a period of  $\sim 331$  days (Burnham 1978).

It is generally thought that at some point during the AGB phase the luminosity increases enough so that the star's envelope becomes unstable to radial pulsations and the star develops large amplitude variations (Habing 1990). At this point the star becomes a variable with the initial period of the pulsations dependent upon the total mass of the star. As the star grows older it continuously loses mass, its luminosity increases, and its period grows. This process is eventually halted when enough matter has been lost such that the star can support its own weight. The result is a white dwarf and a planetary nebula as mentioned above. The relationship between the period and the kinematic properties of Mira variables was first observed by Feast (1963). Through statistical analysis, Feast determined that Miras with longer periods ( $\gtrsim 300$  days) are, in general, more massive than those with shorter periods. These longer period Miras are kinematically younger and belong to the same population as planetary nebulae. The obvious conclusion is that Miras are the progenitors of planetary nebulae (Habing 1990).

As in other variable stars, Mira variables exhibit a relationship between the period, the mass, and the luminosity of the star. Numerous methods for determining the period–luminosity relationship at visual and infrared wavelengths have been developed over the years (e.g. Clayton and Feast 1969; Cahn and Wyatt 1978; Wyatt and Cahn 1983; Feast et al. 1989). These methods are well established and provide a reliable means of determining the distances to Mira variables.

Approximately 90% of the stars classified as Miras belong to the M spectral class, with the rest divided among spectral classes S, R, and N (these latter types are often classified as C-type carbon stars). The optical spectra of M-type Miras are dominated by strong titanium oxide (TiO) absorption bands and hydrogen emission lines. Maser emission occurs in the oxygen-rich M-type Miras, while the carbon stars do not exhibit maser emission from the three classical molecules, SiO, H<sub>2</sub>O, and OH. This is because the oxygen necessary to form SiO, H<sub>2</sub>O, and OH is locked up in CO. Closely related to the M-type Mira variables are the OH/IR stars discussed in § 1.1.3. These stars were not detected in the original searches for Miras made at optical wavelengths because a thick circumstellar dust shell surrounding the star converts the stellar light to infrared radiation which peaks at around 10  $\mu\text{m}$ . These OH/IR stars escaped detection until several were found in the first infrared survey (IRC). The majority of OH/IR stars are very long-period variables with periods ranging from 500 to 1600 days. They also have large amplitude variations; bolometric amplitude shifts of  $\sim 2$  mag are no exception. These long periods can be explained if we assume that the OH/IR stars have evolved up the asymptotic giant branch and have experienced considerable mass loss (Habing 1990).

## 1.2.2 Symbiotic Binaries

The term *symbiotic star* describes an inhomogeneous collection of sources whose spectra (infrared–ultraviolet) show evidence for the presence of a cool late-type star in conjunction with a hot circumstellar nebula. The cool star, generally a red giant or long-period variable, is seen in the optical spectra through absorption bands such as: CO, H<sub>2</sub>O, and TiO. The nebula and hot companion are seen through high-excitation emission lines (i.e. H I, He I, He II, Fe II, [Fe II], [O III] and, [Fe VII]) along with blue continuum emission. There are over 150 stars in our own galaxy and a few in other Local Group galaxies which are classified as symbiotic stars (Kenyon 1992). Although there are models describing symbiotics as single objects such as a red giant/supergiant in transition to a planetary nebula, they are commonly believed to be interacting binaries in which a compact companion (a main-sequence star or white dwarf) accretes matter from a late-type star.

Symbiotic binaries are divided into two categories depending on the temperature of the cool star derived from near-infrared (*JHKL*-band; 1–6  $\mu\text{m}$ ) photometry. These two categories are the *D(usty)-type* and the *S(tellar)-type*. The S-type symbiotics are consistent with low variability ( $\Delta M_K \lesssim 0.1\text{--}0.2$  mag) red giants with strong 2.3  $\mu\text{m}$  CO absorption bands and modest mid-infrared excesses. On the other hand, the D-type systems, usually contain a long-period variable ( $\Delta M_K \approx 1$  mag;  $P \approx 300\text{--}700$  days) with strong 2  $\mu\text{m}$  CO and H<sub>2</sub>O absorption bands and high mid-infrared excesses (Kenyon 1992).

There are two commonly accepted mechanisms by which the symbiotic binaries are thought to produce their unusual characteristics. The first occurs when a red giant primary overflows its Roche-lobe, and the secondary, most likely a main-sequence star, accretes material through a disk. The classical example of this mechanism is CI Cygni in which an M4 giant sheds material onto its main-sequence companion through a thick disk. Temperatures up to 160,000 K are formed near the boundary between the companion and the disk (Allen 1984). The second mechanism involves accretion of outflowing material from primary by the companion, probably a white dwarf or subdwarf. In this case the primary is not large enough to fill its Roche-lobe, so the mass transfer must occur via the primary's stellar wind. This type of symbiotic can be divided into two sub-classes depending on the primary. First is the case where the primary is a non-pulsating red giant. Examples are RW Hydrae, and AG Pegasi. The second class are those symbiotics in which the primary is a Mira variable accompanied by its surrounding dust-shell. Good examples of this type of system are V1016 Cygni and H1-36 Arae (Kenyon 1992). R Aqr most likely belongs to this second sub-class.

Of the 20% of symbiotics that contain Mira variables, relatively few have had their periods determined. The average period of those symbiotic Miras which are known is longer than that of their isolated counterparts. Recalling that the period is related to the mass and the age of a Mira, the D-type symbiotics most likely belong to a younger population than the typical isolated Mira. According to Whitelock (1987) there are two possible explanations for the lack of short-period symbiotic Miras: either they don't exist, or they are not obviously symbiotic. Although there is little information on the frequency of symbiotic Miras among various populations, what little evidence there is suggests that they are not found in older populations (Whitelock 1987). An alternative explanation is the possibility that the short-period symbiotics somehow differ from their long-period counterparts. Since stellar wind capture by the companion is the proposed mechanism responsible for the symbiotic characteristics, and since the mass loss from a Mira is proportional to the period, it is possible that the mass loss in short-period symbiotic Miras is insufficient to produce the observable symbiotic phenomena (Whitelock 1987).

It is clear in the D-type symbiotics that the formation of a dust shell around the Mira is not impeded by the companion. One could therefore expect to find maser emission, at least in SiO which should be shielded from the UV emission of the companion and the nebula, in some of these objects. It is less clear whether we should expect to find H<sub>2</sub>O or OH masers towards symbiotic Miras since they reside further out in the stellar wind where the UV radiation could dissociate the molecules.

Recent studies of the maser emission towards Mira-type symbiotic binaries have yielded interesting results when compared to isolated Miras. In a survey of 29 D-type

symbiotics Schwarz et al. (1995) detected SiO maser emission at 86.243 GHz in only three sources. Two are true symbiotics (R Aqr and H1–36) while the other, *o* Ceti (Mira itself), is only mildly symbiotic. They concluded that symbiotic Miras either typically have no SiO maser emission, or they are extremely underluminous.

In a highly sensitive search for 1612-MHz OH and 22.235-GHz H<sub>2</sub>O line emission towards a sample of 24 symbiotic binaries, Seaquist, Ivison, and Hall (1995) came to the same basic conclusion. Of the 24 sources, they detected H<sub>2</sub>O masers towards R Aqr and H1–36 and OH masers towards only H1–36. Comparing these and the SiO observations by Schwarz et al. to surveys of isolated Miras, they concluded that the most likely explanation for the lack of masers towards symbiotic Miras is the colliding winds model described in Girard and Willson (1987). In this model the hot wind from the companion collides with, and pushes back, the dusty Mira wind exposing the Mira to the UV photons from the companion. All molecules in the evacuated cavity are dissociated; those on the side towards the companion by direct UV photons, and those on the side shadowed by the Mira by Rayleigh scattering of UV photons off the inner wind region. They go on to propose that R Aqr and H1–36 are atypical symbiotics in which the molecules are protected from dissociation either by large binary orbits or by underluminous companions. In either case R Aqr is truly a unique object even by symbiotic standards.

## 1.3 Very Long Baseline Interferometry

### 1.3.1 Basic VLBI Theory

The development of very long baseline interferometry was motivated by two astronomical findings: (1) the radiation emitting regions in quasars were found to be on the order of a few light-days in size, and (2) the discovery of OH masers which proved to be unresolved on existing connected-element interferometers (Burke and Graham-Smith 1997). To study these two phenomena, radio astronomers required an instrument which could provide much higher angular resolution. This instrument is the very long baseline interferometer. This section is meant to be a brief introduction to VLBI, therefore many of the finer details have been excluded. For further information, the reader is referred to the comprehensive reviews on radio interferometry in general (Thompson, Moran, and Swenson 1986 (hereafter TMS); Perley, Schwab, and Bridle 1989), and on VLBI specifically (Felli and Spencer 1989; Zensus, Diamond, and Napier 1995).

We begin the discussion by considering a quasi-monochromatic plane wave with frequency  $\nu$  incident from a distant celestial source. Neglecting the vector nature

of the radiation for the time being, the electric field from direction  $\mathbf{s}(\eta, \xi)$  can be expressed as

$$E(\mathbf{s}, t) = E(\mathbf{s}, \nu)e^{2\pi i\nu t}. \quad (1.21)$$

Among the properties of  $E(\mathbf{s}, t)$  is the correlation of the field at two different locations  $i$  and  $j$  given by

$$\Gamma(\mathbf{r}_i, \mathbf{r}_j) = \langle E(\mathbf{s}_i, t)E^*(\mathbf{s}_j, t - \tau) \rangle, \quad (1.22)$$

where the angle brackets  $\langle \rangle$  indicate the expectation value, the  $*$  denotes the complex conjugate, and

$$\tau = \frac{|\mathbf{r}_i - \mathbf{r}_j| \cdot \mathbf{s}}{c}, \quad (1.23)$$

is the delay between the reception of the wave front at the two locations. Equation 1.22 is called the *spatial coherence function*, and interferometers are devices which measure this function. The vector  $(\mathbf{r}_i - \mathbf{r}_j)$ , generally referred to as the *baseline*, connects the two incident locations which, in the case of an interferometer, are called *stations* or simply *antennas*.

If we make the assumption that the radiation from different parts of the source is spatially incoherent

$$\langle E(\mathbf{s}_i)E^*(\mathbf{s}_j) \rangle = \delta(\mathbf{s}_i - \mathbf{s}_j)\langle E(\mathbf{s})E^*(\mathbf{s}) \rangle. \quad (1.24)$$

and we assume that the source is both very far away ( $\mathbf{s} = \mathbf{s}_0 + \epsilon$ ) and small in angular extent, then the spatial coherence function may be expressed in terms of the intensity distribution of the radiation as

$$\Gamma(u, v, \tau) = \iint I(\eta, \xi, \tau)e^{-2\pi i(u\eta + v\xi)} d\eta d\xi. \quad (1.25)$$

In the above expression,  $(\eta, \xi)$  are the angular coordinates on the sky and  $(u, v)$  are coordinates in the spatial frequency plane (also called the *visibility plane*). The  $(u, v)$  plane is orthogonal to the direction of the source  $\mathbf{s}_0$  called the *phase tracking center*. This form of the source coherence function is a Fourier transform which can be inverted to recover the source intensity distribution (also called the sky brightness distribution)

$$I(\eta, \xi, \tau) = \iint \Gamma(u, v, \tau)e^{2\pi i(u\eta + v\xi)} dudv. \quad (1.26)$$

If we are able to sample enough of the visibility plane by using an array of antennas with varying baselines, then the sky brightness distribution of the source can be recovered.

In practice, interferometers sample the spatial coherence function by receiving the source radiation  $E(\mathbf{r}_i, t)$  at the array elements over time. As the interferometer tracks the source across the sky, the projected baselines of the element pairs change with the rotation of the Earth. This adds information by sampling new spatial frequencies in the  $(u, v)$  plane. The signal received at an antenna is typically very weak and is thus amplified by a low-noise amplifier to a more usable value. The signal is then converted from the sky-frequency measured by the antenna to a lower intermediate frequency (IF) by mixing it with the signal from a phase-stable local oscillator (typically a maser). The signal is then sent to a baseband converter (BBC) which converts the IF to baseband using a single-sideband mixer.

The next step in the signal path is the transmission of the IF to a central location for correlation. At this stage, connected-element interferometers diverge from VLB interferometers. For connected-element interferometers the IF signal is transmitted over the relatively short distances via coaxial cable, waveguide, or fiber optic cable. In the case of VLB instruments even fiber optic cables are impractical for transmission over the long (sometimes intercontinental) distances. Thus, the choice for transmitting the IF signals for VLBI experiments is magnetic tape. In VLB interferometers, the digital signals from the sampler are sent to a formatter which adds a series of time-stamps provided by the local oscillator and writes the data stream out to tape. Figure 1.1 shows the signal path diagram for a typical VLBI setup.

The final stage in the signal path of all interferometers is a device called a correlator. Ideally, the basic function of the correlator is to average and cross-multiply the signals from the interferometer elements. In reality, the implementation of this task is quite complicated mainly due to geometrical effects which are the result of locating the interferometer elements on the surface of a spherical object (the Earth) with complex motion in time. The correlator forms the complex cross-correlation function of the independent signals  $E(\mathbf{r}_i, t)$  and  $E(\mathbf{r}_j, t)$  as

$$r(u, v, \tau) = \langle E(\mathbf{r}_i, t) E^*(\mathbf{r}_j, t - \tau) \rangle. \quad (1.27)$$

The source coherence function  $\Gamma(u, v, \tau)$  can be determined from the cross-correlation function  $r(u, v, \tau)$  if one is able to remove (through calibration) the errors caused by instrumentation, propagation, and geometric effects (Kemball 1992).

### 1.3.2 Spectropolarimetry

Thus far, two important assumptions, which are especially relevant to this thesis, have yet to be discussed. The first is the assumption that the plane wave is quasi-monochromatic. In practice, the selection of a quasi-monochromatic component can be implemented with the use of electronic or digital filtering in the signal path. If the

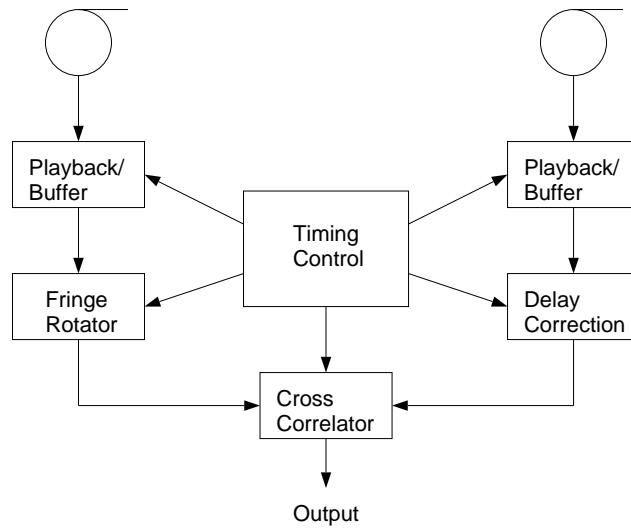
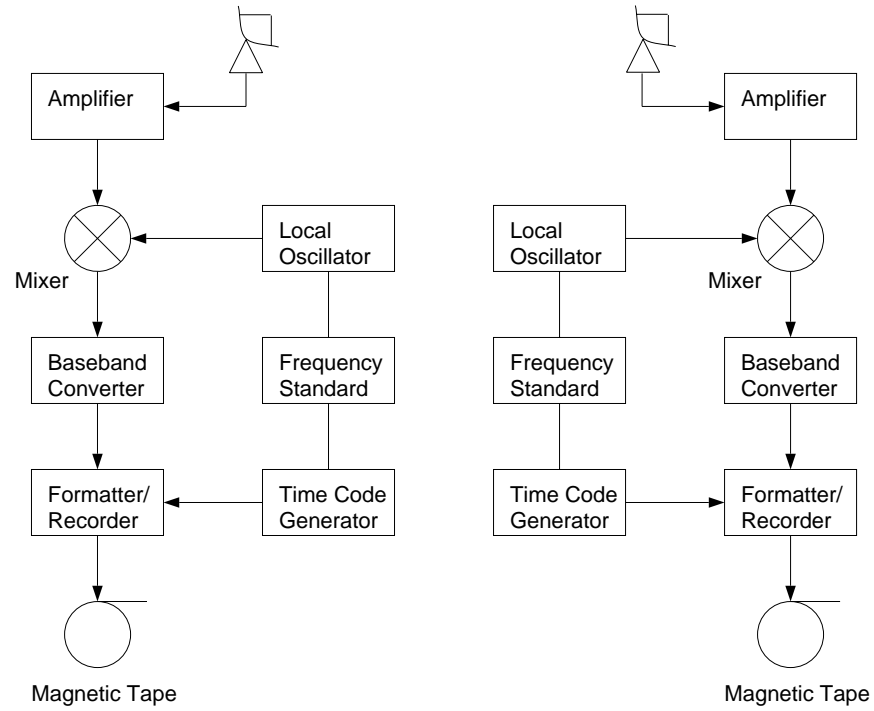


Figure 1.1: Schematic diagram of a generic VLBI signal path.

goal is to do VLBI spectroscopy, then we would like to form a spectrum which includes a range of desired frequencies. An interferometer measures the cross-correlation function  $r(u, v, \tau)$  in equation 1.27 above. Following the notation of Romney (1995), the quasi-monochromatic plane wave may be expressed as

$$E(\mathbf{r}_i, t) = A(\mathbf{r}_i, t)e^{2\pi i\nu_0 t}, \quad (1.28)$$

and equation 1.27 can be rewritten in the form

$$r(u, v, \tau) = \langle A(t + \tau)A^*(t) \rangle e^{2\pi i\nu_0 \tau}. \quad (1.29)$$

A Fourier transform relation holds for  $r(u, v, \tau)$  in the delay-frequency domain as well as the spatial domain. This relationship is given by

$$S(u, v, \nu) = \int r(u, v, \tau)e^{-2\pi i\nu\tau} d\tau, \quad (1.30)$$

where  $S(u, v, \nu)$  is the cross-correlation spectrum. This cross-correlation spectrum is the desired output for spectral line VLBI experiments and it is produced by a device called the correlator.

There are two different approaches to correlating the data collected by the array. The first approach is known as *lag* correlation. The signal that arrives at each antenna  $i$  is delayed an amount  $\delta_i$  and is phase rotated by an amount  $\theta_i(t)$  such that the output  $X_i(t)$  is given by

$$X_i(t) = A(t + \tau_i - \delta_i)e^{2\pi i\nu_0\tau_i - i\theta_i(t)}. \quad (1.31)$$

The phase rotation is corrected prior to correlation in a process that is known as *stopping the fringes*. The lag correlator provides a range of values for  $\delta_i$  or lags. The cross-correlation function  $r(u, v, \tau)$  is then formed by cross-multiplying the lagged signals. Finally, the cross-power spectra are constructed by Fourier transforming  $r(u, v, \tau)$ . Lag correlators are also known as XF (cross-multiplication, Fourier transform) correlators.

The second implementation of the correlation process is known as FX (Fourier transform, cross-multiplication) or *spectral-domain* correlation. Here, the delay and phase compensated signals from each array element  $X_i(u, v, t)$  are Fourier transformed using

$$s_i(u, v, \nu) = \int X_i(u, v, t)e^{-2\pi i\nu t} dt, \quad (1.32)$$

to form the spectra for each station  $s_i(u, v, \nu)$ . These spectra are then cross-multiplied as

$$S_{ij}(u, v, \nu) = s_i(u, v, \nu)s_j^*(u, v, \nu) \quad (1.33)$$

yielding the desired cross-power spectra  $S_{ij}(u, v, \nu)$ .

The second assumption which has yet to be discussed is the vector nature of the received electric field. This is especially relevant with respect to polarization observations (the subject of this dissertation). In the discussion that follows, the notation of Kemball (1992) will be utilized. The electric field from direction  $\mathbf{s}(\eta, \xi)$ , expressed as a scalar in equation 1.21, can be rewritten (explicitly showing the vector nature) in terms of right- and left-circularly polarized components as

$$\begin{aligned} E^R(\eta, \xi, t) &= \frac{1}{\sqrt{2}} E^R(\eta, \xi, \nu) (\mathbf{e}_\delta - i\mathbf{e}_\alpha) e^{2\pi i \nu t} \\ E^L(\eta, \xi, t) &= \frac{1}{\sqrt{2}} E^L(\eta, \xi, \nu) (\mathbf{e}_\delta + i\mathbf{e}_\alpha) e^{2\pi i \nu t}, \end{aligned} \quad (1.34)$$

where  $(\mathbf{e}_\delta, \mathbf{e}_\alpha)$  are unit vectors on the plane of the sky in the direction of increasing declination (north) and right ascension (east) (Kemball 1992). The components  $E^R$  and  $E^L$  describe the polarization state of the electric field. The polarization of an astronomical source is typically characterized by the set of four Stokes parameters which in the circularly polarized bases are defined as

$$\begin{aligned} I(\eta, \xi, \nu) &= 1/2 \times (\langle E^R E^{R*} \rangle + \langle E^L E^{L*} \rangle) \\ Q(\eta, \xi, \nu) &= 1/2 \times (\langle E^R E^{L*} \rangle + \langle E^L E^{R*} \rangle) \\ U(\eta, \xi, \nu) &= 1/2 \times i(\langle E^L E^{R*} \rangle - \langle E^R E^{L*} \rangle) \\ V(\eta, \xi, \nu) &= 1/2 \times (\langle E^R E^{R*} \rangle - \langle E^L E^{L*} \rangle). \end{aligned} \quad (1.35)$$

The interferometer antennas which receive the radiation have orthogonal feeds sensitive to either right- or left-circularly polarized emission (there are interferometers with linearly polarized feeds, but they are not considered here). The correlations derived from the various combinations of the two feeds are denoted  $RR$ ,  $LL$ ,  $RL$ , and  $LR$ , and they are related to the Stokes parameters by

$$\begin{aligned} RR(\eta, \xi, \nu) &= I(\eta, \xi, \nu) + V(\eta, \xi, \nu) \\ LL(\eta, \xi, \nu) &= I(\eta, \xi, \nu) - V(\eta, \xi, \nu) \\ RL(\eta, \xi, \nu) &= Q(\eta, \xi, \nu) + iU(\eta, \xi, \nu) \\ LR(\eta, \xi, \nu) &= Q(\eta, \xi, \nu) - iU(\eta, \xi, \nu). \end{aligned} \quad (1.36)$$

The four Stokes parameters satisfy the Fourier transform relation with counterparts

in the visibility plane given by

$$\begin{aligned}
 I(\eta, \xi, \nu) & \mathcal{F} \quad \mathcal{I}(u, v, \nu) = 1/2 \times [\mathcal{R}\mathcal{R}(u, v, \nu) + \mathcal{L}\mathcal{L}(u, v, \nu)] \\
 Q(\eta, \xi, \nu) & \mathcal{F} \quad \mathcal{Q}(u, v, \nu) = 1/2 \times [\mathcal{R}\mathcal{L}(u, v, \nu) + \mathcal{L}\mathcal{R}(u, v, \nu)] \\
 U(\eta, \xi, \nu) & \mathcal{F} \quad \mathcal{U}(u, v, \nu) = 1/2 \times i[\mathcal{L}\mathcal{R}(u, v, \nu) - \mathcal{R}\mathcal{L}(u, v, \nu)] \\
 V(\eta, \xi, \nu) & \mathcal{F} \quad \mathcal{V}(u, v, \nu) = 1/2 \times [\mathcal{R}\mathcal{R}(u, v, \nu) - \mathcal{L}\mathcal{L}(u, v, \nu)],
 \end{aligned} \tag{1.37}$$

where  $\mathcal{F}$  denotes the Fourier transform (Kemball 1992). With proper calibration of the cross-correlation functions ( $\mathcal{R}\mathcal{R}, \mathcal{R}\mathcal{L}, \mathcal{L}\mathcal{R}, \mathcal{L}\mathcal{L}$ ) the Stokes parameters in the visibility plane ( $\mathcal{I}, \mathcal{Q}, \mathcal{U}, \mathcal{V}$ ) can be determined and Fourier transformed to recover the sky brightness distribution of the source in each of the Stokes parameters ( $I, Q, U, V$ ).

## 1.4 Dissertation Goals

Early VLBI observations of SiO masers were limited to a single 75-km baseline from Haystack Observatory to FCRAO. In these early experiments, the possibility of structure on smaller scales was discussed, but the facilities to investigate such structure were unavailable at the time. In June of 1990, Colomer et al. (1992) observed 18 late-type stars plus Orion A with a three element VLBI array having projected baselines ranging from 330 to 1740 km. Circumstellar SiO emission was detected on baselines as long as  $\sim 1500$  km with estimated spot sizes ranging from 0.4–3.0 mas (0.1–4.5 AU). With the installation of the 7-mm receivers on the Very Long Baseline Array (VLBA) a dedicated VLBI facility of the National Radio Astronomy Observatory (NRAO <sup>1</sup>), circumstellar SiO masers have now been detected on baselines  $\sim 8600$  km (Mauna Kea, HI–St. Croix, VI) implying feature sizes of  $\lesssim 3 \times 10^{11}$  cm ( $\lesssim 0.02$  AU). The VLBA is a homogeneous array consisting of 10 identical 25-m antennas with baselines that stretch across the United States. A diagram of the 10 elements comprising the array is shown in Figure 1.2, and the locations of the individual stations are listed in Table 1.2.

The VLBA has had significant impact on the study of circumstellar SiO masers. The first high-resolution synthesis images of the late-type stars TX Cam and U Her (Diamond et al. 1994) showed that the masers lie in a ring-like structure inside the circumstellar dust shell. In addition, full-polarization images of TX Cam (Kemball and Diamond 1997) have also been made from VLBA observations. Kemball and Diamond have shown that it is now possible to directly map the magnetic field in

---

<sup>1</sup>The National Radio Astronomy Observatory is operated by Associated Universities, Inc., under cooperative agreement with the National Science Foundation.

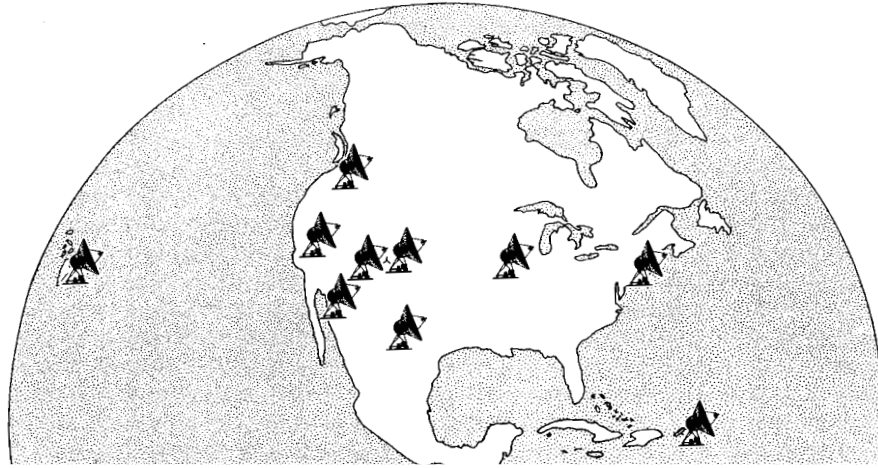


Figure 1.2: Locations of the 10 VLBA antennas. (VLBA-Management 1992)

the extended atmospheres of Mira variables. The positive results from early VLBA observations of circumstellar SiO sources led to a proposed monitoring program of 7 late-type stars (Diamond et al. 1994). Four epochs of observations were granted and were designated: BD21, BD27a, BD27b, and BD27c. This dissertation presents the results of this monitoring program for the most unusual source in the group, the symbiotic binary R Aquarii. The principal objectives of this dissertation are as follows:

1. To map the circumstellar SiO maser emission towards R Aquarii at high resolution, and to compare the resulting images to the ring-like structures exhibited by isolated late-type stars.
2. To monitor changes in the structure of the maser emission in time, and to compare the structure sampled at various phases in the Mira's stellar cycle.
3. To determine the proper motion of individual maser spots and the motion of the masing region as a whole. It is unknown whether the masers lie in a region of outflow or inflow and what effect the pulsations of the Mira have on this region.
4. To determine the polarization structure of the R Aquarii SiO maser emission, and to image the magnetic field in the stellar atmosphere close to the Mira.

Table 1.2: Locations of the antennas of the Very Long Baseline Array (Zensus, Diamond, and Napier 1995).

Physical Location	N. Latitude ( $^{\circ}$ ;';")	W. Longitude ( $^{\circ}$ ;';")	Elevation (m)	Antenna Code
St. Croix, VI	17 45 30.57	64 35 02.61	16	SC
Hancock, NH	42 56 00.96	71 59 11.69	309	HN
North Liberty, IA	41 46 17.03	91 34 26.35	241	NL
Fort Davis, TX	30 38 05.63	103 56 39.13	1615	FD
Los Alamos, NM	35 46 30.33	106 14 42.01	1967	LA
Pie Town, NM	34 18 03.61	108 07 07.24	2371	PT
Kitt Peak, AZ	31 57 22.39	111 36 42.26	1916	KP
Owens Valley, CA	37 13 54.19	118 16 33.98	1207	OV
Brewster, WA	48 07 52.80	119 40 55.34	255	BR
Mauna Kea, HI	19 48 15.85	155 27 28.95	3720	MK

5. To monitor the variations of the polarization structure as a function of time, and to determine the time evolution of the circumstellar magnetic field.

In Chapter 2, I will discuss the data reduction necessary to calibrate and image the full-polarization spectral-line VLBA data taken in the above experiments. The results from each of the four epochs of observation are presented in Chapter 3. Chapter 4 provides some background information on the source R Aquarii including a review of previous observational and theoretical studies. Chapters 5 and 6 discuss the results of the image analysis as they pertain to the kinematics and polarization characteristics of R Aquarii. Finally, Chapter 7 gives a summary of the results from this dissertation and the possibilities for future work.

## Chapter 2

# REDUCTION OF VLBI SPECTROPOLARIMETRY DATA

“Spectral line VLBI could be defined by some people as the most masochistic area of radio interferometry. ”

*Dr. Philip Diamond, Spectral Line Techniques, 1989*

### 2.1 Introduction

In § 1.3 I alluded to the fact that if the errors due to instrumentation, propagation, and geometrical effects could be removed by calibrating the data, then the source coherence function can be derived from the cross-correlation function. The source coherence function may then be Fourier inverted to regain the source brightness distribution through standard self-calibration and imaging techniques. For full-polarization spectral line VLBI observations, this calibration process can be quite complex.

Polarization observations on connected-element interferometers such as the Very Large Array (VLA) have become relatively routine, and the calibration methodology is well established. Observations of continuum sources in polarized light have extended these reduction techniques to the VLBI regimes. Detailed discussions of continuum VLBI polarization reduction methods can be found in Cotton (1993), Roberts, Wardle, and Brown (1994), Cotton (1995) and references therein.

Until recently, calibration techniques for VLBI spectral line polarization observations had not reached a level of development comparable to that of continuum VLBI polarimetry. Early work based on observations of the 1665-MHz OH maser

emission towards W3(OH) (García-Barreto et al. 1988; Bloemhof, Reid, and Moran 1992) showed the feasibility of VLBI spectropolarimetry, but the results reported in these early experiments were produced using less accurate baseline-based calibration methods. Recently, an antenna-based calibration formalism has been developed for spectral line polarization VLBI data sets (Kemball 1992; Kemball, Diamond, and Cotton 1995). These techniques have been applied to observations of the 1612-MHz OH masers towards the OH/IR star IRC+10420 (Kemball 1992; Kemball and Diamond 1993), to observations of the 43-GHz SiO masers towards the Mira variable TX Cam (Kemball and Diamond 1997), and to high-frequency (43-GHz) continuum observations of 3C 454.3 (Kemball, Diamond, and Pauliny-Toth 1996). The reduction of the observations contained in this thesis follow this formalism.

## 2.2 Response of the VLBI Array

Basic VLBI theory was discussed in § 1.3, but little mention was made regarding the errors involved in practical interferometry. For actual interferometer arrays, the cross-power spectrum of equation 1.30 can be expressed in terms of a Fourier transform relation given by

$$S_{ij}^{pq}(u, v, \nu) = [G_i^p(\nu, t)G_j^{q*}(\nu, t)] [B_i^p(\nu)B_j^{q*}(\nu)] \times \iint \langle V_i^p(\eta, \psi, \nu)V_j^{q*}(\eta, \xi, \nu) \rangle e^{-2\pi i(\eta u + \xi v)} d\eta d\xi \quad (2.1)$$

where  $V_i^p$  is proportional to the feed voltage of antenna  $i$  in polarization  $p$ . The complex antenna gain

$$G_i^p(\nu, t) = g_i^p(t)e^{i\phi_i^p(\nu, t)}, \quad (2.2)$$

incorporates all instrumental and atmospheric effects in the form of phase  $\phi_i^p(\nu, t)$  and amplitude  $g_i^p(t)$  gains. The complex bandpass response given by  $B_i^p(\nu)$  is assumed constant over the duration of a typical VLBI experiment. The right- and left-circularly polarized feeds on actual antennas are not perfect, and they admit some fraction of the orthogonal polarization. Thus, the received modes will be slightly elliptical due to this feed *leakage*. The voltages in equation 2.1 above can be expressed in terms of

the linear feed model of Conway and Kronberg (1969) as

$$\begin{aligned} V_i^R &= \frac{1}{\sqrt{1 + D^{R*}D^R}} (E^R e^{-i\alpha(t)} + D^R E^L e^{+i[\alpha(t) + \gamma^{L-R}]}) \\ V_i^L &= \frac{1}{\sqrt{1 + D^{L*}D^L}} (E^L e^{+i\alpha(t)} + D^L E^R e^{-i[\alpha(t) + \gamma^{R-L}]}), \end{aligned} \quad (2.3)$$

where  $D^R$  and  $D^L$  are the complex feed contamination terms, often called *D-terms* representing the degree of contamination by the orthogonal polarization. The two terms in the exponential ( $\alpha(t)$  and  $\gamma^{R-L}$ ) represent undesired phase rotations due to time-dependent changes in the parallactic angle and ionospheric Faraday rotation respectively. The *D-terms* for the feeds are designed to be small and the first term on the right-hand side of the above expression is  $\sim 1$ .

The spectra for the various cross-correlations  $S_{ij}^{pq}$  can be expressed in terms of the feed voltages by substituting equation 2.3 into equation 2.1. In addition, the integrals can be eliminated by taking advantage of the Fourier transform relation given by equation 1.37. The spectra can then be written in terms of the cross-correlation functions in the visibility plane  $[(\mathcal{R}\mathcal{R}, \mathcal{R}\mathcal{L}, \mathcal{L}\mathcal{R}, \mathcal{L}\mathcal{L})(u, v, \nu)]$  as (Kemball 1992)

$$\begin{aligned} S_{ij}^{RR} &= (G_i^R G_j^{R*}) (B_i^R B_j^{R*}) \left[ (\mathcal{R}\mathcal{R}) e^{-i(\alpha_i - \alpha_j)} + (\mathcal{R}\mathcal{L}) D_j^{R*} e^{-i(\alpha_i + \alpha_j)} e^{i\gamma_j^{R-L}} \right. \\ &\quad \left. + (\mathcal{L}\mathcal{R}) D_i^R e^{i(\alpha_i + \alpha_j)} e^{i\gamma_i^{L-R}} + (\mathcal{L}\mathcal{L}) D_i^R D_j^{R*} e^{i(\alpha_i - \alpha_j)} e^{i(\gamma_i^{L-R} - \gamma_j^{L-R})} \right] \\ S_{ij}^{RL} &= (G_i^R G_j^{L*}) (B_i^R B_j^{L*}) \left[ (\mathcal{R}\mathcal{L}) e^{-i(\alpha_i + \alpha_j)} + (\mathcal{R}\mathcal{R}) D_j^{L*} e^{-i(\alpha_i - \alpha_j)} e^{i\gamma_j^{L-R}} \right. \\ &\quad \left. + (\mathcal{L}\mathcal{L}) D_i^R e^{i(\alpha_i - \alpha_j)} e^{i\gamma_i^{L-R}} + (\mathcal{L}\mathcal{R}) D_i^R D_j^{L*} e^{i(\alpha_i + \alpha_j)} e^{i(\gamma_i^{L-R} - \gamma_j^{R-L})} \right] \\ S_{ij}^{LR} &= (G_i^L G_j^{R*}) (B_i^L B_j^{R*}) \left[ (\mathcal{L}\mathcal{R}) e^{i(\alpha_i + \alpha_j)} + (\mathcal{L}\mathcal{L}) D_j^{R*} e^{i(\alpha_i - \alpha_j)} e^{i\gamma_j^{R-L}} \right. \\ &\quad \left. + (\mathcal{R}\mathcal{R}) D_i^L e^{-i(\alpha_i - \alpha_j)} e^{i\gamma_i^{R-L}} + (\mathcal{R}\mathcal{L}) D_i^L D_j^{R*} e^{-i(\alpha_i + \alpha_j)} e^{i(\gamma_i^{R-L} - \gamma_j^{R-L})} \right] \\ S_{ij}^{LL} &= (G_i^L G_j^{L*}) (B_i^L B_j^{L*}) \left[ (\mathcal{L}\mathcal{L}) e^{i(\alpha_i - \alpha_j)} + (\mathcal{L}\mathcal{R}) D_j^{L*} e^{i(\alpha_i + \alpha_j)} e^{i\gamma_j^{L-R}} \right. \\ &\quad \left. + (\mathcal{R}\mathcal{L}) D_i^L e^{-i(\alpha_i + \alpha_j)} e^{i\gamma_i^{R-L}} + (\mathcal{R}\mathcal{R}) D_i^L D_j^{L*} e^{-i(\alpha_i - \alpha_j)} e^{i(\gamma_i^{R-L} - \gamma_j^{R-L})} \right]. \end{aligned} \quad (2.4)$$

The goal of the calibration process is the determination of the complex antenna gain  $G_i^p$ , the bandpass response  $B_i^p$ , the instrumental feed contamination  $D_i^p$ , and the phase errors due to ionospheric  $\gamma_i^{R-L}$  and parallactic angle  $\alpha_i$  effects. Once these quantities are determined, the correlated flux densities in the visibility plane ( $\mathcal{RR}, \mathcal{RL}, \mathcal{LR}, \mathcal{LL}$ ) can be Fourier inverted to yield the sky brightness distribution in each of the four Stokes parameters  $[(I, Q, U, V)(\eta, \xi, \nu)]$ . Stokes  $I(\eta, \xi, \nu)$  is the total intensity of the radiation from the source,  $V(\eta, \xi, \nu)$  is the circularly polarized intensity, and the complex linearly polarized intensity  $P(\eta, \xi, \nu)$  can be formed from Stokes  $Q(\eta, \xi, \nu)$  and  $U(\eta, \xi, \nu)$  using

$$P(\eta, \xi, \nu) = Q(\eta, \xi, \nu) + iU(\eta, \xi, \nu). \quad (2.5)$$

The images formed from the four Stokes parameters after full calibration can be analyzed using on- and off-line image analysis packages.

## 2.3 Data Reduction Path

This section contains a practical guide to the reduction of full-polarization spectral line VLBI data sets. Since this dissertation involves observations obtained with the VLBA and processed within the Astronomical Image Processing System (AIPS), special emphasis will be placed on these aspects. A schematic diagram of the reduction path taken in processing the data for this dissertation is shown in Figure 2.1. The discussion will follow the procedure illustrated in this diagram.

### 2.3.1 Loading and Editing the Data

The first step in processing VLBA data is to load the  $(u, v)$  data from tapes which are distributed from the VLBA correlator in the FITS (Flexible Image Transport System) format. This is accomplished within AIPS using the task FITLD. FITLD applies several online corrections for known effects generated by the VLBA correlator. There are a variety of phenomena collectively referred to as digital effects which result from digital sampling and correlation of the processed signals. FITLD corrects these digital effects independent of polarization and scales the data to values which would be returned by an analog correlator. In addition, FITLD applies second order amplitude corrections caused by delay decorrelation in the VLBA correlator. FITLD is a flexible task allowing the user to load and sort the data in a variety of ways. Data are usually concatenated into multi-source files which contain multiple scans (a scan is a length of time where the array is on source taking data).

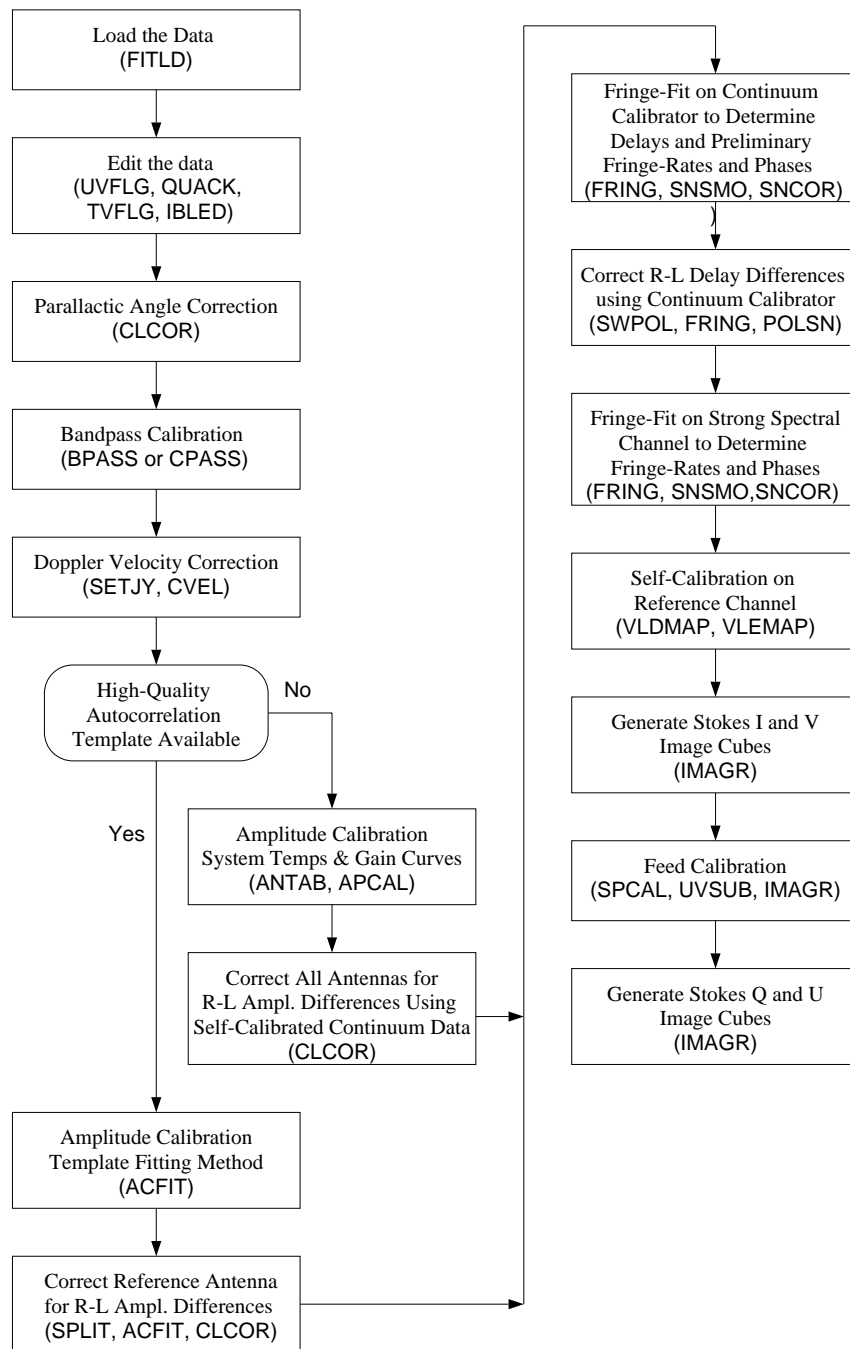


Figure 2.1: Schematic diagram of the data reduction path for the VLBI spectral line polarization data in this dissertation. Shown in parentheses are the primary AIPS tasks associated with each step.

Once all scans have been loaded, the next step is to examine and edit the data. There are several tasks available to the user for inspecting the data in both a text-based format (IMHEAD, LISTR, UVPRT, DTSUM) and a plot-based format (UVPLT, VPLOT, POSSM, FRPLT). Once a cursory examination of the data is performed, the process of editing out bad data can begin. Supplied with a typical VLBA data set is an ascii text file called the calibration file which has a designation *xxxxcal.vlba* (where *xxxx* is the experiment code). This file contains antenna-based information on system temperatures, gain corrections, weather conditions, and bad data points to be edited or *flagged*. The flagging information is applied as the first step in the editing process with the AIPS task UVFLG. Another useful editing task is QUACK, which allows the user to edit data at the beginning or end of a scan. Measurements taken during these time periods, which are adjacent to antenna position changes, are sometimes prone to errors.

The two workhorses for data editing within AIPS are the tasks TVFLG and IBLED. Both tasks are extremely flexible and allow the user to interactively edit the  $(u,v)$  data set. TVFLG displays the data as a grey-scale image on the AIPS TV device with baseline number on the x-axis, time on the y-axis, and pixel intensities representing either the amplitudes or phases of the visibilities. IBLED is useful for data sets with a relatively small number of baselines as is typical for VLBI experiments. In IBLED the visibility function for a single baseline is displayed on the AIPS TV device with time plotted on the x-axis and both amplitude and phase plotted on separate y-axes. Both tasks allow the user to select data by polarization, IF, channel, and time range. TVFLG has the advantage that multiple baselines are displayed and edited together, whereas IBLED requires the user to edit a single baseline at a time.

### 2.3.2 Parallax Angle Correction

Once the data have been edited, the first correction that is usually applied to full-polarization spectral line data is for parallactic angle. Polarization VLBI experiments require observations over a wide range of parallactic angles to separate the instrumental polarization from the source polarization. However, these widely ranging parallactic angles cause errors in the complex antenna gain  $G_i^p(t)$  which have the form

$$G_i^p(t)' = G_i^p(t)e^{is^p\alpha_i(t)}. \quad (2.6)$$

where  $\alpha_i(t)$  is the time-dependent parallactic angle, and  $s^R = -1$  and  $s^L = +1$  (Kemball 1992). The AIPS task CLCOR contains an option which adds the phase of the known parallactic angle to the residual phases in the data. CLCOR applies the parallactic angle correction to the calibration CL table attached to the data.

### 2.3.3 Bandpass Calibration

The bandpass calibration is applied to eliminate the instrumental bandpass response for each antenna in each polarization. Bandpass correction is a two step process which involves correcting both the autocorrelation and cross-correlation spectra separately. These cross-correlation and autocorrelation spectra are denoted  $S_{ij}^{pq}(\nu)$  and  $S_i^{pp}(\nu)$  respectively, where  $p$  and  $q$  represent the nominal sense of polarization at antennas  $i$  or  $j$ . Traditionally, both the autocorrelation and cross-correlation amplitudes were corrected using total power spectra derived from observations of a flat-spectrum continuum calibrator. The autocorrelation bandpass  $A_i^p(\nu)$  is real and thus, has zero phase response. However, Kemball (1992) showed that the phase response, previously assumed to be zero, can become important in VLBI spectropolarimetry experiments if there is aliasing or second-order terms in the phase as a function of frequency.

The bandpass correction for the autocorrelation data is accomplished in the traditional sense using the differenced-ratioed spectrum

$$S_i^{pp}(\nu)' = \frac{S_i^{pp}(\nu) - A_i^p(\nu)}{A_i^p(\nu)}. \quad (2.7)$$

Since the autocorrelation bandpass response is calculated from a normalized autocorrelation function, it is possible to observe a section of blank sky for the purpose of bandpass correction although in practice this is not usually done. The correction for the cross-power data has a different form since the functions involved are not normalized as in the autocorrelation case. The cross-power data are corrected using

$$S_{ij}^{pq}(\nu)' = \frac{S_{ij}^{pq}(\nu)}{B_i^p(\nu)B_j^{q*}(\nu)}, \quad (2.8)$$

where  $B_i^p(\nu)$  and  $B_j^q(\nu)$  are the complex bandpass responses determined from the cross-power continuum calibrator data.

There are two tasks within AIPS which compute the bandpass calibration for both the autocorrelation and cross-power data. These tasks are **BPASS** and **CPASS**. **BPASS** gives the user the choice of two methods for solving for the bandpass response: (1) the traditional method which computes the amplitude response from the autocorrelation data and sets the phase response to zero, or (2) a method which decomposes the baseline-based cross-power functions into an antenna-based complex bandpass response. **BPASS** computes the bandpass response on a channel by channel basis. In contrast, **CPASS** models the instrumental bandpass response as a complex Chebyshev polynomial. This alternative approach has proven useful in both high-frequency and narrow-band experiments in which accurate modeling of the antenna-based fringe-rotation (discussed in the next section) applied by the VLBA correlator is critical.

CPASS also gives the user the choice of solving for the amplitudes only or solving for the full complex bandpass. Each of these tasks produces a bandpass (BP) table which is attached to the data and applied later in the reduction process.

Since the observations presented in this dissertation involve high-frequency measurements, I chose to use CPASS to compute the bandpasses. A two step process was employed in which the amplitude response was computed from the autocorrelation spectra of the continuum calibrator, and the phase response computed from the cross-power continuum data. In the cross-power case, the amplitudes from the autocorrelation data were applied rather than computing new amplitudes using the cross-correlation data. This was done because the amplitude response computed from the cross-power data showed significant variations across the band. This could have been due to coherence problems, and shorter integration times should be explored in the reduction of future data sets. Prior to determining the complex bandpasses, the the continuum cross-correlation data was pre-averaged to improve the signal-to-noise ratio (SNR). This was accomplished by a preliminary *fringe-fit* which removes residual phase slopes in both frequency and time. Fringe-fitting is discussed in detail in § 2.3.6.

### 2.3.4 Doppler Velocity Correction

In spectral line VLBI observations, the observer usually chooses a frequency (actually a velocity is specified and converted to a frequency) for the center of the bandpass and leaves it constant throughout the experiment. Present-day VLBI systems do not employ real-time frequency tracking, and as a result, the motion of the individual stations along the line of sight to the source cause the spectra to wander within the bandpass as a function of time. Motions such as the rotation of the Earth, the revolution of the Earth around the Sun, and the motion of the Sun towards the local standard of rest (LSR) all cause Doppler shifts in the desired velocity. For the VLBA, the most significant of these effects, the motion of the stations due to the Earth's rotation, is removed by the VLBA correlator. The VLBA correlator fringe-rotates all the antenna phases to the same point (the center of the Earth) effectively removing the effect of this motion.

The time-variable residual frequency shifts which remain (typically  $\lesssim 1 \text{ km s}^{-1}$ ) are removed during post-correlation processing. Within AIPS this is accomplished by the task CVEL. CVEL Fourier transforms the spectra to the delay (lag) domain and multiplies the correlation functions by  $e^{2\pi i \Delta\nu \tau}$ , where  $\Delta\nu$  is the desired shift (Diamond 1989). CVEL then Fourier transforms back to the frequency domain where the spectra can be viewed. The result is the removal of the residual shifts and a data set with constant velocities as a function of time. Prior to running CVEL the user

must enter the desired LSR velocity for the center of the band. This is accomplished with the task `SETJY` which places the necessary information into the source (SU) table attached to the data.

### 2.3.5 Amplitude Calibration

The process of calibrating the amplitudes involves determining the amplitude part  $g_i^p(t)$  of the residual complex antenna gain in equation 2.2. For polarization data, both the amplitude in each recorded polarization and the relative gain between the two polarizations must be determined to construct the Stokes parameters. There are two methods for determining the amplitude gains typically used in VLBI. For continuum observations, the calibrated, cross-correlated flux density  $J_{ij}^{pq}(\nu)$  is expressed in terms of the raw cross-power spectra  $S_{ij}^{pq}(\nu)$  using the equation

$$\begin{aligned} J_{ij}^{pq}(\nu) &= \left[ \frac{1}{g_i^p(t)g_j^q(t)} \right] S_{ij}^{pq}(\nu) \\ &= b \left[ \sqrt{P_i^p(\bar{T}_{ant_i}^p + T_{sys_i}^p)P_j^q(\bar{T}_{ant_j}^q + T_{sys_j}^q)} \right] S_{ij}^{pq}(\nu), \end{aligned} \quad (2.9)$$

where  $P_i^p$  is the point source sensitivity of antenna  $i$  in polarization  $p$  in units of  $\text{Jy K}^{-1}$ ,  $T_{sys_i}^p$  is the off-source system temperature,  $\bar{T}_{ant_i}^p$  is the averaged antenna temperature across the band, and  $b$  is a factor which compensates for unmodeled digitization and sampling losses.

It is often possible to use a more powerful approach in the case of spectral line observations. This method utilizes a high-quality total power spectrum obtained from a reference station as a template. This template is then used to scale the autocorrelation spectra of all the other antennas. The calibrated total power spectrum is given by

$$J^{pp}(\nu) = \frac{S_{on}^{pp}(\nu) - S_{off}^{pp}(\nu)}{S_{off}^{pp}(\nu)}, \quad (2.10)$$

where  $S_{on}^{pp}(\nu)$  and  $S_{off}^{pp}(\nu)$  are the on- and off-source autocorrelation spectra respectively. The total power spectrum at antenna  $i$  is then related to the true, calibrated total power spectrum through the relation

$$J_i^{pp}(\nu) = g_i^p(t)J^{pp}(\nu), \quad (2.11)$$

where  $g_i^p$  are the time-dependent, cross-power gain factors (also referred to as the quality factors; Diamond 1989). These cross-power gain factors are determined by

minimizing

$$\text{Error} = \sum_{\nu=\nu_1}^{\nu_2} [S_i^{pp}(\nu) - (g_i^p)^2 J^{pp}(\nu)]^2. \quad (2.12)$$

In practice, this is accomplished by performing a least-squares fit of each antenna’s total-power spectrum to the calibrated template spectrum over the frequency range  $(\nu_1, \nu_2)$ . The template fitting method can be applied to VLBI spectral line polarization data by determining the gain correction curves independently for each antenna in each hand of polarization (Kemball, Diamond, and Cotton 1995).

In either method of amplitude calibration, the differential polarization gain  $g_i^{R-L}$  for each antenna must also be determined and the appropriate correction applied. This can be done in one of two ways for the spectral line case. First, the differential offsets can be estimated from the cross-power spectra of the continuum calibrator source after the removal of bandpass effects and residual phase errors. If the data have been amplitude calibrated using the template fitting method, then only the differential gain of the reference antenna  $g_0^{R-L}$  needs to be determined since all other antennas are scaled relative to this station. If the system temperatures and gain curves are used to correct the amplitude gains, then all antennas must be corrected for  $g_i^{R-L}$ . This technique assumes that the continuum source has no net circular polarization.

The second method of determining the differential amplitudes is used only in the template fitting case. Here, the differential gain of the reference antenna is also determined using the template fitting method, with the autocorrelation spectrum of the antenna in the reference polarization used to fit the orthogonal polarization. The SN table produced is averaged over the entire run since to first order,  $g_0^{R-L}$  remains constant over the duration of a typical VLBI experiment (Kemball, Diamond, and Cotton 1995).

Unfortunately, a “high-quality” template spectrum was not available for each of the four epochs of observations presented in this dissertation. The spectra for two of the epochs displayed significant variations in the wings of the spectra. This could be due to low values for the ratio of the antenna temperature to the system temperature for these epochs. For the data from two of the observing runs, I was forced to use the former method of amplitude calibration usually reserved for continuum data. This method was applied within AIPS using the tasks `ANTAB` and `APCAL`. The task `ANTAB` reads in the antenna-dependent system temperatures and the gain curves from an ascii file prepared by the user and attaches `TY` and `GC` tables containing this information to the data. System temperatures are taken from the aforementioned `xxxxcal.vlba` file, and gain curves are extracted from a file called `vlba.gains.key`. The system temperatures and gain curves are converted to a solution (SN) table which

contains the amplitude and gain calibration information using the task `APCAL`. In these cases, the differential amplitude gains were estimated using the self-calibrated continuum data.

The template method, typically used for spectral line data, was applied in two of the experiments where high-quality total power spectra were available. This method was implemented within `AIPS` using the task `ACFIT`. `ACFIT` uses a linear least-squares algorithm to generate an `SN` table containing the relative gains of the antennas as a function of time. The differential amplitude gain for the reference antenna was determined by fitting the parallel-hand reference polarization to the orthogonal polarization again using `ACFIT`.

The `SN` tables produced in the amplitude calibration process and in subsequent phase calibration procedures can be viewed, edited, and smoothed using the tasks `SNPLT`, `SNCOR`, and `SNSMO` respectively. These `SN` tables are applied steps to calibration (`CL`) tables with the highest number `CL` table containing all the calibration information up to the current point in the process.

### 2.3.6 Phase Calibration

Many of the various effects on the phases of the received radiation are modeled within the correlator, but often residual phases due to instrumentation and propagation through the ionosphere remain. The process of phase calibration involves the determination and removal of these residual effects on the phase  $\phi_i^p(\nu, t)$  portion of the complex antenna gain  $G_i^p(\nu, t) = g_i^p(t)e^{i\phi_i^p(\nu, t)}$ . Part of the phase calibration was discussed previously in § 2.3.2 with reference to the parallactic angle and will not be repeated here.

#### Fringe-Fitting

Fringe-fitting is a procedure by which the residual delays and fringe-rates are determined so that the data may be coherently averaged. There are two formulations of the fringe-fitting technique: the baseline-based method and the *global* or antenna-based method. The baseline-based method requires that the source be detected on all baselines which are to be calibrated and does not maintain the antenna-based phase *closure* relationships given by Rogers et al. (1974). This method is sufficient for arrays in which a few powerful antennas dominate the array, but is less desirable in homogeneous arrays such as the VLBA. For the VLBA, the global fringe-fitting approach is better for source detection. In this technique, the delays and rates are jointly computed for all antennas. This allows the calibration of antennas which lack the SNR on individual baselines but have sufficient SNR when used with the rest of

the array. The global fringe fitting technique uses the equation

$$\phi_i^p(\nu, t) = (\varphi_i^p - \varphi_0^p) + (\tau_i^p - \tau_0^p)(\nu - \nu_0) + (\dot{\phi}_i^p - \dot{\phi}_0^p)(t - t_0) \quad (2.13)$$

where the phase offset  $\varphi_i^p$ , the delay  $\tau_i^p$ , and the fringe-rate  $\dot{\phi}_i^p$  at antenna  $i$  in polarization  $p$  are referred to a reference antenna at a reference time and reference frequency (all subscript 0). The delays, rates, and phases of this reference antenna are arbitrarily assigned a value of zero, thus the differences in these quantities are computed rather than their absolute values. The global fringe-fitting technique also obeys the closure relations which are the basis of the self-calibration technique discussed later.

Residual group delays  $\tau_i^p = \partial\phi_i^p/\partial\nu$  appear as phase slopes in the frequency domain. The process of determining the delays is sometimes referred to as *finding the clocks* since errors in the clocks are the primary source of residual delays. In spectral line VLBI, the delays are usually determined during a fringe-fit on a continuum calibrator. The continuum calibrator is chosen to have a broad flat spectrum. This spectrum, when Fourier transformed to the lag domain, becomes sharply peaked allowing the delay to be easily found. This delay, once determined, can be applied across the band for the spectral line source. The delay would be much more difficult to compute on the spectral line source since it usually consists of several sharp peaks in the spectral domain, which when Fourier transformed to the delay domain, are broad. The fringe-fit on the continuum calibrator is accomplished within AIPS using the task **FRING**. **FRING** produces a solution (SN) table which can be examined and applied to the spectral line data set. Since the continuum calibrator sources observed in VLBI spectropolarimetry experiments are chosen to be circularly unpolarized, the delay calibration follows that for continuum VLBI polarimetry. In this case the antenna-based delay solutions are obtained by fringe-fitting the parallel-hand (*RR* and *LL*) correlations independently.

During the fringe-fit on the continuum calibrator, preliminary fringe-rates  $\dot{\phi}_i^p = \partial\phi_i^p/\partial t$  are also computed. The fringe-rates appear as phase oscillations in the time domain of the data and are caused by drifts in the clocks, source position errors, and atmospheric propagation errors. Over short periods of time, the rates are approximated as linear phase slopes, which when Fourier transformed to the frequency domain, appear as sharp peaks. For this reason, the fringe-rate determination is usually done in frequency space. A first-order solution for the fringe-rates is generally estimated during the determination of the delays from the continuum calibrator. Since the spectral line source is typically not in the same region of the sky as the continuum calibrator, a second fringe-fit is done on a strong channel of the spectral line target source. This reference channel in the cross-power spectrum is chosen to have compact structure and high signal-to-noise. The fringe-rate and phase solutions determined in this second run of **FRING** (with the delay solution suppressed) locate the phase center at the centroid of emission in the reference channel. This final fringe-rate solution

can then be applied to the other channels in the spectrum since the phase offset due instrumental effects is weakly dependent on frequency (Reid et al. 1980). Since the spectral line source often has non-negligible circular polarization, the fringe-fit on the reference channel cannot be performed in each polarization independently as was done in the delay solution. Instead, a reference polarization is chosen ( $RR$  or  $LL$ ), the fringe-rate solutions determined in this polarization, and the solutions applied to the orthogonal polarization.

### Differential Phase Effects

In VLBI spectropolarimetry, the observer must also be concerned with differential effects in the delay  $\delta\tau_i^{R-L} = \tau_i^R - \tau_i^L$ , the fringe-rate  $\delta\dot{\phi}_i^{R-L} = \dot{\phi}_i^R - \dot{\phi}_i^L$  and the phase offset  $\delta\varphi_i^{R-L} = \varphi_i^R - \varphi_i^L$  in order to get a proper calibration of the data. Assuming that left-circular polarization (LCP) is used as the reference polarization, then equation 2.13 can be modified to include these differential effects and takes on the form

$$\begin{aligned} \phi_i^L(\nu, t) &= (\varphi_i^L - \varphi_0^L) + (\tau_i^L - \tau_0^L)(\nu - \nu_0) + (\dot{\phi}_i^L - \dot{\phi}_0^L)(t - t_0) \\ \phi_i^R(\nu, t) &= (\varphi_i^R - \varphi_0^R + \delta\varphi_i^{R-L}) + (\tau_i^R - \tau_0^R + \delta\tau_i^{R-L})(\nu - \nu_0) \\ &\quad + (\dot{\phi}_i^R - \dot{\phi}_0^R + \delta\dot{\phi}_i^{R-L})(t - t_0). \end{aligned} \tag{2.14}$$

The delay and fringe-rate phase solutions must have the same reference antenna before these polarization offsets can be applied (Kemball, Diamond, and Cotton 1995).

The delay offset  $\delta\tau_i^{R-L}$  is the difference between the RCP and LCP delays derived from the global fringe-fit using the reference antenna. This offset is mainly due to the differing paths through the electronics for the two polarizations. The Faraday rotation in the Earth's ionosphere can also cause differential delay differences. In terms of the phase difference due to Faraday rotation  $\gamma^{R-L}$  and the angular frequency  $\omega$ , the ionospheric group delay offset  $\partial\gamma^{R-L}/\partial\omega$  can be approximated by the relationship  $\partial\gamma^{R-L}/\partial\omega \approx -0.3\nu_{\text{GHz}}^{-3}$  nanoseconds (ns) (Kemball, Diamond, and Cotton 1995). This offset is on the order of 0.004 picoseconds and completely negligible for the 43-GHz observations in this thesis. The delay offset due to the instrumentation is expected to be fairly stable over the duration of a typical VLBI observing run for a well-behaved system (Cotton 1989). This delay offset can be determined from the baseline-based cross-correlation delays which are estimated from the continuum

calibrator using (Brown, Roberts, and Wardle 1989)

$$\begin{aligned}
 \delta\tau_i^{R-L} &= \tau_{ij}^{RL} - \tau_{ij}^{LL} \\
 \delta\tau_i^{R-L} &= \tau_{ij}^{RR} - \tau_{ij}^{LR} \\
 \delta\tau_j^{R-L} &= \tau_{ij}^{RL} - \tau_{ij}^{RR} \\
 \delta\tau_j^{R-L} &= \tau_{ij}^{LL} - \tau_{ij}^{LR}.
 \end{aligned}
 \tag{2.15}$$

In practice, this estimation is done in AIPS by first swapping the cross-hand ( $RL$ ,  $LR$ ) and parallel-hand ( $RR$ ,  $LL$ ) data streams for the reference antenna using the task SWPOL. A fringe-fit on the cross-hand data streams is then performed using the task FRING to find the delays. The delay offset solutions are then written to an SN table using the task POLSN. The average delay offset for the four epochs of VLBA observations made for this dissertation is  $\sim 15$  ns.

The fringe-rate offset due to instrumental variations can be assumed negligible over the time periods in which the fringe-rates are assumed linear (Kemball 1992). In addition, the fringe-rate offset due to ionospheric Faraday rotation ( $\dot{\gamma}^{R-L}/\omega$ ) can be approximated by the relation  $\dot{\gamma}^{R-L}/\omega \approx 40\nu_{\text{GHz}}^{-2} \mu\text{Hz}$  (Kemball, Diamond, and Cotton 1995). At 43 GHz this offset is  $\sim 0.02 \mu\text{Hz}$ , and as in the delay case, can be neglected. Since fringe-rate offsets are small for both instrumentation and propagation effects, at 43 GHz  $\delta\dot{\phi}_i^{R-L}$  can be considered insignificant.

### Self-Calibration

Once the fringe-fitting has been completed, the data may be coherently averaged in time, and the process of calibrating the residual phase offsets  $\varphi_i^p(\nu, t) = \phi_i^p(\nu, t) - \phi_i^p(\nu_0, t_0)$  can begin. This correction is typically performed using a technique called self-calibration. The process of self-calibration basically involves assuming a plausible model for the sky brightness distribution  $I(\eta, \xi, \nu)$ , Fourier transforming that model to the visibility plane, and correcting the complex antenna gains such that the cross-correlation functions are reproduced to within the noise estimates. The visibilities are rarely reproduced on the first pass, therefore self-calibration is an iterative process in which the corrected cross-correlations are used to form a new model which is then used to compute new antenna gains and so on. Detailed discussions on self-calibration techniques can be found in Cornwell and Fomalont (1989) and Wilkinson (1989) and will not be repeated here.

With respect to VLBI spectral line polarization data, the self-calibration process is similar to the fringe-rate calibration in that the inherent circular polarization of the program source confuses the calibration procedure. In continuum VLBI polarimetry, the self-calibration of both parallel-hand data streams ( $RR$  and  $LL$ ) can be performed

with the same total-intensity (Stokes  $I$ ) image. For VLBI spectropolarimetry data, the self-calibration is done on the reference polarization ( $RR$  or  $LL$ ) and applied to the orthogonal polarization.

The difference in the phase offset between RCP and LCP ( $\delta\varphi_i^{R-L}$  in equation 2.14) is affected by the instrumentation and ionospheric Faraday rotation as in the case of the delays and fringe-rates. The ionospheric Faraday rotation is expected to have a worst case value of  $\gamma^{R-L} \approx 0.94\nu_{\text{GHz}}^{-2}$  radians. This effect is again negligible for 43-GHz observations, with a phase rotation of  $\sim 0.5$  milliradians ( $\sim 0.03$  degrees). The phase offsets due to instrumental effects are not negligible and are dominated by the feed contamination errors ( $D$ -terms). The correction of these effects are the subject of the next section.

### 2.3.7 Feed Calibration

The purpose of the feed calibration is to separate the instrumental polarization response from the inherent source polarization. Often the polarization of the source used to determine the feed response is unknown and the two must be determined simultaneously. This can be accomplished in arrays with at least one antenna with an altitude-azimuth mount by observing the source over a range of parallactic angles (Conway and Kronberg 1969). The parallactic angle causes a phase rotation of the source polarization which can be distinguished from the instrumental response. For this reason, it is desirable to observe the source over as wide a range of parallactic angle as possible.

To first order, the bandpass- and gain-calibrated cross-power spectra of equation 2.1 are given by

$$\begin{aligned}
 S_{ij}^R(u, v, \nu) &= \mathcal{R}\mathcal{R} \\
 S_{ij}^{RL}(u, v, \nu) &= \mathcal{R}\mathcal{L} + (\mathcal{R}\mathcal{R})D_j^{L*}e^{2i\alpha_j} + (\mathcal{L}\mathcal{L})D_i^R e^{2i\alpha_i} \\
 S_{ij}^{LR}(u, v, \nu) &= \mathcal{L}\mathcal{R} + (\mathcal{R}\mathcal{R})D_i^L e^{-2i\alpha_i} + (\mathcal{L}\mathcal{L})D_i^{R*} e^{-2i\alpha_i} \\
 S_{ij}^{LL}(u, v, \nu) &= \mathcal{L}\mathcal{L}
 \end{aligned} \tag{2.16}$$

where the effects due to Faraday rotation have been shown to be negligible at 43 GHz. In theory, if the polarization structure of a continuum calibrator source is known, then the  $D$ -terms can be determined using a linear least-squares fit. This requires that the SNR in the cross-hand functions ( $\mathcal{R}\mathcal{L}$  and  $\mathcal{L}\mathcal{R}$ ) of the continuum calibrator be sufficiently high to determine the solutions. Often in the VLBI case, finding a suitable compact calibrator source is difficult. Sources typically used to calibrate polarization data observed with connected-element arrays such as the VLA are often resolved on VLBI baselines. The prospect of using resolved polarization calibrators is discussed

in Cotton (1993). An additional difficulty in spectral line VLBI polarimetry is the fact that the  $D$ -terms may vary with frequency. Observations of the program source are often made using narrow bands, therefore the continuum polarization calibrator must also be observed at this narrow bandwidth.

To alleviate the above difficulties in calibrating VLBI spectropolarimetry data with less than desirable continuum calibrators, Kemball (1992) developed an iterative technique in which a number of spectral channels with simple linear polarization structure are used to determine the feed response. This technique dubbed *polarization self-calibration* determines the source structure and the  $D$ -terms simultaneously.

These two methods of calibrating the feed response can each be applied to the data within AIPS. If the calibration is performed using a continuum polarization calibrator, the tasks PCAL or SPCAL can be used to determine the feed leakage terms. These terms are written to the antenna AN table attached to the data and can be applied using the task SPLIT. If the iterative approach is used, a suitable portion of the spectrum is chosen and both the  $D$ -terms and source structure determined using SPCAL. As in the standard self-calibration procedure, the model of the source structure is used to refine the  $D$ -term estimates on subsequent iterations until the solution converges. Models are produce using the task IMAGR and subtracted from the data using the task UVSUB.

### 2.3.8 Imaging

The techniques of Fourier inversion and deconvolution used to produce synthesis images are discussed in detail in Perley, Schwab, and Bridle (1989) and Wilkinson (1989). Two tasks, IMAGR and MX are available within AIPS for this function. These tasks are also used in conjunction with the task CALIB during the self-calibration process. For spectral line VLBI data, the self-calibration is usually performed on a single spectral channel and the solutions applied to the remaining channels. Two procedures have been written which simplify the self-calibration procedure for spectral line data. These procedures are VLDMAP and VLEMAP and both were used in the production of the images shown in Chapter 3.

Once the phase solutions from the self-calibration have been applied, images of all desired spectral channels can be formed using one of the imaging tasks. These individual channel maps are placed together in what is referred to as an *image cube*. The Stokes  $I(\eta, \xi, \nu)$  and  $V(\eta, \xi, \nu)$  image cubes can be formed prior to the calibration of the  $D$ -terms since  $I$  and  $V$  depend only on  $\mathcal{RR}(u, v, \nu)$  and  $\mathcal{LL}(u, v, \nu)$ . The Stokes  $Q(\eta, \xi, \nu)$  and  $U(\eta, \xi, \nu)$  images must instead be formed after the calibration of the  $D$ -terms since they depend on the cross-correlations  $\mathcal{RL}(u, v, \nu)$  and  $\mathcal{LR}(u, v, \nu)$ . The calibration procedure described above leaves the RCP and LCP phase solutions

offset by an unknown phase constant. The absolute position angle of the linearly polarized emission is therefore unknown, but the relative position angles of various features remain unaffected. The absolute position angle may be determined through observations of a continuum calibrator with a known polarization position angle. This correction is applied to the program source after the feed calibration in the formation of the linear polarization images.

The details pertinent to the calibration and imaging of each of the four epochs of observations for this thesis are discussed in the next chapter.

# Chapter 3

## VLBA OBSERVATIONS OF R AQUARII

“Gotta tune in – pico waves . . .  
Gotta tune out – atomic lasers falling from the sky.”

*the B-52's, Channel Z*

### 3.1 Introduction

This chapter describes the four epochs of VLBI observations of the 43-GHz SiO maser emission towards the Mira variable in the symbiotic binary R Aquarii (R Aqr). Observations were made of the line source (R Aqr) and two calibrator sources (0420–014 and 3C 454.3) over a period of 9 months from June 1995 through April 1996. Source coordinates in both B1950 and J2000 coordinates are listed in Table 3.1 below.

Table 3.1: Coordinates of observed sources.

Source	B1950		J2000	
	R. A.	Dec.	R. A.	Dec.
0420–014	04 <sup>h</sup> 20 <sup>m</sup> 43.540 <sup>s</sup>	–01°27′28.66″	04 <sup>h</sup> 23 <sup>m</sup> 15.801 <sup>s</sup>	–01°20′33.09″
3C 454.3	22 <sup>h</sup> 51 <sup>m</sup> 29.520 <sup>s</sup>	+15°52′54.35″	22 <sup>h</sup> 53 <sup>m</sup> 57.749 <sup>s</sup>	+16°08′53.54″
R Aqr	23 <sup>h</sup> 41 <sup>m</sup> 14.269 <sup>s</sup>	–15°33′42.89″	23 <sup>h</sup> 43 <sup>m</sup> 49.445 <sup>s</sup>	–15°17′03.56″

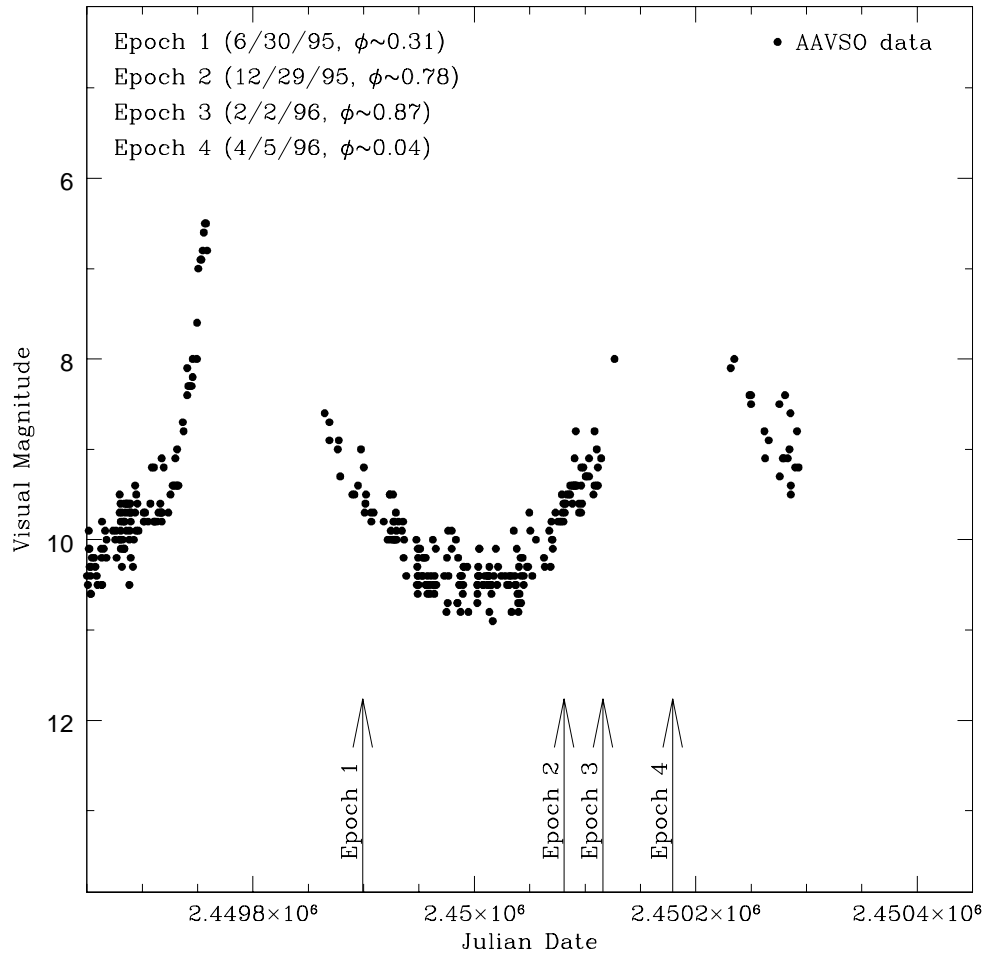


Figure 3.1: Four epochs of VLBA observations plotted on the visual light curve of R Aqr. AAVSO optical data (Mattei 1996) cover a time period from December 1994 through July 1996.

Observing dates for the four epochs of observations are plotted on the visual light curve shown in Figure 3.1. The optical data were supplied to me by the American Association of Variable Star Observers (AAVSO <sup>1</sup>). As is seen in Figure 3.1, the observations sample four stages of the Mira’s 387 day stellar pulsation cycle. Observations for Epoch 1 were taken at a phase of 0.31 as the Mira was nearing its minimum light ( $\phi \approx 0.5$ ). Epochs 2, 3, and 4, observed at phases 0.78, 0.87, and 0.04 respectively, sample that part of the stellar cycle where R Aqr is approaching an optical maximum.

The 43-GHz maser emission was monitored using the 10 antennas of the VLBA plus a single VLA antenna. The line source data were recorded in dual circular polarization in a 4 MHz ( $\sim 27.8 \text{ km s}^{-1}$ ) band. This band was centered on an LSR velocity of  $-27.0 \text{ km/s}$  assuming a line rest frequency of 43.122027 GHz. Typical system temperatures and point source sensitivities for the VLBA at 43 GHz are 150 K and  $11 \text{ Jy K}^{-1}$  respectively.

All four epochs were recorded in the VLBA format and correlated with the VLBA correlator in Socorro, New Mexico. NRAO’s Astronomical Image Processing System (AIPS) was used to analyze the 128-channel autocorrelation and cross-correlation spectra with spectral resolutions of 31.25 kHz ( $\sim 0.2 \text{ km s}^{-1}$ ) in uniform weighting. The next four sections describe the specifics pertaining to the reduction of each of the four data sets and show the resulting images for each epoch.

## 3.2 Epoch 1

### 3.2.1 Observations

Observations for Epoch 1 were recorded during a 24-hour observing run beginning at 00:00 UT on June 30, 1995. A total of 18 scans were recorded on R Aqr from 09:00 UT to 15:00 UT. At  $\sim 12.5$  minutes per scan the total time on source was  $\sim 3.8$  hours. In addition, 6 scans were recorded on the nearby continuum calibrator 3C 454.3 interspersed with the R Aqr scans. Over the entire 24-hour run, 3 scans were recorded on the source 0420–014. This source was used to calibrate the absolute position angle for the linear polarization vectors. Data were recorded in a single IF for the line source and 4 IF’s for the continuum sources. The data integration time for both the cross-power and total power spectra was  $\sim 2.1$  seconds.

---

<sup>1</sup>I acknowledge with thanks, data from the AAVSO International Database, based on observations submitted to the AAVSO by variable star observers worldwide.

### 3.2.2 Calibration and Imaging

The data for R Aqr and the two continuum calibrators were imported into AIPS and the scans concatenated into three separate source files. For 3C 454.3, only the first IF was loaded to match that of the line source R Aqr. In the case of 0420–014 all four IF’s were loaded. An initial edit was performed using the flagging table supplied with the data in conjunction with the task UVFLG. The data were further edited interactively using the task TVFLG.

The phase rotation due to the parallactic angle, which is known analytically, was corrected using the task CLCOR. Bandpasses for both the cross-power and autocorrelation data were generated using the task CPASS on the continuum calibrator 3C 454.3. The bandpass amplitude response for both the autocorrelation and cross-correlation data was determined from the total-power spectra of 3C 454.3. The bandpass phases were computed from the cross-power spectra of 3C 454.3.

At this point, the autocorrelation and cross-correlation data for the line source were separated into different files using the task UVCOP. Each file was corrected for small Doppler shifts in the desired LSR velocity. The tasks SETJY and CVEL were used to center the band on the LSR velocity of  $-27.0 \text{ km s}^{-1}$ . The bandpass corrections were applied at this stage as part of CVEL.

The total power spectra were examined, and a high-quality spectrum found for a single scan on the chosen reference antenna at Los Alamos (antenna code LA). This scan had a relatively high elevation at  $39^\circ$  with a point source sensitivity of  $10.4 \text{ Jy K}^{-1}$  and average system temperatures of 126.0 K and 124.5 K in RCP and LCP respectively. Antenna amplitude gains were determined for the entire data set at 2 minute intervals using the above scan as a template with the task ACFIT. The template fitting method was also used to compute the R–L amplitude difference for the reference antenna. ACFIT was used to compute a  $RR/LL$  correction of 1.007 averaged over the entire scan. This correction was applied by multiplying the LCP gains of the reference antenna by the above factor.

Residual group delays along with preliminary residual fringe-rates were determined from the 3C 454.3 data using the task FRING with a solution interval of 30 seconds. Discrepant delays and rates were removed and the phase solutions applied to the R Aqr cross-power data. R–L residual delay differences were estimated by fringe-fitting the cross-hand ( $RL$  and  $LR$ ) data streams. The residual delay differences were edited and averaged over the entire scan interval with the result  $\Delta\tau^{R-L} \approx 12 \text{ ns}$ .

Residual fringe-rates were estimated by performing a fringe-fit on a reference channel ( $-28.5 \text{ km s}^{-1}$ ) from the R Aqr cross-power spectrum. All phase corrections were applied at this stage using the task SPLIT. A cross-power spectrum of the calibrated data is shown in Figure 3.2.

Data from the Hancock (HN), Mauna Kea (MK), and St Croix (SC) antennas were flagged after it was determined that the masers were not detected on baselines to these stations. Synthesis images of Stokes  $I$  and  $V$  were constructed using the standard self-calibration and imaging techniques. A self-calibration of the phases was performed using the above reference channel, and the final phase solution was applied to all channels in the spectrum. Image cubes consisting of individual channel maps were made for velocities between  $-32.9 \text{ km s}^{-1}$  and  $-17.4 \text{ km s}^{-1}$ . Each map is  $1024 \times 1024$  pixels in size with a pixel spacing of  $\sim 0.09 \text{ mas}$ . The synthesized beam for these images is  $1.15 \times 0.60 \text{ mas}$ . From the  $I$  and  $V$  image cubes, integrated flux density images were formed by summing the intensity over the above velocity range. These images are shown in Figures 3.3 and 3.4. The image cube used to form the integrated Stokes  $I$  map is shown in Appendix A.

Antenna  $D$ -terms were estimated using the polarization self-calibration technique (described in § 2.3.7) on channels from  $-30.3 \text{ km s}^{-1}$  to  $-21.8 \text{ km s}^{-1}$ . These solutions were applied to the data set and the Stokes  $Q$  and  $U$  image cubes formed. Integrated flux density images in  $Q$  and  $U$  are shown in Figures 3.5 and 3.6. Corrections to the absolute position angle of the linear polarization vectors were determined by comparing the position angles determined for 0420–014 from the Epoch 1 VLBA observations and VLA observations taken on July 6, 1995. The linearly polarized intensity images were then formed from the integrated  $Q$  and  $U$  images with the  $-88^\circ$  correction applied. This integrated linear polarized intensity image is shown in Figure 3.7.

In addition to the flux density images, a map of the velocity structure of the SiO maser emission towards R Aqr was also formed. This image was made using the AIPS tasks **TRANS** and **XGAUSS**. These two tasks allow the user to fit one or more Gaussians at each pixel location over the entire LSR velocity range. **TRANS** was used to transpose the Stokes  $I$  image cube such that velocity, rather than intensity, was the the first axis of the cube. The task **XGAUS** was then used on this transposed image cube to computed the parameters of the Gaussian fits and to form images of each parameter. Figure 3.8 shows the center velocity at the peak flux density derived from the fit of a single Gaussian at each pixel location.

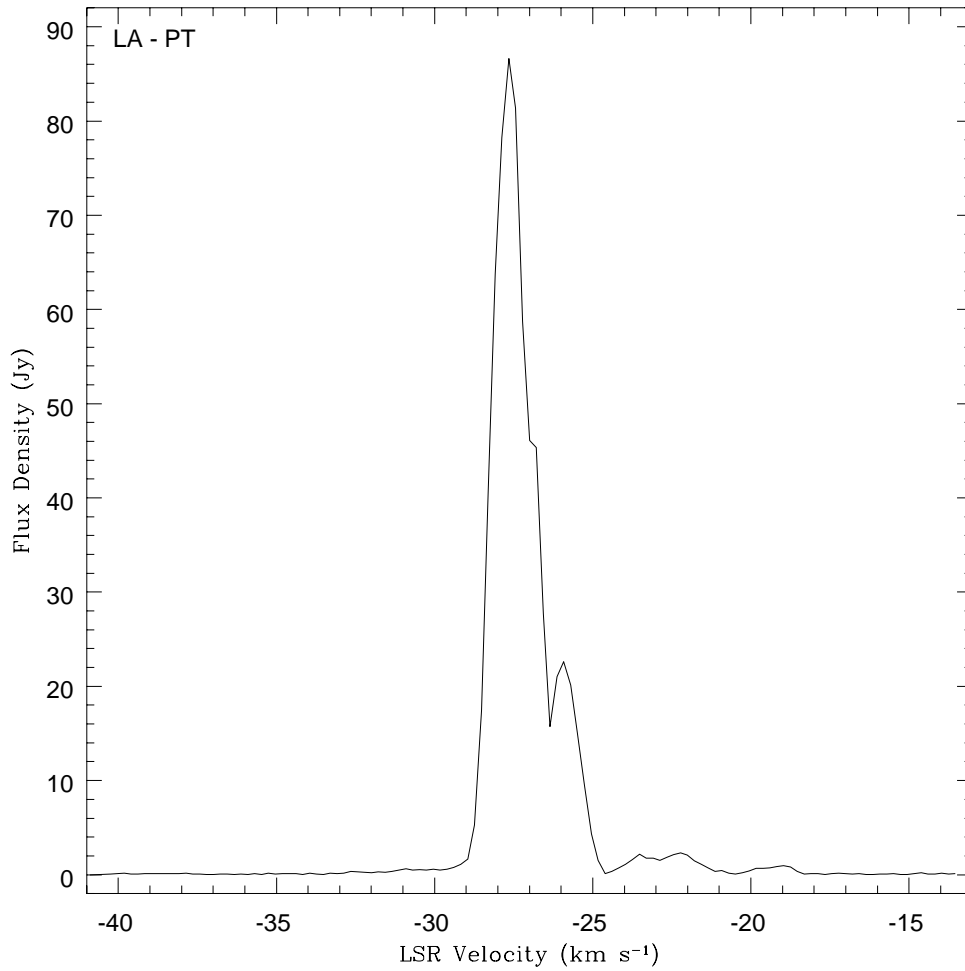


Figure 3.2: Stokes  $I$  cross-power spectrum of the  $v = 1, J = 1 - 0$  SiO maser emission towards R Aqr as observed for Epoch 1. Baseline from Los Alamos, NM to Pietown, NM.

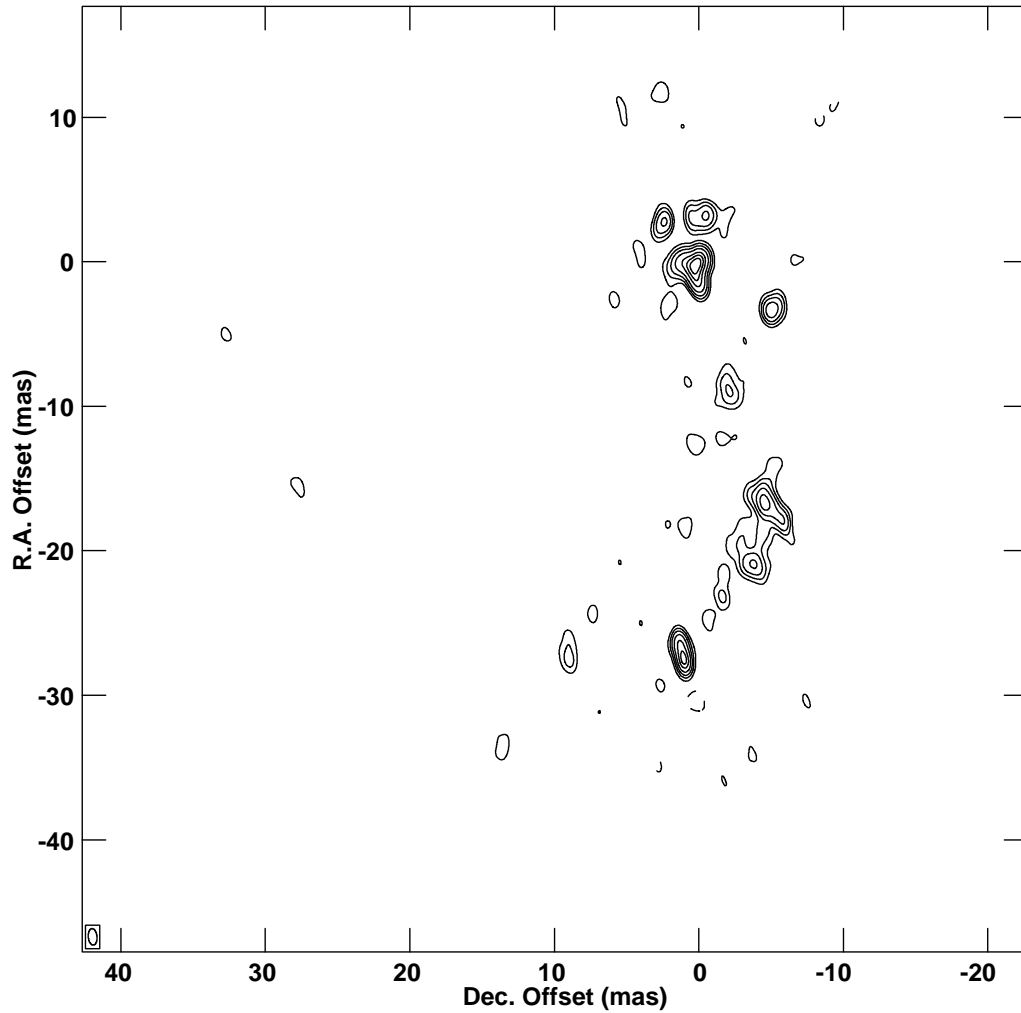


Figure 3.3: Epoch 1 total intensity (Stokes  $I$ ) image of the  $v = 1, J = 1 - 0$  SiO maser emission towards R Aqr integrated over the LSR velocity range of  $-32.9 \text{ km s}^{-1}$  to  $-17.4 \text{ km s}^{-1}$ . Contour levels are  $-10, -5, 5, 10, 20, 40, 60, 80,$  and  $100\%$  of the peak integrated flux density  $134.5 \text{ Jy/beam}$ .

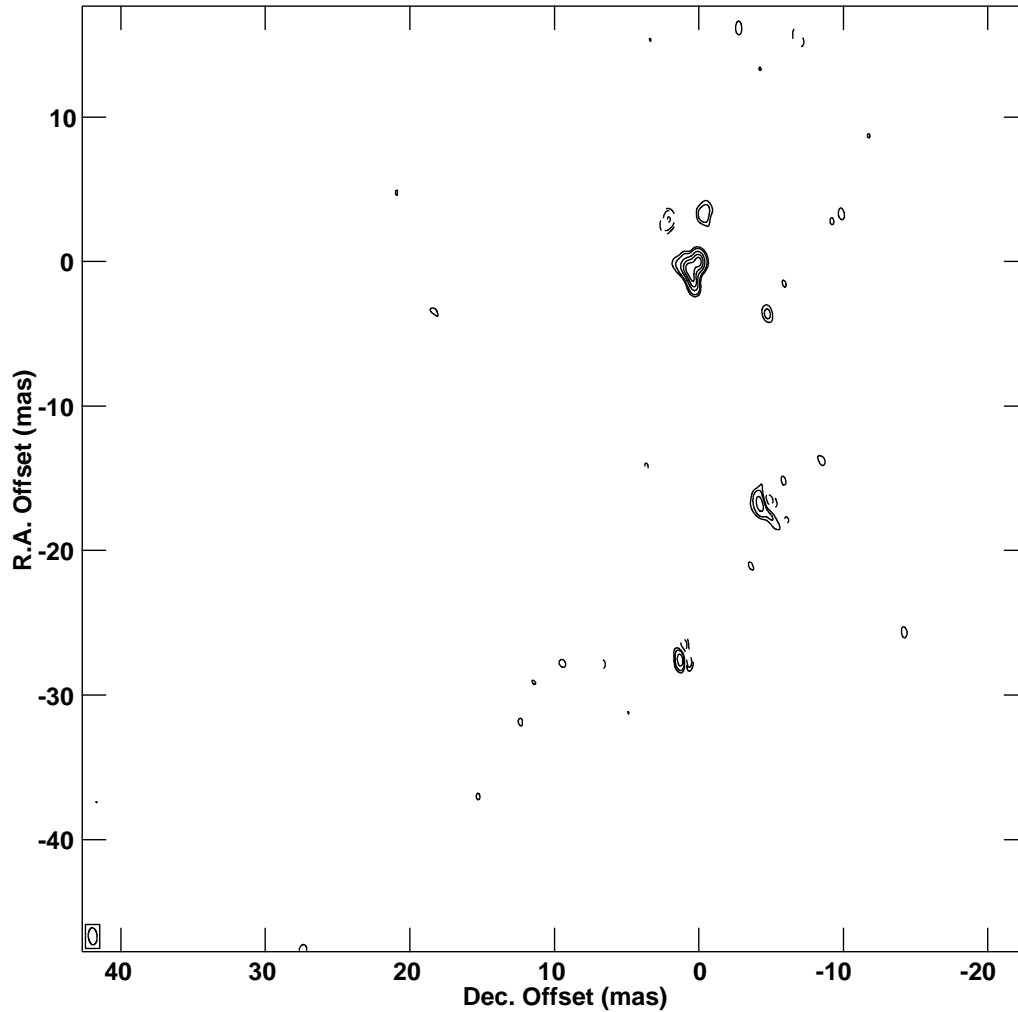


Figure 3.4: Epoch 1 circular polarization (Stokes  $V$ ) image of the  $v = 1, J = 1 - 0$  SiO maser emission towards R Aqr integrated over the LSR velocity range of  $-32.9 \text{ km s}^{-1}$  to  $-17.4 \text{ km s}^{-1}$ . Contour levels are  $-100, -80, -60, -40, -20, -12, 12, 20, 40, 60, 80,$  and  $100\%$  of the peak integrated flux density  $4.4 \text{ Jy/beam}$ . Negative flux densities are represented by dashed contours.

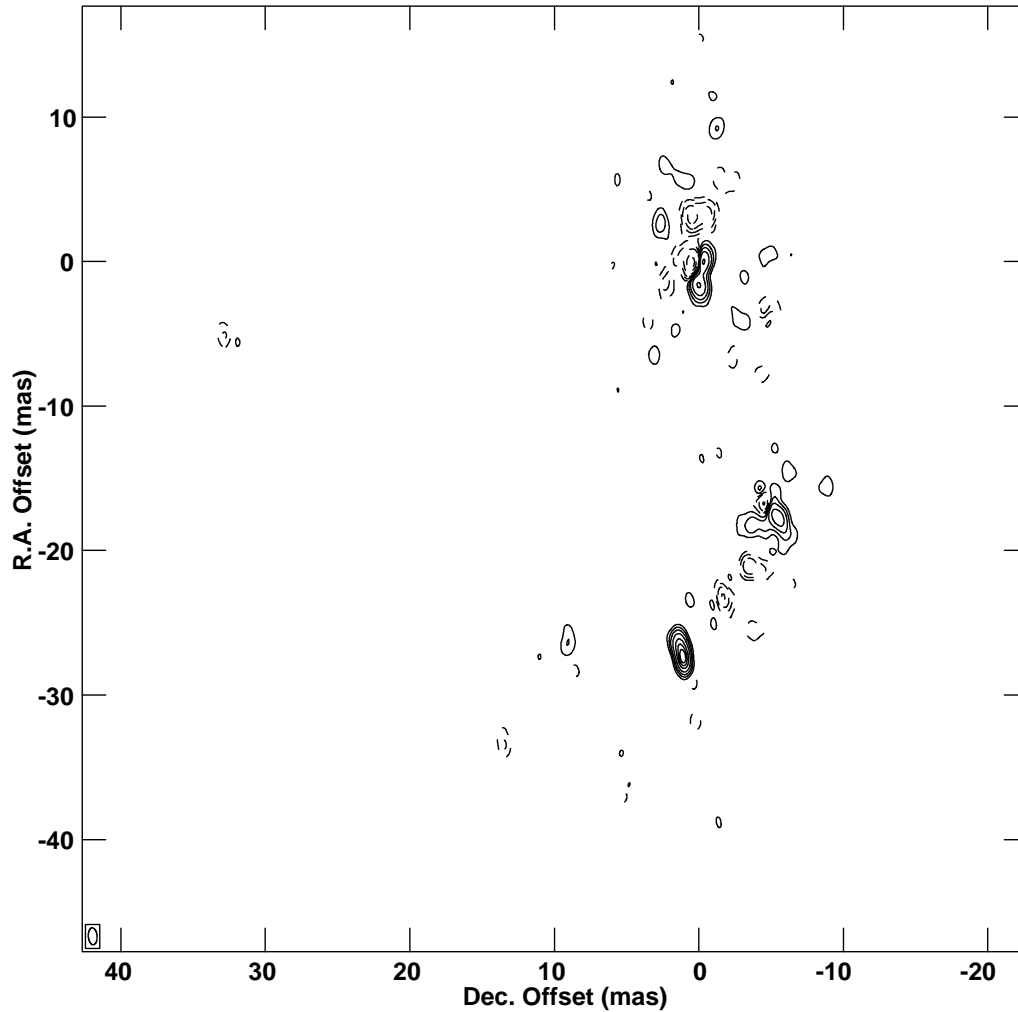


Figure 3.5: Epoch 1 Stokes  $Q$  image of the  $v = 1, J = 1-0$  SiO maser emission towards R Aqr integrated over the LSR velocity range of  $-32.9 \text{ km s}^{-1}$  to  $-17.4 \text{ km s}^{-1}$ . Contour levels are  $-100, -80, -60, -40, -20, -10, -5, -2, 2, 5, 10, 20, 40, 60, 80,$  and  $100\%$  of the peak integrated flux density  $25.2 \text{ Jy/beam}$ . Negative flux densities are represented by dashed contours.

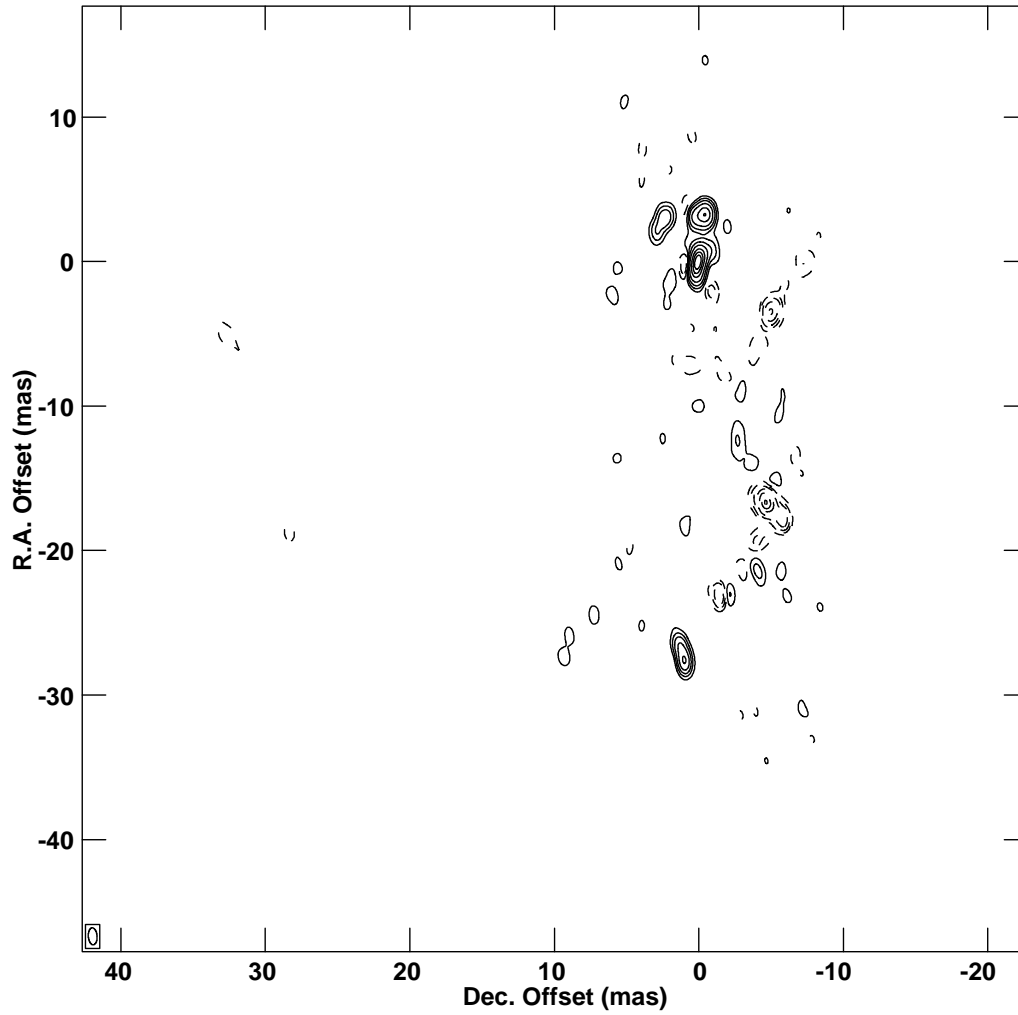


Figure 3.6: Epoch 1 Stokes  $U$  image of the  $v = 1, J = 1-0$  SiO maser emission towards R Aqr integrated over the LSR velocity range of  $-32.9 \text{ km s}^{-1}$  to  $-17.4 \text{ km s}^{-1}$ . Contour levels are  $-100, -80, -60, -40, -20, -10, -5, -2, 2, 5, 10, 20, 40, 60, 80,$  and  $100\%$  of the peak integrated flux density  $26.2 \text{ Jy/beam}$ . Negative flux densities are represented by dashed contours.

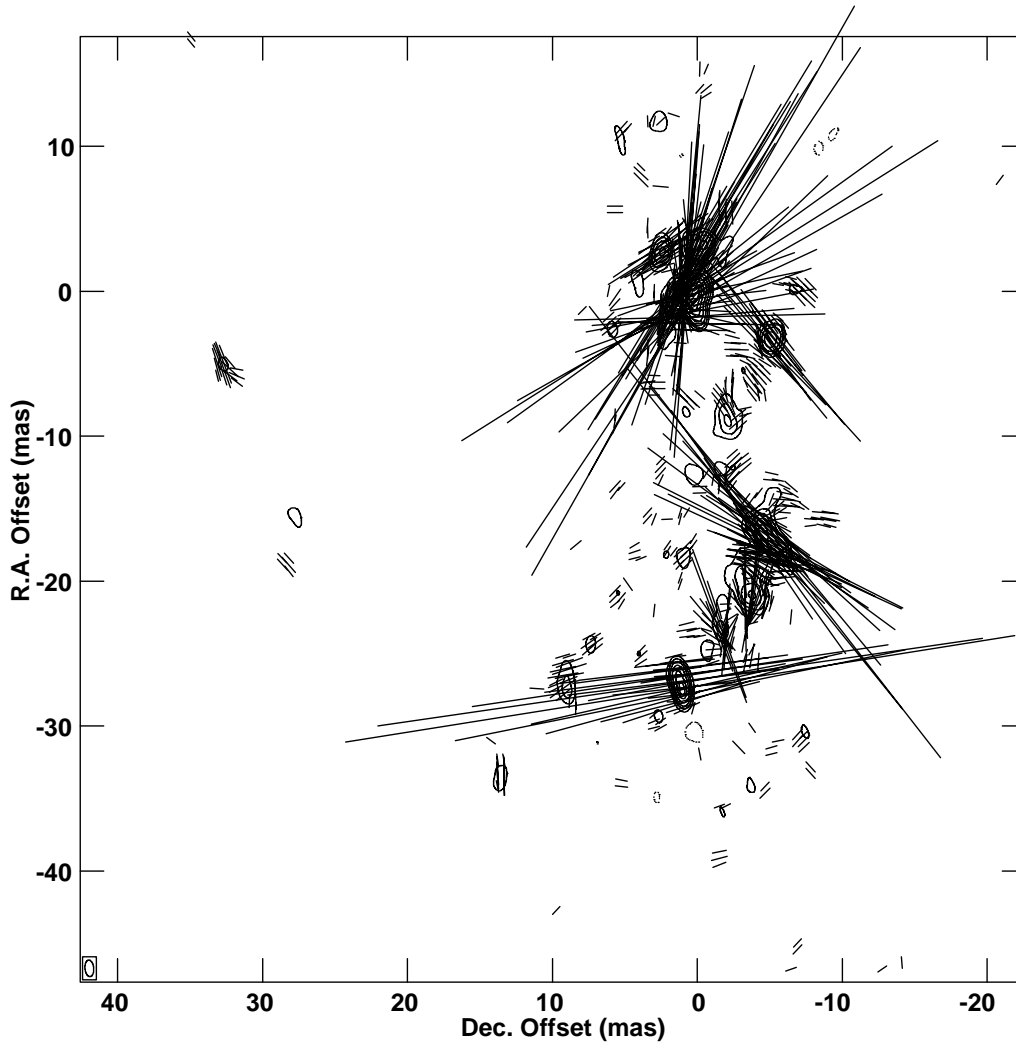


Figure 3.7: Epoch 1 linear polarization image of the  $v = 1, J = 1 - 0$  SiO maser emission towards R Aqr integrated over the LSR velocity range of  $-32.9 \text{ km s}^{-1}$  to  $-17.4 \text{ km s}^{-1}$ . Stokes  $I$  is plotted as a contour map with levels  $-10, -5, -2, 2, 5, 10, 20, 40, 60, 80$ , and  $100\%$  of the peak integrated flux density  $134.5 \text{ Jy/beam}$ . The vectors indicate the plane of the electric field vector and have lengths proportional to the linearly polarized intensity, where  $10 \text{ mas} = 5.6 \text{ Jy/beam}$ . Polarization vectors are plotted at all points where the total intensity exceeds  $0.1 \text{ Jy/beam}$  and the linearly polarized intensity exceeds  $0.4 \text{ Jy/beam}$ .

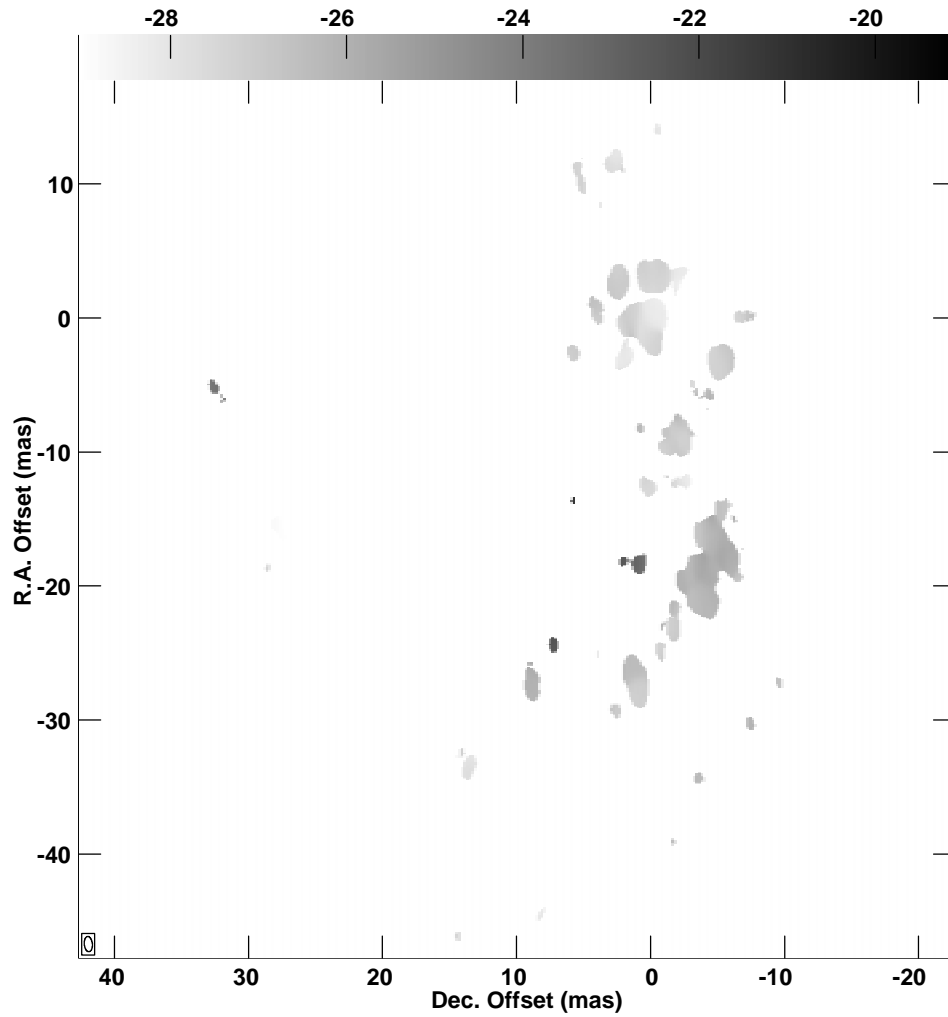


Figure 3.8: Epoch 1 velocity map of the  $v = 1, J = 1 - 0$  SiO maser emission towards R Aqr. Velocities are plotted on a greyscale ranging from  $-29.0 \text{ km s}^{-1}$  to  $-19.1 \text{ km s}^{-1}$ . The LSR velocity of R Aqr is  $\sim 27.0 \text{ km s}^{-1}$ .

## 3.3 Epoch 2

### 3.3.1 Observations

Observations for Epoch 2 were recorded during a second 24-hour observing run beginning at 18:00 UT on December 29, 1995. A total of 16 scans were recorded on R Aqr from 22:30 UT to 03:45 UT. At  $\sim 12.5$  minutes per scan the total time on source was  $\sim 3.3$  hours. In addition, 2 scans were recorded on the nearby continuum calibrator 3C 454.3 interspersed with the R Aqr scans. Over the entire 24-hour run, 7 scans were recorded on the source 0420–014. This source was used to calibrate the absolute position angle for the linear polarization vectors. Data were recorded in 4 IF's for both the continuum and line sources. For R Aqr, the first IF contained the 43-GHz maser emission. The data integration time for both the cross-power and total power spectra was  $\sim 3.0$  seconds.

### 3.3.2 Calibration and Imaging

The data for R Aqr and the two continuum calibrators were imported into AIPS and the scans concatenated into three separate source files. One IF was loaded for R Aqr and 3C 454.3, and all four IF's for 0420–014. An initial edit was performed using the flagging table supplied with the data in conjunction with the task UVFLG. The data were further edited interactively using the task TVFLG.

The phase rotation due to the parallactic angle was corrected using the task CLCOR. Bandpasses for both the cross-power and autocorrelation data were generated using the task CPASS on the continuum calibrator 3C 454.3. The bandpass amplitude response for both the autocorrelation and cross-correlation data was determined from the total-power spectra of 3C 454.3. The bandpass phases were computed from the cross-power spectra of 3C 454.3.

At this point, the autocorrelation and cross-correlation data for the line source were separated into different files using the task UVCOP. Each file was corrected for small Doppler shifts in the desired LSR velocity. The tasks SETJY and CVEL were used to center the band on the LSR velocity of  $-27.0 \text{ km s}^{-1}$ . The bandpass corrections were applied at this stage as part of CVEL.

For Epoch 2, the total power spectra are relatively poor. Nevertheless, I attempted to determine the amplitude calibration using the template fitting method applied to several different scans with several different antennas used as the reference. Various runs of ACFIT yielded widely varying amplitude gains, therefore I decided to use the system temperatures and antenna gain curves supplied with the Epoch 2 ob-

servations to calibrate the amplitudes for Epoch 2. System temperatures and gain curves were read into AIPS and used to create a solution (SN) table using the tasks ANTAB and APCAL. Since the template fitting method was not used to determine the amplitude gains, the R–L amplitude differences had to be estimated and applied to each antenna. These differences were determined from the fully calibrated (including self-calibration) continuum source 3C 454.3. Antenna amplitudes were smoothed over the entire time period for the two scans on 3C 454.3 and the RCP/LCP ratios computed. These ratios, which were used to correct the LCP of each antenna, are shown in Table 3.2.

Table 3.2: Correction factors for the R–L amplitude differences for Epoch 2.

Antenna	RCP/LCP
Brewster (BR)	1.004
Fort Davis (FD)	1.012
Hancock (HN)	1.013
Kitt Peak (KP)	1.026
Los Alamos (LA)	0.984
Mauna Kea (MK)	1.006
North Liberty (NL)	1.038
Owens Valley (OV)	0.996
Pietown (PT)	1.024
Saint Croix (SC)	1.048
VLA (Y)	1.006

Residual group delays along with preliminary residual fringe-rates were determined from the 3C 454.3 data using the task FRING with a solution interval of 30 seconds. Discrepant delays and rates were removed and the phase solutions applied to the R Aqr cross-power data. R–L residual delay differences were estimated by fringe-fitting the cross-hand ( $RL$  and  $LR$ ) data streams. The residual delay differences were edited and averaged over the entire scan interval with the result  $\Delta\tau^{R-L} \approx 23$  ns.

Residual fringe-rates were estimated by performing a fringe-fit on a reference channel ( $-28.3$  km s $^{-1}$ ) from the R Aqr cross-power spectrum. All phase corrections were applied at this stage using the task SPLIT. A cross-power spectrum of the calibrated data is shown in Figure 3.9.

As in Epoch 1, data from the Hancock (HN), Mauna Kea (MK), and St Croix

(SC) antennas were flagged after it was determined that the masers were not detected on baselines to these stations. Synthesis images of Stokes  $I$  and  $V$  were constructed using the standard self-calibration and imaging techniques. A self-calibration of the phases was performed using the above reference channel, and the final phase solution was applied to all channels in the spectrum. Image cubes consisting of individual channel maps were made for velocities between  $-32.9 \text{ km s}^{-1}$  and  $-17.4 \text{ km s}^{-1}$ . Each map is  $1024 \times 1024$  pixels in size with a pixel spacing of  $\sim 0.09$  mas. The synthesized beam for these images is  $1.30 \times 0.59$  mas. From the  $I$  and  $V$  image cubes, integrated flux density images were formed by summing the intensity over the above velocity range. These images are shown in Figures 3.10 and 3.11. The image cube used to form the integrated Stokes  $I$  map is shown in Appendix A.

Antenna  $D$ -terms were estimated using the polarization self-calibration technique on channels from  $-31.3 \text{ km s}^{-1}$  to  $-22.9 \text{ km s}^{-1}$ . These solutions were applied to the data set and the Stokes  $Q$  and  $U$  image cubes formed. Integrated flux density images in  $Q$  and  $U$  are shown in Figures 3.12 and 3.13. Corrections to the absolute position angle of the linear polarization vectors were determined by comparing the position angles determined for 0420–014 from the Epoch 2 VLBA observations and VLA observations taken on January 4, 1996. The linearly polarized intensity images were then formed from the integrated  $Q$  and  $U$  images with the  $-102^\circ$  correction applied. This integrated linear polarized intensity image is shown in Figure 3.14.

Similar to Epoch 1, TRANS and XGAUSS were used to form a velocity map of the emission for Epoch 2. Figure 3.15 shows the center velocity at the peak flux density derived from the fit of a single Gaussian at each pixel location.

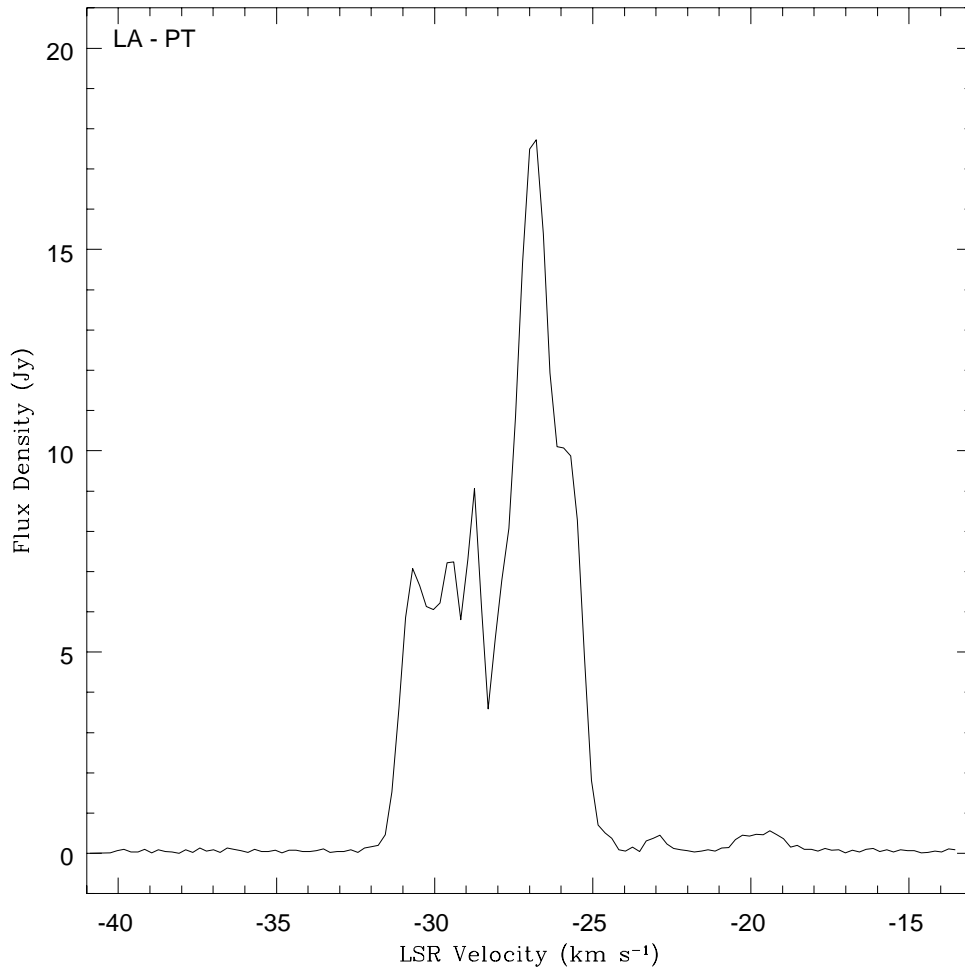


Figure 3.9: Stokes  $I$  cross-power spectrum of the  $v = 1, J = 1 - 0$  SiO maser emission towards R Aqr as observed for Epoch 2. Baseline from Los Alamos, NM to Pietown, NM.

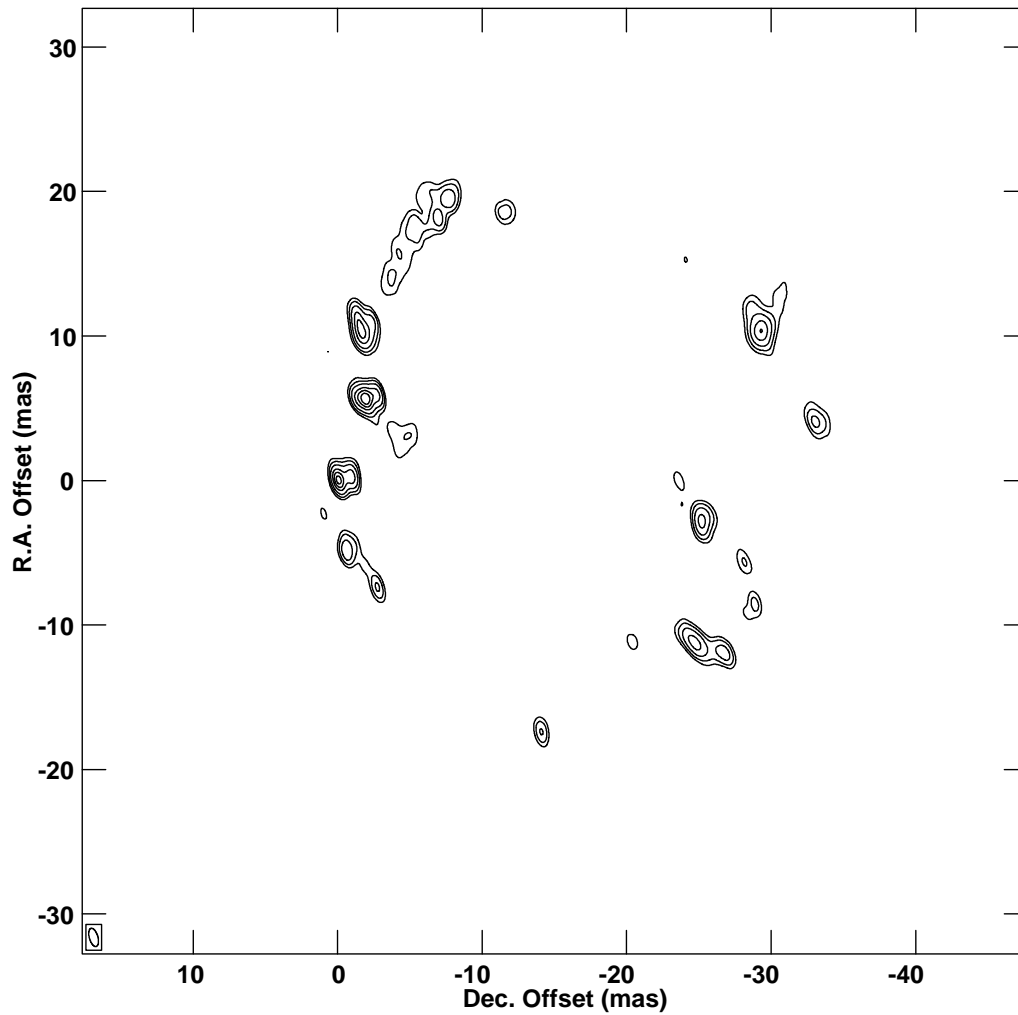


Figure 3.10: Epoch 2 total intensity (Stokes  $I$ ) image of the  $v = 1, J = 1 - 0$  SiO maser emission towards R Aqr integrated over the LSR velocity range of  $-32.9 \text{ km s}^{-1}$  to  $-17.4 \text{ km s}^{-1}$ . Contour levels are  $-10, -5, 5, 10, 20, 40, 60, 80,$  and  $100\%$  of the peak integrated flux density  $36.0 \text{ Jy/beam}$ .

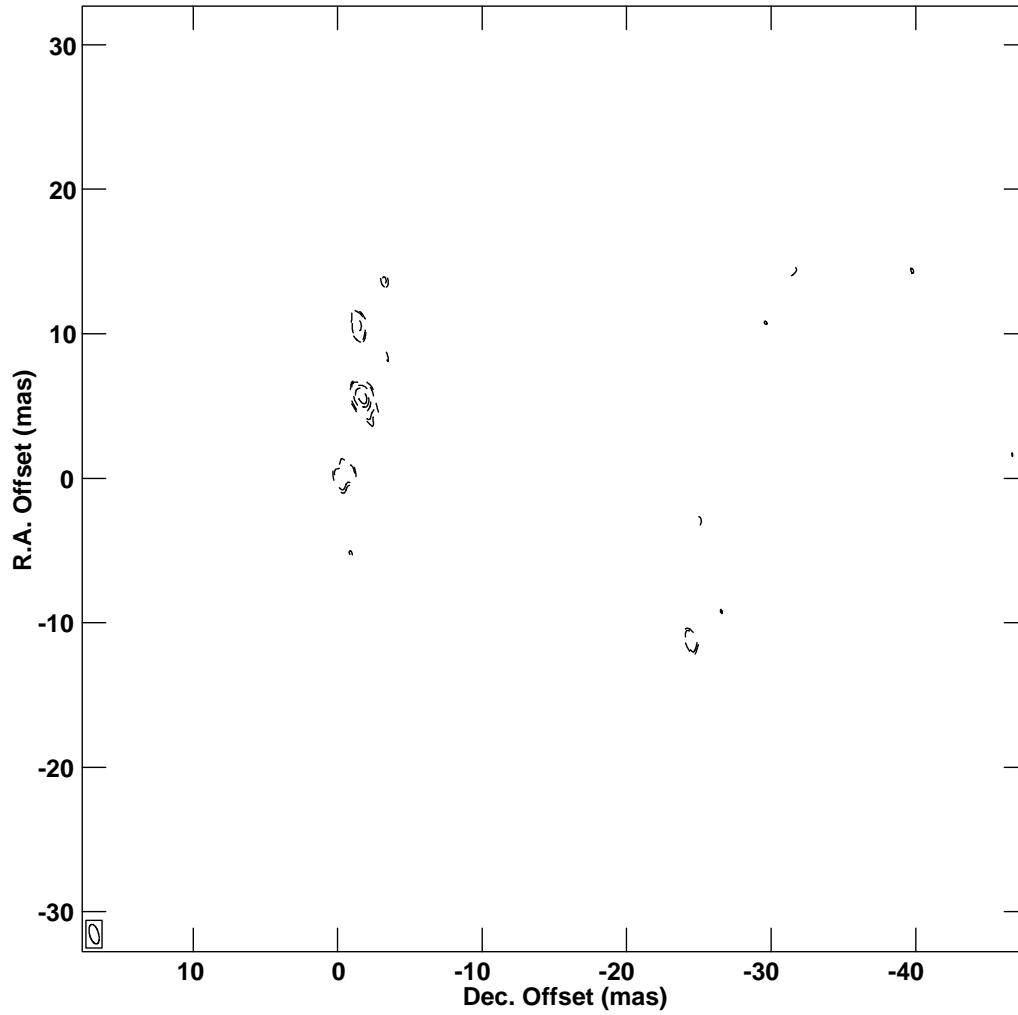


Figure 3.11: Epoch 2 circular polarization (Stokes  $V$ ) image of the  $v = 1, J = 1-0$  SiO maser emission towards R Aqr integrated over the LSR velocity range of  $-32.9 \text{ km s}^{-1}$  to  $-17.4 \text{ km s}^{-1}$ . Contour levels are  $-100, -80, -60, -40, -20, -15, 15, 20, 40, 60, 80,$  and  $100\%$  of the peak integrated flux density  $-3.0 \text{ Jy/beam}$ . Negative flux densities are represented by dashed contours.

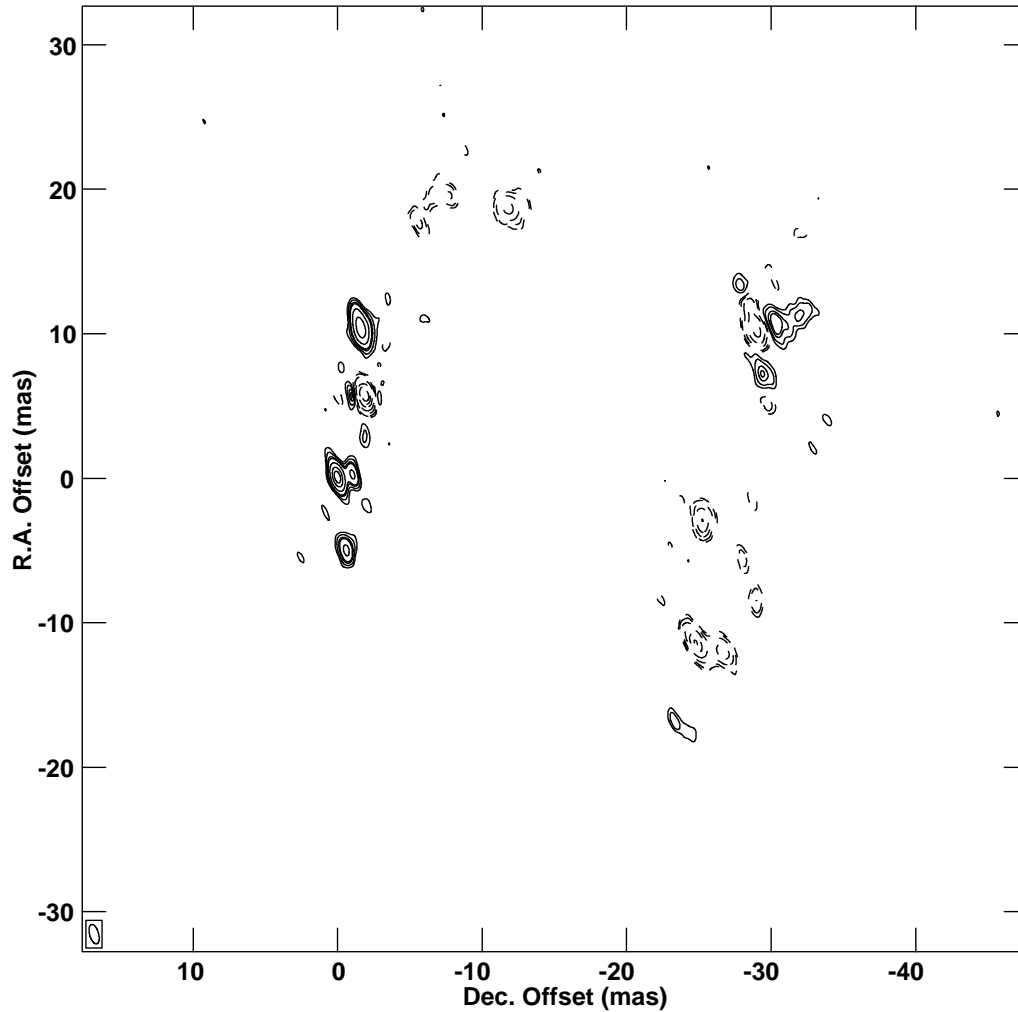


Figure 3.12: Epoch 2 Stokes  $Q$  image of the  $v = 1, J = 1 - 0$  SiO maser emission towards R Aqr integrated over the LSR velocity range of  $-32.9 \text{ km s}^{-1}$  to  $-17.4 \text{ km s}^{-1}$ . Contour levels are  $-100, -80, -60, -40, -20, -10, -5, -3, 3, 5, 10, 20, 40, 60, 80,$  and  $100\%$  of the peak integrated flux density  $-10.2 \text{ Jy/beam}$ . Negative flux densities are represented by dashed contours.

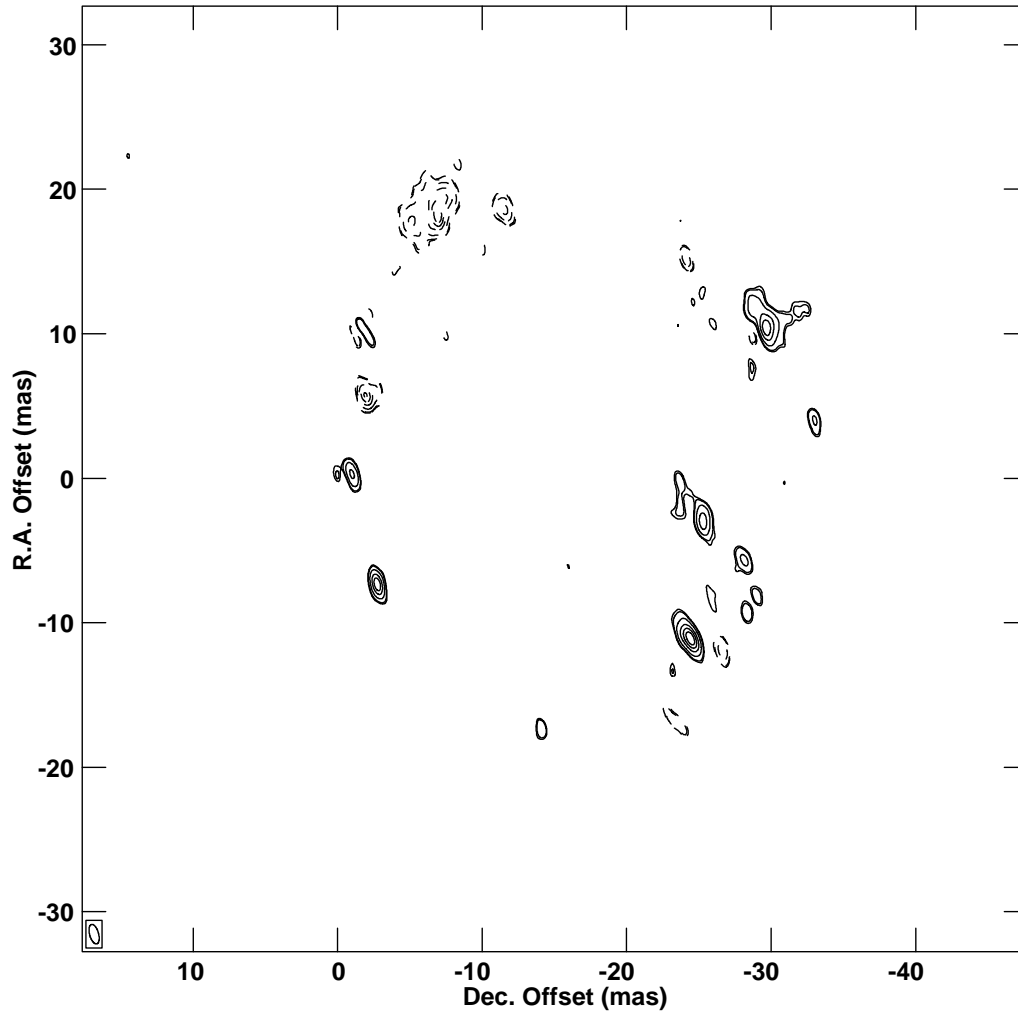


Figure 3.13: Epoch 2 Stokes  $U$  image of the  $v = 1, J = 1 - 0$  SiO maser emission towards R Aqr integrated over the LSR velocity range of  $-32.9 \text{ km s}^{-1}$  to  $-17.4 \text{ km s}^{-1}$ . Contour levels are  $-100, -80, -60, -40, -20, -10, -8, 8, 10, 20, 40, 60, 80$ , and  $100\%$  of the peak integrated flux density  $4.6 \text{ Jy/beam}$ . Negative flux densities are represented by dashed contours.

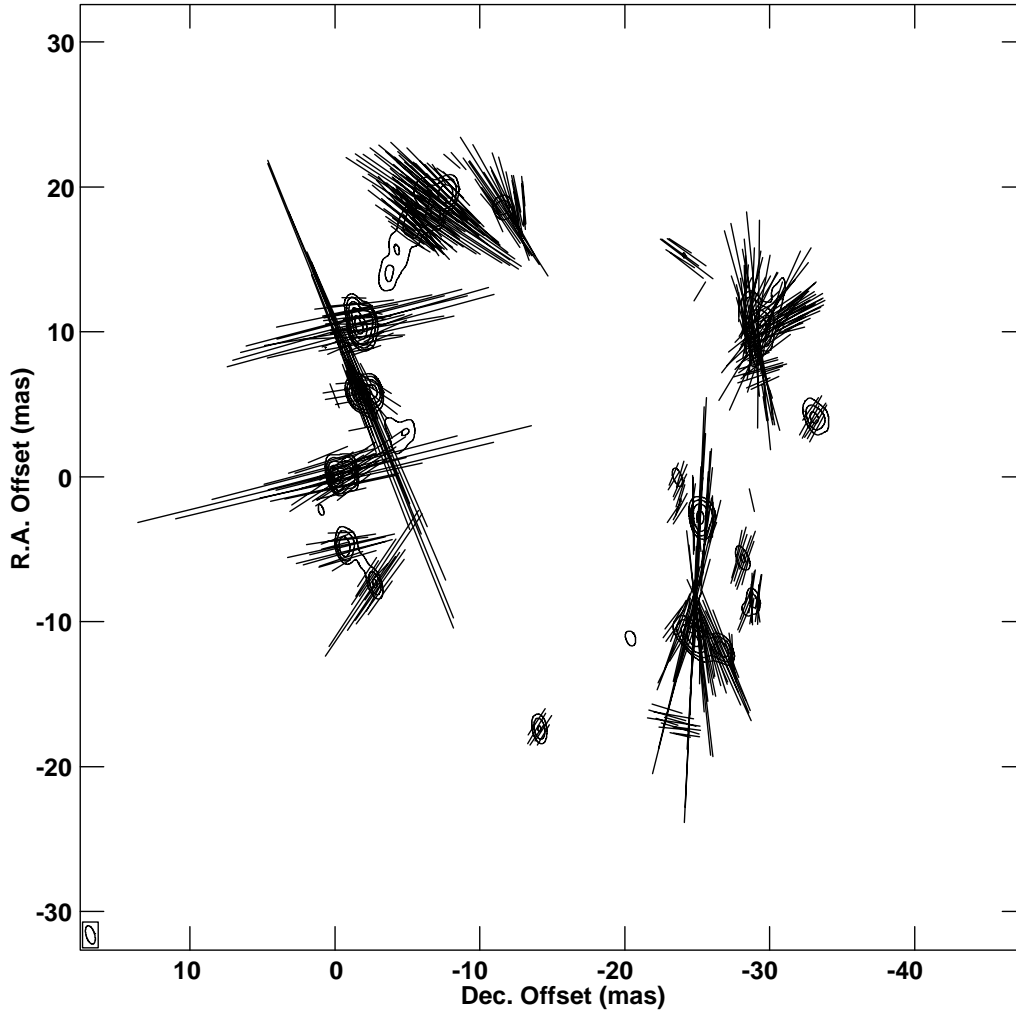


Figure 3.14: Epoch 2 linear polarization image of the  $v = 1, J = 1 - 0$  SiO maser emission towards R Aqr integrated over the LSR velocity range of  $-32.9 \text{ km s}^{-1}$  to  $-17.4 \text{ km s}^{-1}$ . Stokes  $I$  is plotted as a contour map with levels  $-10, -5, 5, 10, 20, 40, 60, 80,$  and  $100\%$  of the peak integrated flux density  $36.0 \text{ Jy/beam}$ . The vectors indicate the plane of the electric field vector and have lengths proportional to the linearly polarized intensity, where  $10 \text{ mas} = 2.8 \text{ Jy/beam}$ . Polarization vectors are plotted at all points where the total intensity exceeds  $0.1 \text{ Jy/beam}$  and the linearly polarized intensity exceeds  $0.4 \text{ Jy/beam}$ .

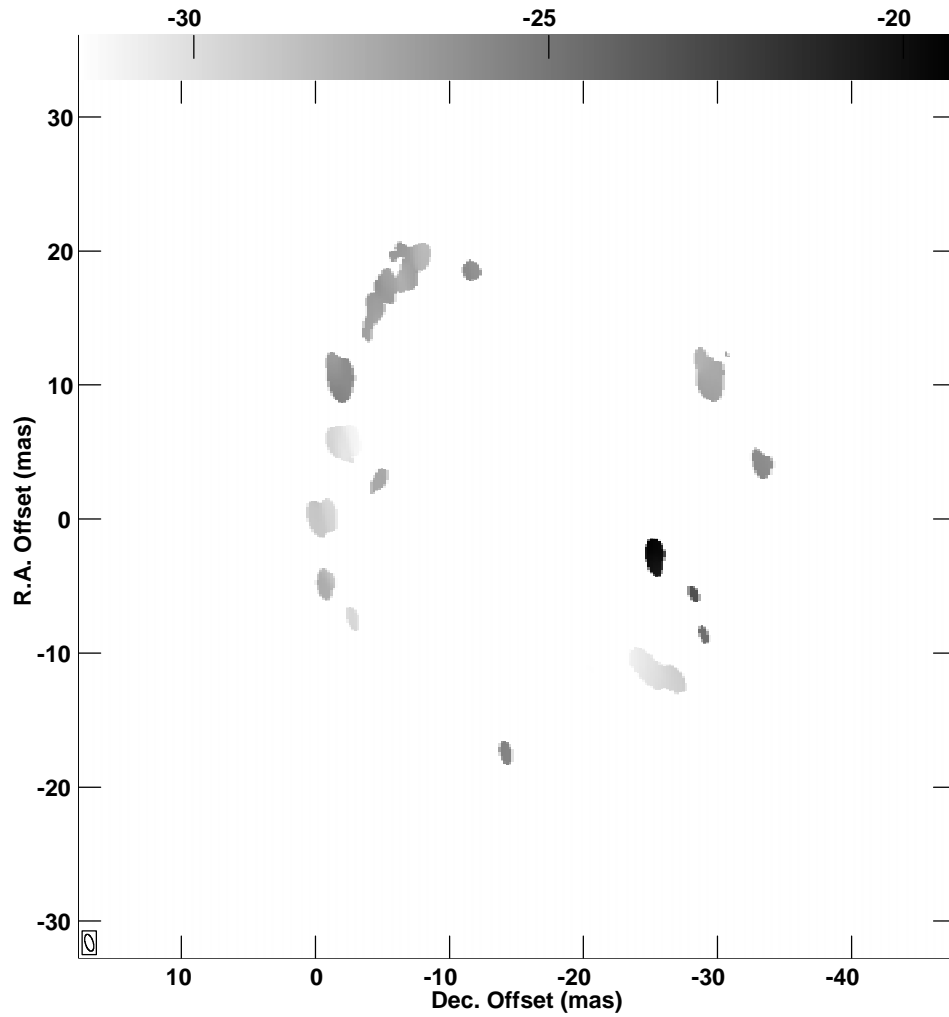


Figure 3.15: Epoch 2 velocity map of the  $v = 1, J = 1 - 0$  SiO maser emission towards R Aqr. Velocities are plotted on a greyscale ranging from  $-31.6 \text{ km s}^{-1}$  to  $-19.3 \text{ km s}^{-1}$ . The LSR velocity of R Aqr is  $\sim 27.0 \text{ km s}^{-1}$ .

## 3.4 Epoch 3

### 3.4.1 Observations

Observations for Epoch 3 were recorded during a third 24-hour observing run beginning at 20:00 UT on February 2, 1996. A total of 17 scans were recorded on R Aqr beginning at 20:00 UT and ending at 01:30 UT. At  $\sim 12.5$  minutes per scan the total time on source was  $\sim 3.5$  hours. In addition, 3 scans were recorded on the nearby continuum calibrator 3C 454.3 interspersed with the R Aqr scans. Over the entire 24-hour run, 8 scans were recorded on the source 0420–014. Data were recorded in 4 IF's for both the continuum and line sources. For R Aqr, the first IF contained the 43-GHz maser emission. The data integration time for both the cross-power and total power spectra was  $\sim 6.0$  seconds.

### 3.4.2 Calibration and Imaging

The data for R Aqr and the two continuum calibrators were imported into AIPS and the scans concatenated into three separate source files. One IF was loaded for R Aqr and 3C 454.3, and all four IF's for 0420–014. An initial edit was performed using the flagging table supplied with the data in conjunction with the task UVFLG. The data were further edited interactively using the task TVFLG.

The phase rotation due to the parallactic angle was corrected using the task CLCOR. Bandpasses for both the cross-power and autocorrelation data were generated using the task CPASS on the continuum calibrator 3C 454.3. The bandpass amplitude response for both the autocorrelation and cross-correlation data was determined from the total-power spectra of 3C 454.3. The bandpass phases were computed from the cross-power spectra of 3C 454.3.

UVCOP was used to separate the autocorrelation and cross-correlation data into separate files. Each file was corrected for small Doppler shifts in the desired LSR velocity. The tasks SETJY and CVEL were used to center the band on the LSR velocity of  $-27.0 \text{ km s}^{-1}$ . The bandpass corrections were applied at this stage as part of CVEL.

The total power spectra were examined, and a high-quality spectrum found for a single scan on the chosen reference antenna at Fort Davis (antenna code FD). This scan had a relatively high elevation at  $43^\circ$  with a point source sensitivity of  $10.4 \text{ Jy K}^{-1}$  and average system temperatures of 95.7 K and 91.1 K in RCP and LCP respectively. Antenna amplitude gains were determined for the entire data set at 2 minute intervals using the above scan as a template with the task ACFIT. The

template fitting method was also used to compute the R–L amplitude difference for the reference antenna. ACFIT was used to compute a  $RR/LL$  correction of 1.022 averaged over the entire scan. This correction was applied by multiplying the LCP gains of the reference antenna by the above factor.

Residual group delays along with preliminary residual fringe-rates were determined from the 3C 454.3 data using the task FRING with a solution interval of 30 seconds. Discrepant delays and rates were removed and the phase solutions applied to the R Aqr cross-power data. Because the SNR in the cross-hand polarizations ( $RL$  and  $LR$ ) for 3C 454.3 was too low to get reliable solutions from the fringe-fit, it was not possible to determine the R–L residual delay differences from this source. As a substitute, 3 scans from a second continuum calibrator 3C 273 were loaded onto disk. This calibrator was recorded later in the 24 hour run and was to be used to calibrate a different program source. A fringe-fit was performed on the 3C 273 cross-hand data streams, and the residual delay differences edited and averaged over the entire scan interval with the result  $\Delta\tau^{R-L} \approx 7$  ns.

Residual fringe-rates were estimated by performing a fringe-fit on a reference channel ( $-30.7$  km s $^{-1}$ ) from the R Aqr cross-power spectrum. All phase corrections were applied at this stage using the task SPLIT. A cross-power spectrum of the calibrated data is shown in Figure 3.16.

Data from the Hancock (HN), Mauna Kea (MK), and St Croix (SC) antennas were flagged after it was determined that the masers were not detected on baselines to these stations. In addition, much of the data for the Pietown (PT) antenna were lost due poor weather. Synthesis images of Stokes  $I$  and  $V$  were constructed using the standard self-calibration and imaging techniques. A self-calibration of the phases was performed using the above reference channel, and the final phase solution was applied to all channels in the spectrum. Image cubes consisting of individual channel maps were made for velocities between  $-32.9$  km s $^{-1}$  and  $-17.4$  km s $^{-1}$ . Each map is  $1024 \times 1024$  pixels in size with a pixel spacing of  $\sim 0.09$  mas. The synthesized beam for these images is  $1.54 \times 0.71$  mas. From the  $I$  and  $V$  image cubes, integrated flux density images were formed by summing the intensity over the above velocity range. These images are shown in Figures 3.17 and 3.18. The image cube used to form the integrated Stokes  $I$  map is shown in Appendix A.

Antenna  $D$ -terms were estimated using the polarization self-calibration technique on channels from  $-31.3$  km s $^{-1}$  to  $-22.8$  km s $^{-1}$ . These solutions were applied to the data set and the Stokes  $Q$  and  $U$  image cubes formed. Integrated flux density images in  $Q$  and  $U$  are shown in Figures 3.19 and 3.20. The polarization position angle for 0420–014 could not be determined from the VLBA data for Epoch 3. This is most likely due to the variability of the source itself. The position angle correction for Epoch 3 was therefore interpolated using Epochs 1, 2, and 4. The

linearly polarized intensity images were formed from the integrated  $Q$  and  $U$  images with a  $-110^\circ$  correction applied. This integrated linear polarized intensity image is shown in Figure 3.21.

The AIPS tasks **TRANS** and **XGAUSS** were again used to form an image of the velocity structure of the SiO emission towards R Aqr for Epoch 3. Figure 3.22 shows the center velocity at the peak flux density derived from the fit of a single Gaussian at each pixel location.

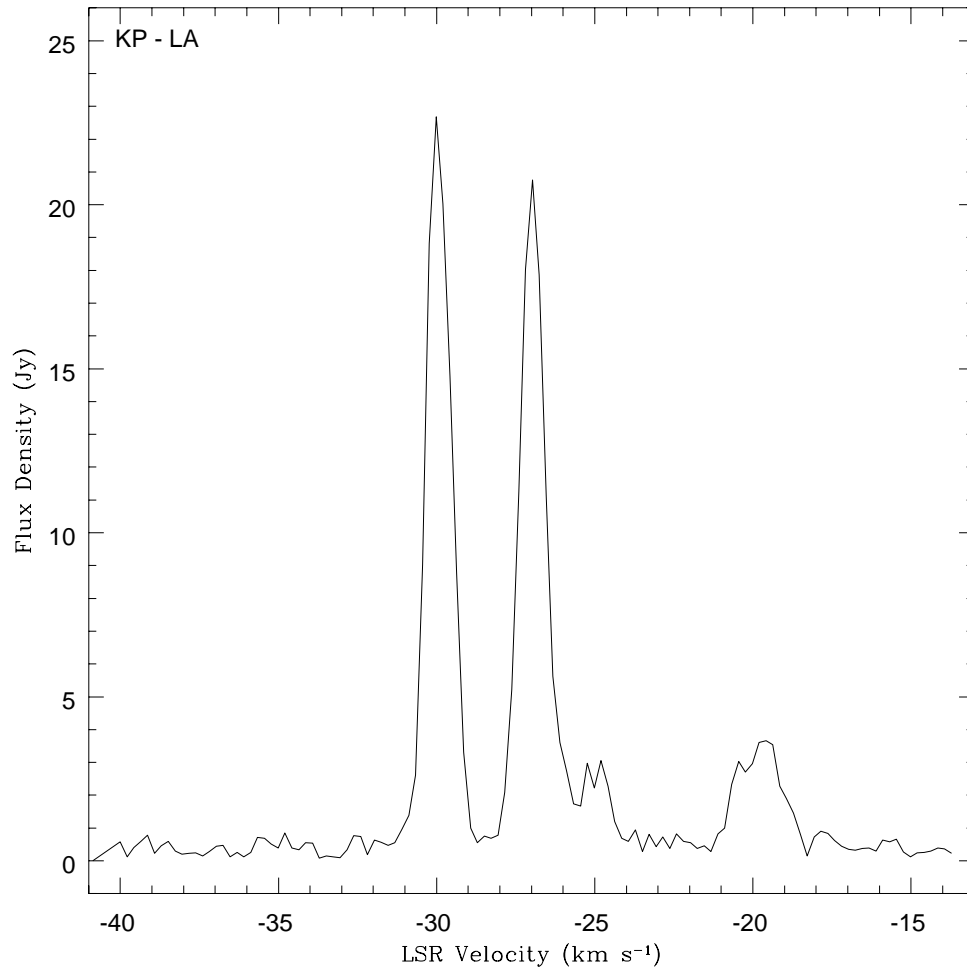


Figure 3.16: Stokes  $I$  cross-power spectrum of the  $v = 1, J = 1-0$  SiO maser emission towards R Aqr as observed for Epoch 3. Baseline from Kitt Peak, AZ to Los Alamos, NM.

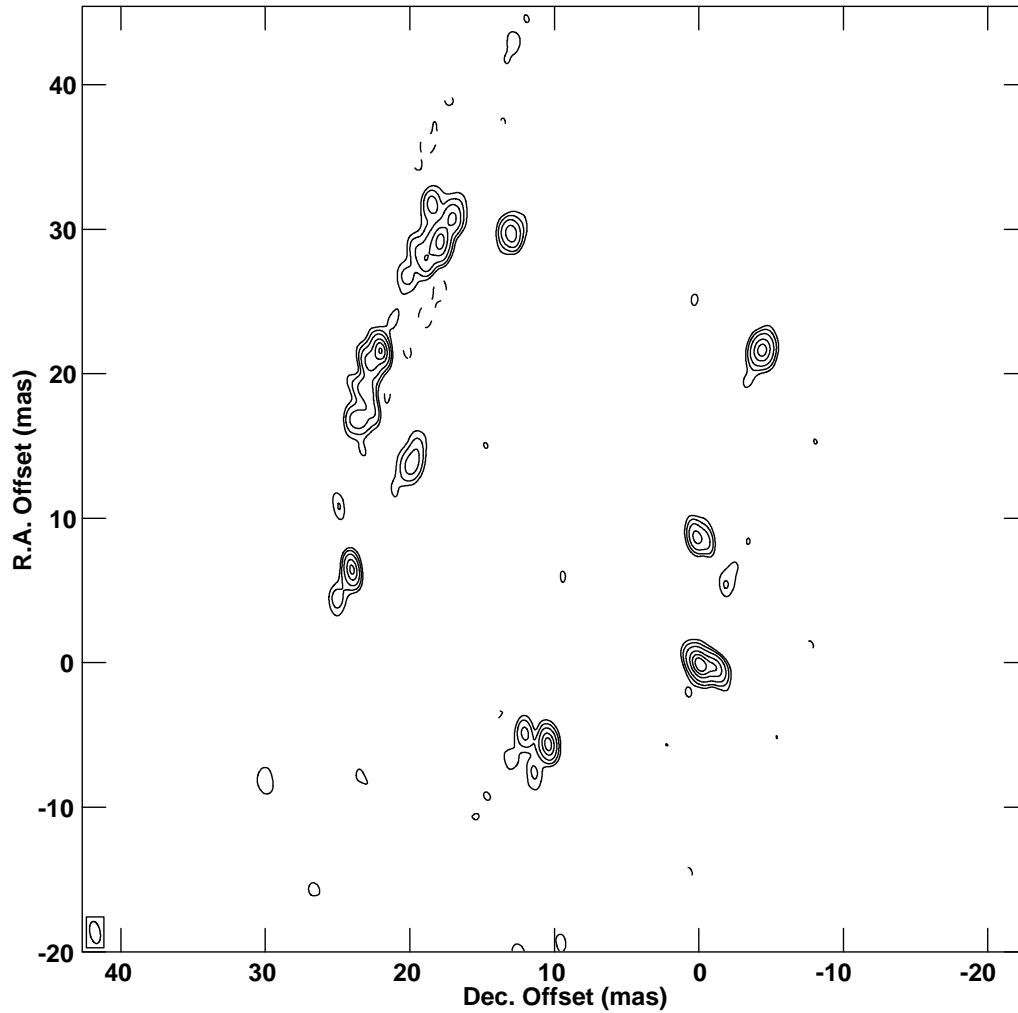


Figure 3.17: Epoch 3 total intensity (Stokes  $I$ ) image of the  $v = 1, J = 1 - 0$  SiO maser emission towards R Aqr integrated over the LSR velocity range of  $-32.9 \text{ km s}^{-1}$  to  $-17.4 \text{ km s}^{-1}$ . Contour levels are  $-10, -5, 5, 10, 20, 40, 60, 80,$  and  $100\%$  of the peak integrated flux density  $44.0 \text{ Jy/beam}$ .

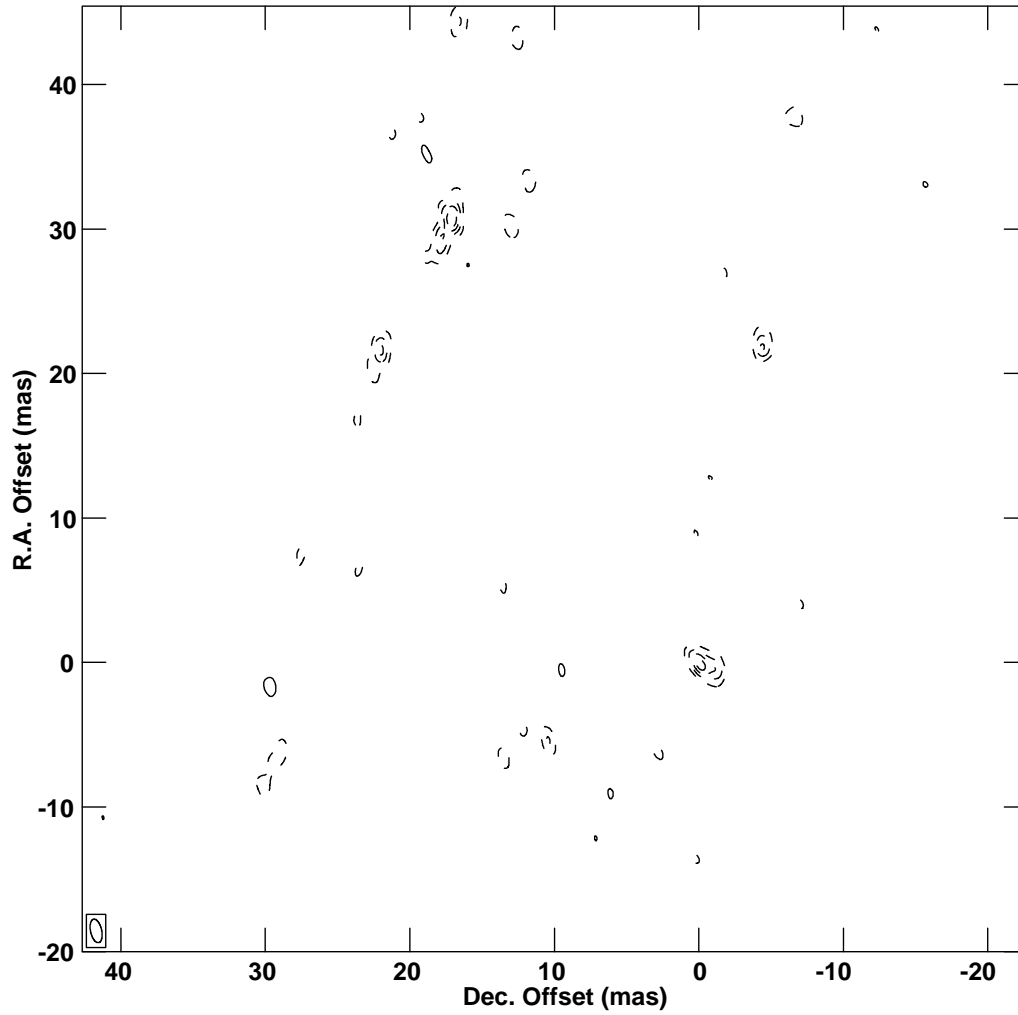


Figure 3.18: Epoch 3 circular polarization (Stokes  $V$ ) image of the  $v = 1, J = 1-0$  SiO maser emission towards R Aqr integrated over the LSR velocity range of  $-32.9 \text{ km s}^{-1}$  to  $-17.4 \text{ km s}^{-1}$ . Contour levels are  $-100, -80, -60, -40, -20, 20, 40, 60, 80,$  and  $100\%$  of the peak integrated flux density  $-9.7 \text{ Jy/beam}$ . Negative flux densities are represented by dashed contours.

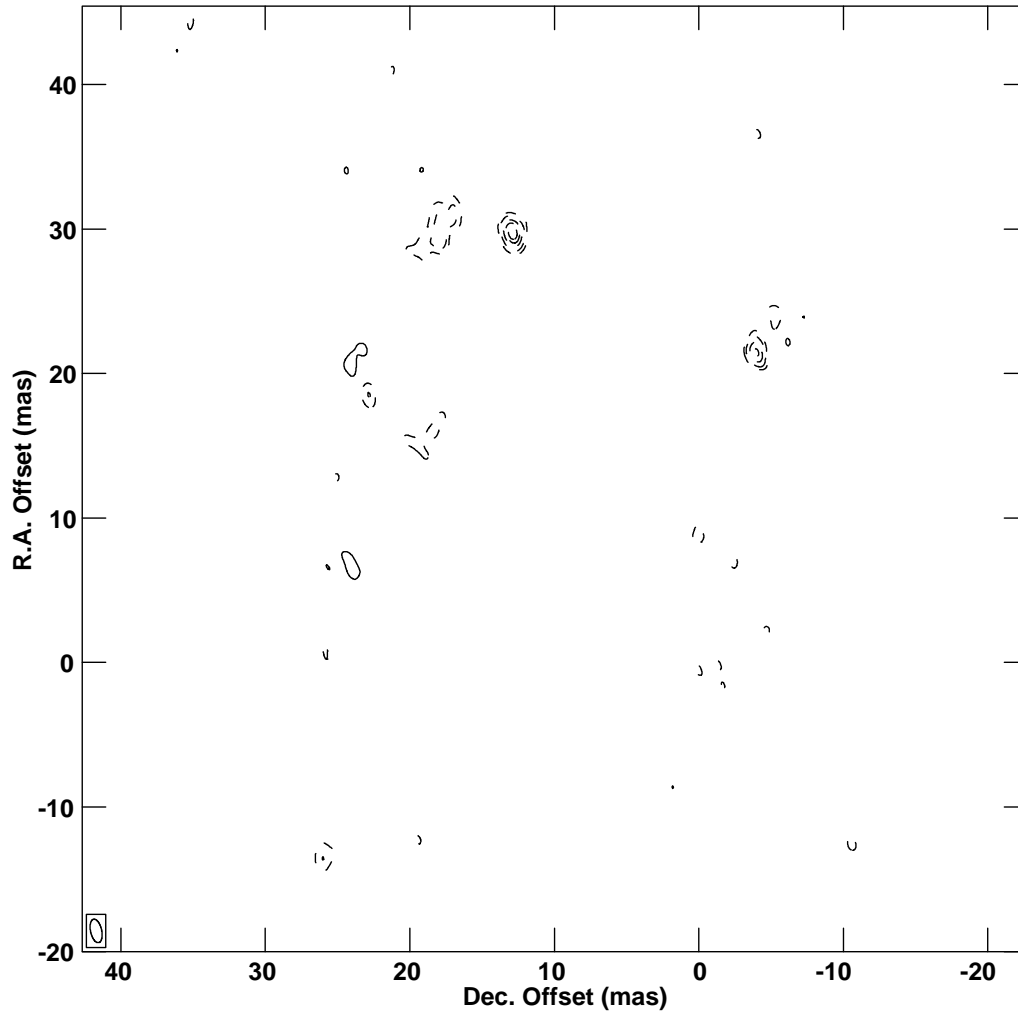


Figure 3.19: Epoch 3 Stokes  $Q$  image of the  $v = 1, J = 1 - 0$  SiO maser emission towards R Aqr integrated over the LSR velocity range of  $-32.9 \text{ km s}^{-1}$  to  $-17.4 \text{ km s}^{-1}$ . Contour levels are  $-100, -80, -60, -40, -20, -10, 10, 20, 40, 60, 80,$  and  $100\%$  of the peak integrated flux density  $-12.9 \text{ Jy/beam}$ . Negative flux densities are represented by dashed contours.

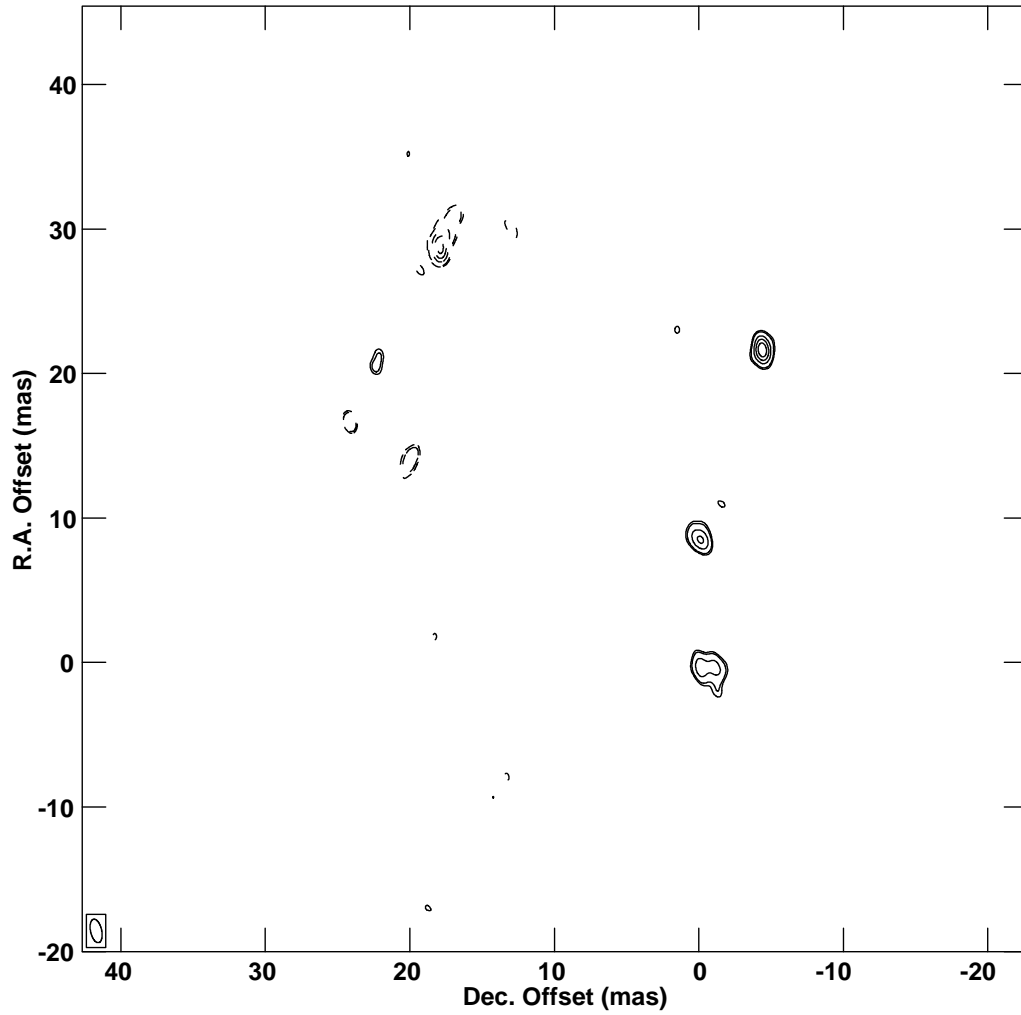


Figure 3.20: Epoch 3 Stokes  $U$  image of the  $v = 1, J = 1 - 0$  SiO maser emission towards R Aqr integrated over the LSR velocity range of  $-32.9 \text{ km s}^{-1}$  to  $-17.4 \text{ km s}^{-1}$ . Contour levels are  $-100, -80, -60, -40, -20, -15, 15, 20, 40, 60, 80,$  and  $100\%$  of the peak integrated flux density  $10.0 \text{ Jy/beam}$ . Negative flux densities are represented by dashed contours.

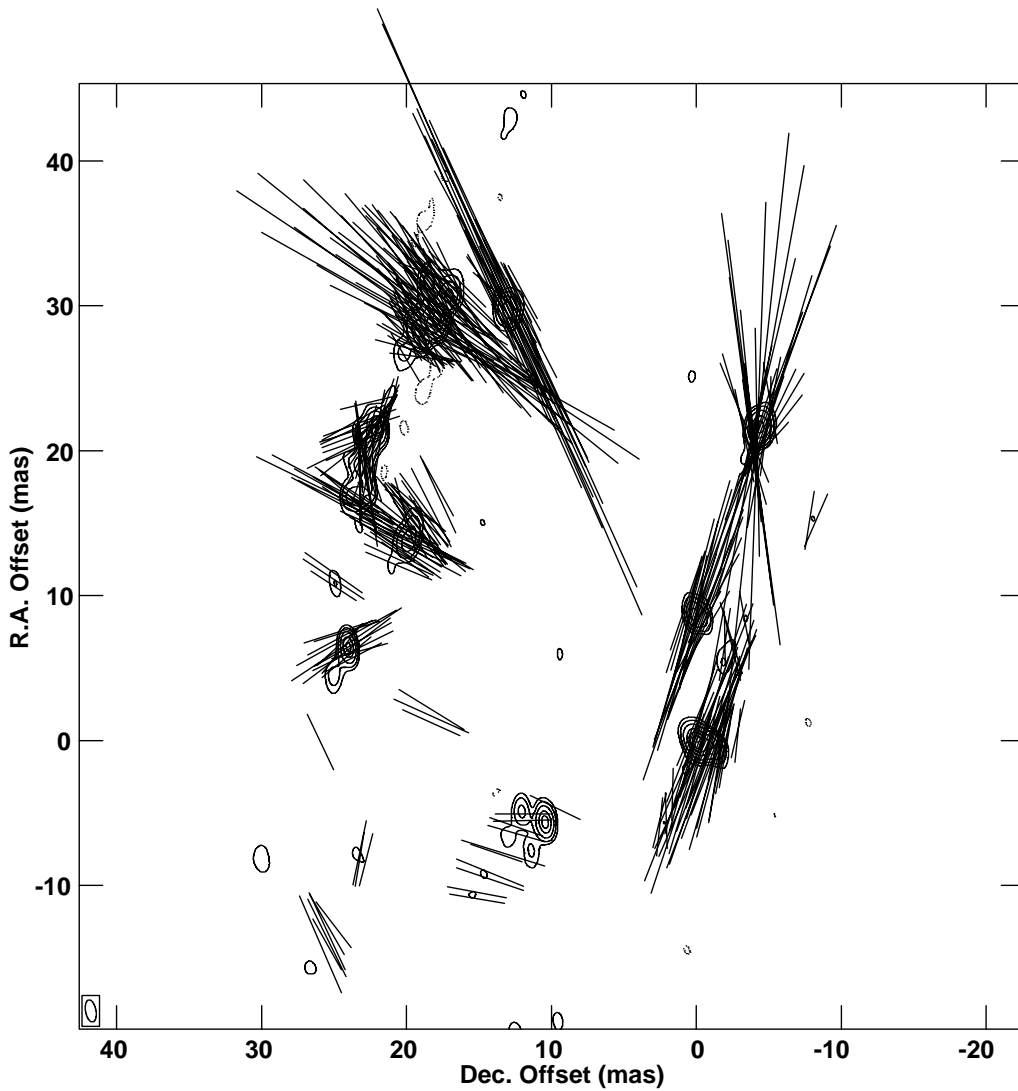


Figure 3.21: Epoch 3 linear polarization image of the  $v = 1, J = 1 - 0$  SiO maser emission towards R Aqr integrated over the LSR velocity range of  $-32.9 \text{ km s}^{-1}$  to  $-17.4 \text{ km s}^{-1}$ . Stokes  $I$  is plotted as a contour map with levels  $-10, -5, 5, 10, 20, 40, 60, 80,$  and  $100\%$  of the peak integrated flux density  $36.0 \text{ Jy/beam}$ . The vectors indicate the plane of the electric field vector and have lengths proportional to the linearly polarized intensity, where  $10 \text{ mas} = 2.8 \text{ Jy/beam}$ . Polarization vectors are plotted at all points where the total intensity exceeds  $1.2 \text{ Jy/beam}$  and the linearly polarized intensity exceeds  $1.0 \text{ Jy/beam}$ .

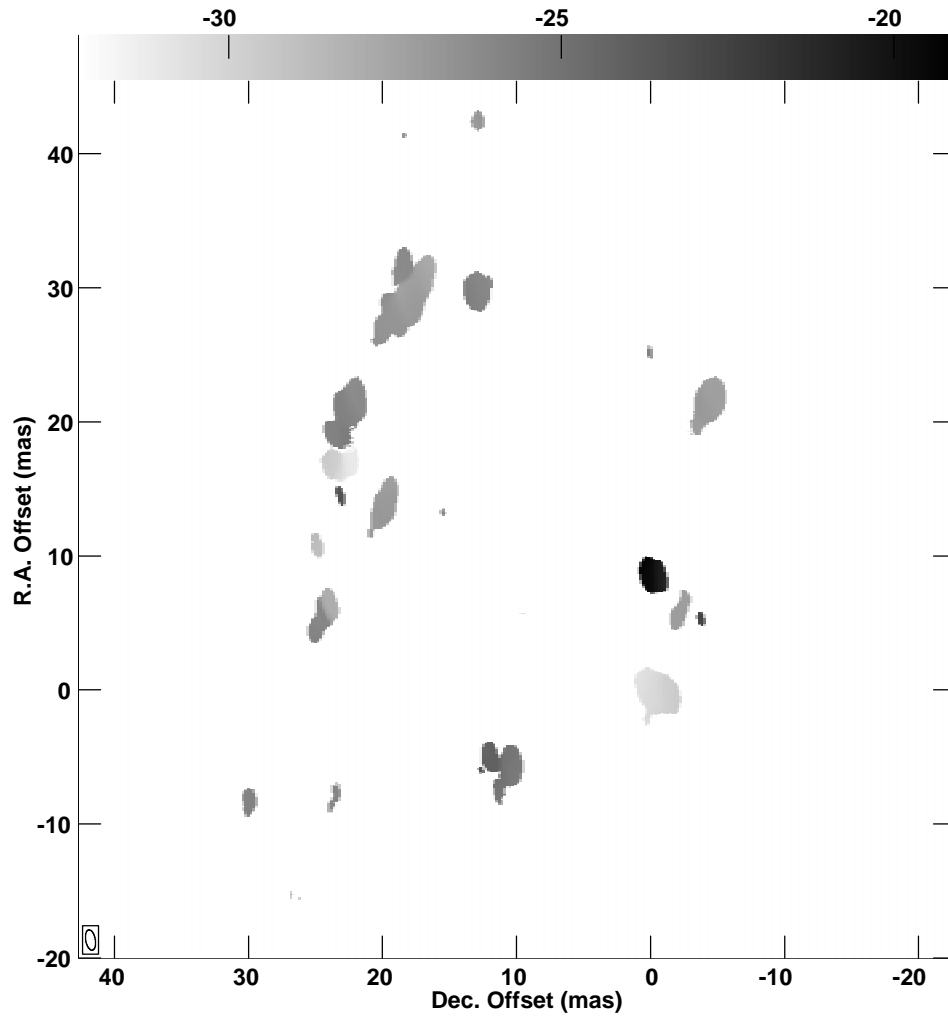


Figure 3.22: Epoch 3 velocity map of the  $v = 1, J = 1 - 0$  SiO maser emission towards R Aqr. Velocities are plotted on a greyscale ranging from  $-32.2 \text{ km s}^{-1}$  to  $-19.1 \text{ km s}^{-1}$ . The LSR velocity of R Aqr is  $\sim 27.0 \text{ km s}^{-1}$ .

## 3.5 Epoch 4

### 3.5.1 Observations

Observations for Epoch 4 were recorded during the final 24-hour observing run beginning at 00:00 UT on April 5, 1996. A total of 21 scans were recorded on R Aqr from 13:00 UT to 19:45 UT. At  $\sim 12.5$  minutes per scan the total time on source was  $\sim 4.4$  hours. In addition, 4 scans were recorded on the nearby continuum calibrator 3C 454.3 interspersed with the R Aqr scans. Over the entire 24-hour run, 9 scans were recorded on the source 0420–014. Which would be used to determine the absolute position angle of the linear polarization vectors. Data were recorded in 4 IF's for for both the continuum and line sources. For R Aqr, the first IF contained the 43-GHz maser emission. The data integration time for both the cross-power and total power spectra was  $\sim 6.0$  seconds.

### 3.5.2 Calibration and Imaging

The data for R Aqr and the two continuum calibrators were imported into AIPS and the scans concatenated into three separate source files. One IF was loaded for R Aqr and 3C 454.3, and all four IF's for 0420–014. An initial edit was performed using the flagging table supplied with the data in conjunction with the task UVFLG. The data were further edited interactively using the task TVFLG.

The phase rotation due to the parallactic angle was corrected using the task CLCOR. Bandpasses for both the cross-power and autocorrelation data were generated using the task CPASS on the continuum calibrator 3C 454.3. The bandpass amplitude response for both the autocorrelation and cross-correlation data was determined from the total-power spectra of 3C 454.3. The bandpass phases were computed from the cross-power spectra of 3C 454.3.

Autocorrelation and cross-correlation data for the line source were separated into different files using the task UVCOP. Each file was corrected for small Doppler shifts in the desired LSR velocity. The tasks SETJY and CVEL were used to center the band on the LSR velocity of  $-27.0 \text{ km s}^{-1}$ . The bandpass corrections were applied at this stage as part of CVEL.

An attempt was made to perform an amplitude calibration using the template fitting method but failed due to poor total power spectra. Instead, system temperatures and antenna gain curves supplied with the Epoch 4 observations were used to calibrate the amplitudes. System temperatures and gain curves were read into AIPS via ANTAB and used to create a solution (SN) table using the task APCAL. Since the

template fitting method was not used to determine the amplitude gains, the R–L amplitude differences had to be estimated and applied to each antenna. These differences were determined from the fully calibrated (including self-calibration) continuum source 3C 454.3. Antenna amplitudes were smoothed over the entire time period for the four scans on 3C 454.3 and the RCP/LCP ratios computed. These ratios, which were used to correct the LCP of each antenna, are shown in Table 3.3.

Table 3.3: Correction factors for the R–L amplitude differences for Epoch 4.

Antenna	RCP/LCP
Brewster (BR)	1.013
Fort Davis (FD)	0.901
Hancock (HN)	1.015
Kitt Peak (KP)	1.021
Los Alamos (LA)	0.972
Mauna Kea (MK)	1.056
North Liberty (NL)	1.033
Owens Valley (OV)	0.973
Pietown (PT)	1.082
Saint Croix (SC)	1.031
VLA (Y)	0.935

Residual group delays along with preliminary residual fringe-rates were determined from the 3C 454.3 data using the task `FRING` with a solution interval of 1 minute. Discrepant delays and rates were removed and the phase solutions applied to the R Aqr cross-power data. R–L residual delay differences were estimated by fringe-fitting the cross-hand ( $RL$  and  $LR$ ) data streams. The residual delay differences were edited and averaged over the entire scan interval with the result  $\Delta\tau^{R-L} \approx 18$  ns.

Residual fringe-rates were estimated by performing a fringe-fit on a reference channel ( $-24.8$  km s $^{-1}$ ) from the R Aqr cross-power spectrum. All phase corrections were applied at this stage using the task `SPLIT`. A cross-power spectrum of the calibrated data is shown in Figure 3.23.

Once again, data from the Hancock (HN), Mauna Kea (MK), and St Croix (SC) antennas were flagged after it was determined that the masers were not detected on baselines to these stations. Synthesis images of Stokes  $I$  and  $V$  were constructed using the standard self-calibration and imaging techniques. A self-calibration of the phases

was performed using the above reference channel, and the final phase solution was applied to all channels in the spectrum. Image cubes consisting of individual channel maps were made for velocities between  $-32.9 \text{ km s}^{-1}$  and  $-17.4 \text{ km s}^{-1}$ . Each map is  $1024 \times 1024$  pixels in size with a pixel spacing of  $\sim 0.09 \text{ mas}$ . The synthesized beam for these images is  $1.54 \times 0.71 \text{ mas}$ . From the  $I$  and  $V$  image cubes, integrated flux density images were formed by summing the intensity over the above velocity range. These images are shown in Figures 3.24 and 3.25. The image cube used to form the integrated Stokes  $I$  map is shown in Appendix A.

Antenna  $D$ -terms were estimated using the polarization self-calibration technique on channels from  $-30.5 \text{ km s}^{-1}$  to  $-21.8 \text{ km s}^{-1}$ . These solutions were applied to the data set and the Stokes  $Q$  and  $U$  image cubes formed. Integrated flux density images in  $Q$  and  $U$  are shown in Figures 3.26 and 3.27. Corrections to the absolute position angle of the linear polarization vectors were determined by comparing the position angles determined for 0420–014 from the Epoch 4 VLBA observations and VLA observations taken on February 4, 1996. The linearly polarized intensity images were then formed from the integrated  $Q$  and  $U$  images with the  $-120^\circ$  correction applied. This integrated linear polarized intensity image is shown in Figure 3.28.

The AIPS tasks TRANS and XGAUSS were again used to form an image of the velocity structure of the SiO emission towards R Aqr for Epoch 4. Figure 3.29 shows the center velocity at the peak flux density derived from the fit of a single Gaussian at each pixel location.

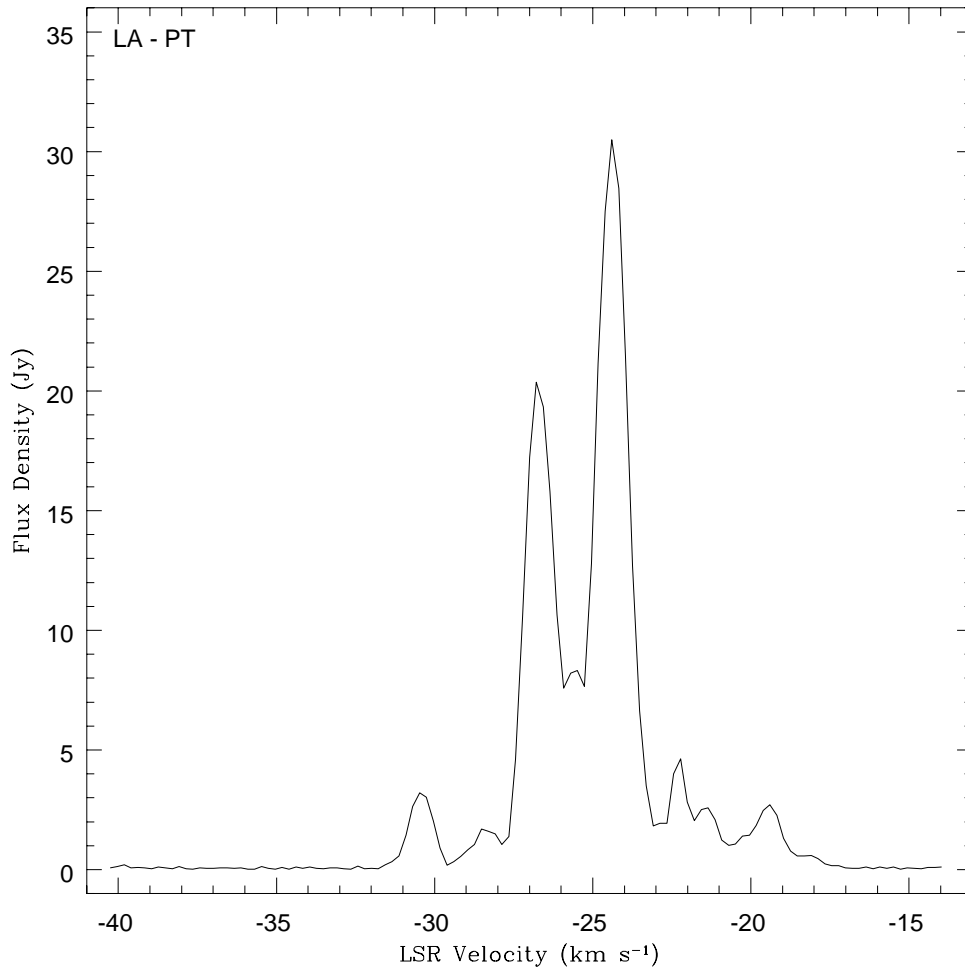


Figure 3.23: Stokes  $I$  cross-power spectrum of the  $v = 1$ ,  $J = 1-0$  SiO maser emission towards R Aqr as observed for Epoch 4. Baseline from Los Alamos, NM to Pietown, NM.

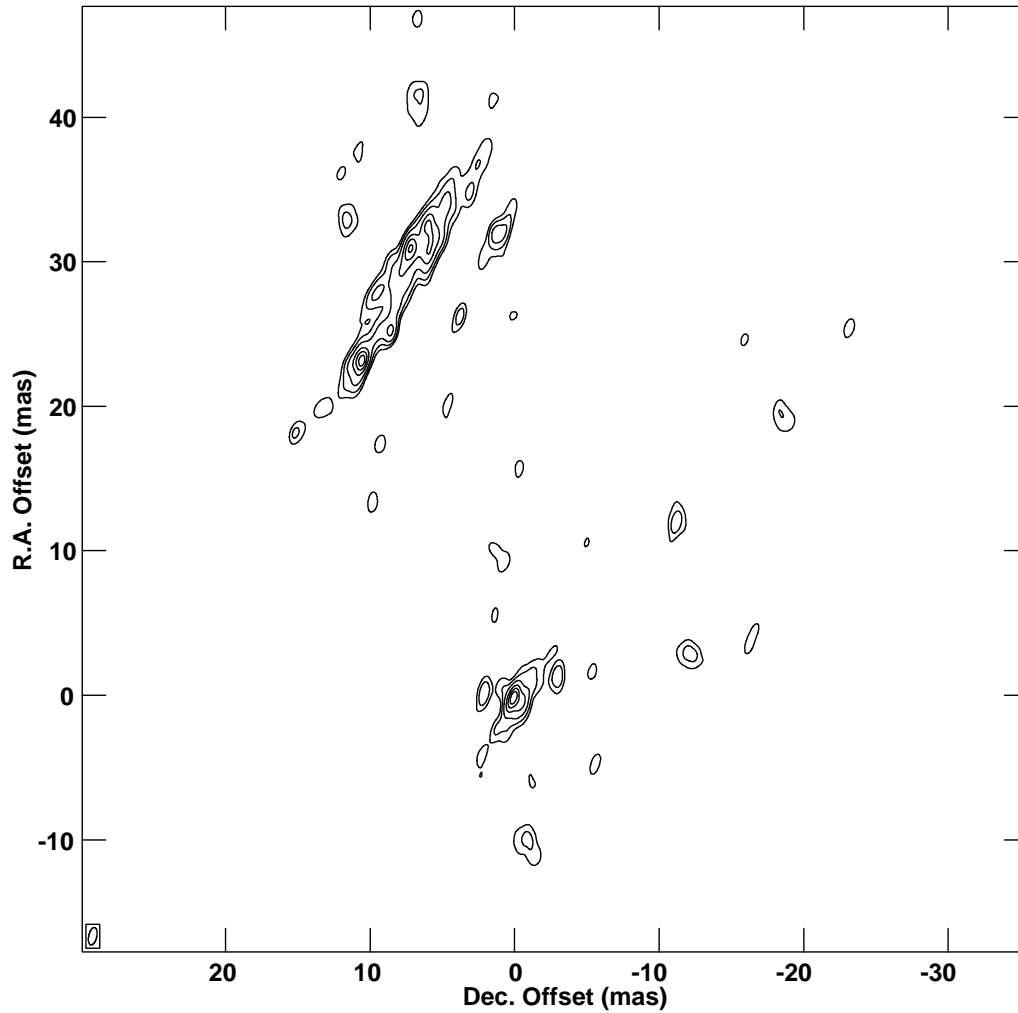


Figure 3.24: Epoch 4 total intensity (Stokes  $I$ ) image of the  $v = 1, J = 1 - 0$  SiO maser emission towards R Aqr integrated over the LSR velocity range of  $-32.9 \text{ km s}^{-1}$  to  $-17.4 \text{ km s}^{-1}$ . Contour levels are  $-10, -5, 5, 10, 20, 40, 60, 80,$  and  $100\%$  of the peak integrated flux density  $50.7 \text{ Jy/beam}$ .

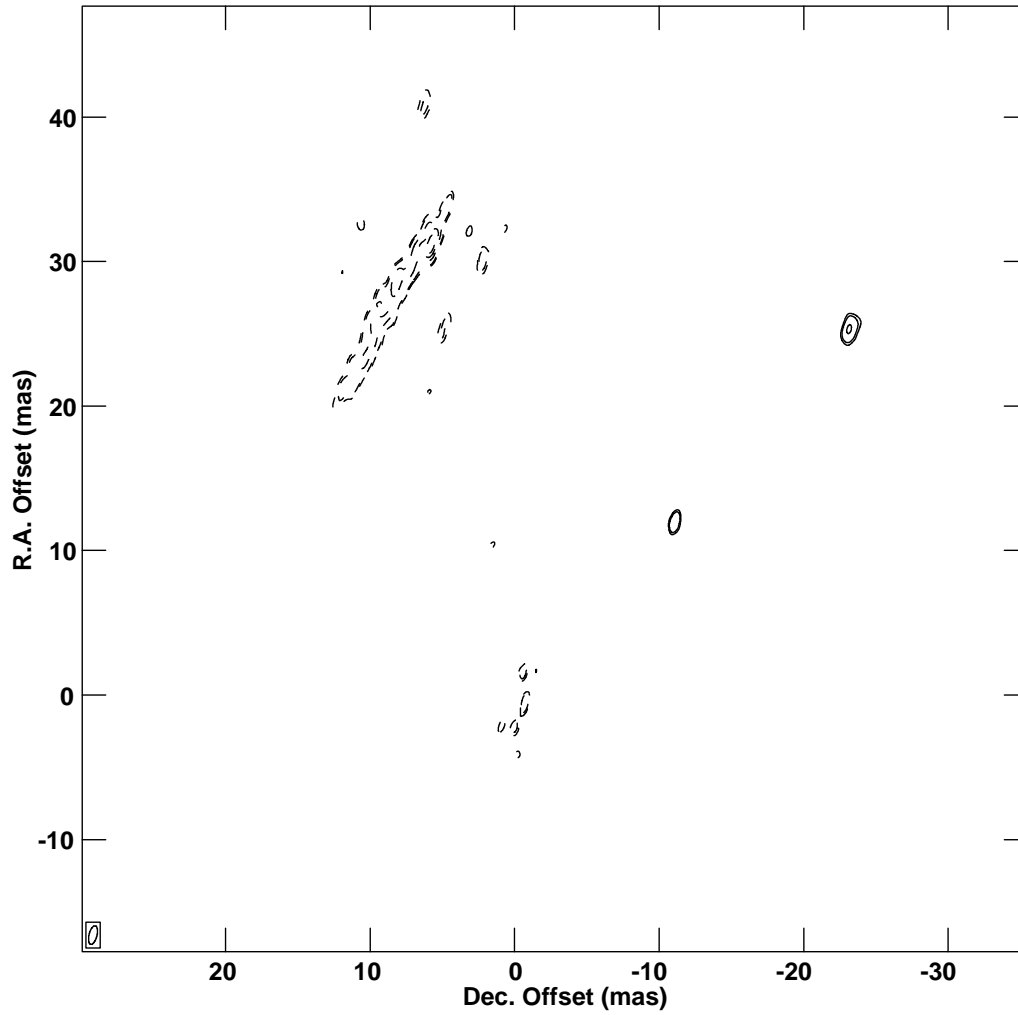


Figure 3.25: Epoch 4 circular polarization (Stokes  $V$ ) image of the  $v = 1, J = 1-0$  SiO maser emission towards R Aqr integrated over the LSR velocity range of  $-32.9 \text{ km s}^{-1}$  to  $-17.4 \text{ km s}^{-1}$ . Contour levels are  $-100, -80, -60, -40, -20, -15, 15, 20, 40, 60, 80,$  and  $100\%$  of the peak integrated flux density  $-2.5 \text{ Jy/beam}$ . Negative flux densities are represented by dashed contours.

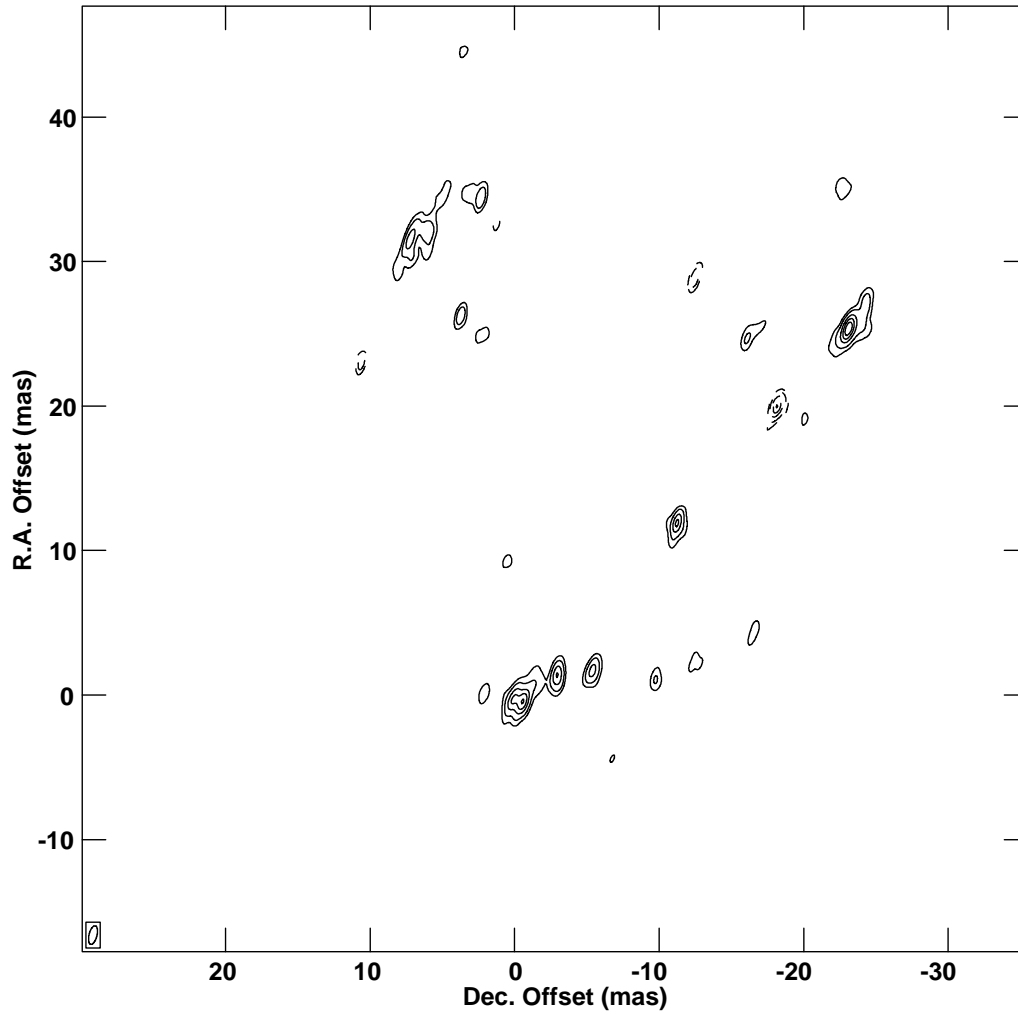


Figure 3.26: Epoch 4 Stokes  $Q$  image of the  $v = 1, J = 1 - 0$  SiO maser emission towards R Aqr integrated over the LSR velocity range of  $-32.9 \text{ km s}^{-1}$  to  $-17.4 \text{ km s}^{-1}$ . Contour levels are  $-100, -80, -60, -40, -20, -10, 10, 20, 40, 60, 80,$  and  $100\%$  of the peak integrated flux density  $4.0 \text{ Jy/beam}$ . Negative flux densities are represented by dashed contours.

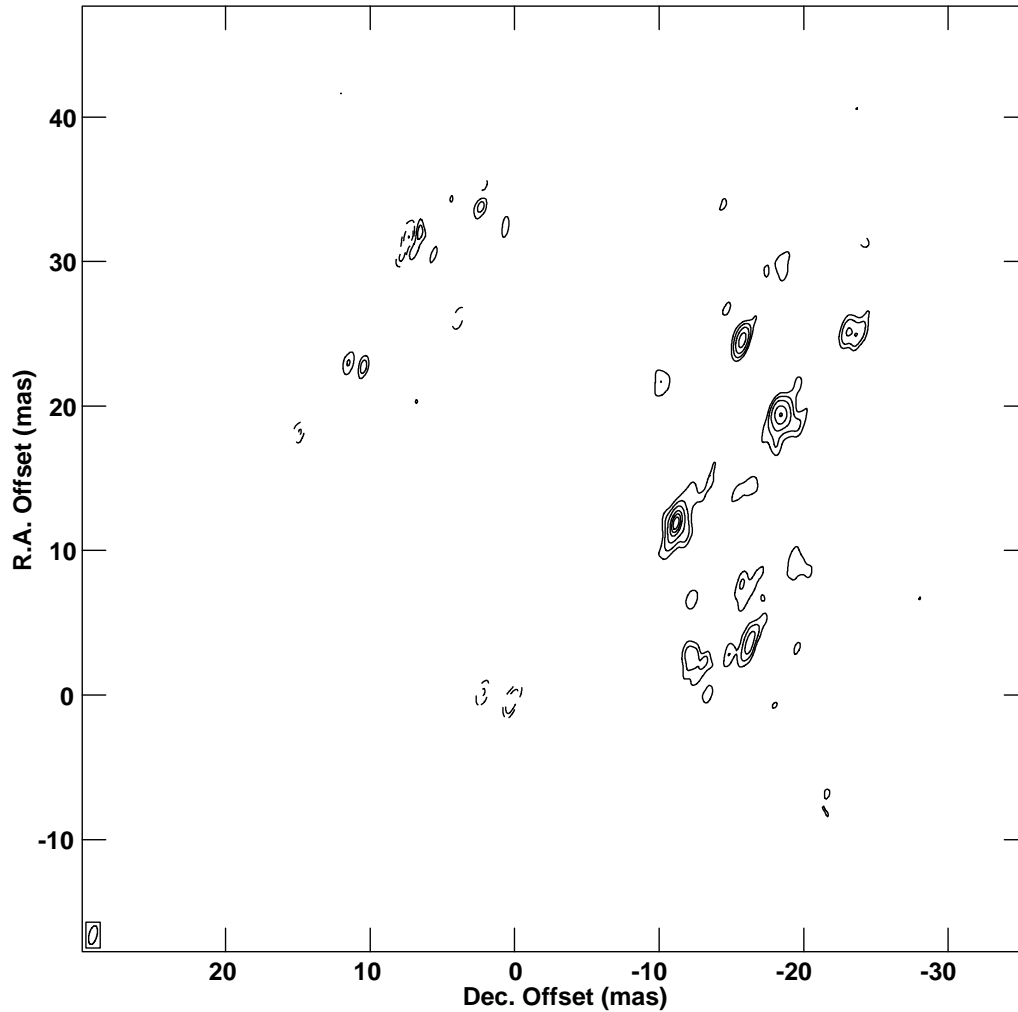


Figure 3.27: Epoch 4 Stokes  $U$  image of the  $v = 1, J = 1 - 0$  SiO maser emission towards R Aqr integrated over the LSR velocity range of  $-32.9 \text{ km s}^{-1}$  to  $-17.4 \text{ km s}^{-1}$ . Contour levels are  $-100, -80, -60, -40, -20, -10, -5, 5, 10, 20, 40, 60, 80$ , and  $100\%$  of the peak integrated flux density  $5.8 \text{ Jy/beam}$ . Negative flux densities are represented by dashed contours.

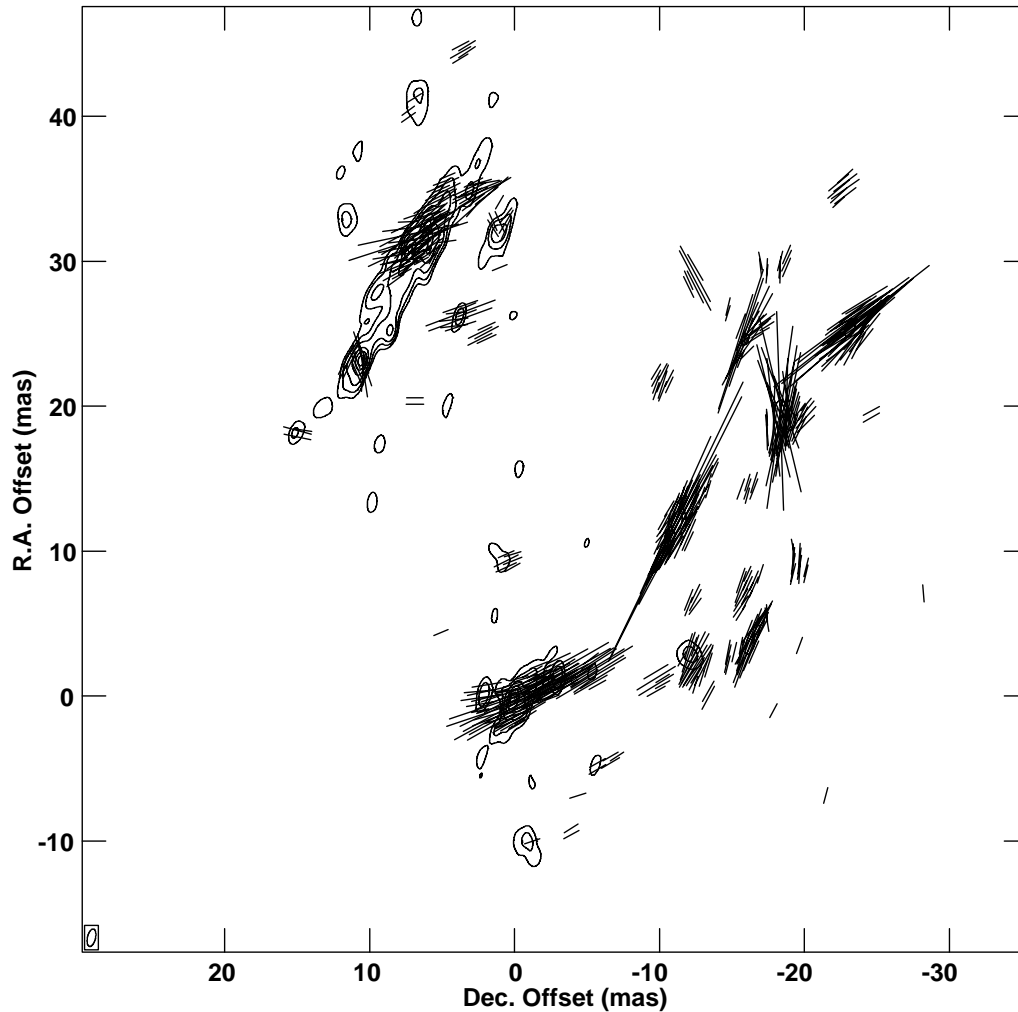


Figure 3.28: Epoch 4 linear polarization image of the  $v = 1, J = 1 - 0$  SiO maser emission towards R Aqr integrated over the LSR velocity range of  $-32.9 \text{ km s}^{-1}$  to  $-17.4 \text{ km s}^{-1}$ . Stokes  $I$  is plotted as a contour map with levels  $-10, -5, 5, 10, 20, 40, 60, 80,$  and  $100\%$  of the peak integrated flux density  $36.0 \text{ Jy/beam}$ . The vectors indicate the plane of the electric field vector and have lengths proportional to the linearly polarized intensity, where  $10 \text{ mas} = 2.8 \text{ Jy/beam}$ . Polarization vectors are plotted at all points where the total intensity exceeds  $0.1 \text{ Jy/beam}$  and the linearly polarized intensity exceeds  $0.3 \text{ Jy/beam}$ .

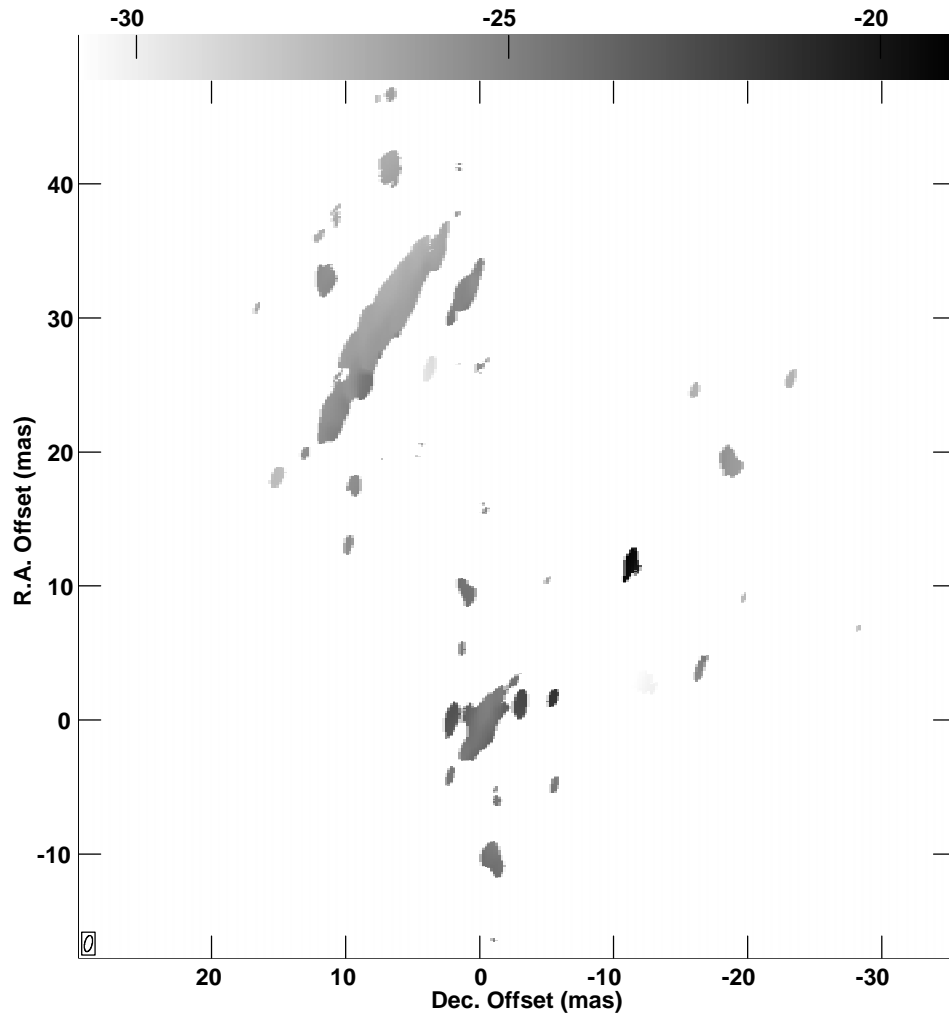


Figure 3.29: Epoch 4 velocity map of the  $v = 1, J = 1 - 0$  SiO maser emission towards R Aqr. Velocities are plotted on a greyscale ranging from  $-30.8 \text{ km s}^{-1}$  to  $-19.0 \text{ km s}^{-1}$ . The LSR velocity of R Aqr is  $\sim 27.0 \text{ km s}^{-1}$ .

# Chapter 4

## R AQUARII: REVIEW OF SOURCE PROPERTIES

“This is the dawning of the age of Aquarius . . . ”

*Ragni, Rado, & MacDermot, Aquarius*

### 4.1 Introduction

R Aquarii, located at  $\alpha = 23^h43^m49.5^s$ ,  $\delta = -15^\circ17'04.1''$  (J2000 coordinates), is probably the most well-studied of the modest number of known symbiotic binary systems described in Chapter 1. It is a unique object in several respects:

- It is the closest known symbiotic system.
- It is one of only a few symbiotics to have associated nebulosity, in this case, two extended filamentary nebulae.
- It is the closest known example of an astrophysical jet.
- It is one of only two symbiotics to have circumstellar masers associated with the long-period variable.

R Aquarii has been extensively studied at radio, infrared (IR), optical, ultraviolet (UV), and X-ray wavelengths. Reviews of the system can be found in Kenyon (1986) and Michalitsianos and Kafatos (1988), but a number of exciting observations have taken place since. This chapter contains a review of the current literature and a summary of the properties of this unusual source.

## 4.2 History and General Properties of R Aquarii

### 4.2.1 Identification as a Symbiotic Star

Numerous contributions to the photometric light curve of R Aquarii (R Aqr) have been made over the years. The variable nature of R Aqr was first noted by Harding (1816), and fluctuations were soon found to have a period of  $\sim 387$  days. The long-period variable (LPV or Mira) was classified as an M7e through spectrograms taken at the Mount Wilson Observatory (Merrill 1935). Merrill (1935) was also the first to describe the system as a symbiotic. In 1922, the appearance of peculiar high-temperature emission lines in H, He, and Fe led Merrill to the conclusion that the system contained a blue “companion” in addition to the Mira variable. He noted that three separate spectra (the LPV, a gaseous nebula, and the companion) all appeared to originate from the same stellar object. From 1928–1934 the system underwent a violent outburst in which the continuum emission from the companion rivaled that of the Mira reaching a visual magnitude  $M_V \approx 8$ . Since this outburst, R Aqr has returned to a quiescent state in which only the Mira and the gaseous nebula have been visible in both continuum and spectroscopic observations.

### 4.2.2 The Nebulae Surrounding R Aquarii

The complex inner and outer nebulae that surround R Aqr were first observed by Lampland (1923a,b). The outer nebula consists of two intersecting arcs shaped like a double convex lens extending  $\sim 2$  arcmin in the E-W direction. The inner nebula, which has an hour-glass shape, extends  $\sim 1$  arcmin N-S, perpendicular to the outer nebula. The inner and outer nebulae can be seen in the optical images shown in Figure 4.1.

Hubble (1940, 1943) was the first to suspect outward motions of the outer nebula. These motions were later detected by Baade (1943, 1944) who compared optical plates taken 16 years apart. From the motion of the outer nebula, Baade deduced an expansion age of approximately 600 yr for the outer nebula and a kinematic distance to R Aqr of  $\sim 260$  pc. Wallerstein and Greenstein (1980) suggested that the elliptical shape of the outer nebula is reminiscent of the toroidal dust cloud model used to explain the bipolar nebulae of the Red Rectangle and the Egg nebula. The problem with the torus explanation is that the arcs that form the outer nebula in R Aqr extend well past their intersection points.

The most extensive study on the nebulosity of R Aqr was carried out by Solf and Ulrich (1985). From 1982–1983, they performed high-spectral and high-spatial resolution long-slit optical spectroscopy on the inner and outer nebulae. From these

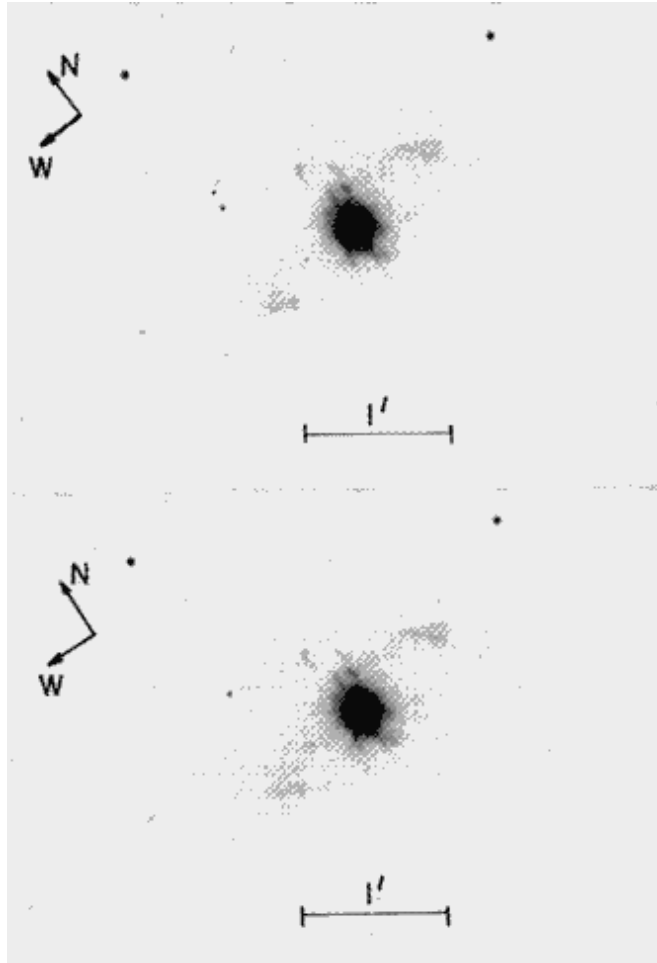


Figure 4.1: Images of the R Aqr nebulae in red light. (Wallerstein and Greenstein 1980)

observations, they confirmed that the southern arc of the outer nebula is moving toward us while the northern arc is moving away from us. In addition, Solf and Ulrich proposed that the nebulae are the result of two distinct ejection events which occurred approximately 180 and 640 years ago. Assuming previously proposed expansion ages for the outer nebula  $\sim 600$  yr (Baade 1944) and for the inner nebula  $\sim 185$  yr (Sopka et al. 1982), Solf and Ulrich derived kinematic distances to R Aqr of 180 pc and 185 pc respectively.

To explain their observations, Solf and Ulrich invoked a model of bipolar outflow in which the expansion velocity, the electron density, and surface brightness of the shells are all latitude dependent. They used this model to explain the structure of

both the inner and outer nebulae. From the model fit, they found that both nebulae have the same bipolar axis which has a position angle (p.a.) of  $355^\circ$  and an inclination of  $18^\circ$  relative to the line of sight. The equatorial expansion velocities for the inner and outer nebulae were found to be  $32 \text{ km s}^{-1}$  and  $55 \text{ km s}^{-1}$  respectively, and a polar expansion velocity of  $\sim 200 \text{ km s}^{-1}$  was derived for the inner nebula.

The bipolar outflow pattern is thought to be the result of the density distribution within the R Aqr system. Stellar wind material from the LPV which is not accreted by the companion is thought to form a thick disk coincident with the orbital plane. The unique hour-glass shapes of the two nebulae are the direct result of this density distribution which perturbs the expansion near the plane of the dusty disk. Because of the low electron density in the outer shell, only the denser equatorial region is still detectable giving the outer nebula its ring-like shape which is actually just the equatorial part of a truncated hour glass. This model appears to provide a better explanation for the fact that intersecting arcs that form the outer nebula extend past their intersection points.

Hollis et al. (1987) performed the first radio observations of the large-scale R Aqr nebulae at 6 cm using the VLA in D configuration. Their 6-cm map is shown in Figure 4.2. Hollis et al. found the radio morphology of the outer nebula to be similar to the optical morphology and the 6-cm structure to be the result of thermal Bremsstrahlung emission by a hot, optically thin gas. In addition, the calculated kinetic energy of the radio nebulosity is consistent with a recurrent nova outburst. Complimentary CCD imagery in  $H\alpha$  and  $H\beta$ , and optical spectroscopy were done (Hollis, Oliverson, and Wagner 1989) for comparison with the radio data. Hollis, Oliverson, and Wagner found the spectra of the outer nebula to favor collisional ionization by a shock-wave heating mechanism rather than photoionization by the central source. This seems a more likely explanation for the ionization of the outer nebula since the thick accretion disk which may surround the binary would probably occult the outer nebula.

### 4.2.3 Distance to R Aquarii

R Aqr is the closest known symbiotic binary with distance measurements ranging from 180–260 pc. Measurements, thus far, can be divided into two categories: distances computed using the kinematics of the nebulae surrounding R Aqr, and distances found using derived Mira luminosities in conjunction with optical and infrared photometry. A summary of the various distance measurements obtained from the literature is given in Table 4.1 below.

Baade (1943) was the first to determine a distance to R Aqr. Using the kinematics of the outer nebula Baade found the distance to R Aqr assuming an expansion age

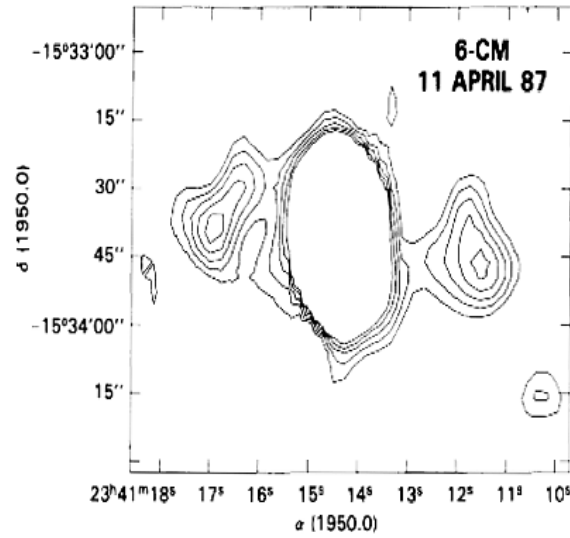


Figure 4.2: Uniformly weighted (untapered) 6-cm continuum image of the R Aqr nebulae. Contour levels are 30, 45, 60, 75 and 90% of the  $0.23 \text{ mJy beam}^{-1}$  peak flux. (Hollis, Oliverson, and Wagner 1989)

of  $\sim 600$  yr. The kinematic method was also used by Solf and Ulrich (1985) in their comprehensive paper on the inner and outer nebulae of R Aqr. Using the expansion age from Baade for the outer nebula, and an expansion age for the inner nebula from Sopka et al. (1982), they computed distances that were roughly self-consistent.

The first estimate of the distance to R Aqr from a derived luminosity was made by Lépine, LeSqueren, and Scalise (1978). They assumed an absolute  $4 \mu\text{m}$  magnitude (independent of the period) of  $-8.1$  for all Mira variables which they determined from a sample of stars with known distances. By comparing the  $4 \mu\text{m}$  magnitude of R Aqr, Lépine, LeSqueren, and Scalise were able to compute a distance of 181 pc similar to the distance of Solf and Ulrich. Wyatt and Cahn (1983) used a modified version of the relationship between the period, the mass, and the luminosity for Mira variables, developed in Cahn and Wyatt (1978) to determine a distance. Given a known period and mean spectral type they used their period–mass–luminosity diagram to determine the mean luminosity. This mean luminosity was converted to a mean absolute bolometric magnitude using the equation:

$$M_{\text{bol}} = 4.75 - 2.75 \log L. \quad (4.1)$$

The distance was computed by comparing the mean apparent bolometric magnitude, derived from measured  $V$ ,  $I$ , and  $K$  band fluxes, to the above absolute magnitude.

Table 4.1: Measurements of the distance to R Aqr.

Reference	Distance	
	(pc)	Method of Determination
Baade (1943).....	260	kinematic (outer nebula)
Solf and Ulrich (1985).....	180	kinematic (outer nebula)
Solf and Ulrich (1985).....	185	kinematic (inner nebula)
Lépine et al. (1978).....	181	assumed 4.4 $\mu\text{m}$ Mira variable absolute magnitude = $-8.1$
Wyatt and Cahn (1983)...	230	period–mass–luminosity relationship
Whitelock (1987).....	250	period–infrared luminosity relationship
van Belle et al. (1996).....	222	error weighted average of period–mass–luminosity and period–infrared luminosity relationships

Whitelock (1987) applied the period–luminosity relationship in the near-infrared K band:

$$M_K = 1.69 - 3.79 \log P, \quad (4.2)$$

to compute the distance to R Aqr in a similar fashion. In the above equation,  $P$  is the period of the Mira variable determined from observations. Most recently, van Belle et al. (1996) computed the distance using both the period–mass–luminosity relationship of Wyatt and Cahn and a modified period–infrared luminosity relationship (Jura and Kleinmann 1992) in conjunction with their 2.2  $\mu\text{m}$  observations. The distance they report is an average of the two methods weighted by the errors in each. In this text, I will adopt the distance of van Belle et al. ( $\sim 220$  pc) for use in later calculations.

#### 4.2.4 The Binary Orbit of R Aquarii

To date, the determination of the orbital parameters of the R Aqr system is still a topic of considerable discussion. Merrill (1950) first predicted an orbital period of 26.7 years using the radial velocities of the [O III] and the [Ne III] nebular emission lines. Merrill himself considered this prediction questionable, and his orbital parameters were later disproved by Jacobsen and Wallerstein (1975) who showed that the [O III] and the

[Ne III] emission lines were not periodic. From 1974–1978, R Aqr underwent a period in which the optical variations of the Mira were depressed (Mattei and Allen 1979). In addition, considerable reddening of both the infrared (Whitelock et al. 1983) and visible (Brugel et al. 1984) light occurred during this period. This reddening is almost certainly internal, given the galactic latitude of R Aqr ( $-70^\circ$ ) interstellar reddening is probably negligible (Wallerstein and Greenstein 1980). Both the reduction and reddening of the visible light have been attributed to the obscuration of the LPV by an extended cloud of dust. Willson, Garnavich, and Mattei (1981) interpreted this event as being similar to the event from 1928–1934 and proposed that the companion, surrounded by a dusty envelope, is eclipsing the Mira variable. They deduced a period of  $\sim 44$  yr for the binary orbit. High-resolution spectroscopic observations of the Mira in the optical by Wallerstein (1986) and in the infrared by Hinkle et al. (1989) inferred values for the orbital period consistent with the 44-yr period of Willson, Garnavich, and Mattei.

Willson, Garnavich, and Mattei also suggested that the eclipses of the Mira occur when the companion is at apastron. Kafatos and Michalitsianos (1982) subsequently proposed that the eclipses instead occurred at periastron, and could be the cause of the emergence of the jet (discussed in § 4.3) first observed in 1977 during the time of the latest eclipse. Using the 44-yr period, Kafatos and Michalitsianos found the semi-major axis of the orbit to be  $a \approx 2.5 \times 10^{14}$  cm. If the companion were in a circular orbit with this proposed separation, the Mira would always fail to fill its Roche-lobe. If instead, the companion were in a highly elliptical orbit, then at periastron, the Mira could overflow its Roche-lobe and enhanced mass transfer could excite the jet as proposed by Kafatos and Michalitsianos.

Hege, Allen, and Cocke (1991) attempted to resolve the stellar components of the binary system by performing speckle interferometry with the National Optical Astronomy Observatory (NOAO) 4-m Mayall telescope at Kitt Peak. They observed in a 1.8 nm bandpass centered on  $H\alpha$  ( $\lambda 6563 \text{ \AA}$ ) in October 1983. In the  $H\alpha$  image the central region of R Aqr is resolved into three sources: (1) a bright central source consistent with the radio component C1 discussed in § 4.3, (2) a  $\sim 3.3$  mag fainter source lying  $\sim 0.53$  arcsec NE of C1 which has a corresponding radio feature C2 in the jet (see § 4.3), and (3) a  $\sim 2.4$  mag fainter feature lying  $\sim 0.124$  arcsec SW of C1 which had no radio counterpart. The third component was designated C3 by Hege, Allen, and Cocke who speculated that this feature could be the LPV or another knot of emission in the inner jet.

The recent addition of Q-band receivers to 13 VLA antennas and new calibration techniques have allowed simultaneous imaging of weak H II regions in close proximity to SiO masers. Following the procedure outlined in Reid and Menten (1997) in which SiO spectral line observations are used to calibrate the continuum amplitudes and

phases, Hollis, Pedelty, and Lyon (1997) were able to resolve the R Aqr binary system into its stellar components. The weak H II region which presumably marks the position of the hot companion was found to lie  $55 \pm 2$  mas away at a p.a.  $\sim 18^\circ \pm 2^\circ$  relative to the LPV which is traced out by the SiO maser emission. With reasonable assumptions including a 44 yr period for the orbit, they were able to make a preliminary estimate of the orbital parameters. If these parameters are accurate, then the component C3 observed by Hege, Allen, and Cocke is probably a knot of emission in the jet rather than the hot companion.

### 4.3 The R Aquarii Radio/Optical/UV Jet

In September of 1977 (a time of deep minimum for the Mira emission), Wallerstein and Greenstein (1980) were the first to observe what they termed a “spike” of emission to the north of R Aqr. Herbig (1980) was probably the first to refer to this emission as a jet, and determined that the jet must have appeared some time between 1970 and 1977. The first radio identification of the jet was made by Sopka et al. (1982) through observations made with the VLA in C configuration in November of 1981. They mapped the 6 cm continuum emission and found the jet to extend 7–10 arcsec to the northeast of the central H II region at a position angle of  $\sim 24^\circ$ . The map produced by Sopka et al. is shown in Figure 4.3. These observations were verified by Spergel, Giuliani, and Knapp (1983) who also made 6-cm observations of R Aqr at about the same time (October 1981) and detected the same double source radio structure.

The first ultraviolet observations of the R Aqr jet were made by Michalitsianos and Kafatos (1982) who obtained far-UV spectra of both the jet feature and the central region from the International Ultraviolet Explorer (IUE). They found that the continuum emission from 1200–2000 Å is relatively flat for the inner structure, while the continuum flux of the jet region rises with decreasing wavelength over the same spectral range. This result suggests that the jet is cooler and less dense than the inner region. Further radio observations were made by Kafatos, Hollis, and Michalitsianos (1983) in late 1982 at 6 cm. With the VLA in the B antenna configuration Kafatos, Hollis, and Michalitsianos were able to resolve R Aqr into three distinct regions of emission: (1) the compact H II region, (2) feature A  $\sim 2.5$  arcsec from the central region at p.a.  $\approx 45^\circ$ , and (3) feature B  $\sim 6.5$  arcsec to the NE at p.a.  $\approx 29^\circ$ . In addition, they saw weak evidence for a SW counterpart to the NE radio jet.

The latter part of the 1980’s was marked by observations of increasing resolution towards R Aqr and the search for the elusive counter-jet expected to the SW of the inner H II region. In December of 1983, Mauron et al. (1985) observed R Aqr in the

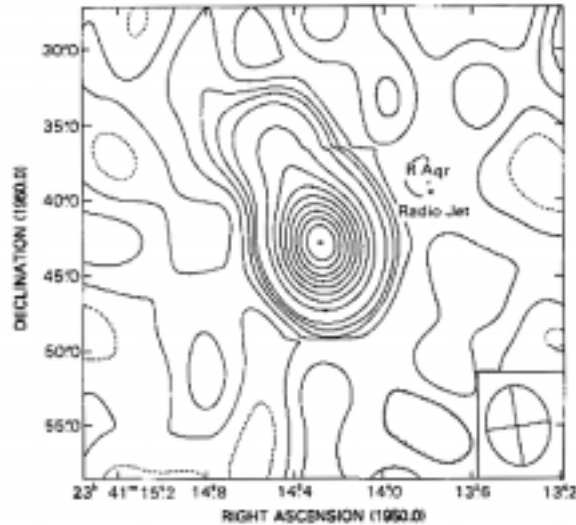


Figure 4.3: The 6-cm VLA continuum image showing the R Aqr jet at  $\text{p.a.} \approx 24^\circ$ . Contour levels are  $-2, 2, 4, 6, 8, 10, 20, 30, 40, 50, 60, 70, 80, 90$ , and  $100\%$  of the peak intensity of  $8.79 \text{ mJy per beam}$  (from Sopka et al. 1982).

near-UV ( $3500\text{--}3900 \text{ \AA}$ ) with the Canada-France-Hawaii  $3.6 \text{ m}$  telescope. They were able to obtain  $\sim 1$  arcsec resolution images which indicated a symmetrical feature to the SW of the central core of emission. Images made from VLA observations taken in early 1984 (Hollis et al. 1985) show even stronger evidence for the existence of the counter-jet feature. Hollis et al. observed R Aqr at  $2, 6,$  and  $20 \text{ cm}$  using the VLA in B configuration. The  $6\text{-cm}$  map shows an unresolved extension to the SW of the central region which they labeled  $A'$ . From the observations at three wavelengths, they were also able to compute spectral indices for the compact H II region and for the jet (feature B) of  $\sim 0.6$  and  $\sim 0$  respectively. These spectral indices are indicative of optically thin thermal emission for the jet and optically thick thermal emission for the central H II feature.

In January 1985, Hollis et al. (1986) obtained the first sub-arcsecond resolution radio image of R Aqr. Observations made with the VLA in A configuration produced a  $2\text{-cm}$  image with a resolution of  $\sim 0.15$  arcsec. In this image the compact H II region is resolved into two discrete components labeled C1 and C2. C1 was assumed to correspond to the LPV-companion binary while C2,  $\sim 0.5$  arcsec away at a position angle of  $\sim 55^\circ$ , was assumed part of the jet. On the far NE end of the jet, Paresce, Burrows, and Horne (1988) detected a new feature which they labeled feature D. They used the Space Telescope Science Institute (STScI) coronagraph on the European

Southern Observatory (ESO) 2.2 m telescope to image R Aqr in the light of the  $H\alpha$ , 6563 Å and  $[N\text{ II}]$ , 6584 Å nebular emission lines. Paresce, Burrows, and Horne detected the new feature at a distance of 8.4 arcsec from the nucleus at a  $20^\circ$  position angle.

Kafatos et al. (1989) finally provided convincing evidence for a symmetric counterpart to the NE jet. By combining new VLA 6-cm A-configuration observations with previously reported 6-cm B and D-configuration data, Kafatos et al. were able to resolve the A' feature from the C1–C2 complex and were able to image the weak counterpart to feature B which they called B'. Feature A' was found to lie at a p.a. of  $\sim 231^\circ$  and the B' feature was found to extend out  $\sim 10$  arcsec to the SW at a p.a. of  $\sim 209^\circ$ . In addition to the new 6-cm data, Kafatos et al. also obtained 2-cm continuum data from the VLA in A/B hybrid configuration. From the two sets of data, they were able to compute spectral indices for the inner features thereby inferring the types of emission from these components: C1 and A indicated optically thick thermal emission; C2 and A' had indices consistent with nonthermal emission.

The first Hubble Space Telescope (HST) images of R Aqr were taken in August of 1990 (Paresce et al. 1991) with the F501N ( $[O\text{ III}]$  5007 Å) and the F372M ( $[O\text{ II}]$  3727 Å) narrow-band interference filters. Unfortunately, these early images suffer from severe saturation of the Faint Object Camera (FOC). Subsequent images, using a variety of filters, revealed additional detail in the inner arcsecond of R Aqr. The C1 radio feature was resolved into several features using the F120M filter centered on  $\lambda = 1230$  Å by Burgarella and Paresce (1992). In these and later images, the jet is clearly detected as a narrow collimated stream extending from  $\sim 15$  AU out to  $\sim 700$  AU (Paresce and Hack 1994). This can be seen in the UV image shown in Figure 4.4 below. By comparing HST images taken with optical (F501N and F550M+F4ND) filters to those taken with UV (F253M and F190M) filters, Paresce and Hack (1994) were able to establish component M as the position of the Mira in R Aqr. The Mira dominates the emission at the longer wavelengths causing an aberration halo in the F501N and F550M+F4ND images centered on feature M, whereas in the UV images feature M is much weaker as expected for an LPV.

In August 1993, high resolution radio images were taken which resolved radio features C1, C2, and A' into multiple discrete knots of radio emission (Dougherty et al. 1995). Two of their images are shown in Figure 4.5. Observations were made with the Multi-Element Radio Linked Interferometer Network (MERLIN) at 1.7 and 5 GHz, and when compared to the previous HST images, show the association between radio features and their optical/UV counterparts. The core feature, C1, was resolved into three knots labeled C1a, C1b, and C1c. The latter component, C1c, was found to coincide with feature M of Paresce and Hack. Dougherty et al. (1995) also determined values for the spectral indices of C1, C2 and A' which they found

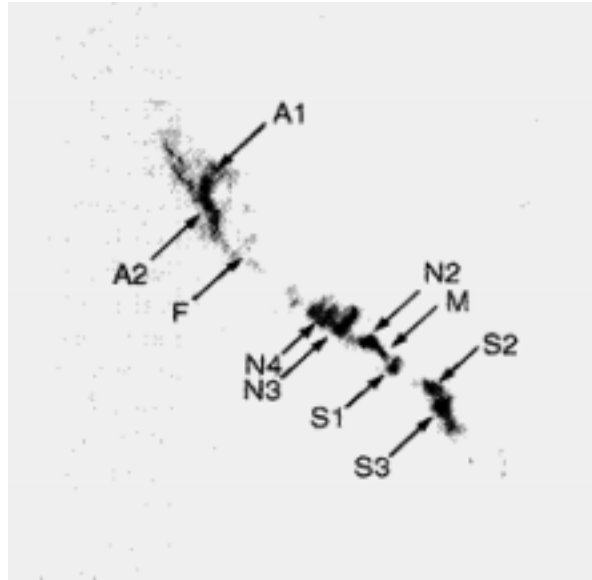


Figure 4.4: Restored image of R Aqr taken in October 1991 through the F190M filter sensitive to C III] 1909 Å emission (from Paresce and Hack 1994).

to be all positive indicating partially optically thick thermal free-free emission. This contradicted earlier indications of non-thermal emission from components C2 and A' (Kafatos et al. 1989). More recently, Dougherty et al. (1996) have determined the proper motions for features C1a, C1b, and C1c and find that both the position and motion of C1c is consistent with values measured for the Mira by the Carlsberg Meridian Telescope.

The velocities of jet features have been investigated by several groups. Solf and Ulrich (1985), mentioned earlier in § 4.2.2 with regards to long-slit spectroscopy of the inner and outer nebulae, also used this technique on the R Aqr jet. They found typical radial velocities of  $\sim -60 \text{ km s}^{-1}$  with a  $\sim 2.8 \text{ km s}^{-1}$  gradient for the NE jet. Long-slit spectroscopy was also used by Hollis, Wagner, and Oliverson (1990) who looked at the [O III] emission line at 5007 Å. They found LSR radial velocities of  $-46 \text{ km s}^{-1}$  and  $+41 \text{ km s}^{-1}$  for the NE and SW jet respectively. Lehto and Johnson (1992) measured the proper motions of the individual components in the jet by comparing 3.6 and 6.2 cm images taken with the VLA in A configuration with earlier observations (Kafatos, Hollis, and Michalitsianos 1983; Hollis et al. 1985; Hollis et al. 1986). Tangential velocities ranging from 44 to 160  $\text{km s}^{-1}$  with respect to the Mira were derived for four of the five jet features. Paresce and Hack (1994) also measured the proper motions of the features in the jet from HST data taken at three different epochs. They found the components of the very inner structure of

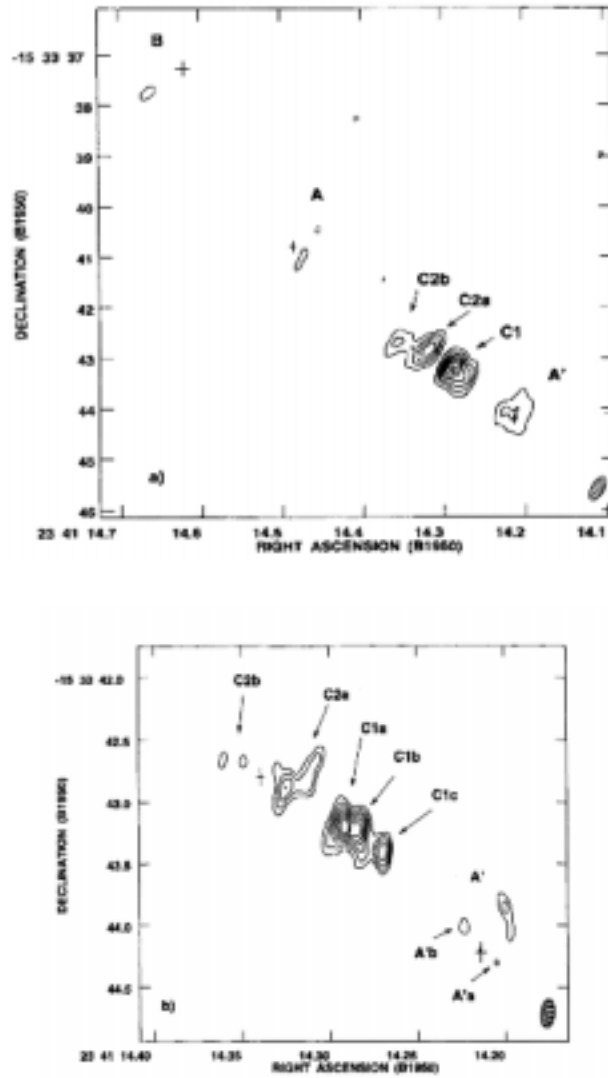


Figure 4.5: C-band radio images of the inner R Aqr jet taken with MERLIN (from Dougherty et al. 1995).

the jet (components N1, N2, N3-N6, S1, S2 and S3 in Figure 4.4) to have an upper limit which indicates velocities  $<40 \text{ km s}^{-1}$ . They found this not to be the case for the outer features (around A1 and beyond) where they determined proper motions of  $150\text{--}200 \text{ km s}^{-1}$  consistent with Lehto and Johnson (1992). Dougherty et al. (1996) verified the result of Paresce and Hack (1994) for the inner jet, finding the proper motions of features C1a and C1b to be 44 and  $51 \text{ km s}^{-1}$  respectively.

The most recent work on the R Aqr jet (Hollis et al. 1997) shows the sub-arcsecond motion of the inner 5 arcsec of the jet over a 2 yr period. The results are a combination of more recent (post-COSTAR) data with restored archival (pre-COSTAR) data both taken through the F253M filter sensitive to  $[\text{O II}] 2470 \text{ \AA}$  emission. Three-dimensional maps of the jet emission are shown in Figure 4.6. The proper motion analysis performed by Hollis et al. revealed transverse velocities in the range  $36\text{--}235 \text{ km s}^{-1}$  increasing with increasing distance from the source. The proper motion analysis also showed a possible 40.2 yr period between ejection events roughly consistent with the  $\sim 44$  yr event separation times for the radio components in the jet (Hollis and Michalitsianos 1993) and the predicted  $\sim 44$  yr binary orbit (§ 4.2.4). Unlike the radio components which seem to be best described by a constant acceleration model, the UV features seem to follow a nonlinear acceleration law. Hollis et al. also find that the UV knots are not cospatial with the corresponding radio features. They suggest that the UV features trace out the leading edge of shocked material while the radio regions delineate the post-shock gas.

## 4.4 Maser Emission Towards R Aquarii

### 4.4.1 Single-Dish Observations

Maser emission was first detected towards R Aqr by Lépine, LeSqueren, and Scalise (1978) through observations of the 43.122-GHz,  $v = 1, J = 1 - 0$  SiO transition at an LSR velocity of  $-25.0 \text{ km s}^{-1}$ . This detection was followed by the detection of the 86.243-GHz  $v = 1, J = 2 - 1$  line at  $v_{\text{LSR}} = -28.0 \text{ km s}^{-1}$  (Zuckerman 1979). Cohen and Ghigo (1980) were the first to observe what they called a “pedestal” of 43.122-GHz SiO emission from  $-28.1 \text{ km s}^{-1}$  to  $-20.6 \text{ km s}^{-1}$  with a maximum at  $-26.4 \text{ km s}^{-1}$ . This plateau of emission was confirmed for the 43.122-GHz masers and also found in the first 42.821-GHz,  $v = 2, J = 1 - 0$  SiO observations by Barcia et al. (1985). More recently, Gray et al. (1995) have detected the  $v = 1$  and  $v = 2, J = 7 - 6$  SiO transitions at 301.814 and 299.704 GHz respectively using the James Clerk Maxwell Telescope (JCMT).

The first long-term short-spaced monitoring program of the 43.122-GHz and

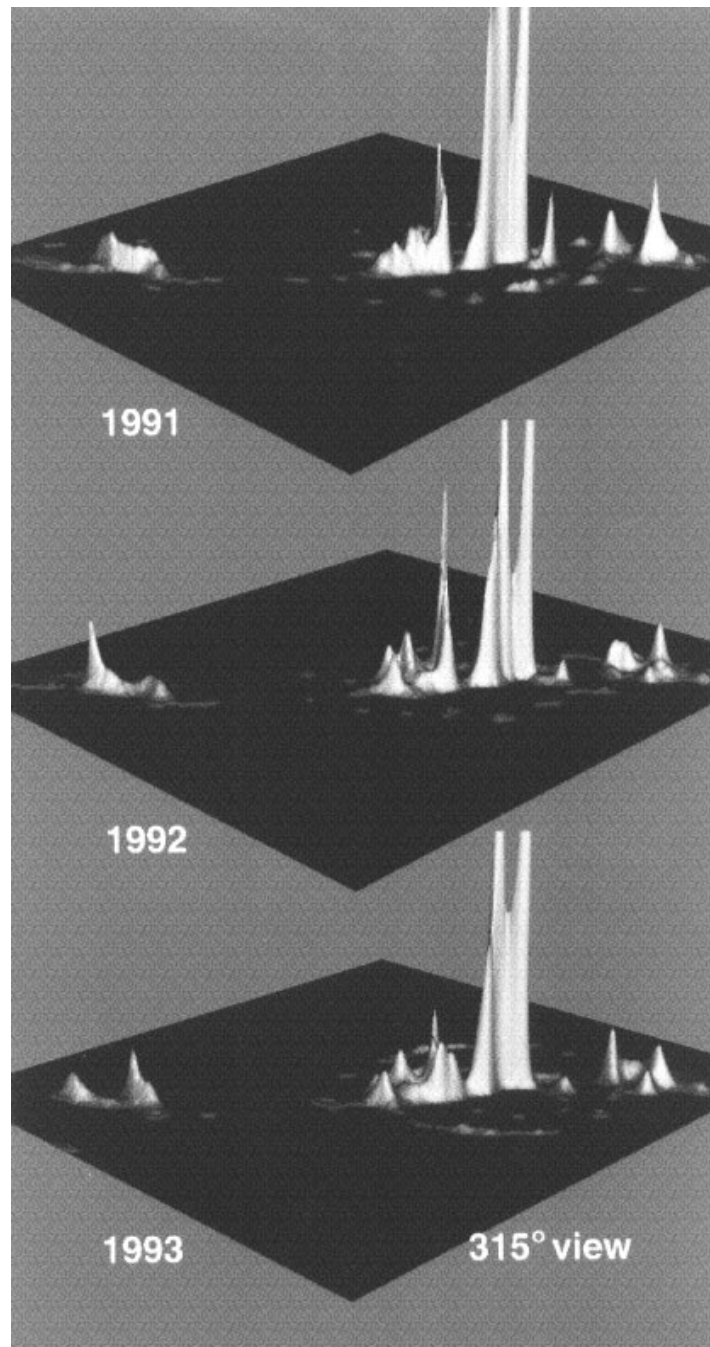


Figure 4.6: Restored HST/FOC three-dimensional images of the R Aqr jet. The position of the Mira is the rightmost truncated peak (from Hollis et al. 1997).

the 86.243-GHz SiO emission was carried out by Martínez, Bujarrabal, and Alcolea (1988) using the 14-m radio telescope at the Centro Astronómico de Yebes. Through observations every 20–30 days from June 1984 to February 1987 they found the velocity structure of the emission to vary from one period to the next. They also found that the SiO light curves follow the optical variability with a phase lag of 0.1 – 0.2.

These observations were followed by a monitoring program (Allen et al. 1989; Hall, Allen, Troup, Wark, and Wright 1990; Hall, Wright, Troup, Wark, and Allen 1990) in which the first polarization measurements were taken. Using the Parkes radio telescope, Allen et al. (1989) averaged the spectra at various position angles to determine the full velocity range of the 43.122-GHz SiO emission. They found the extrema to lie at  $-37.0 \text{ km s}^{-1}$  and  $-17.0 \text{ km s}^{-1}$ . From this they inferred an outflow velocity for the maser region of  $10 \text{ km s}^{-1}$ . Linear polarization was only reliably detected for 4 of the features in the spectrum with position angles ranging from 0 to 155 degrees. The main peak was found to be weakly polarized at  $\sim 15\%$  linear polarization, while the three lower intensity peaks were found to have higher ( $\sim 70\%$ ) linear polarization. Follow-up observations (Hall, Allen, Troup, Wark, and Wright 1990) again found the stronger features more weakly polarized, which they suggest may be caused by Faraday depolarization along longer gain paths or by blending of radiation. Hall, Wright, Troup, Wark, and Allen (1990) added observations of the 42.821-GHz,  $v = 2, J = 1 - 0$  emission and found the  $v = 1$  to  $v = 2$  flux ratio to be  $\sim 0.3$ . This is less than the typical value for Mira variables ( $\sim 1.0$ ) reported by Alcolea, Bujarrabal, and Gómez-González (1990). This, along with the finding that the two transitions have different polarization position angle profiles, suggests spatially separate masers (Hall, Wright, Troup, Wark, and Allen 1990).

#### 4.4.2 Spectral Line Interferometry

The first spectral line interferometric observations of R Aqr were made by Hollis et al. (1986) using the Hat Creek Observatory millimeter interferometer. They found the SiO maser position to be  $\sim 1$  arcsec to the south of the radio continuum feature C1 mentioned in § 4.3. This position for the SiO emission was later corrected by follow-up observations (Hollis et al. 1990). Using the Hat Creek interferometer and the United States Naval Observatory (USNO) 8-inch transit circle they found the SiO maser position to be coincident with both component C1 and the optical position of the long-period variable.

Recent interferometry (Ivison, Seaquist, and Hall 1994, 1995) has found the first circumstellar H<sub>2</sub>O masers towards two symbiotic binaries one of which was R Aqr. Using both the VLA and the Australia Telescope Compact Array (ATCA) they de-

tected the 22.235-GHz,  $6_{16} - 5_{23}$  H<sub>2</sub>O transition and found the masers to coincide with the 22-GHz continuum emission.

Radio interferometry at Q-band by Hollis, Pedelty, and Lyon (1997) was discussed earlier in § 4.2.4 with regards to the spatial resolution of the binary system. A byproduct of this study was a super-resolved (10 mas beam) VLA map of the 43.122-GHz SiO maser emission towards the LPV. The structure of the emission in this image confirms the general ring-like maser structure determined in Boboltz, Diamond, and Kemball (1997) and presented in this dissertation.

## 4.5 Models for R Aquarii

Since the early 1980's a number of models have been proposed to explain the characteristics of R Aqr. Some mention was made of models in previous sections, but this section will be devoted to the review of proposed theory in regards to R Aqr. The main thrust of theoretical arguments on the R Aqr jet attempt to answer three basic questions:

1. Is the jet made up of distinct blobs of material ejected by a central engine, or are the observed emission features just condensations somehow illuminated by the core region?
2. What is the ionization mechanism responsible for the observed emission features?
3. What is the source powering the jet?

Early papers, following its discovery, attempted to explain the jet as discrete blobs of material ejected periodically and photoionized by an intense radiation field provided by the hot companion and/or an accretion disk (Sopka et al. 1982; Kafatos and Michalitsianos 1982; Kafatos, Hollis, and Michalitsianos 1983). These early theories attempted to tie in the eclipsing of the Mira and the 44-yr binary orbit by suggesting that the eclipses occur at periastron rather than apastron as discussed in § 4.2.4. A highly elliptical orbit has been proposed for the companion with the jet resulting from supercritical accretion of matter from the Mira (which normally fails to fill its Roche-lobe) near the time of eclipse (Kafatos and Michalitsianos 1982).

In 1983, Spergel, Giuliani, and Knapp (1983) proposed that the jet was not a series of ejections, but instead, the ionization of individual clumps of material in the Mira stellar wind differentially illuminated by the hot companion as it orbits the LPV. To support this claim, Spergel, Giuliani, and Knapp argued that: (1) the

radio component was coincident with the optical component of the jet which had remained stationary for several years, (2) the two sources did not appear to be part of a continuous stream as one would expect for a jet, and (3) the radial velocities observed by Sopka et al. (1982) were uncharacteristically small for a jet. Solf and Ulrich (1985) also rejected the notion that the jet is made up of parcels of ejected material. Their theory involves the ionization of dusty condensations of material belonging to the inner nebula by shocks created as an expanding gas shell overtakes the clumps. They point to the apparent deceleration towards the leading edge of the spike of emission indicative of an expanding gas impacting a denser medium, and anomalies such as [O I] in the presence of [O III] and the relative strength of [S II] indicating shock excitation as evidence supporting their scenario.

Hollis et al. (1985) argued against the model of Spergel, Giuliani, and Knapp (1983) citing inconsistencies in the size and mass of the jet features, the lack of evidence demonstrating a shadowing effect, and the possibility of a symmetrical counter-jet feature. Earlier models of blob ejection were modified to remain consistent with the increasing number of observations. Kafatos, Michalitsianos, and Hollis (1986) suggested that the accretion disk consists of a hot inner region which is the source of ionizing radiation and a cooler outer region. The ejection of gas takes place from the cooler outer region by radiation pressure on the dust grains, thus explaining the moderate ( $\sim 50\text{--}100 \text{ km s}^{-1}$ ) velocities of the jet features. They also argued against the shock excitation mechanism citing the observed increase in the N V, C IV, and He II emission at UV wavelengths over a period of 1.5 yr and the detection of soft X-rays (Viotti et al. 1987). Their UV observations indicate an increase in the electron temperature of jet components inconsistent with deceleration induced shock excitation.

The discovery of each new feature seems to have been accompanied by modifications of existing models. The resolution of feature C into components C1 and C2 brought on the suggestion that precession of the object ejecting the knots might be the cause of the progression of position angle with distance of features C2 ( $\sim 55^\circ$ ,  $\sim 0.5 \text{ arcsec}$ ), A ( $\sim 45^\circ$ ,  $\sim 2.7 \text{ arcsec}$ ), and B ( $\sim 29^\circ$ ,  $\sim 6 \text{ arcsec}$ ) relative to C1 (Hollis et al. 1986). The sudden brightening of feature D, and its resulting discovery, led Paresce, Burrows, and Horne (1988) to support the shock heating mechanism. The large intensity variation with respect to the closer feature B over a short time span could not be the result of ionization by the central source (Paresce, Burrows, and Horne 1988). The discovery of counter-jet features A' and B' (Kafatos et al. 1989) provided evidence supporting the claim that the R Aqr emission truly constitutes a jet with structures reminiscent of double-sided extragalactic jets.

Burgarella and Paresce (1991) introduced the possibility of photoionization by a nonthermal power-law continuum (i.e. Seyfert 2 and narrow-line galaxies). They

attempted to identify the emission mechanism using line ratios observed for knots B and D. Burgarella and Paresce found these ratios to favor either the shock-wave or power-law ionization mechanism. Hollis et al. (1991) explained the difficulties in determining the excitation mechanism, but also found line ratios to be consistent with shock ionization.

As mentioned in § 4.3, the first HST observations of the R Aqr jet found a well-collimated stream of material emanating from the central source and extending 3.6 arcsec out to the northeast. To explain this stream-like morphology and the presence of large velocity widths ( $\sim 350 \text{ km s}^{-1}$ ) in optical spectrograms, Solf (1992) modified a previous model to include a supersonic stellar wind blowing against the back side of much slower condensations from the inner nebula ejected  $\sim 190$  yr ago. This wind causes a bow shock with velocities of  $300\text{--}500 \text{ km s}^{-1}$  which Solf used to justify the enormous line widths observed for components A and D and the morphology of component A revealed by HST observations.

This model of a highly collimated wind impinging on slower denser clumps of material has gained acceptance in recent years although the source of the jet is still unknown. Paresce and Hack (1994) suggested two scenarios for the formation of the collimated jet: (1) the collision of the two stellar winds from the companion and the Mira, and (2) expansion into an anisotropic medium creating a nozzle effect. Recent studies attempting to relate the radio emission in the jet to the optical [O III]  $5007 \text{ \AA}$  (Hollis and Michalitsianos 1993) and to the UV  $\sim 2550 \text{ \AA}$  (Hollis et al. 1997) emission have shown evidence for two different streams of gas. The former showed that the optical emission and the radio emission are not cospatial, and led Hollis and Michalitsianos to propose a “garden hose” model in which the [O III] emission defines the leading edge of a rotating collimated stream as it encounters the ambient medium. This is followed at some distance by the compressed “recombination” region which gives rise to the radio emission. They also suggest some sort of confining mechanism or “nozzle” imparting the transverse component to the proper motion. Comparison with the UV data led Hollis et al. (1997) to suggest a similar model in which two streams of gas exist, with the UV stream delineating the leading edge of shocked material and the radio region delineating the post-shock gas. Unlike the radio components which seem to be undergoing constant acceleration, the UV components are best explained by a nonlinear acceleration model suggestive of magnetohydrodynamic effects (Hollis et al. 1997). Both studies found evidence for event separation times consistent with the suggested binary period with the radio components showing times of  $\sim 44$  yr (Hollis and Michalitsianos 1993) and the UV emission suggestive of separation times of  $40.2$  yr (Hollis et al. 1997)

Observations continue to narrow down the possible mechanisms responsible for the unusual behavior of R Aqr. The current state of theories on the R Aqr jet can

be generalized in the following picture:

- Radiation pressure from the LPV wind moves material in its own dust shell outward.
- An accretion disk forms around the hot companion and a fast stellar wind forms outside this accretion disk.
- There is a highly-collimated stream of supersonic material ejected from the central core.
- This stream could possibly be the result of a collision between the two winds, or material could be squirting out a path of least resistance in a confining medium, possibly a thick outer accretion disk.
- This stream impacts slower denser clumps of material from either the Mira wind or the inner nebula ejected  $\sim 190$  yr ago causing shock-wave heating.
- These clumps of shock-ionized (and possibly photoionized) material show up as knots of emission (observed at radio, optical, and UV wavelengths) with an overall S-shape structure reminiscent of a helix projected on the plane of the sky.
- The observed helical structure could be caused by the precession of the accretion disk as material streams out or by material moving along twisted magnetic field lines frozen into the ejected material.
- The  $\sim 44$  yr separation time between ejection events could be the result of enhanced mass transfer during periastron passage of the companion.

The above provides a plausible description of the mechanisms occurring in R Aqr, but the actual details are still highly debatable. Clearly R Aqr is an excellent candidate for continued study.

# Chapter 5

## STRUCTURE AND DYNAMICS OF THE SiO MASERS

“The more I thought about them, the stranger they seemed.  
They are, after all, not just images but moments of time . . .  
and there is something so peculiar about them.”

*Stephen King, Four Past Midnight*

### 5.1 Introduction

In this chapter, the results and astrophysical interpretation of the total intensity observations presented in Chapter 3 will be discussed. The overall morphology of the SiO maser emission as seen in the total intensity images, and the variability of this emission with time is considered in § 5.2. In § 5.3, the process of selecting individual maser features from the image cubes for further analysis is described. The dynamics of the extended atmosphere of R Aqr as indicated by the analysis of the proper motions of the SiO maser features are discussed in § 5.4.

### 5.2 Structure and Variability

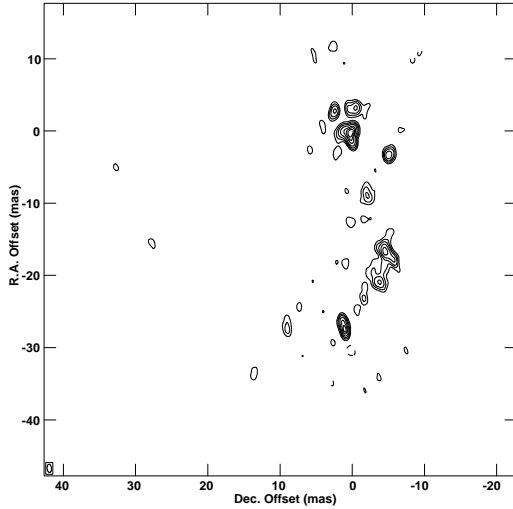
The observations presented in this thesis represent the first time that SiO maser emission has been mapped at several periods within a single stellar pulsation cycle. As such, this set of observations provides a unique insight into the morphological

changes that the SiO maser shell undergoes within a single cycle. Figure 5.1 shows a composite of the four integrated total intensity images from Chapter 3. Errors in the absolute flux density scale are on the order of 5% for Epochs 1 and 3 and 15% for epochs 2 and 4. These differences are due to the nature of the amplitude calibration scheme used for each epoch of observations (template fitting or system temperatures and antenna gains). Figure 5.1(a) (Epoch 1) shows an arc or partial ring of maser emission extending in the N-S direction. In Epoch 2, which was observed only six months later, the masers form nearly a full ring. This structure is evident in all three subsequent epochs spanning a time period of approximately three months. Assuming a distance of 220 pc to R Aqr, the projected ring of emission has a diameter of  $\sim 6.8$  AU, with an average width (FWZP) of  $\sim 0.7$  AU. The structure is slightly elongated in the N-S direction, and there appears to be a gap in the emission which has a NNW-SSE orientation. This gap could be related to the formation of the R Aqr jet which extends in a roughly perpendicular NE-SW direction (Kafatos et al. 1989).

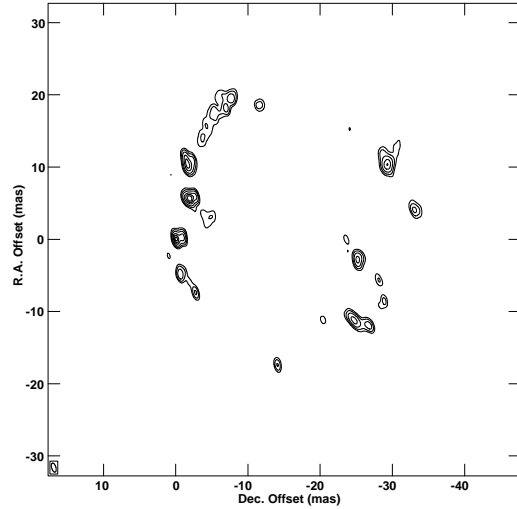
The existence of a ring of emission and the lack of any masers within this ring implies that the masers are tangentially amplified as was first noted by Diamond et al. 1994. From the spectra presented in Chapter 3 it can be seen that the emission covers a velocity range of  $\sim 15$  km s $^{-1}$  from  $-33$  to  $-18$  km s $^{-1}$ . There does not appear to be any coherent velocity structure around the ring. Figures 3.8, 3.15, 3.22, and 3.29 show that features both blue shifted and red shifted from the adopted LSR velocity of the star ( $-27$  km s $^{-1}$ ) appear randomly distributed about the ring. From these images there does not appear to be any systematic velocity changes or obvious signatures of stellar rotation.

The four epochs shown in Figure 5.1 clearly show the strong time-variable nature of the maser emission. Epoch 1, which in general has the strongest features, appears to have few related features in Epoch 2. Over the six month time period from Epoch 1 to Epoch 2, the entire eastern side of the ring appears accompanied by significant changes in the western portion of the ring. New features appear on timescales as short as  $\sim 1$  month as is evident in the evolution of the southern most feature in Figure 5.1(b). This feature consists of a single maser spot in Epoch 2, two distinct spots of emission in Epoch 3, and three spots of maser emission in Epoch 4. In addition to the formation of new features, existing features also vary with time. The structure of the NE section of the ring, which is made up of several individual features in Epoch 2, changes significantly over 98 days appearing as a linear filamentary structure by Epoch 4. The components comprising the western side of the ring are relatively strong in Epochs 2 and 3, but appear much weaker in Epoch 4.

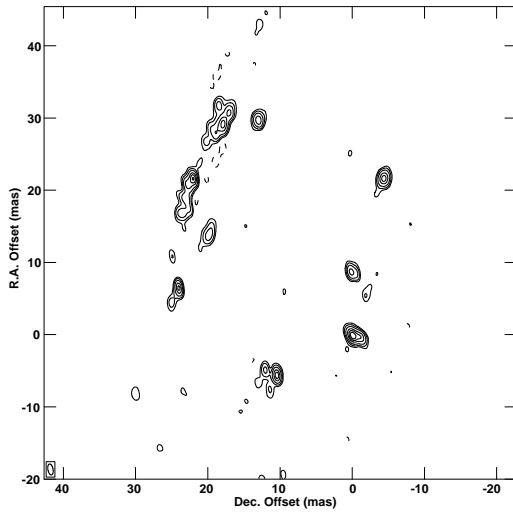
Previous observations for other late-type stars (Diamond et al. 1994; Miyoshi et al. 1994; Greenhill et al. 1995) have shown that the SiO masers typically exhibit



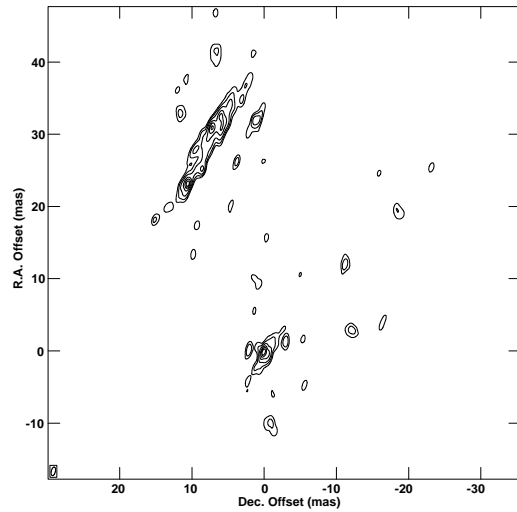
(a) Epoch 1 (June 30, 1995)



(b) Epoch 2 (December 29, 1995)



(c) Epoch 3 (February 2, 1996)



(d) Epoch 4 (April 5, 1996)

Figure 5.1: Total intensity VLBI images of the  $v = 1, J = 1 - 0$  SiO maser emission towards R Aqr integrated over the LSR velocity range of  $-32.9 \text{ km s}^{-1}$  to  $-17.4 \text{ km s}^{-1}$ . Contour levels are  $-10, -5, 5, 10, 20, 40, 60, 80,$  and  $100\%$  of the peak integrated flux density in each image. Peak integrated flux densities obtained by summing over all channels within the above velocity range are: (a)  $134.5 \text{ Jy/beam}$ , (b)  $36.0 \text{ Jy/beam}$ , (c)  $44.0 \text{ Jy/beam}$ , and (d)  $50.7 \text{ Jy/beam}$ .

a ring-like morphology at a distance of  $\sim 2\text{--}4 R_*$  from the center of the star. The VLBA observations presented here show that the maser ring, which has a projected radius of  $\sim 3.4$  AU, is located in a region outside the stellar photosphere and inside the circumstellar dust shell. From  $2.2 \mu\text{m}$  near-infrared observations, van Belle et al. (1996) estimate the photospheric radius of R Aqr to be  $\sim 385 R_\odot$  ( $\sim 1.8$  AU). This places the the maser shell at  $\sim 1.9 R_*$  slightly less than the typical  $2\text{--}4 R_*$ . Danchi et al. (1994) used a radiative transfer model to deduce the inner radius of the circumstellar dust shell from their  $11.15 \mu\text{m}$  mid-infrared observations. They found this inner radius to be  $70 \text{ mas}$  ( $\sim 8.6 R_*$ ) for R Aqr. The SiO masers are thus well inside the dust shell and lie closer to the stellar photosphere.

The very presence of the SiO maser ring around the Mira in R Aqr demonstrates that the dust shell is able to completely shield the SiO maser region from the UV photons of the companion. As mentioned in § 1.2.2, the colliding winds model described by Girard and Willson (1987) has been used to explain the lack of maser emission towards Miras in symbiotic binaries. The ring-like structure formed by the SiO masers towards R Aqr is similar to the morphology of the maser emission towards isolated long-period variables. This implies that the either the companion is sufficiently far away or its stellar wind is too weak to dissociate even those molecules on the side facing the companion protected by the circumstellar dust shell.

## 5.3 Locating SiO Maser Features

### 5.3.1 Component Selection

In order to determine the characteristics of the masers in the shell, individual features were determined for each of the four epochs. Features were first identified by fitting a two-dimensional Gaussian the size of the synthesized beam to potential sources within each spectral channel of the total intensity (Stokes  $I$ ) image cube. Components below eight times the  $1\sigma$  off-source noise level or 80% of the deepest negative in the image were rejected. This was accomplished within AIPS using the task **SAD** (Search and Destroy). **SAD** generates a model fit (**MF**) table which contains the relevant information for each feature identification. Unfortunately, **SAD** does not determine the fluxes in the Stokes  $Q$ ,  $U$ , and  $V$  images at the positions of the identifications. To determine these quantities, I wrote a new AIPS task called **MFQUV**. This task takes the **MF** table attached to the Stokes  $I$  image cube and searches each of the other associated image cubes for the Stokes  $Q$ ,  $U$ , and  $V$  fluxes. **MFQUV** does not fit Gaussians in these images, but instead locates the pixel associated with the center position of each feature and determines the flux at that location in each Stokes image. This approach avoids the probable systematic bias created by fitting Gaussians to

features in all four Stokes image cubes. The MF table produced for each epoch was written to disk for further analysis outside of AIPS.

The remainder of the component derivation was accomplished through a series of small FORTRAN programs written to extract and manipulate the relevant information from the MF tables. From the lists of possible identifications in these tables, components were selected to meet the following criteria:

1. For each component, only identifications spatially coincident within a  $30 \mu\text{s}$  radius ( $\sim 1/3 \theta_{\text{beam}}$ ) were accepted.
2. The component was detected in at least two adjacent velocity channels.
3. The peak flux density of a component was greater than 400 mJy.

The 400 mJy cutoff was chosen to be lower than the absolute value of the lowest contour in the individual channel maps of all four epochs.

Component positions in right ascension, declination, and velocity were determined using a flux density square weighted average over the above identifications. The peak value in each of the four Stokes parameters was assigned to this average position and final lists of components produced. These lists for each of the four epochs are presented in Appendix B. From these tables of components total intensity component maps were produced. These maps are shown in Figures 5.2–5.5. It is apparent that these maps accurately reproduce the structure seen in the integrated total intensity images of Figure 5.1.

### 5.3.2 Error Estimation

The errors involved in fitting two-dimensional Gaussians to digital images have been extensively analyzed by Condon (1997) and references therein. For a typical two-dimensional Gaussian fit, the parameters involved are the peak amplitude  $A$ , the center position of the peak  $(x_0, y_0)$ , and the root mean square (RMS) major and minor axes  $(\sigma_x, \sigma_y)$ . Condon derives the errors in the fit in terms of the coordinate system along the major and minor axes of the ellipse assuming uncorrelated noise in each pixel. In addition, Condon replaces  $\sigma_x$  and  $\sigma_y$  with parameters generally used by astronomers, namely, the full width at half maximum (FWHM) of the major and minor axes of the ellipse,  $\theta_M$  and  $\theta_m$  respectively. These error estimates were translated to the right ascension–declination  $(\alpha, \delta)$  coordinate system typically used by astronomers by Kogan (1996). In this system, the errors in the center position of

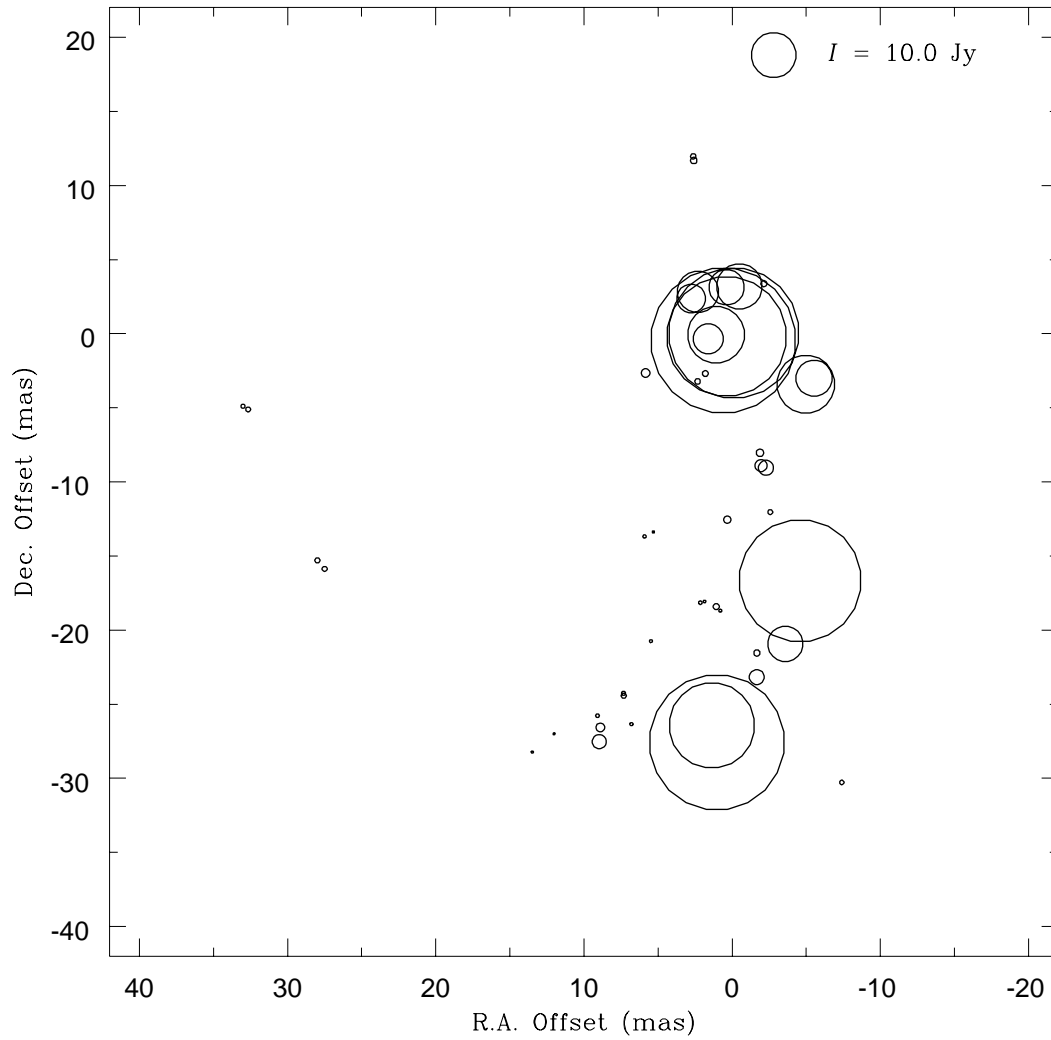


Figure 5.2: Distribution of components for Epoch 1. Components are plotted with a peak total intensity (Stokes  $I$ ) greater than 400 mJy. The radius of each circle is proportional to the total intensity of the component.

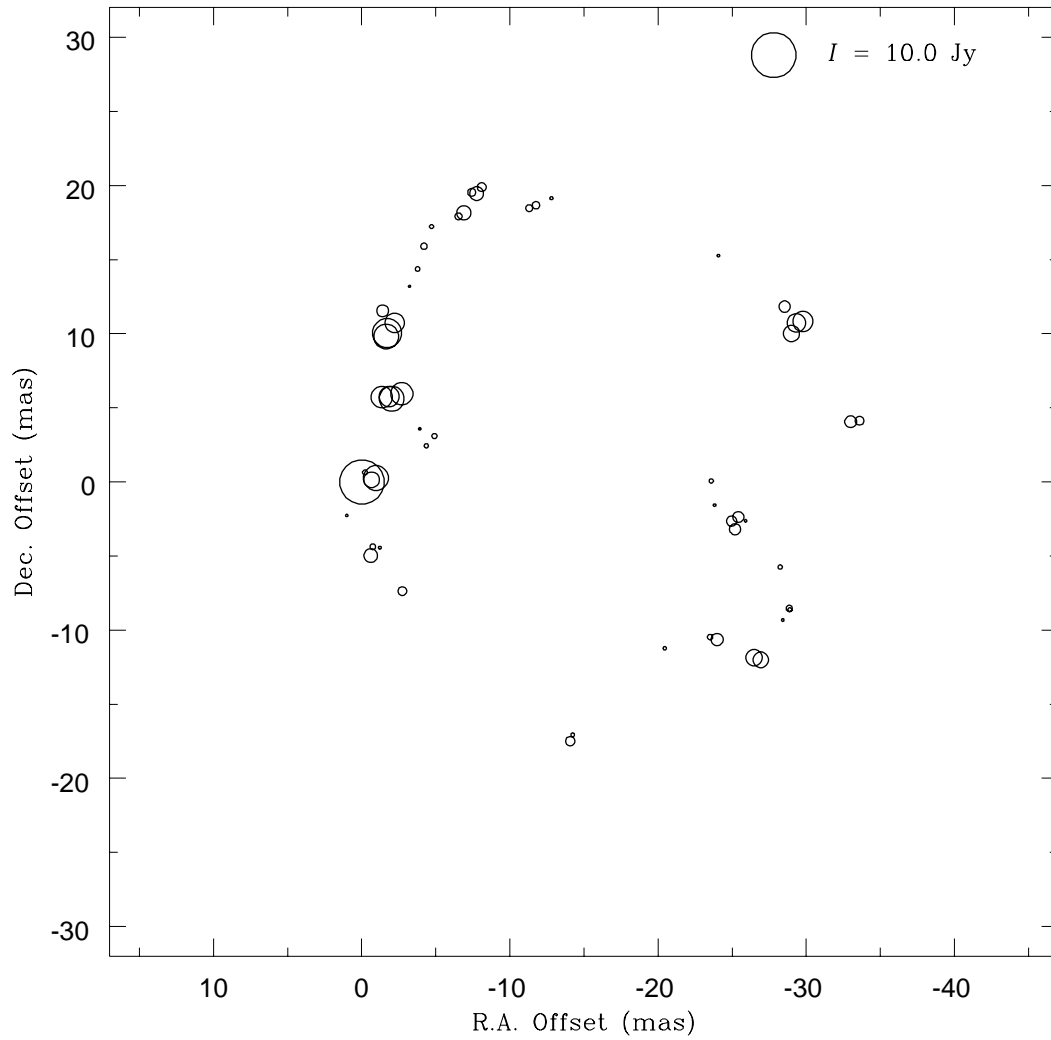


Figure 5.3: Distribution of components for Epoch 2. Components are plotted with a peak total intensity (Stokes  $I$ ) greater than 400 mJy. The radius of each circle is proportional to the total intensity of the component.

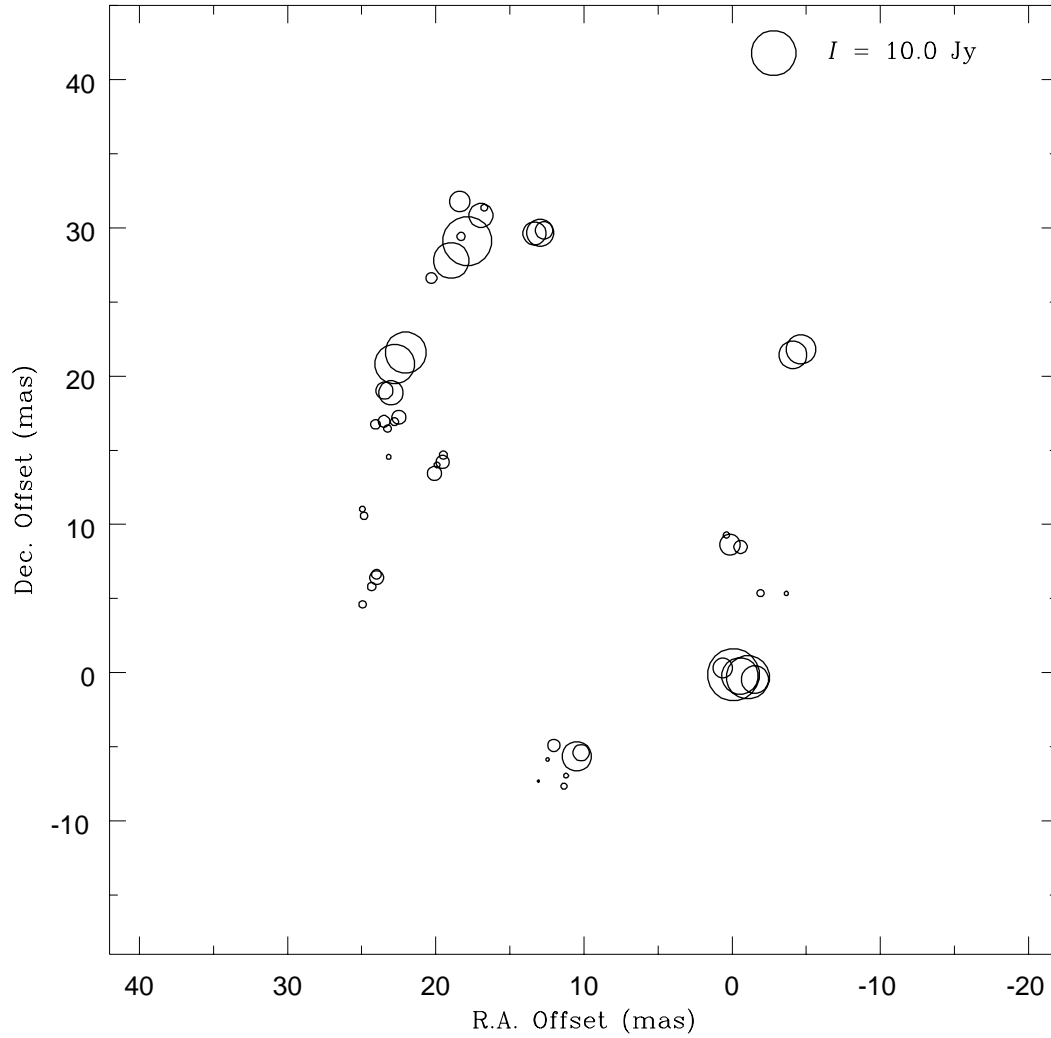


Figure 5.4: Distribution of components for Epoch 3. Components are plotted with a peak total intensity (Stokes  $I$ ) greater than 400 mJy. The radius of each circle is proportional to the total intensity of the component.

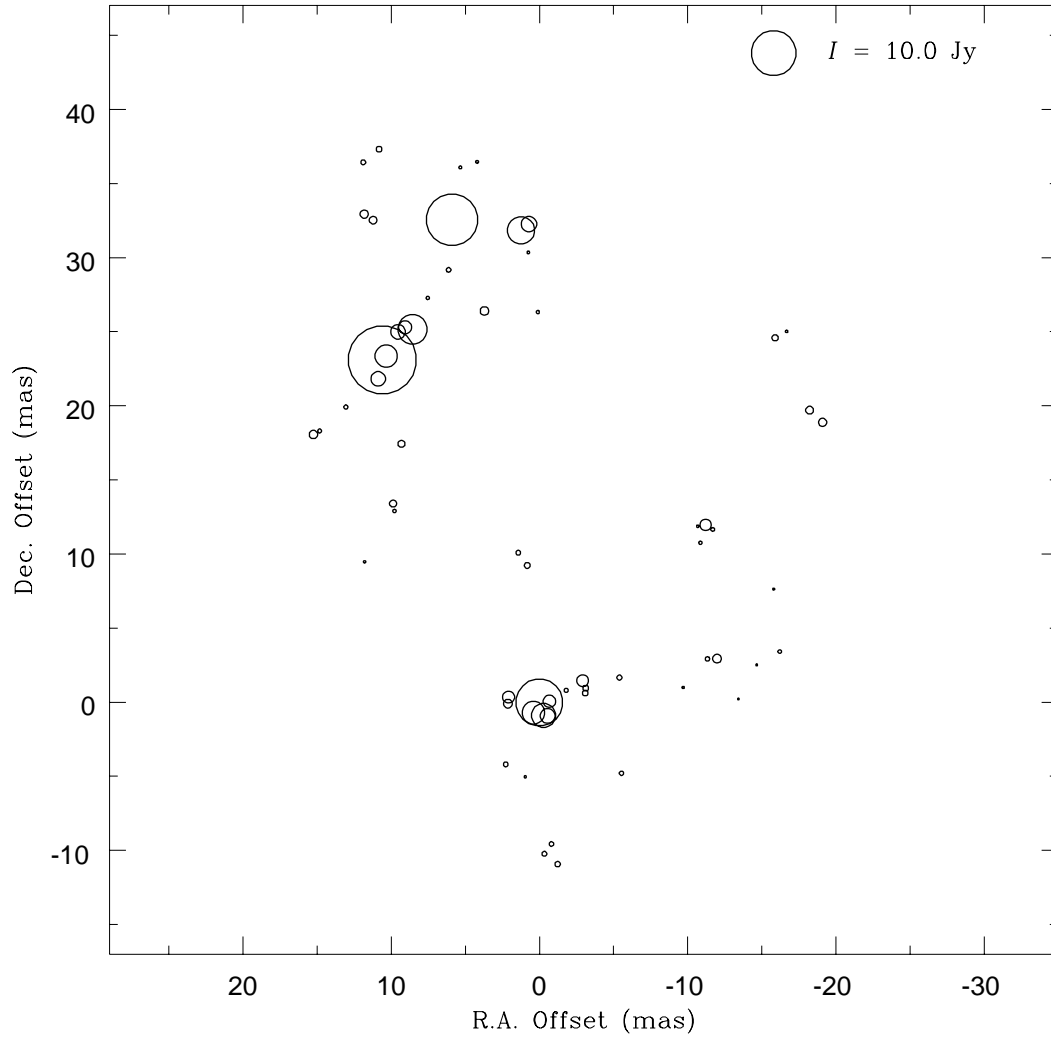


Figure 5.5: Distribution of components for Epoch 4. Components are plotted with a peak total intensity (Stokes  $I$ ) greater than 400 mJy. The radius of each circle is proportional to the total intensity of the component.

the peak can be written

$$\begin{aligned}\sigma_\alpha^2 &= \frac{2}{\rho^2} \left[ \frac{\theta_M^2 \sin^2 \phi + \theta_m^2 \cos^2 \phi}{8 \ln(2)} \right], \\ \sigma_\delta^2 &= \frac{2}{\rho^2} \left[ \frac{\theta_m^2 \sin^2 \phi + \theta_M^2 \cos^2 \phi}{8 \ln(2)} \right],\end{aligned}\tag{5.1}$$

where  $\phi$  is the position angle of the major axis and the overall signal-to-noise ratio ( $\rho$ ) obeys (Condon 1997)

$$\rho^2 = \frac{\pi \theta_M^2 \theta_m^2 A^2}{8 \ln(2) h^2 \sigma^2}.\tag{5.2}$$

In the above equation,  $\sigma$  is the RMS noise in the image and  $h$  is the pixel separation.

In general, the assumption that the noise in each pixel is independent is not a valid one since images are the result of convolution of the real image with the synthesized beam. The situation is much more complicated for the case of correlated pixel noise. Kogan (1996) examines two limiting cases: (1) the extended source case where the beam size is much smaller than the source size,  $\theta_M^{beam} \theta_m^{beam} \ll \theta_M \theta_m$ , and (2) the point source case in which the beam size is on the order of the source size,  $\theta_M^{beam} \theta_m^{beam} \approx \theta_M \theta_m$ . Since I used the synthesized beam to fit potential features in the image cubes generated for this thesis, the latter situation applies. In this case,  $\rho$  is given by

$$\frac{2}{\rho^2} = \frac{\sigma^2}{A^2} = \frac{1}{(\text{SNR})^2},\tag{5.3}$$

and the errors in the right ascension and declination offsets are then

$$\begin{aligned}\sigma_\alpha &= \frac{1}{\text{SNR}} \left[ \frac{\theta_M^2 \sin^2 \phi + \theta_m^2 \cos^2 \phi}{8 \ln(2)} \right]^{1/2}, \\ \sigma_\delta &= \frac{1}{\text{SNR}} \left[ \frac{\theta_m^2 \sin^2 \phi + \theta_M^2 \cos^2 \phi}{8 \ln(2)} \right]^{1/2}.\end{aligned}\tag{5.4}$$

The errors in right ascension and declination shown in the lists of components in Appendix B were determined using the above equations.

The accuracy of the component positions can also be affected by systematic delay errors. The positional error  $\Delta\theta$  due to systematic effects is estimated by Greenhill et al. (1990) to be

$$\Delta\theta \approx \left( \frac{\Delta\nu}{\nu_R} \right) \left( \frac{\Delta\tau}{\tau_d} \right) (\text{rad}),\tag{5.5}$$

where  $\nu_R$  is the frequency of the reference feature,  $\Delta\nu$  is the frequency offset of the maser feature from the reference feature,  $\Delta\tau$  is the delay error, and  $\tau_d$  is the baseline length expressed in units of light travel time. For a delay uncertainty of 5 ns on a 2800 km baseline, a feature offset from the reference feature by 2 MHz ( $\sim 12 \text{ km s}^{-1}$ ) would have a position error of  $\sim 5 \mu\text{as}$  if only that baseline is used. This error is a factor of 5 less than the typical error resulting from the fitting of a two-dimensional Gaussian to the feature.

The off-source RMS noise in each velocity channel of an image cube provides an estimate of the image quality in each of the four Stokes parameters. This value was measured in the corner of each image plane of each Stokes image cube and is denoted by  $\sigma_I^0, \sigma_Q^0, \sigma_U^0$ , and  $\sigma_V^0$ . Calibration defects often show up as striping or regions of negative brightness in the Stokes  $I$  image. Assuming a Gaussian noise distribution then the magnitude of the deepest negative in the image  $|I_{neg}|$  provides an estimate of these defects. The probability distribution for  $I$  is given by

$$P(I) = \frac{1}{\sqrt{2\pi}\sigma_I} e^{-\frac{(I-I_0)^2}{2\sigma_I^2}}. \quad (5.6)$$

A broader estimate of the noise in the Stokes  $I$  image  $\sigma_I$  can be determined by setting  $\sigma_I = |I_{neg}|/\gamma$ . The factor  $\gamma$  can be computed by assuming that the probability of finding the deepest negative pixel in an image of area  $A_p$  is  $1/A_p$ , and solving

$$1 - \frac{2}{\sqrt{2\pi}\sigma_I} \int_0^{\gamma\sigma_I} e^{-\frac{(I-I_0)^2}{2\sigma_I^2}} dI = \frac{1}{A_p}. \quad (5.7)$$

Equation 5.7 was solved numerically for a  $1024 \times 1024$  image and a value  $\gamma = 4.9021$  was determined. A more robust estimate of the noise in the Stokes  $I$  images is then  $\sigma_I = I_{neg}/4.9021$ . The errors for Stokes  $I$  listed in Tables B.1–B.4 were determined using the above estimate from the deepest negative in each plane of the image cube. Errors in the Stokes  $Q$ ,  $U$ , and  $V$  images are simply the off-source noise estimate described above ( $\sigma_Q = \sigma_Q^0; \sigma_U = \sigma_U^0; \sigma_V = \sigma_V^0$ ).

## 5.4 Proper Motions

From Figures 5.1(b)–5.1(d) it is apparent that some of the maser features span multiple epochs. This suggests the possibility of determining the motion of these maser features across the plane of the sky. Because of the strong time variability of the SiO masers, the six month time interval between Epochs 1 and 2 was too long to allow the proper motions to be determined between these epochs. It was, however, possible to determine the motion over the time periods between each of the final three epochs.

The implied velocity for an object at a distance  $D$  away from the observer with a measured angular separation  $\Delta\theta$  over time  $\Delta t$  is given in Kemball (1992) as

$$\left(\frac{v}{\text{km s}^{-1}}\right) \approx 1.732 \left(\frac{\Delta\theta}{\text{mas}}\right) \left(\frac{D}{\text{pc}}\right) \left(\frac{\Delta t}{\text{days}}\right)^{-1}. \quad (5.8)$$

From the component lists in Appendix B the it is possible to compute the angular separations and the velocities of the individual features.

Due to the nature of standard VLBI data reduction as discussed in Chapter 2, the absolute astrometric position of the phase center in each image is unknown. Different epochs, thus, have slightly different coordinate frame origins which correspond to the reference feature used to determine the phase center for each epoch. To overcome this difficulty, the coordinate frames for the final three epochs were shifted to align the origin for each set of components on the same feature at  $v_{\text{LSR}} \approx -19.5 \text{ km s}^{-1}$ . Components were then matched from one epoch to another. The final set of matched components used in the proper motion analysis is shown in Figure 5.6 after being rereferenced to this common feature.

The proper motions of the components common from Epoch 2 to Epoch 4 are shown in Figure 5.7. Points are plotted at their Epoch 2 locations with the vectors indicating the magnitude and direction of the velocity computed using Equation 5.8. It is often the case in OH and H<sub>2</sub>O maser observations that there is an extreme blue shifted component near the center of the maser distribution. This component is usually taken to be a maser in front of the actual star amplifying the stellar background radiation. This component provides a convenient means for aligning the two different epochs in the proper motion analysis. Unfortunately, there appears to be no such component in the circumstellar SiO maser distributions. Therefore, the components must be aligned using a feature located on the ring as discussed above. The process of aligning all three epochs on a feature located on the edge of the shell introduces a systematic bias in the proper motions of the features. Derived proper motions are, therefore, uncertain by a constant offset vector representing the motion of the alignment feature. In order to present a better representation of the actual expansion or contraction of the shell, the mean proper motion was subtracted from each of the determined proper motion vectors. Figure 5.8 shows the proper motion vectors from Epochs 2 to 4 with the mean proper motion vector subtracted. The proper motion vectors in Figure 5.8 indicate a general inward motion for the majority of components and overall contraction of the maser shell.

One way to test for any net expansion or contraction of the masers is to compute separations between pairwise combinations of components. This technique has been applied to both OH masers (Chapman, Cohen, and Saika 1991; Bloemhof, Reid, and Moran 1992; Kemball 1992) and H<sub>2</sub>O masers (Marvel 1996), and is non-parametric

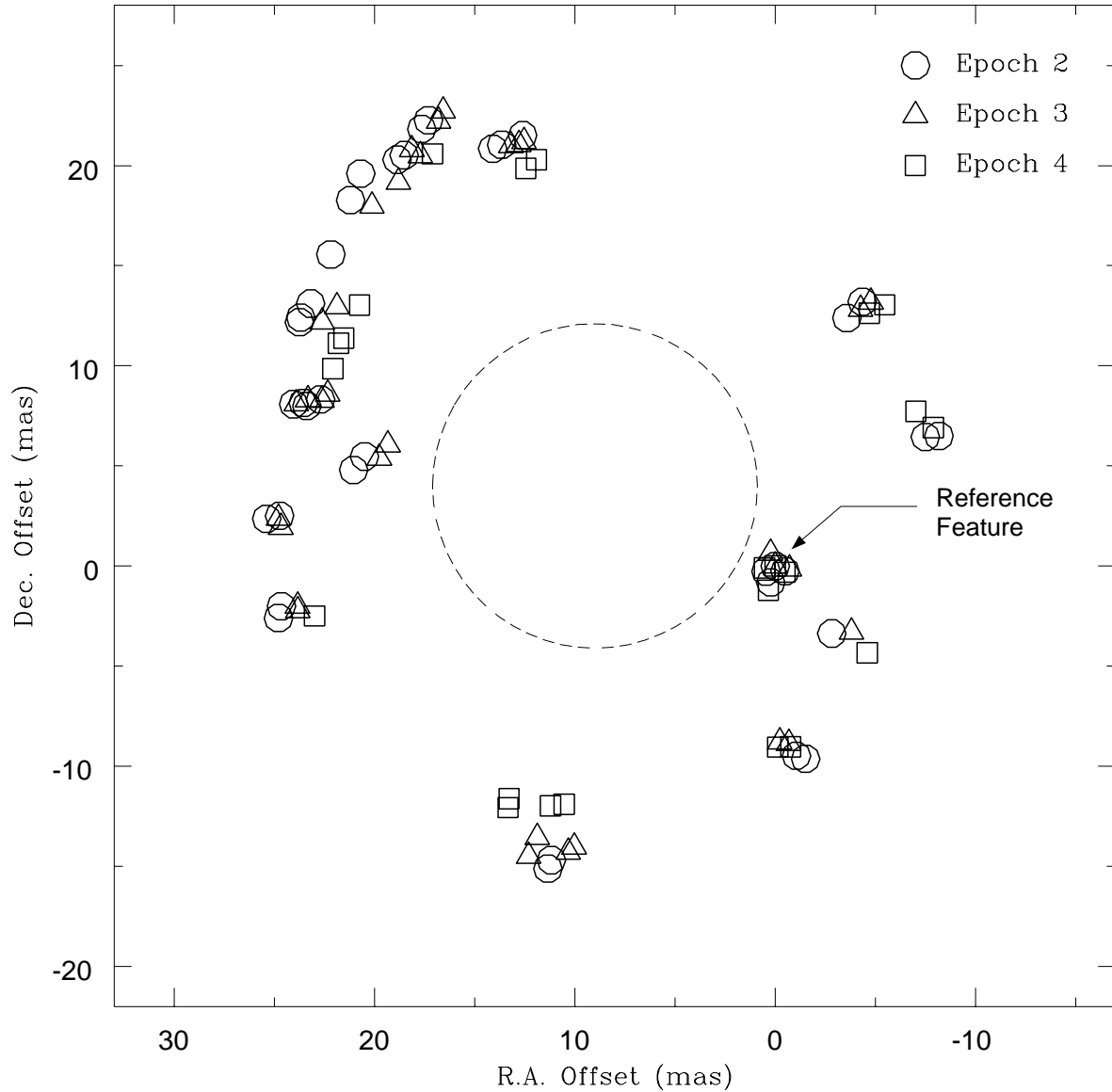


Figure 5.6: Individual maser component positions for epochs 2, 3, and 4. Features have positional errors generally less than  $\sim 0.1$  mas and peak flux densities greater than  $0.4$  Jy. The dashed circle in the center represents a stellar disk with a diameter of  $3.6$  AU at the adopted distance of  $220$  pc.

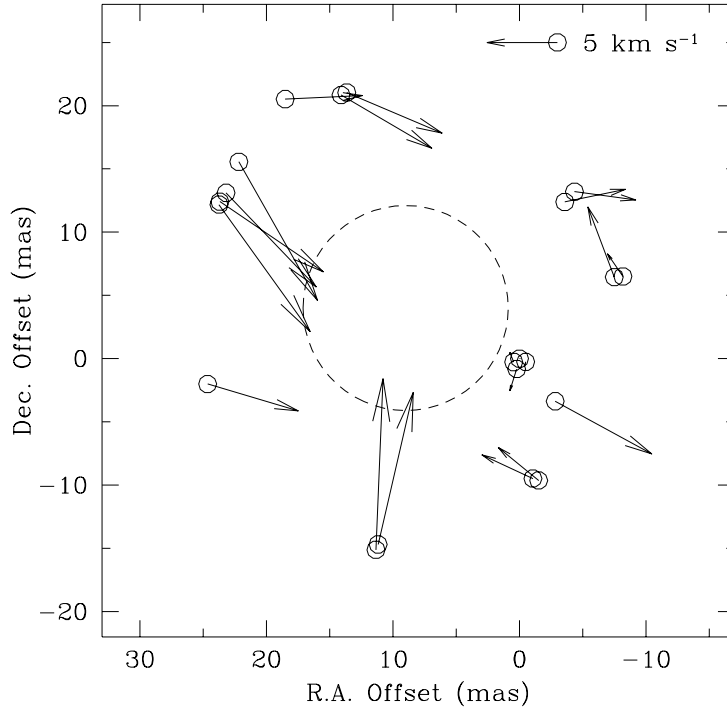


Figure 5.7: Map representing the distribution of proper motion velocity vectors from Epoch 2 to Epoch 4 at the assumed distance of 220 pc. The length of the vector is proportional to the velocity of the component. Proper motions are uncertain by an absolute velocity vector representing the motion of the feature used to align the three epochs. The dashed circle in the center represents a stellar disk with a diameter of 3.6 AU at the adopted distance.

since it has no dependence on the alignment of the maps or prior knowledge of the velocity field. In this procedure, the distance between two components around the ring at one epoch and the distance between the corresponding components for a second epoch are computed. The difference between these two distances is the pairwise separation. The calculation is repeated for all possible combinations of matched component pairs. The histograms in Figure 5.9 plot the results of the computation of pairwise separations using

$$|r_{bi} - r_{bj}| - |r_{ai} - r_{aj}|, \quad i = 1, n; \quad j = i + 1, n \quad (5.9)$$

where  $r_{ai} = (x_{ai}, y_{ai})$ ,  $r_{bi} = (x_{bi}, y_{bi})$ , and  $(r_{ai}, r_{bi})$  are assumed to be matched components for epochs  $a$  and  $b$  respectively (Kemball 1992). Figures 5.9(a)–5.9(c) show the separations over time intervals of 35, 63 and 98 days respectively. All three histograms

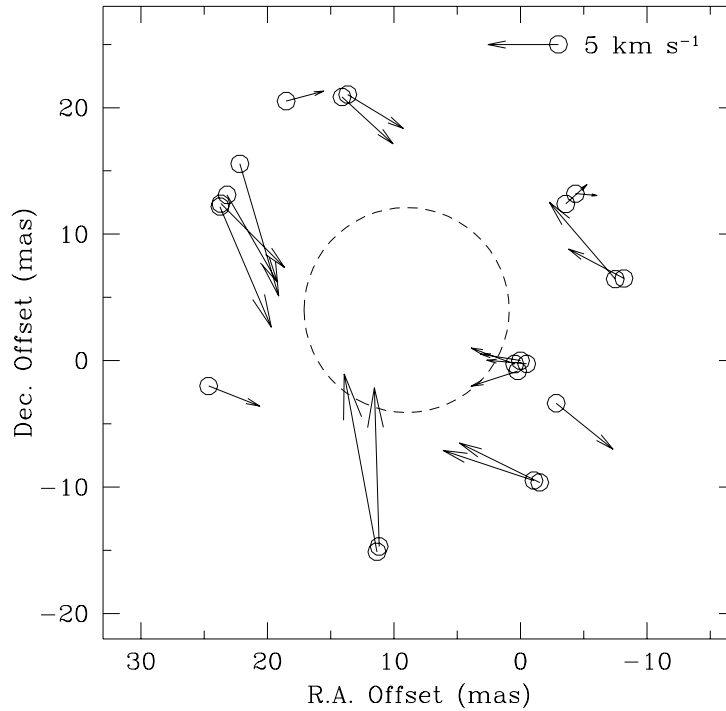


Figure 5.8: Map representing the distribution of proper motion velocity vectors from Epoch 2 to Epoch 4 at the assumed distance of 220 pc. The length of the vector is proportional to the velocity of the component. Proper motions are uncertain by an absolute velocity vector representing the motion of the feature used to align the three epochs. The mean proper motion vector has been subtracted from all components. The dashed circle in the center represents a stellar disk with a diameter of 3.6 AU at the adopted distance.

have centroids which are biased toward negative values indicating overall contraction of the maser shell. Figures 5.9(b) and 5.9(c) show a bimodal distribution with the peak near zero representing separations of component pairs which are spatially close to one another on the ring.

To determine a representative value for the shifts due to the proper motion, we computed pairwise separations for only those pairs separated by more than 15 mas. By requiring the component pairs be separated by more than 15 mas, closely spaced components on the same side of the ring are eliminated. These components bias the distribution towards zero. The resulting histograms are plotted in Figures 5.10(a)–5.10(c). These figures clearly show the contraction of the maser shell. The mean of

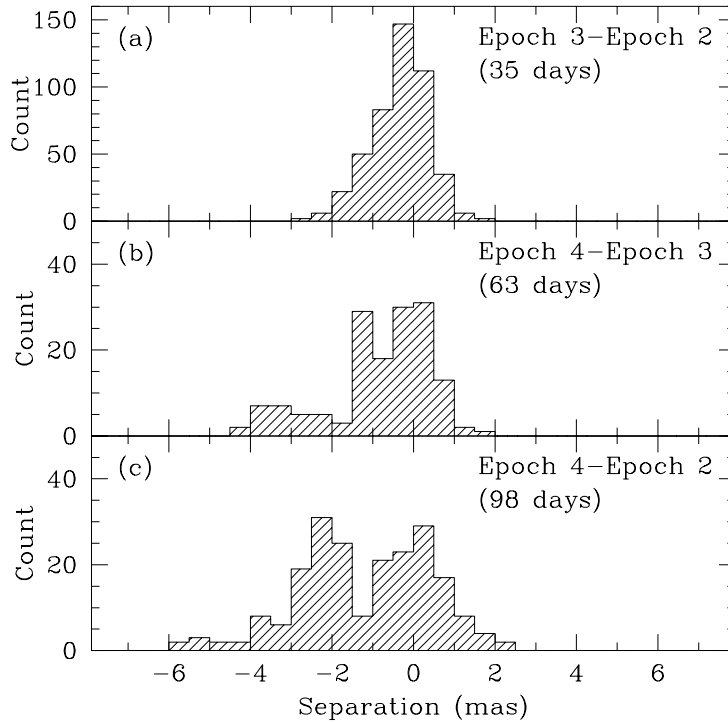


Figure 5.9: Histograms showing the change in pairwise component separations for (a) Epoch 2 to Epoch 3, (b) Epoch 3 to Epoch 4, and (c) Epoch 2 to Epoch 4. Bias towards negative shifts indicates contraction of the maser shell.

each of these distributions provides a value for the shift free of any bias towards zero caused by small separations. These shifts were found to increase over time with mean values  $\Delta\theta_{\text{mean}} = -0.5 \pm 0.1$ ,  $-1.2 \pm 0.1$  and  $-1.9 \pm 0.2$  mas for 35, 63 and 98 days respectively. Errors in the shifts are simply

$$|\Delta\theta_{\text{mean}} - \Delta\theta_{\text{med}}|/\sqrt{2}, \quad (5.10)$$

where  $\Delta\theta_{\text{mean}}$  and  $\Delta\theta_{\text{med}}$  are the mean and median shifts for each distribution respectively. We performed a linear least squares fit to the three values of  $\Delta\theta_{\text{mean}}$  in order to determine the overall infall velocity for the maser distribution. From this fit, an infall speed  $v_{\text{mean}} = 4.2 \pm 0.9$  km s<sup>-1</sup> was computed. The uncertainty in this velocity was calculated using

$$|v_{\text{mean}} - v_{\text{med}}|/\sqrt{2}, \quad (5.11)$$

where  $v_{\text{mean}}$  and  $v_{\text{med}}$  are the velocities determined from the fits to the mean and median shifts respectively.

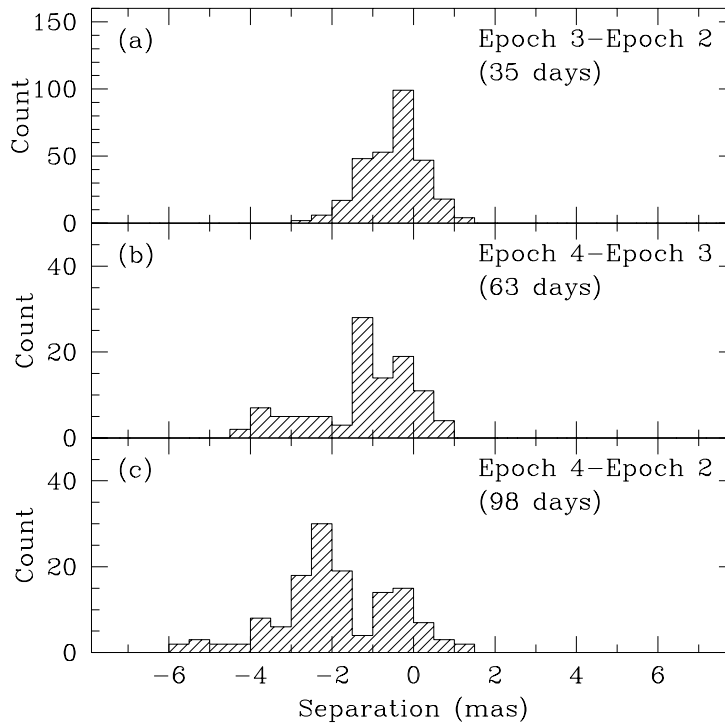


Figure 5.10: Histograms showing the change in pairwise component separations for (a) Epoch 2 to Epoch 3, (b) Epoch 3 to Epoch 4, and (c) Epoch 2 to Epoch 4. Component pairs spaced closer than 15 mas have been rejected. Bias towards negative shifts indicates contraction of the maser shell.

To independently verify the inward proper motion of the maser distribution, we fit a simple circle to the ring of emission in each of the final three epochs. The results of the fits are shown in Figure 5.11. A circle was chosen because it provides a scale size for the structure with the minimum number of free parameters. Using a least squares fit to only those components found in all three epochs, we determined the representative radius for each distribution. This radius was found to decrease in time indicating an overall contraction of the emission. The differences in radii between epochs are roughly consistent with the shifts found using the pairwise separations with  $\Delta r \approx -0.5, -0.7,$  and  $-1.1$  mas for 35, 63, and 98 days respectively. These values are dominated by systematic errors and are meant only to confirm the trend towards contraction of the shell. They were not used in the determination of overall maser shell velocities.

Inevitably, maser proper motion studies must address the question of whether

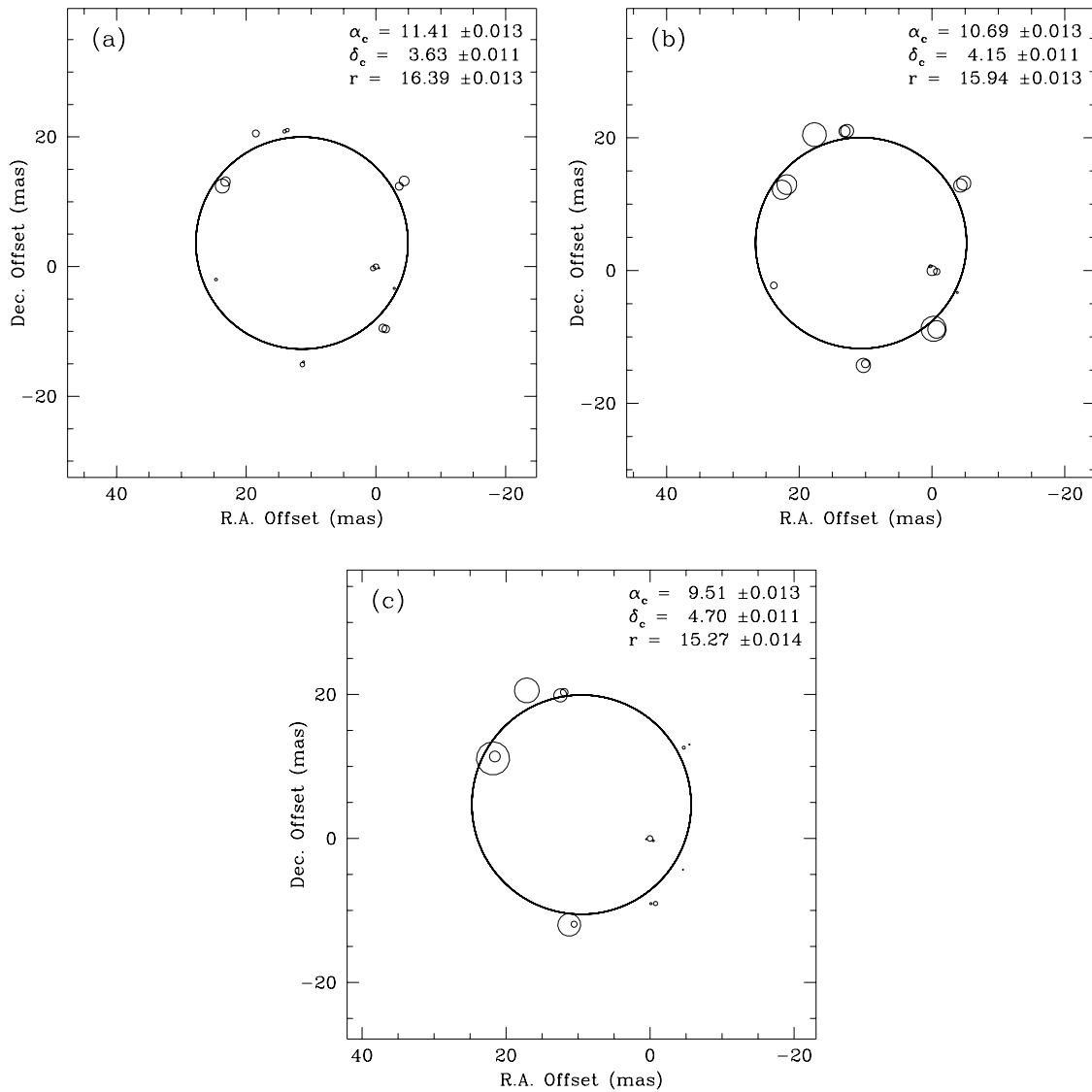


Figure 5.11: Least squares fit of a circle to components in Epochs 2, 3, and 4. Maps (a), (b), and (c) show the fit to Epoch 2, Epoch 3, and Epoch 4 respectively. Only those features common to all three epochs were used in the fit. The computed radius and coordinates of the center of the circle are shown in the upper righthand corner of each plot. The radius of each point is proportional to the total intensity of the component.

the data actually reveal true mass motion in the source, or whether the motion is in the conditions conducive to maser action. The latter situation is sometimes referred to as the Christmas tree effect (Bloemhof, Reid, and Moran 1992). Multi-epoch VLBI studies of various H<sub>2</sub>O maser sources (Genzel et al. 1981; Reid et al. 1988; Gwinn et al. 1992) and OH maser sources (Bloemhof, Reid, and Moran 1992; Kemball 1992) maser sources have demonstrated that the spot motions vary smoothly in time without any unphysical accelerations or jumps in position. The most convincing evidence to date of the motion of discrete maser-emitting clumps was presented by Bloemhof, Moran, and Reid (1996). In a study of the 1665-MHz OH masers towards the ultracompact HII region W3(OH) Bloemhof, Moran, and Reid measured the actual morphology of the individual spots which they found to persist from one epoch to the next. These observations provided the first direct evidence of physical movement of masing clumps of gas. The data presented in this thesis also supports the idea of physical motion of the maser spots. It seems unlikely in the highly variable SiO maser region around R Aqr, that random changes in conditions conducive to maser emission would be able to mimic the proper motion of components while maintaining consistent characteristics such as velocity structure, polarization, and large-scale motion.

The pulsating atmosphere of a late-type star is a region of complex dynamics permeated by shocks. The prospect of material infall inside the circumstellar dust shell of a Mira was first noted by Hinkle, Hall, and Ridgway (1982). Through time-series, near-infrared spectroscopy of  $\chi$  Cygni they derived a picture in which stellar oscillation drives an outwardly propagating wave through the photosphere between the premaximum and maximum phases of the star. This wave sets up a shock between material being accelerated outward and material falling inward from the previous cycle. By  $\phi = 0.1$ , the shock has passed through the envelope and material falls inward under the influence of gravity from  $\phi = 0.1$  to 0.8. The numerical calculations by Bowen (1988) demonstrate that the shock passage can occur later and that the infall can extend beyond phase 0.8 for the outer portions of the extended atmosphere.

The observations presented here provide the first direct evidence for infall during the stellar pulsation cycle. As shown above, the shell of SiO maser emission, which is inside the circumstellar dust shell, contracted through phases 0.78, 0.87, and 0.04. The contraction of the shell over the final three epochs yields an infall speed of  $4.2 \pm 0.9$  km s<sup>-1</sup>. Such a velocity is easily explained assuming only gravitational infall and does not require complex mechanisms such as reverse shocks. For comparison purposes, the velocity of a particle falling in from the dust shell at 15.4 AU to a point on the SiO maser shell at 3.4 AU is  $\sim 25$  km s<sup>-1</sup>. The measured infall velocity is also consistent with the finding of Reid and Menten (1997) that the shock velocities in the radio photospheres of long-period variables are below 5 km s<sup>-1</sup> at distances beyond  $\sim 2 R_*$ . While the observations presented here only provide confirmation of the infall of material during part of the stellar cycle, monitoring the SiO masers over the entire

range of phases would be of great benefit in determining the overall motion of the gas in the extended atmosphere of the Mira.

# Chapter 6

## POLARIZATION OF THE SiO MASERS

“There comes a time when you’ve got to shine your pants.”

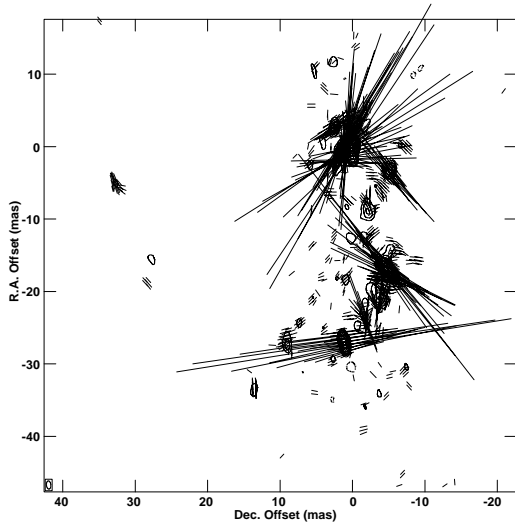
*Dr. Lay Nam Chang*

### 6.1 Introduction

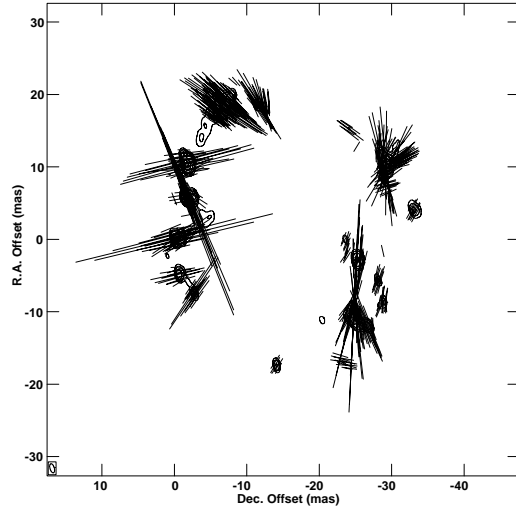
The linear and circular polarization of the SiO maser emission towards R Aqr can provide important information about the physical conditions and the magnetic fields in the extended atmosphere of the long-period variable. This chapter analyzes and interprets the polarization observations presented in Chapter 3. The determination of component polarization and the associated errors are discussed in § 6.2. In § 6.3 and § 6.4 the component circular and linear polarizations are analyzed. Finally, § 6.5 covers the implications of the polarization structure on the strength and geometry of the magnetic field in the extended atmosphere of R Aqr.

### 6.2 Component Polarization Determination

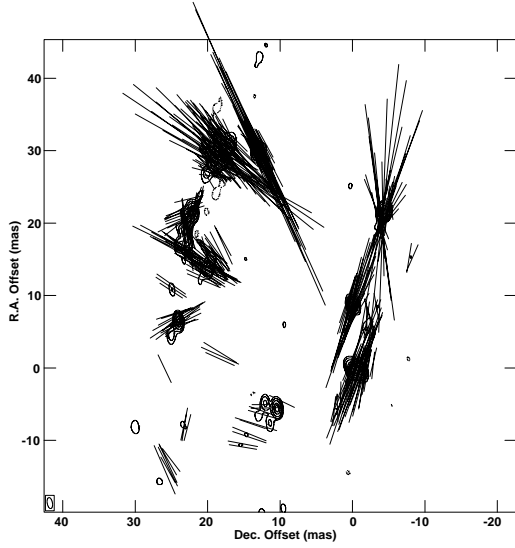
Figure 6.1 shows a composite of the four integrated linear polarization images. The orientation of the vectors represent the plane of the electric field vector and their length is proportional to the linearly polarized intensity  $P = \sqrt{Q^2 + U^2}$ . From the images in Figure 6.1 and the Stokes  $V$  images in Chapter 3, it is apparent that the



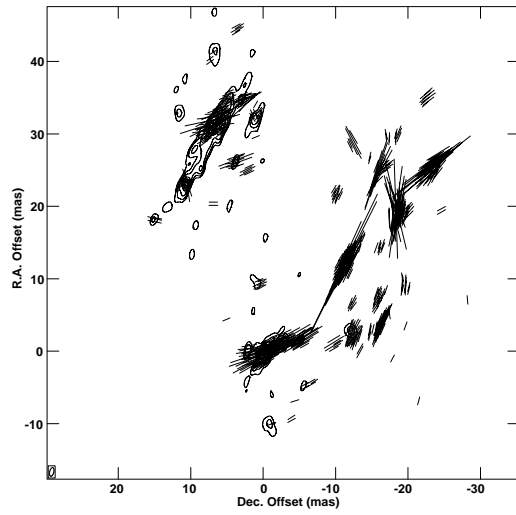
(a) Epoch 1 (June 30, 1995)



(b) Epoch 2 (December 29, 1995)



(c) Epoch 3 (February 2, 1996)



(d) Epoch 4 (April 5, 1996)

Figure 6.1: Linear polarization VLBI images of the  $v = 1, J = 1 - 0$  SiO maser emission towards R Aqr integrated over the LSR velocity range of  $-32.9 \text{ km s}^{-1}$  to  $-17.4 \text{ km s}^{-1}$ . Contour levels are the same as in Figure 5.1. The vectors indicate the plane of the electric field vector and have lengths proportional to the linearly polarized intensity, where  $10 \text{ mas} =$  (a)  $5.6 \text{ Jy/beam}$ , (b)  $2.8 \text{ Jy/beam}$ , (c)  $1.2 \text{ Jy/beam}$ , and (d)  $2.8 \text{ Jy/beam}$ .

SiO masers towards R Aqr are significantly polarized.

In order to quantify the polarization properties observed for the SiO emission towards R Aqr, the fractional circular and linear polarization given by

$$m_c = \frac{V}{I}, \quad (6.1)$$

and

$$m_l = \frac{P}{I} = \frac{\sqrt{Q^2 + U^2}}{I}, \quad (6.2)$$

respectively were determined for each set of components. Both  $m_c$  and  $m_l$  are drawn from non-Gaussian probability distributions and the significance of a detection must be carefully scrutinized. Criteria for the rejection of false detections have been formulated by Kemball (1992) for both the fractional circular and the fractional linear polarization. These criteria were developed for data taken with an array of relatively few inhomogeneous antennas and are rather conservative for data taken with a dedicated VLBI array such as the VLBA.

A non-zero fractional circular polarization can be established with a 95% confidence level if  $m_c > u_c$  where  $u_c$  is determined by solving

$$\int_{-u_c}^{u_c} \phi_0^c(m_c) dm_c = 0.95, \quad (6.3)$$

where  $\phi_c(m_c)$  is a complicated probability distribution for  $m_c$  with  $V = 0$  given in Kemball (1992). This equation was solved numerically by Kemball (1992) and can be approximated to within a few percent by

$$u_c \approx \frac{1.96\sigma_V}{I}. \quad (6.4)$$

Fractional circular polarization values less than this cutoff were set to zero in Tables B.1–B.4. The distribution for the fractional circular polarization  $m_c$  is symmetric about zero, and no correction for bias is therefore necessary. Uncertainties in the fractional circular polarization were computed for those components with non-zero  $m_c$  using

$$\sigma_c = \frac{1}{I} \sqrt{\sigma_V^2 + \frac{\sigma_I^2 V^2}{I^2}}. \quad (6.5)$$

The errors associated with each component's circular polarization  $\sigma_c$  are listed in Tables B.1–B.4.

The hypothesis that the fractional linear polarization is drawn from a zero-mean distribution can be rejected at a 95% confidence level if  $P/I > u_l$  where

$$u_l \approx \frac{1.65}{\sqrt{2}} \left[ \frac{P + \sigma_P}{I - \sigma_I} - \frac{P - \sigma_P}{I + \sigma_I} \right]. \quad (6.6)$$

The uncertainty in the linearly polarized intensity  $\sigma_P$  is calculated as

$$\sigma_P = \frac{\sqrt{Q^2 \sigma_Q^2 + U^2 \sigma_U^2}}{P}. \quad (6.7)$$

This approximation for the linear polarization rejection criterion was also derived in Kemball (1992) and was used in this thesis to set components with  $P/I < u_l$  equal to zero in Tables B.1–B.4.

The fractional linear polarization has a Rice distribution which is not symmetric about zero (Wardle and Kronberg 1974). The calculated value of  $m_l$  must therefore be corrected for bias. The true fractional linear polarization is given by

$$m_l = \frac{\sqrt{Q^2 + U^2 - \sigma_{QU}^2}}{I}, \quad (6.8)$$

where  $\sigma_{QU} = \sqrt{\sigma_Q \sigma_U}$  for  $\sigma_Q \approx \sigma_U$ . The values of  $m_l$  given in Tables B.1–B.4 were calculated using the above equation. Uncertainties in the fractional linear polarization  $\sigma_l$  were computed for those components with non-zero  $m_l$  using

$$\sigma_l = \frac{1}{I} \sqrt{\sigma_P^2 + \frac{\sigma_I^2 P^2}{I^2}}, \quad (6.9)$$

and are listed in Tables B.1–B.4.

For components with non-zero fractional linear polarization, the linear polarization position angle  $\chi$  and its associated uncertainty  $\sigma_\chi$  were computed using

$$\chi = \frac{1}{2} \arctan\left(\frac{U}{Q}\right), \quad (6.10)$$

and

$$\sigma_\chi = \frac{1}{2P^2} \sqrt{U^2 \sigma_Q^2 + Q^2 \sigma_U^2}. \quad (6.11)$$

The position angle is drawn from a symmetric probability distribution and no correction for bias is needed (Wardle and Kronberg 1974). The position angles listed in Tables B.1–B.4 are measured counterclockwise from zero which is due north (positive declination offset).

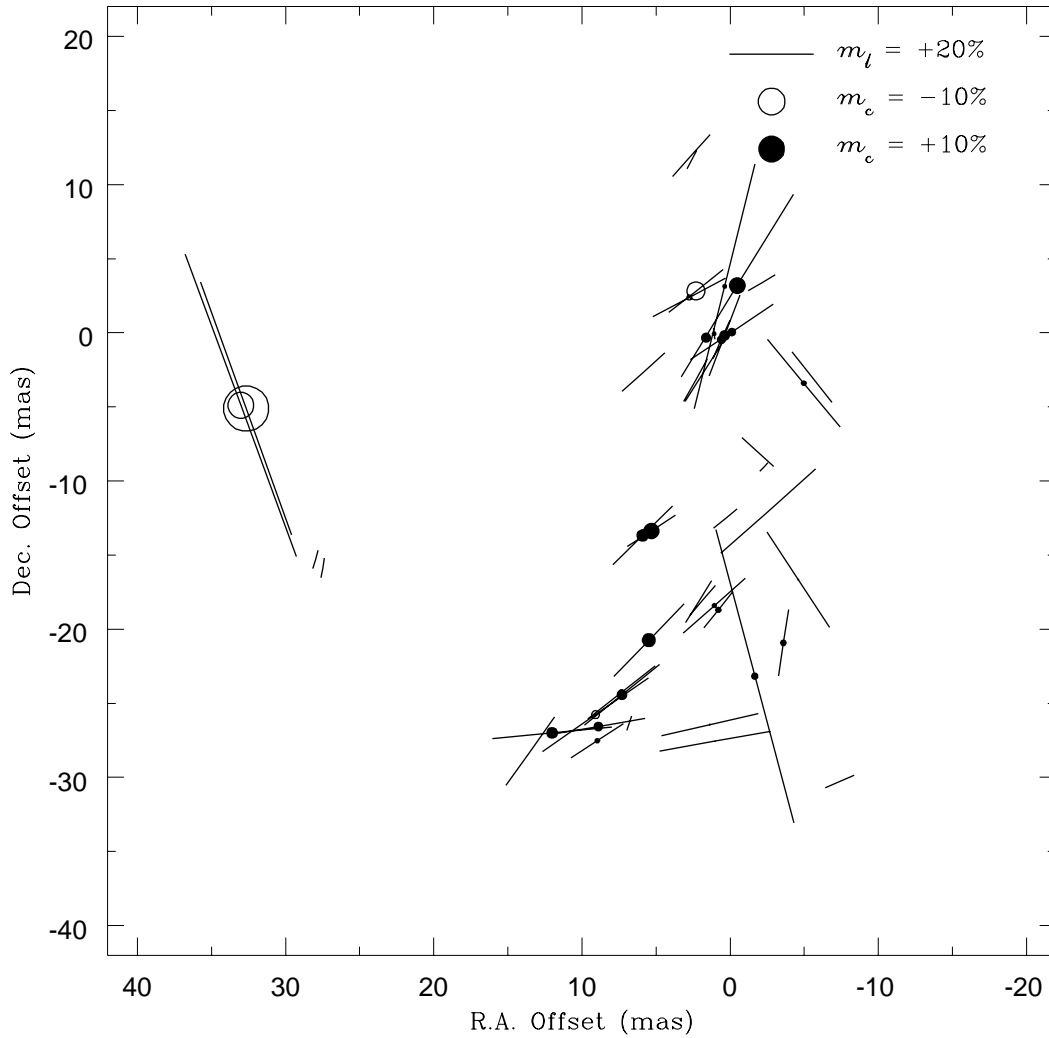


Figure 6.2: Distribution of polarized components for Epoch 1. Components are plotted with a peak total intensity greater than 400 mJy. The radius of each circle is proportional to the degree of circular polarization  $m_c$ . Open circles denote negative sense of circular polarization while filled circles denote positive circular polarization. The degree of linear polarization  $m_l$  is represented by the length of the line segments which are plotted at the polarization position angle  $\chi$  for the component.

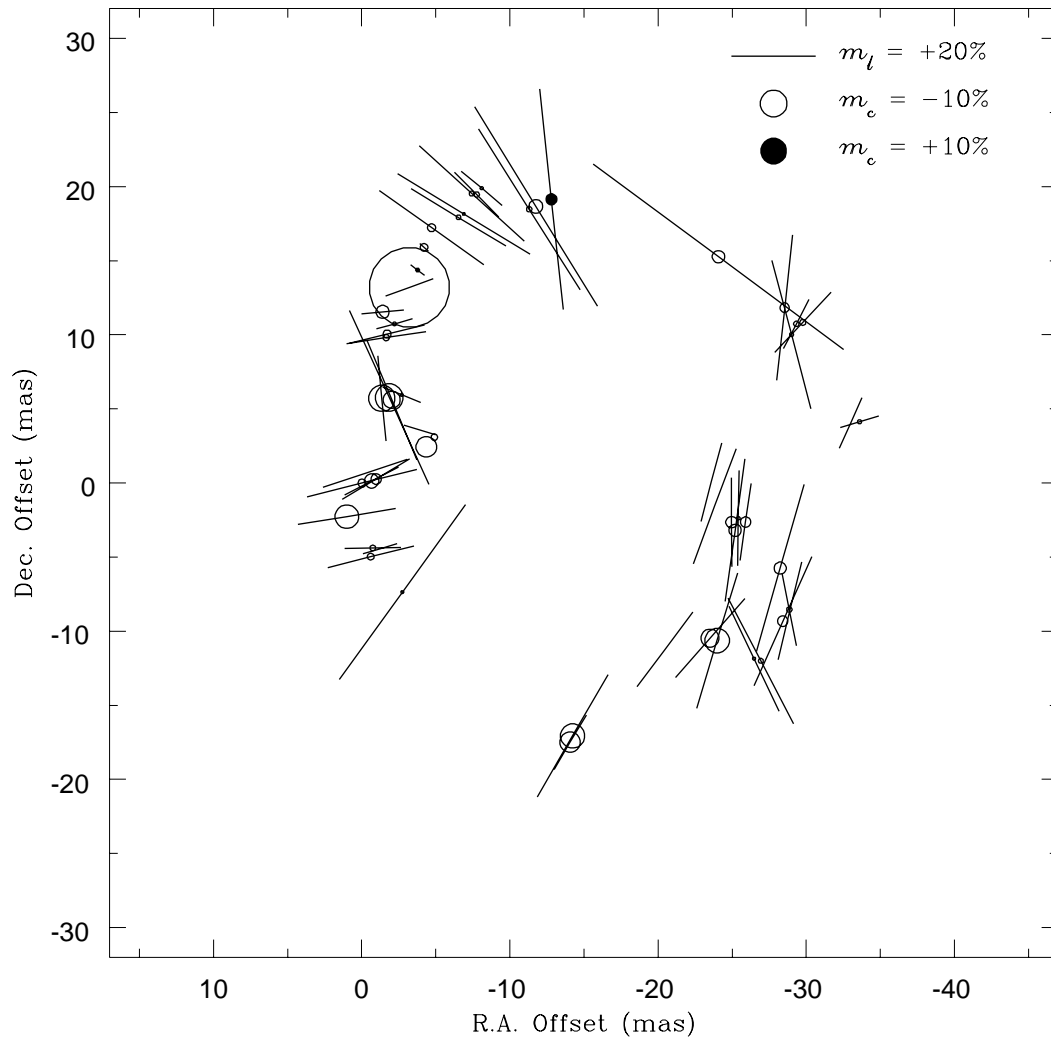


Figure 6.3: Distribution of polarized components for Epoch 2. Components are plotted with a peak total intensity greater than 400 mJy. The radius of each circle is proportional to the degree of circular polarization  $m_c$ . Open circles denote negative sense of circular polarization while filled circles denote positive circular polarization. The degree of linear polarization  $m_l$  is represented by the length of the line segments which are plotted at the polarization position angle  $\chi$  for the component.

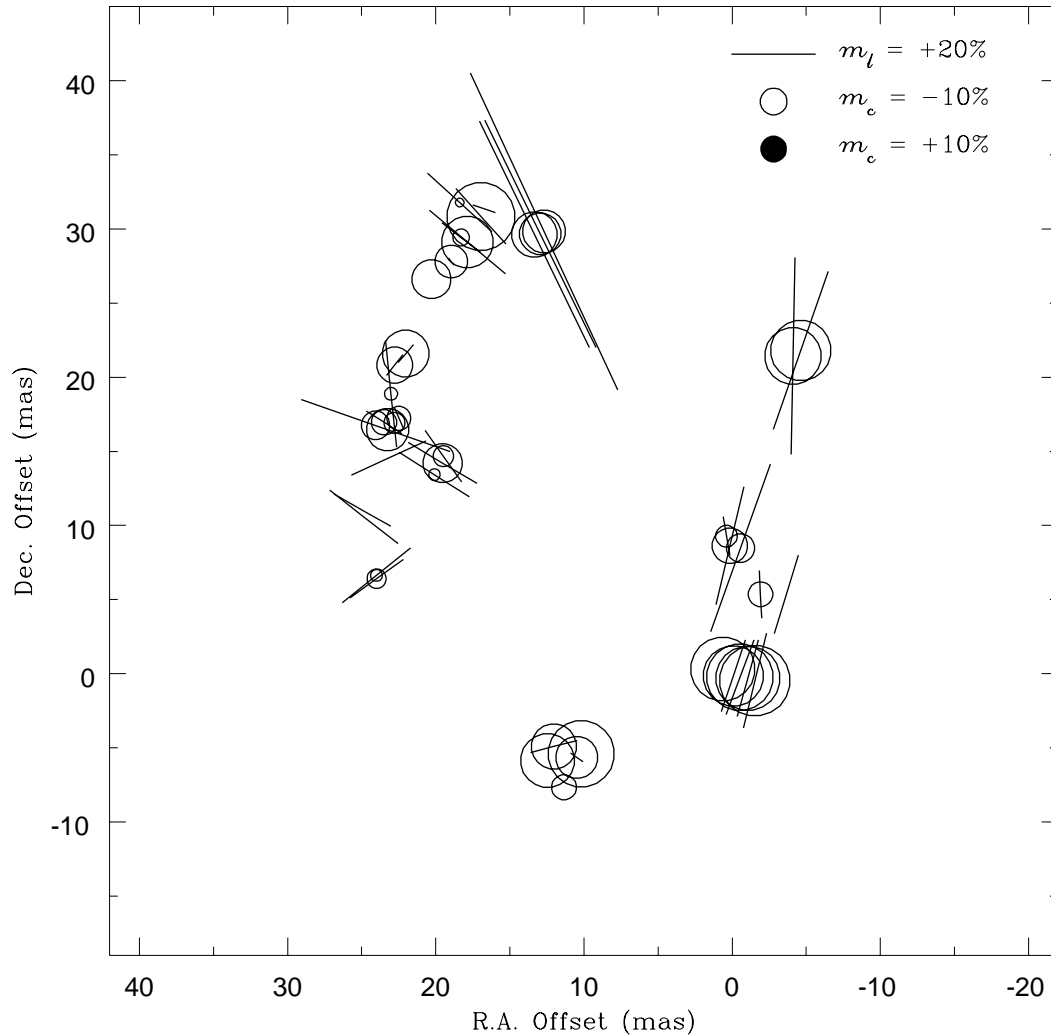


Figure 6.4: Distribution of polarized components for Epoch 3. Components are plotted with a peak total intensity greater than 400 mJy. The radius of each circle is proportional to the degree of circular polarization  $m_c$ . Open circles denote negative sense of circular polarization while filled circles denote positive circular polarization. The degree of linear polarization  $m_l$  is represented by the length of the line segments which are plotted at the polarization position angle  $\chi$  for the component.

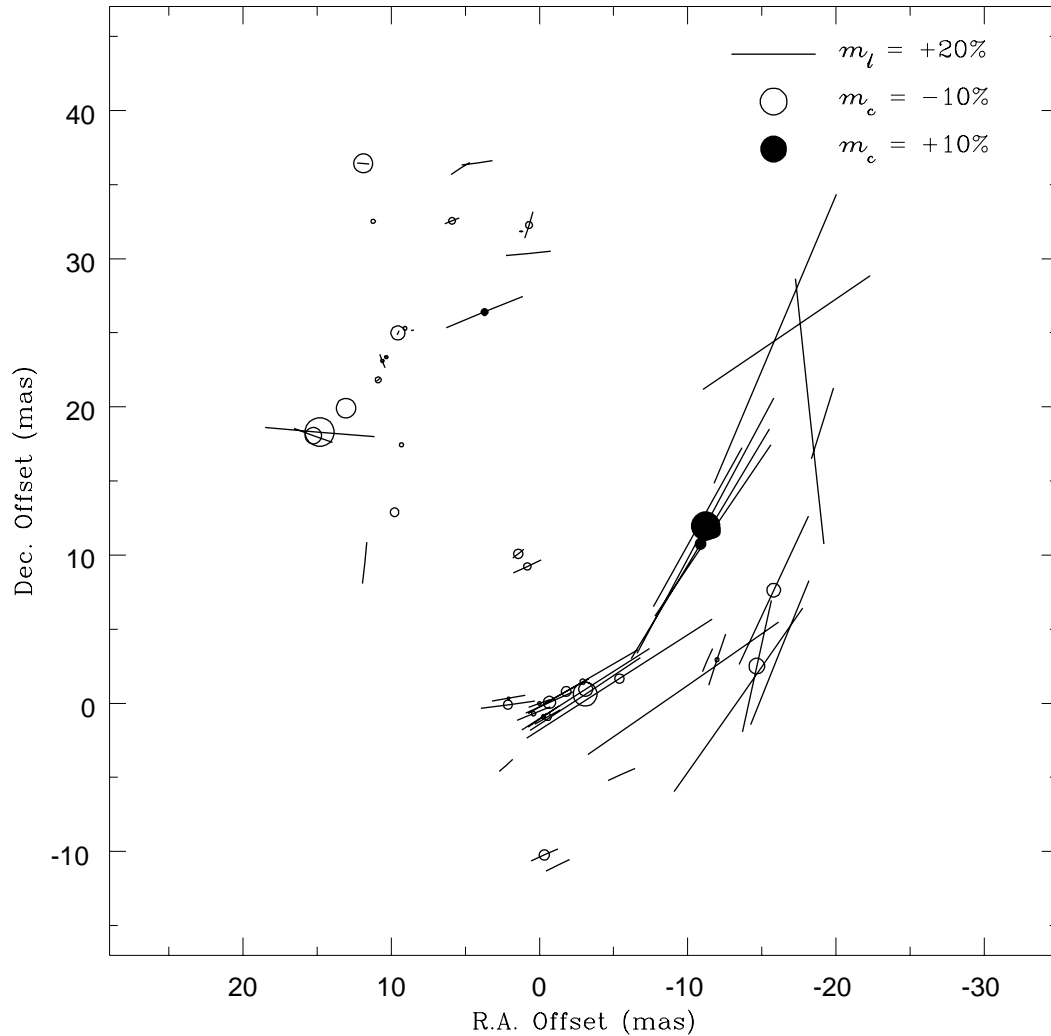


Figure 6.5: Distribution of polarized components for Epoch 4. Components are plotted with a peak total intensity greater than 400 mJy. The radius of each circle is proportional to the degree of circular polarization  $m_c$ . Open circles denote negative sense of circular polarization while filled circles denote positive circular polarization. The degree of linear polarization  $m_l$  is represented by the length of the line segments which are plotted at the polarization position angle  $\chi$  for the component.

The component polarization information, computed using the above equations and listed in Appendix B, was plotted for each of the four epochs. The resulting component polarization maps are shown in Figures 6.2–6.5. In these maps, the circular polarization is represented by open and filled circles, which indicate negative and positive values of  $m_c$  respectively. The sizes of the points are proportional to the fractional circular polarization. Component linear polarization is plotted as a line segment which has a length proportional to  $m_l$  at a position angle  $\chi$ . The polarization structures displayed in these maps accurately reproduce those of the polarization images of Figure 6.1 and Chapter 3. The polarized intensity, like the total intensity, is highly time variable and changes on timescales as short as  $\sim 1$  month. This can clearly be seen in the changing morphology of these figures. In the next three sections, the component polarization information presented in these maps is analyzed, and the implications for the magnetic field of R Aqr are discussed.

### 6.3 Circular Polarization

In this section, the degree of circular polarization is discussed and compared to previous observations of other late-type stars. Figures 6.6 and 6.7 plot the distribution of component circular polarization for each epoch. Figure 6.6 shows the actual distribution of the fractional circular polarization  $m_c$  as a series of four histograms. The absolute value  $|m_c|$  is plotted in the histograms of Figure 6.7. The time variability of the circular polarization is readily seen in Figure 6.6. In Epoch 1, the circular polarization of the majority of the components is positive. Epoch 2, on the other hand, primarily shows negative component circular polarization indicating that the polarization has switched from one sense to the opposite sense over the  $\sim 6$  month time period between the two epochs. Recall that the total intensity also shows little similarity between Epochs 1 and 2. The negative sense of circular polarization continues to dominate the Stokes  $V$  emission through Epochs 3 and 4, although the degree of polarization changes dramatically.

In Figure 6.7, it can be seen that peak circular polarizations as high as  $\sim 30\%$  have been detected for features towards R Aqr. Fractional circular polarizations this high have also been observed in isolated SiO maser features towards the Mira variable TX Cam (Kemball and Diamond 1997). The mean circular polarization for Epochs 1, 2, and 4 ranges from 3.9–4.3%. These values are consistent with single dish observations (Barvainis, McIntosh, and Predmore 1987; McIntosh, Predmore, and Patel 1994) and with VLBI observations by Kembell and Diamond (1997). Epoch 3, however, shows a distribution with a mean circular polarization of 14.4% with values distributed over a range of  $\sim 3$ –26%. This excessive value for the mean circular polarization has never before been observed for the SiO emission towards a late-type

star.

Upon determining the circular polarization distribution for Epoch 3, it was natural to suspect a problem in the calibration procedure applied to the data for this epoch. The most obvious sign of an amplitude calibration error would be if the Stokes  $V$  images appear to be scaled down versions of the Stokes  $I$  emission. Although the circular polarization is negative over the entire distribution, the Stokes  $V$  emission does not appear to simply be a reduced version of the  $I$  emission. In Figure 6.8, I have plotted the fractional circular polarization as a function of the Stokes  $I$  flux density for each of the four epochs. Although there is a noticeable difference between the distributions of Epochs 1, 2, and 4 when compared to Epoch 3, none of the epochs show this sign of amplitude calibration errors. If  $V$  were truly a scaled version of  $I$  for Epoch 3, then Figure 6.8(c) should show the data to be clustered around some constant value of  $|m_c|$ . This is not the case in Figure 6.8(c) or for any of the other epochs. For example, in Epoch 3 there are several features with Stokes  $I$  flux densities near  $\sim 4\text{--}6$  Jy which show a range of  $\sim 25\%$  in fractional circular polarization. If there were an amplitude calibration problem, these points should be tightly distributed around some constant fractional circular polarization.

One might also expect that if there was a mistake in the the amplitude calibration, that it might show up in the linearly polarized intensity. The fractional linear polarization for Epoch 3 shows no such evidence of calibration errors. However, it should be noted that the linear polarization is formed from the Stokes  $Q$  and  $U$  images which, in turn, depend on cross-correlations  $\mathcal{RL}$  and  $\mathcal{LR}$ . Amplitude calibration errors could, therefore, go unnoticed in the linearly polarized intensity.

The best check of an erroneous amplitude calibration is to apply the gain corrections, computed for the line source, to one of the continuum calibrator sources which is known to be circularly unpolarized. If these gain corrections produce some net circular polarization in the calibrator source, then the corrections are most likely in error. I performed this test by applying the amplitude gains derived for R Aqr in Epoch 3 to the continuum calibrator 0420–014, which was observed during the same time period. This source was previously found to have zero flux in the Stokes  $V$  image after calibration using the standard continuum polarization techniques. Upon applying the R Aqr amplitude calibration table and recalibrating the phases using the same procedure as before, the circular polarization for 0420–014 was again found to be negligible to within the estimated noise in the image. This indicates that the amplitude gains used for R Aqr are correct, and the unusually high fractional circular polarization is most likely real. The magnetic field strengths implied by the circular polarization as determined for each epoch are discussed later in this chapter.

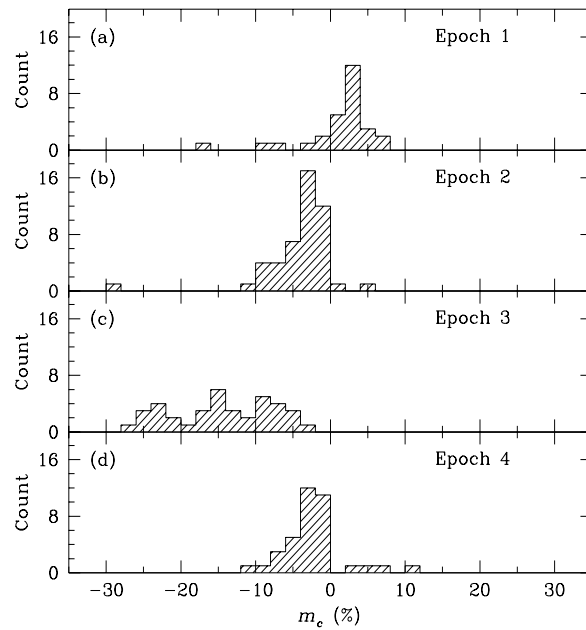


Figure 6.6: Histograms showing the distribution of component fractional circular polarization  $m_c$  for all four epochs.

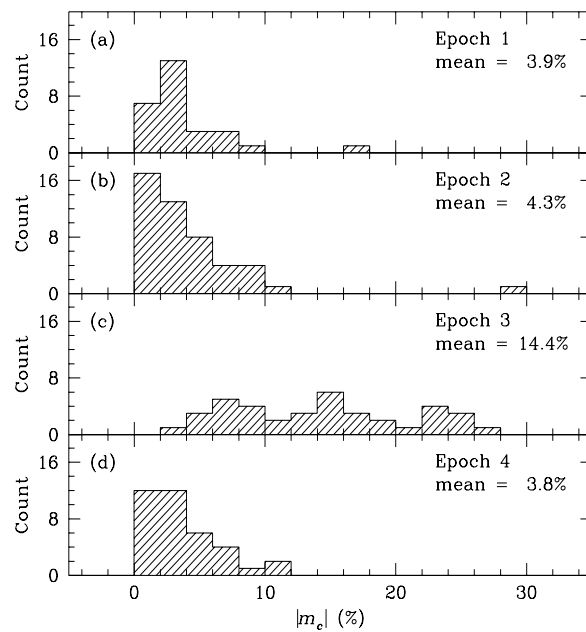


Figure 6.7: Histograms showing the absolute value of the fractional component circular polarization  $|m_c|$  for all four epochs. The mean of each distribution is indicated in the upper righthand corner.

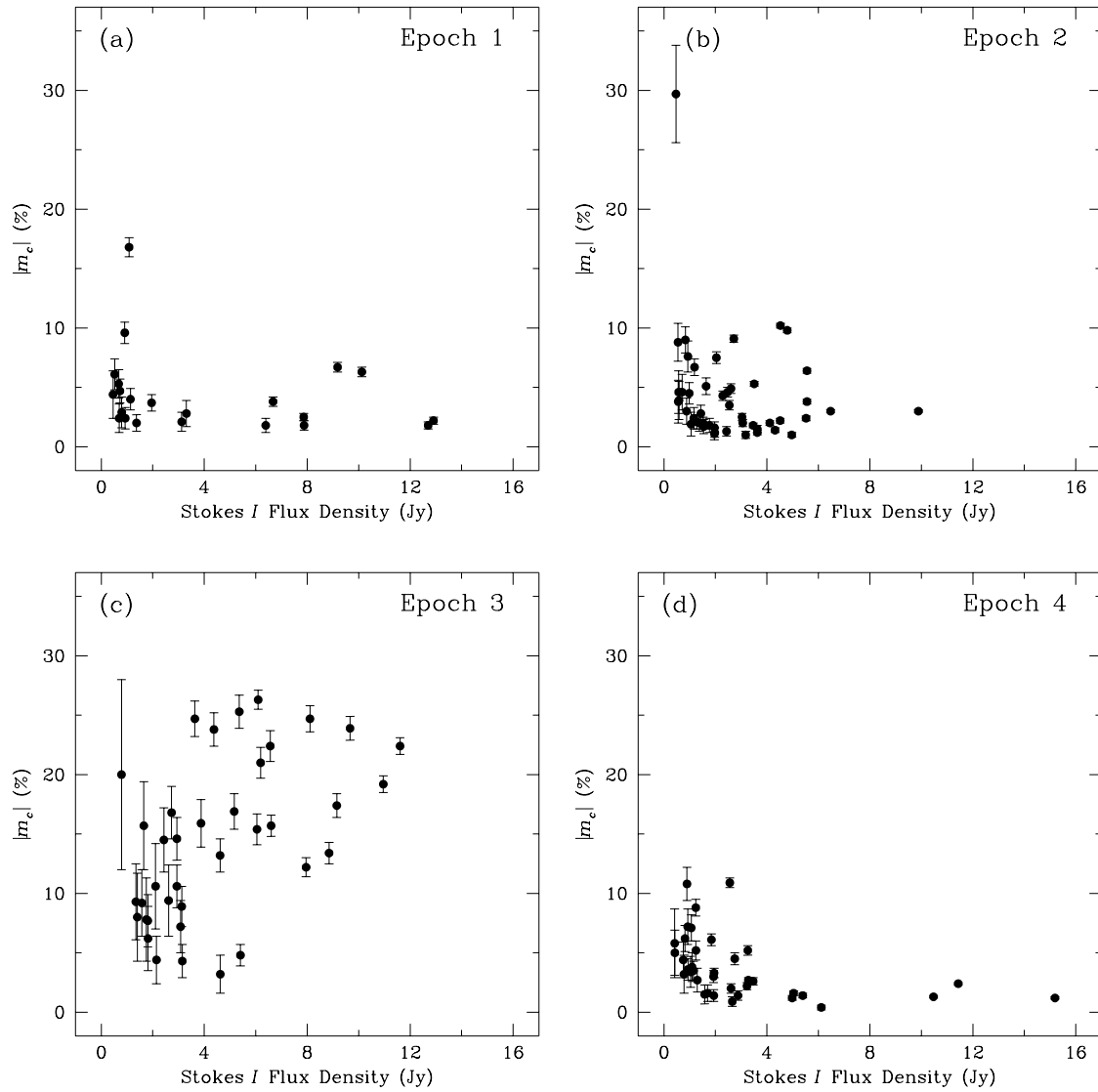


Figure 6.8: Fractional circular polarization  $|m_c|$  plotted against the total intensity (Stokes  $I$ ) flux density for each of the four epochs of observations. Some of the error bars are smaller than the size of the points.

## 6.4 Linear Polarization

### 6.4.1 Fractional Linear Polarization

The distribution of component linear polarization for each of the four epochs is displayed in Figure 6.9. This figure shows that the degree of linear polarization remains relatively constant over the four epochs, with mean values  $m_l \approx 20.8\text{--}25.0\%$ . There are features in each epoch with linear polarizations greater than 50% with a few isolated components reaching as high as  $\sim 83\%$ . The mean and peak linear polarizations found here are consistent with recent VLBI measurements of the SiO maser polarization towards TX Cam (Kemball and Diamond 1997). In addition, single dish observations of the R Aqr SiO emission have found fractional linear polarization ranging from 15–76% (Allen et al. 1989). It is also apparent from this figure that the distribution of the linear polarization for Epoch 3 is similar to those of Epochs 1, 2, and 4 in contrast to what was found for the circular polarization. This might be an indication that the amplitude calibration is correct for Epoch 3 as discussed above.

An interesting aspect of the fractional linear polarization measurements presented here is that the features with the highest fractional linear polarization are relatively weak in total intensity, while many of the stronger features are weakly polarized. This can be seen in Figure 6.10 where the fractional linear polarization has been plotted against the component total intensity. This trend is most evident in Epochs 1 and 4 (Figures 6.10(a), and 6.10(d) respectively) but also appears in Epochs 2 and 3 to a lesser extent. This relatively low percent linear polarization, in components with strong total intensities, has been noted in previous studies. VLBI observations of the SiO masers towards the long-period variable R Cas (McIntosh 1987; McIntosh et al. 1989) and single dish observations of the SiO masers towards R Aqr (Allen et al. 1989; Hall et al. 1990) have also shown this characteristic. It is possible that this is a selection effect since the weaker components, in general, have larger uncertainties. However, the trend seems to persist even after accounting for the larger error bars in the data points with lower intensities.

McIntosh et al. (1989) proposed two potential explanations for this observed characteristic. First, is the possibility of Faraday depolarization due to free electrons within the region of the SiO emission. Features with the highest flux densities probably have the longest gain paths through the medium and therefore greater Faraday rotations. This Faraday rotation causes a reduction in the corresponding fractional linear polarization. The second possible cause of low-polarization high-intensity features is that the higher flux density radiation emerges from less uniform regions, perhaps close to the stellar surface. According to McIntosh et al. these non-uniformities might include the direction and/or magnitude of the magnetic field or the degree of

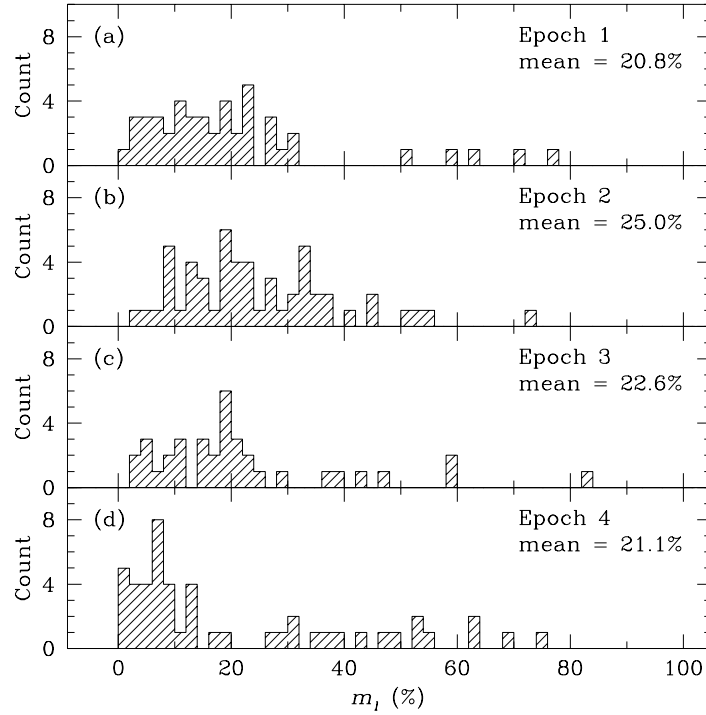


Figure 6.9: Histograms showing the distribution of component linear polarization for all four epochs.

anisotropy in the medium. They also suggest the possibility of blending by overlapping features. These non-uniformities could depolarize the higher flux density features if they are found to reside in this region.

Faraday depolarization has been a topic of recent discussion in the literature. In observations of the SiO emission from *o* Ceti (Mira), McIntosh and Predmore (1993) discovered that the lower frequency transition ( $\nu = 1, J = 1 - 0$ , 43 GHz) exhibited a significantly reduced fractional linear polarization as compared to higher frequency transitions ( $\nu = 1, J = 2 - 1$ , 86 GHz and  $\nu = 1, J = 3 - 2$ , 129 GHz). Elitzur (1992) describes the effects of Faraday rotation on polarized maser emission and shows that the linear polarization can be reduced as the path length through the medium increases. However, Elitzur (1992) does not describe the effect that Faraday depolarization would have on the position angle of the polarized emission. More recently, Wallin and Watson (1997) have investigated the consequences of Faraday rotation through numerical simulations aimed at reproducing the frequency dependent results of McIntosh and Predmore (1993). They find that appreciable Faraday rota-

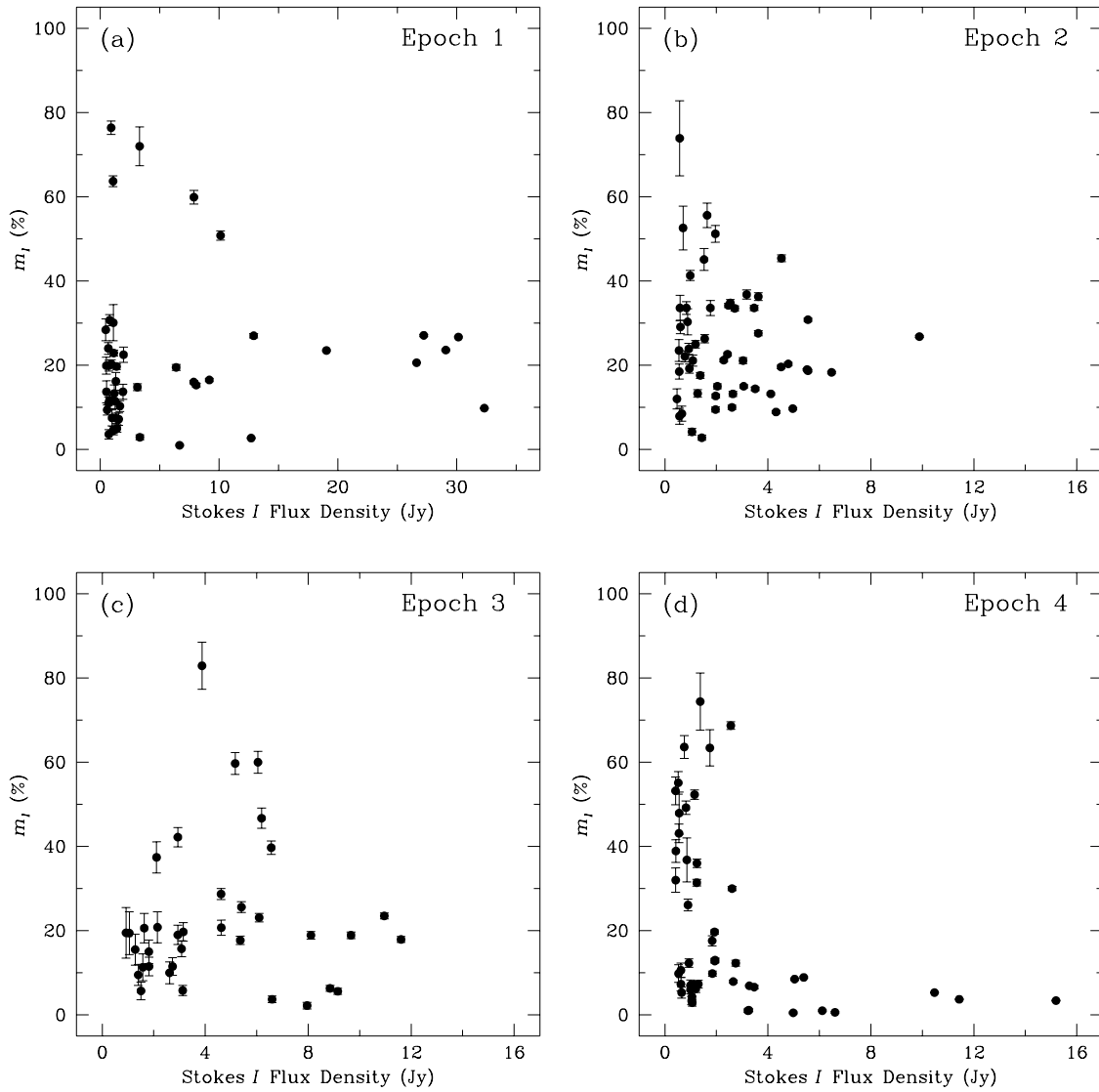


Figure 6.10: Fractional linear polarization  $m_l$  plotted against the total intensity (Stokes  $I$ ) flux density for each of the four epochs of observations. Some of the error bars are smaller than the size of the points.

tion would cause significant rotation of the position angle of the linear polarization and conclude that it would be unlikely if the Faraday rotation were alike in nearby features such that the similarity in position angle would be preserved for nearby components as observed by McIntosh (1987) and McIntosh et al. (1989). In the next section, the position angle of the linear polarization for R Aqr will be discussed in more detail. However, it seems unlikely that Faraday depolarization could cause the observed reduction in fractional linear polarization while sustaining the uniform position angle structure apparent in Figure 6.1 and Figures 6.2–6.5.

From the R Aqr data presented here, it is not possible to either support or refute the latter suggestion of non-uniform regions as the cause for the decrease in fractional linear polarization with increased total intensity. We do not, however, find that the stronger components lie in regions significantly closer to the star (see Figures 5.2–5.5). Also, in the next section, it will become apparent that the linear polarization angle has a uniform distribution over large portions of the SiO maser shell. This suggests that the magnetic field, at least, is fairly uniform over parts of the extended atmosphere of R Aqr. The result that the lower intensity masers often have the highest fractional polarizations is addressed further in § 6.5.

### 6.4.2 Linear Polarization Position Angle

The linear polarization position angle provides information about the local and global structure of the circumstellar magnetic field in the circumstellar envelope of R Aqr. From Figures 6.1–6.5, the linear polarization structure appears to have a mixture of components which are oriented both perpendicular and tangential to the ring forming the distribution. The southwestern (SW) side of the shell is clearly dominated by electric field vectors which are roughly tangential to the maser distribution in Epochs 2, 3, and 4. In contrast, for Epochs 2 and 3, the northeastern (NE) part of the shell is dominated by polarization vectors which are nearly perpendicular to the shell. Epoch 1 appears to have a mixture of both radial and tangential vectors while Epoch 4 has nearly all tangential vectors. There also appears to be an obvious plane of symmetry in Epochs 2 and 3 separating the radial from the tangential polarization structure. This plane coincides with the gap in the maser emission discussed in Chapter 5.

In order to investigate the arrangement of linear polarization vectors in the SiO maser emission towards R Aqr, simulations of purely tangential and purely radial distributions of linear polarization vectors were computed. In addition, a distribution in which the SW shell has purely tangential linear polarization, while the NE shell is purely radial was determined for each epoch. Figures 6.11–6.14 show the observed linear polarization (a) along with each of the three simulations (b), (c), and (d). In all cases, the lengths of the vectors are proportional to the calculated value of the

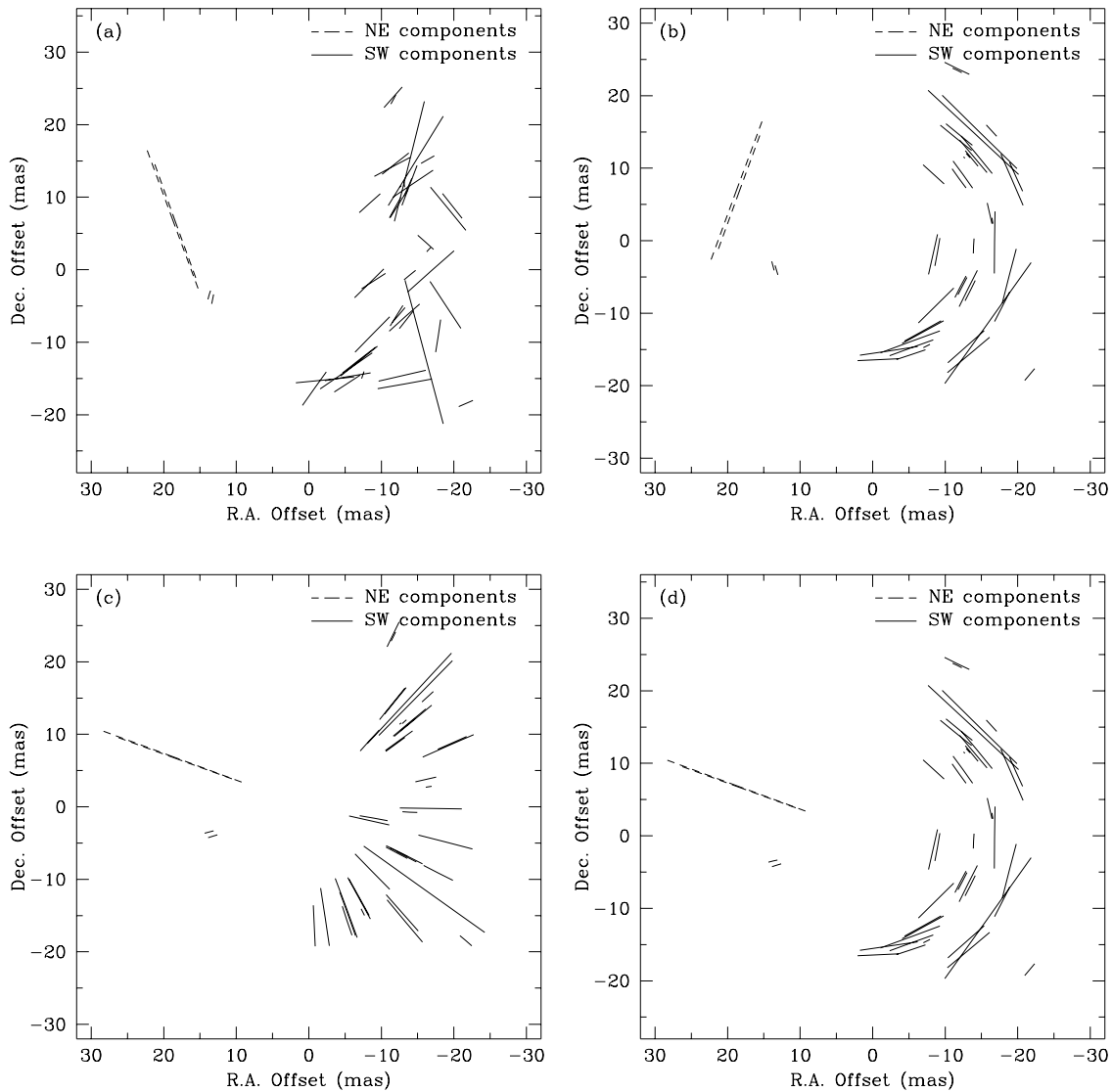


Figure 6.11: Component maps of the linear polarization for Epoch 1. Map (a) shows the true polarization structure. Map (b) shows a simulation of the distribution of the electric field vectors for a purely tangential polarization structure. Map (c) shows a purely radial polarization structure, and map (d) shows a combination of radial and tangential polarization. In each map, the length of the lines indicate the percent linear polarization.

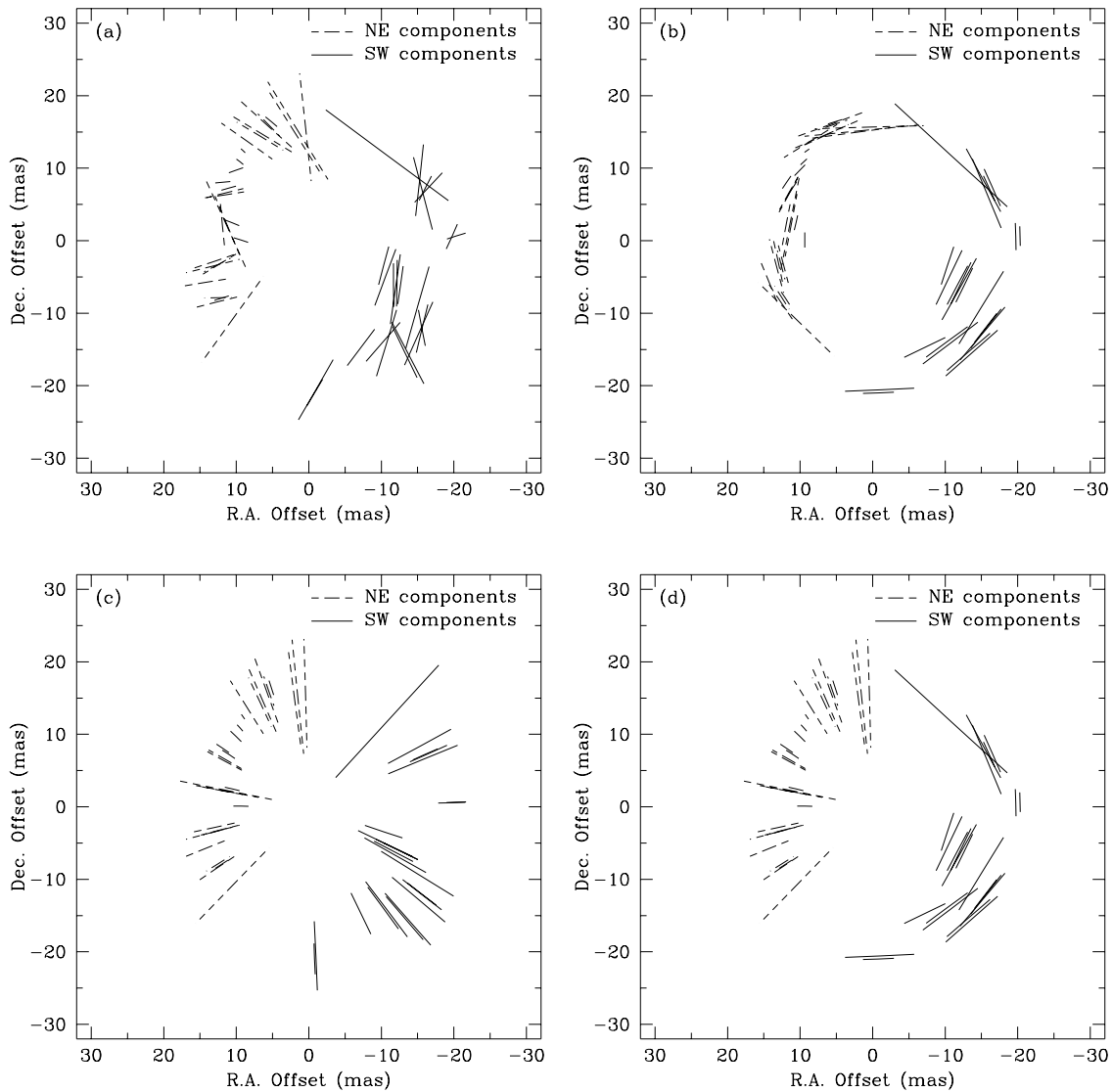


Figure 6.12: Component maps of the linear polarization for Epoch 2. Map (a) shows the true polarization structure. Map (b) shows a simulation of the distribution of the electric field vectors for a purely tangential polarization structure. Map (c) shows a purely radial polarization structure, and map (d) shows a combination of radial and tangential polarization. In each map, the length of the lines indicate the percent linear polarization.

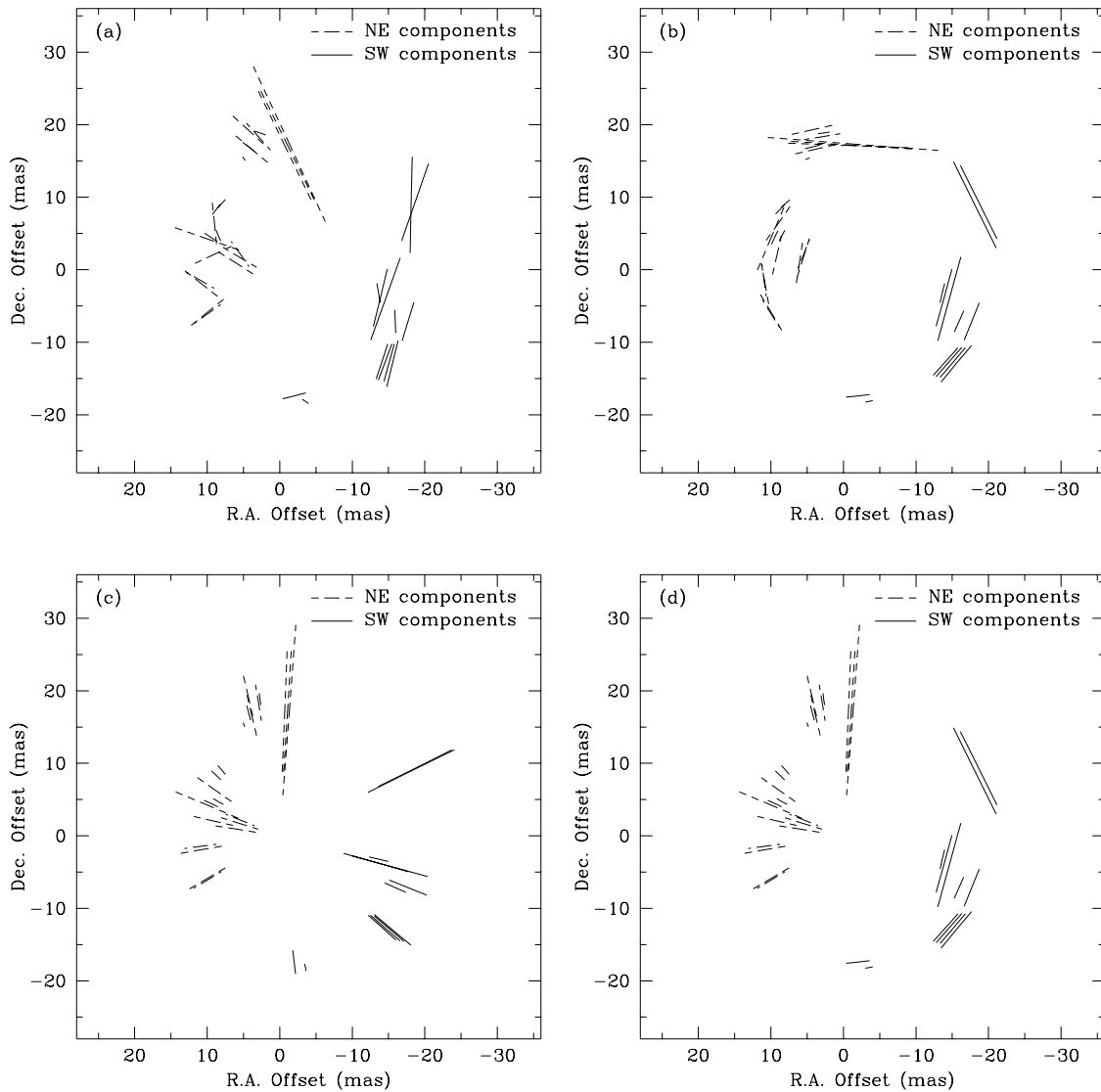


Figure 6.13: Component maps of the linear polarization for Epoch 3. Map (a) shows the true polarization structure. Map (b) shows a simulation of the distribution of the electric field vectors for a purely tangential polarization structure. Map (c) shows a purely radial polarization structure, and map (d) shows a combination of radial and tangential polarization. In each map, the length of the lines indicate the percent linear polarization.

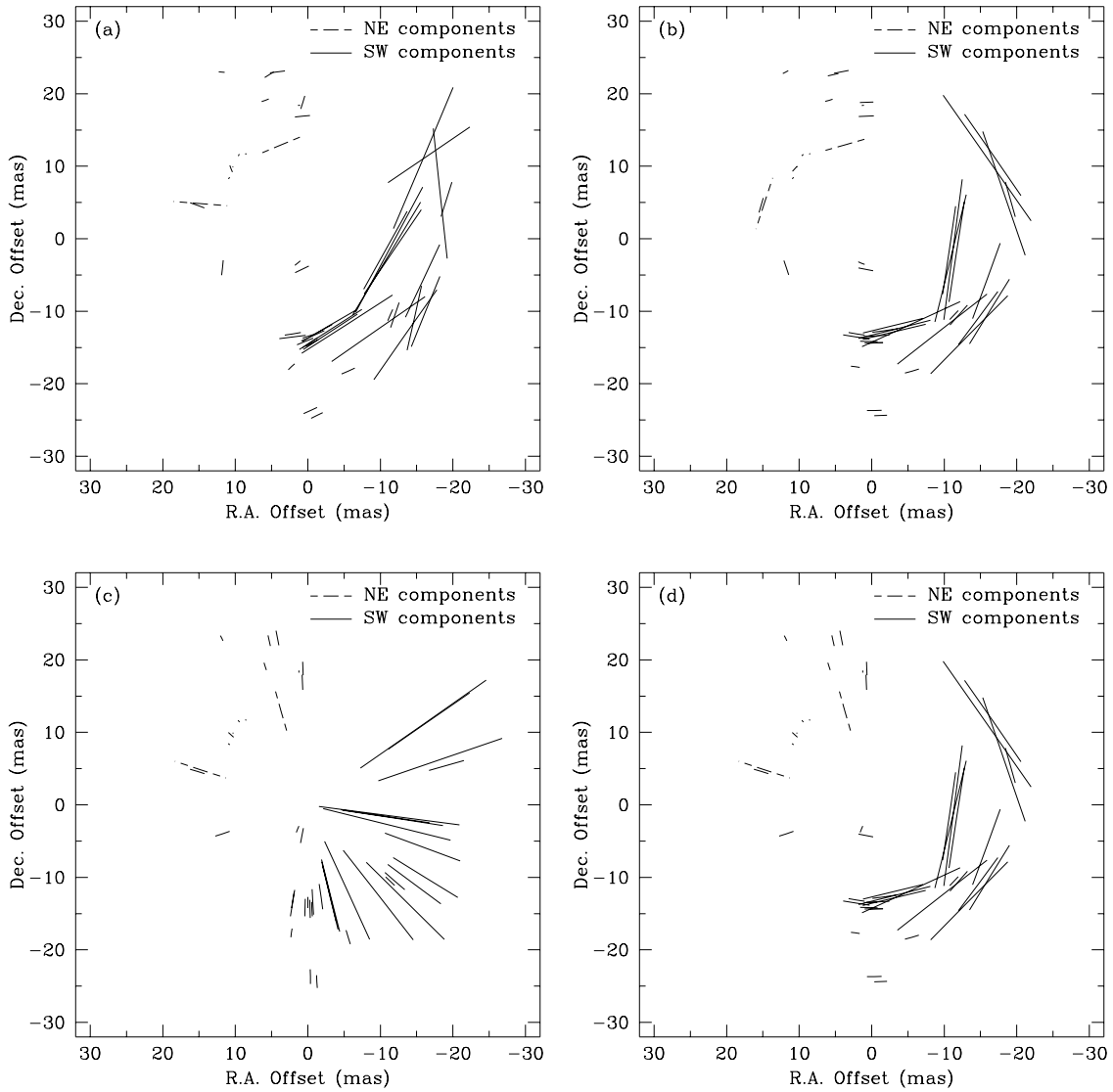


Figure 6.14: Component maps of the linear polarization for Epoch 4. Map (a) shows the true polarization structure. Map (b) shows a simulation of the distribution of the electric field vectors for a purely tangential polarization structure. Map (c) shows a purely radial polarization structure, and map (d) shows a combination of radial and tangential polarization. In each map, the length of the lines indicate the percent linear polarization.

fractional linear polarization. The tangential distribution of simulated vectors, shown in (b) of each figure, was derived by computing the local tangent to the maser shell at each component location. This local tangent  $\psi$  was calculated as the perpendicular to the line connecting the maser component to the mean center of the overall distribution. The radial distributions, shown in (c) of each figure, were formed from vectors which are parallel to this line connecting the component to the mean. The third simulated distribution, displayed in (d) of Figures 6.11–6.14, is simply a combination of the tangential and radial components discussed above. Components in the NE portion of the ring from position angles  $70.1^\circ$ – $250^\circ$  were plotted as radial polarization vectors, and SW components from  $250.1^\circ$ – $360^\circ$  and  $0^\circ$ – $70^\circ$  were plotted as tangential vectors. The component position angle is measured counterclockwise from zero which is due west (negative right ascension). Since Epoch 1 exhibits only an arc of emission, the center of the maser structure derived from the mean, does not reflect the true center position in right ascension. Therefore, the center position used in the simulations of Epoch 1 was arbitrarily offset from the mean by 10 mas in right ascension.

The simulated vectors displayed in each of these figures are meant to aid the eye in distinguishing the linear polarization distribution of the SiO masers towards R Aqr. None of the simulations matches the true morphology for any of the epochs of observation, but in three of the four cases the simulations do bear a striking resemblance to the actual linear polarization. The true arrangement of the linear polarization vectors in Epoch 1 (Figure 6.11(a)) shows little agreement with any of the simulations shown in Figure 6.11. It appears that a simulation in which components at position angles from  $0^\circ$ – $90^\circ$  are distributed radially and those from  $270^\circ$ – $360^\circ$  are arranged tangentially would better explain the morphology of Epoch 1. On the other hand, Epochs 2 and 3 show remarkable agreement between the actual distributions, 6.12(a) and 6.13(a), and the radial-tangential combinations plotted in 6.12(d) and 6.13(d). In Epoch 4, the true distribution most closely resembles the purely tangential structure of Figure 6.14(b). This implies that over the 63 day period between Epochs 3 and 4, the NE portion of the shell has switched from a predominantly radial structure to one with predominantly tangential vectors.

In order to quantify the above impressions of morphology, the absolute value of the difference between the local tangent and the linear polarization vector  $|\chi - \psi|$  was determined for each component and was plotted against the component position angle. Figures 6.15–6.18 show the results of these calculations. All four figures show distributions which are obviously bimodal. Each epoch shows values of  $|\chi - \psi|$  clustered near  $0^\circ$  and near  $90^\circ$  indicating components which have polarization vectors which are parallel and perpendicular to the local tangent respectively. Components were again separated into NE and SW features using the position angles as described above. NE components are plotted as open triangles, and SW components are dis-

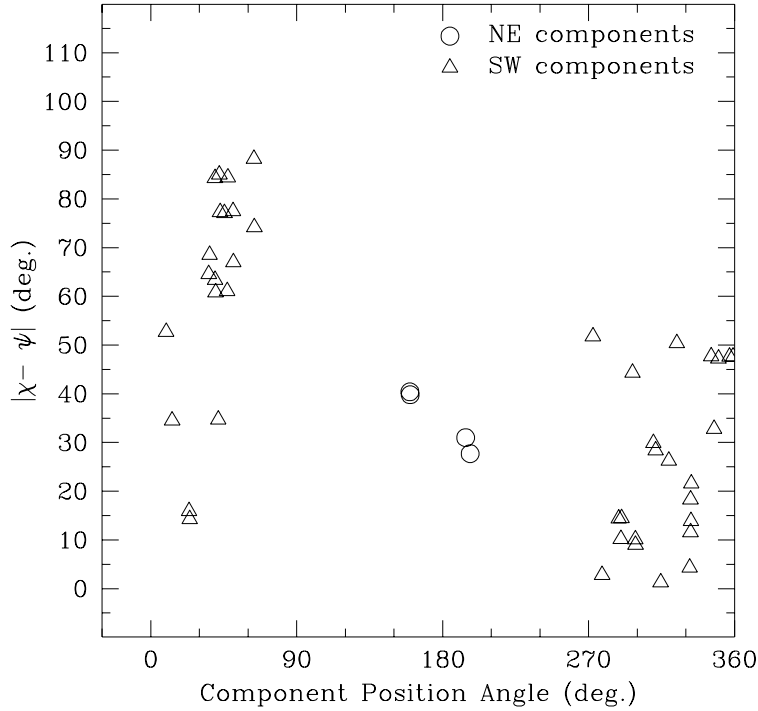


Figure 6.15: Difference between the linear polarization position angle  $\chi$  and the local tangent  $\psi$  plotted against component position angle for Epoch 1. The local tangent is the perpendicular to the radius connecting the mean of the distribution and each component. Since Epoch 1 is a non-symmetric distribution, an additional 10 mas was arbitrarily added to the mean in right ascension. Position angles for the components are measured counterclockwise from zero which is due west (negative R.A. direction).

played as open circles.

Figure 6.15 verifies the impression that the Epoch 1 components from  $0^\circ$ – $90^\circ$  are primarily radial while those from  $270^\circ$ – $360^\circ$  are mostly tangential. The plane of symmetry we adopted for the combined radial–tangential simulations obviously does not apply for Epoch 1. Figures 6.16 and 6.17, however, show that this assumption is correct for Epochs 2 and 3. These figures both show a bimodal distribution which is also separated by position angle. In both epochs the circles (NE components) are clustered near  $|\chi - \psi| \approx 90^\circ$  implying a radial polarization distribution, whereas the triangles (SW components) tend to be near  $|\chi - \psi| \approx 0^\circ$  signifying tangential polarization. In Figure 6.18 (Epoch 4) the conclusion inferred from the comparison of the simulations to the observed distribution is also verified. Here, both the NE and

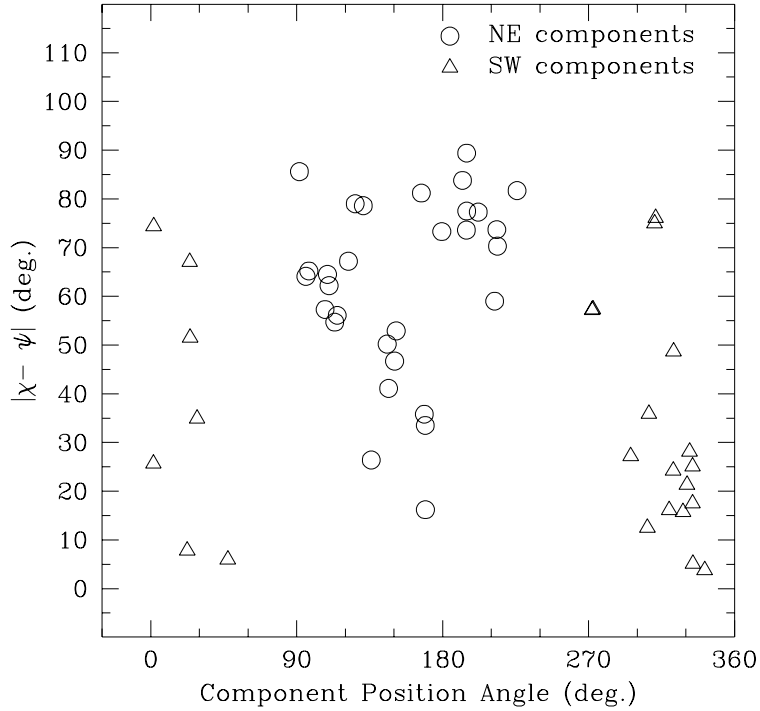


Figure 6.16: Difference between the linear polarization position angle  $\chi$  and the local tangent  $\psi$  plotted against component position angle for Epoch 2. The local tangent is the perpendicular to the radius connecting the mean of the distribution and each component. Position angles for the components are measured counterclockwise from zero which is due west (negative R.A. direction).

SW components are bunched towards  $|\chi - \psi| \approx 0^\circ$  indicating that the polarization is primarily tangential in all regions of the shell. There is a theoretical basis for the finding of this bimodal distribution which will be discussed in the next section.

## 6.5 The Magnetic Field of R Aqr

The polarization structure can reveal some important insights into the circumstellar magnetic field around the Mira in the symbiotic binary R Aqr. The interpretation of the magnetic field strength and structure is subject to the theoretical model employed. There are currently two theories which describe the formation of polarized SiO maser emission. Both of these treatments are based on the fundamental

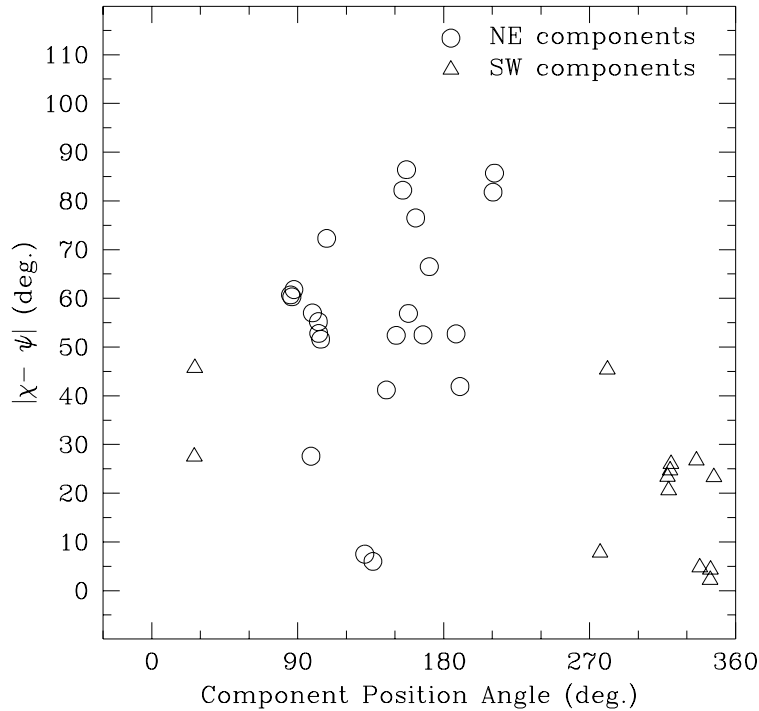


Figure 6.17: Difference between the linear polarization position angle  $\chi$  and the local tangent  $\psi$  plotted against component position angle for Epoch 3. The local tangent is the perpendicular to the radius connecting the mean of the distribution and each component. Position angles for the components are measured counterclockwise from zero which is due west (negative R.A. direction).

work of Goldreich, Keely, and Kwan (1973). The first has been set forth in a series of papers by Elitzur (Elitzur 1991; Elitzur 1993; Elitzur 1996). In these papers, an analytical treatment of maser polarization in the presence of magnetic fields is presented. The most recent work (Elitzur 1996) considers arbitrary absorption coefficients and anisotropic pumping of the maser radiation. The second treatment of maser polarization is described in a series of works by the group at the University of Illinois (Western and Watson 1984; Deguchi, Watson, and Western 1986; Deguchi and Watson 1986; Nedoluha and Watson 1990; Nedoluha and Watson 1994; Wallin and Watson 1995). These studies are based on numerical computations in which the differential equations of radiative transfer are integrated allowing the investigators to follow the growth of the maser polarization over a wide range of parameters. The above descriptions grossly understate the great complexity involved in the two different theoretical treatments of maser polarization. For a more detailed description, the

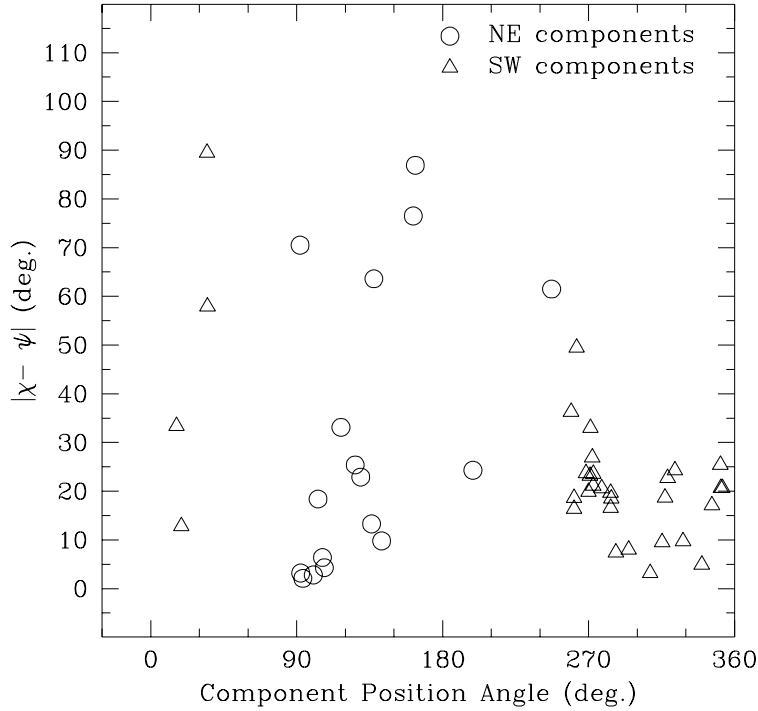


Figure 6.18: Difference between the linear polarization position angle  $\chi$  and the local tangent  $\psi$  plotted against component position angle for Epoch 4. The local tangent is the perpendicular to the radius connecting the mean of the distribution and each component. Position angles for the components are measured counterclockwise from zero which is due west (negative R.A. direction).

reader is referred to the works referenced above.

The observations presented in this thesis cannot distinguish between these two theoretical models of maser polarization, however, some important conclusions can be drawn from this work. In the model of Nedoluha and Watson (1994) circular polarization can be generated by linear polarization as it propagates through an anisotropic medium if the polarization direction is not aligned with one of the principal optical axes of the medium. Although they are not necessary for the formation of circular polarization, anisotropic pumping, incident linearly polarized radiation, or a change in direction of the magnetic field can provide a significant enhancement of the circularly polarized radiation that is created in this process. The intensity-dependent circular polarization resulting from this effect is not strongly dependent on the strength of the magnetic field, therefore, the circular polarization observations

presented here cannot be used to distinguish between fields on the order of several milliGauss and fields on the order of several Gauss in the context of this model.

Since the circular polarization is created by the propagation of the linear polarization in this model, one might expect the linear and circular polarization to be correlated. There is little evidence in the data presented here that the linear and circular polarization are correlated. Figure 6.19 plots the fractional linear polarization  $m_l$  against the fractional circular polarization  $|m_c|$  for each of the four epochs. In the upper righthand corner of each plot are the two different measures of the correlation of the two distributions. The first is the Pearson linear correlation coefficient  $r_p$ . The second is the Spearman rank-order correlation coefficient  $r_s$ . For both correlation coefficients, values of +1 or -1 indicate complete correlation or anti-correlation respectively. Values near zero indicate that  $m_l$  and  $|m_c|$  are uncorrelated. From the values listed in each figure it is clear that the two distributions are uncorrelated.

Nedoluha and Watson (1990) find that the linear polarization position angle can vary with the stimulated emission rate, but this effect is highly dependent on the magnetic field strength and the anisotropy in the pumping. In addition, the stimulated emission rate cannot be directly related to the intensity due to the uncertainty in the effect of beaming (Nedoluha and Watson 1990). Nevertheless, the finding of uniform tangential linear polarization over the SW portion of the R Aqr maser shell in multiple epochs seems to argue against randomly distributed linear polarization vectors.

The model presented in Nedoluha and Watson (1990) does provide an explanation for the observation that the lower intensity masers often have the highest fractional linear polarizations. They suggest that the low-intensity high-polarization features are probably unsaturated with large angles between the direction of propagation and the direction of the magnetic field. Alternatively, the high-intensity low-polarization features could be saturated with propagation angles close to the direction of the magnetic field. Again, the uniform position angles observed for the linear polarization are difficult to resolve in this situation. Nedoluha and Watson (1994) state that there is a tendency for the linear polarization to rotate by a few tens of degrees when the ratio of the stimulate emission rate  $R$  to the decay rate  $\Gamma$  changes by an order of magnitude. If saturation (which is indicated by  $R/\Gamma$ ) were the cause of the decreased fractional polarization then one might expect a more random distribution of linear polarization vectors.

Predictions for the magnetic field strength can be made from the circular polarization data presented here if we assume the model described in Elitzur (1996). An important parameter in the analytical treatment is the dimensionless parameter  $x_B$ , which is the ratio of the Zeeman splitting  $\Delta v_B$  to the Doppler linewidth  $\Delta v_D$ . Previous theoretical work considered only two limiting cases for  $x_B$ : the first case is

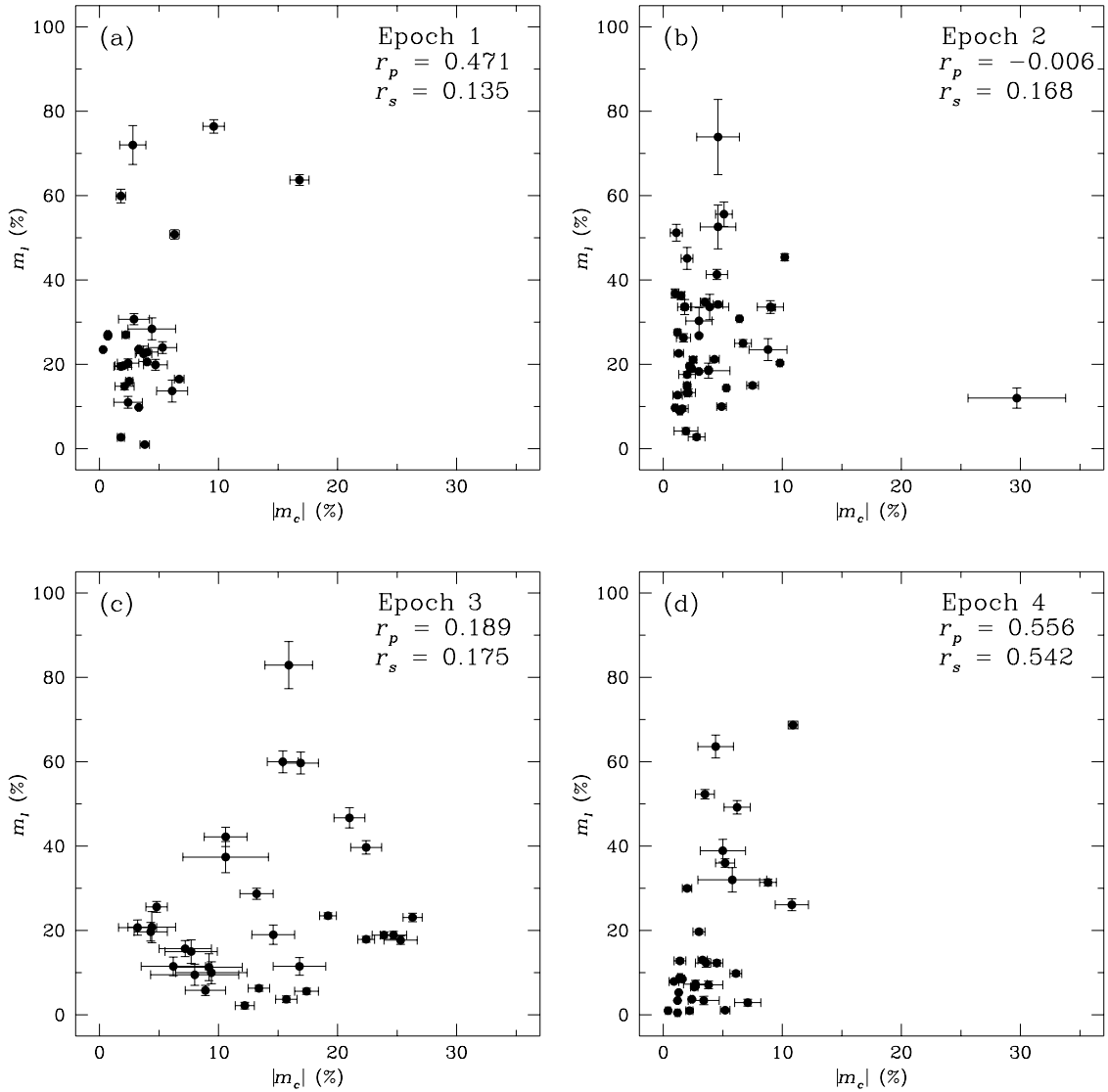


Figure 6.19: Fractional linear polarization  $m_l$  plotted against the fractional circular polarization  $|m_c|$  for each of the four epochs of observations. Some of the error bars are smaller than the size of the points. In the upper righthand corner of each plot are the Pearson linear correlation coefficient  $r_p$  and the Spearman rank-order correlation coefficient  $r_s$ . Values of +1 or -1 indicate complete correlation or anti-correlation respectively. Values near zero indicate that  $m_l$  and  $|m_c|$  are uncorrelated.

when the Zeeman splitting is greater than the Doppler linewidth ( $x_B \gg 1$ ) approximated by  $x_B \rightarrow \infty$ ; the second case is the situation in which the Zeeman components overlap ( $x_B < 1$ ) approximated by the unphysical limit  $x_B = 0$ . Elitzur (1996) extended the theory to include the case in which  $x_B \rightarrow 0$  without assuming  $x_B = 0$  at the outset. This work verifies the previous finding of significant linear polarization (Goldreich, Keely, and Kwan 1973), but also predicts that this linear polarization can be accompanied by circular polarization.

The ratio of the Zeeman splitting to the Doppler linewidth is related to the magnetic field in Elitzur (1996) by

$$x_B = 14g\lambda \frac{(B/\text{Gauss})}{(\Delta v_D/\text{km s}^{-1})}, \quad (6.12)$$

where  $g$  is the Landé factor and  $\lambda$  is the transition wavelength in centimeters. For the  $v = 1$  state of SiO, the Landé factor  $g = -0.1545$  (McIntosh 1987). This factor should be multiplied by the ratio of the Bohr magneton to the nuclear magneton in the above relationship since SiO is a non-paramagnetic molecule. At the wavelength of the  $v = 1, J = 1 - 0$ , 43-GHz SiO transition ( $\lambda \approx 0.7$  cm), the expression for  $x_B$  becomes

$$x_B = 8.2 \times 10^{-4} \frac{(B/\text{Gauss})}{(\Delta v_D/\text{km s}^{-1})}, \quad (6.13)$$

as derived in Kemball and Diamond (1997). Elitzur (1996) also relates  $x_B$  to the degree of circular polarization  $V/I$  in the case where the Zeeman splitting is less than the Doppler width ( $x_B < 1$ ) through

$$x_B = \frac{3\sqrt{2}}{16} \frac{V}{I} \cos \theta, \quad (6.14)$$

where  $\theta$  is the angle between the line of sight and the direction of the magnetic field. Combining equations 6.13 and 6.14 we can derive an expression for the magnetic field strength in terms of the fractional circular polarization  $m_c$  and the Doppler width which is given by

$$(B/\text{Gauss}) \sec \theta = 3.2m_c(\Delta v_D/\text{km s}^{-1}). \quad (6.15)$$

This relationship was first expressed in Kemball and Diamond (1997).

In § 6.3 mean circular polarization was found to be in the range of 3.9–4.3% for Epochs 1, 2, and 4. A fractional circular polarization of 4% implies a magnetic field  $B \sec \theta \approx 13$  G if a Doppler linewidth  $\Delta v_D \approx 1$  km s<sup>-1</sup> is assumed. For Epoch 3, a mean circular polarization  $m_c = 14.4\%$  was determined. This fractional circular polarization implies a magnetic field  $B \sec \theta \approx 46$  G. From equation 6.14, the Zeeman

splitting corresponding to these magnetic field strengths can be computed, again assuming a Doppler linewidth of  $\sim 1 \text{ km s}^{-1}$ . The calculated values are  $\Delta v_B \approx 0.01 \text{ km s}^{-1}$  for a  $B$  field strength of 13 G and  $\Delta v_B \approx 0.04 \text{ km s}^{-1}$  for a 46 G magnetic field. These line splittings are much smaller than the channel spacing in this experiment which could explain the lack of components showing the traditional anti-symmetric S-shaped Zeeman pattern in these observations, even for Epoch 3 where the magnetic field is extremely high.

This lack of components exhibiting the typical Zeeman pattern in the polarization data for R Aqr is relatively common in SiO maser observations. The symmetry-breaking required to change the Stokes  $V$  profile in the Elitzur (1996) model cannot be performed in a quiescent medium or with a uniform magnetic field. Elitzur (1996) suggests that the various filter mechanisms (magnetic and/or velocity gradients) employed by the Illinois group, could be integrated into his model to remove one component from the S-shaped profile.

The polarization model investigated by Elitzur also provides a prediction for the relationship between the position angle of the linear polarization  $\chi$ , and the direction of the projected magnetic field  $\gamma_B$ . The relationship between these two quantities is dependent on  $\theta$ , the angle between the magnetic field direction and the observer's line of sight. This connection is such that  $\chi$  is parallel to  $\gamma_B$  for  $\sin^2 \theta < 2/3$  ( $\theta < 55^\circ$ ) and  $\chi$  is perpendicular to  $\gamma_B$  for  $\sin^2 \theta > 2/3$  ( $\theta > 55^\circ$ ) Elitzur (1992). The more recent work of Elitzur (1996) shows that there are no stationary physical solutions for the propagation of polarized maser radiation for  $\sin^2 \theta < 1/3$  ( $\theta < 35^\circ$ ).

The linear polarization position angles discussed in the previous section show that the distribution is primarily bimodal, with large portions of the shell having either radial or tangential electric field vectors. The relationships between  $\chi$  and  $\gamma_B$  as determined by  $\theta$  indicate that the projected magnetic field is either parallel or perpendicular to the linear polarization vectors. The overall tangential structure in the SW portion of the ring implies a magnetic field which is primarily radial in nature over that part of the shell. The radial vectors towards the NE portion of the shell suggest that the projected magnetic field is roughly tangential to the ring in this region during Epochs 2 and 3.

The linear polarization structure resulting from various magnetic field geometries have been investigated by Kembal and Diamond (1997). For a purely radial magnetic field (for which  $\theta > 55^\circ$ ), a tangential polarization structure would be observed over the entire ring of emission for any arbitrary stellar orientation. For a toroidal magnetic field confined to the surface of the extended atmosphere, tangential polarization is created for less than  $\sim 33\%$  of the shell. Kembal and Diamond do find that, for a dipole field confined to the surface of the extended atmosphere, inclinations of  $\sim 40\text{--}60^\circ$  with respect to the line of sight can produce tangential polarization structure

over 40–66% of the maser shell with  $\theta < 55^\circ$ . As the inclination angle is increased the polarization structure becomes predominantly radial for  $\theta > 55^\circ$ .

Examining the changing polarization structure obtained in Epochs 1–4, it is obvious that the geometry and the strength of the magnetic field must be highly dynamic. The western portion of the shell changes from a mixture of radial and tangential polarization to one of primarily tangential polarization over a time period of  $\sim 6$  months. Over the 63 days separating Epochs 3 and 4, the NE side of the shell switches from primarily radial to primarily tangential linear polarization. Surprisingly, there is little change in the linear polarization between Epochs 2 and 3. This is the time period in which the fractional circular polarization has grown from a mean of 4.3% to a mean of 14.4%. This rapid change in the magnetic field should perhaps be seen in the proper motions of the SiO masers discussed in Chapter 5. It should be noted that the field strengths estimated above are highly dependent on the  $\sec \theta$  term. For large angles of  $\theta$ , a change of only  $10^\circ$  can produce the observed change in  $B \sec \theta$ , however,  $\theta < 45^\circ$  is required to explain fractional linear polarization in excess of 33% (Elitzur 1992).

Barvainis, McIntosh, and Predmore (1987) determined that for a field of 50 G, the magnetic field energy density is  $\sim 10^6$  times the thermal energy density of the gas. Thus, the magnetic field should dominate the motions in the gas. The magnetic field energy density  $\varepsilon_B$  can be computed using

$$\varepsilon_B = \frac{B^2}{8\pi}. \quad (6.16)$$

For magnetic field strengths of 13 G and 46 G (determined by applying the model of Elitzur (1996) to the R Aqr fractional circular polarizations),  $\varepsilon_B$  has values roughly equal to  $7 \text{ erg cm}^{-3}$  and  $84 \text{ erg cm}^{-3}$  respectively. The gas velocities implied by these magnetic field energy densities can be computed by setting  $\varepsilon_B$  equal to the kinetic energy density  $\varepsilon_{KE}$  given in Barvainis, McIntosh, and Predmore (1987) as

$$\varepsilon_{KE} = \frac{1}{2} n_H m_H v^2. \quad (6.17)$$

Setting  $\varepsilon_B = \varepsilon_{KE}$  the velocity due to the magnetic field pressure (which is equivalent to the Alfvén wave velocity  $v_A$ ) can be determined using

$$\left( \frac{v_A}{\text{km s}^{-1}} \right) = 10^{-5} \sqrt{\frac{B^2}{4\pi n_H m_H}}. \quad (6.18)$$

In the equations listed above, the gas is assumed to consist primarily of neutral hydrogen where  $n_H \approx 10^9 \text{ cm}^{-3}$  (Barvainis, McIntosh, and Predmore 1987). For the previously determined magnetic fields of 13 G and 46 G, the Alfvén wave speeds are  $\sim 900 \text{ km s}^{-1}$  and  $\sim 3200 \text{ km s}^{-1}$  respectively. It is quite obvious that magnetic fields

of this strength should dominate the dynamics of the extended atmosphere, but the effects of these fields are not apparent in the proper motion study of R Aqr presented in Chapter 5.

# Chapter 7

## CONCLUSIONS

“We are here to make history, neither to ignore the past nor to turn back to the past, but to move forward in a way that opens up new vistas for the future.”

*Richard Nixon, Seize the Moment*

This work has described the results and interpretations for a spectral line VLBA observing program undertaken to image the  $v = 1, J = 1 - 0$ , 43-GHz SiO maser emission towards R Aqr. These are the first multi-epoch, high-resolution total intensity and polarization images of the extended atmosphere of a long-period variable in a symbiotic binary. This chapter presents a summary of the results in §7.1 and the possibilities for future work in § 7.2.

### 7.1 Summary of Results

In Chapter 1 a series of goals were outlined for this dissertation project. In this section, the results of this dissertation are summarized within the context of these goals. The primary aims of this dissertation were as follows:

**1. To map the circumstellar SiO maser emission towards R Aquarii at high resolution, and to compare the resulting images to the ring-like structures exhibited by isolated late-type stars previously studied.**

The first high-resolution VLBI images of the circumstellar SiO maser emission towards the symbiotic Mira R Aqr have been presented. These images demonstrate that the SiO masers form a ring-like structure similar to previously studied isolated

evolved stars. The SiO maser shell has an estimated diameter of  $\sim 31$  mas. With a projected radius of  $\sim 3.4$  AU, the maser emission lies outside the radius of the stellar photosphere, which is estimated to be  $\sim 1.8$  AU (van Belle et al. 1996) and well within the estimated radius of the circumstellar dust shell at  $\sim 15.4$  AU (Danchi et al. 1994). Figure 7.1 shows a diagram of the R Aqr system as it appears projected onto the sky. The schematic is based on information from this thesis and the references previously cited. Although the companion appears to be inside the circumstellar dust shell, this is simply a projection effect resulting from the two-dimensional representation of a three-dimensional system. In the diagram, the SW jet has been left off for the purpose of clarity.

The emission in the total intensity images shows a slight elongation in the N–S direction. The final three epochs of observations show a gap in the SiO maser emission at an angle of  $\sim 65^\circ$  to the horizontal. This gap could possibly be related to the R Aqr jet which is thought to emerge from the hot companion at an angle of  $\sim 135^\circ$  roughly perpendicular to the gap. The jet is thought to be formed by accretion of the Mira’s stellar wind onto the companion. If the orbit of the companion is perpendicular to the jet then it is possible that the gap in the SiO maser emission is related to the formation of the accretion disk powering the jet.

The existence of a coherent ring of maser emission implies that the companion is unable to dissociate the SiO molecules which are protected by the circumstellar dust shell. Since R Aqr is one of only two symbiotics which exhibit SiO maser emission (the other is H1-36 Arae) there must be something unique which prevents the companion from disrupting the maser shell. Possible explanations which have been previously presented are that the binary orbits for these two symbiotics are sufficiently large such that the companion is too far away to significantly effect the Mira, or that the companion’s stellar wind is simply too weak to push back the Mira’s wind exposing the inner envelope to the UV photons of the hot companion. It is obvious from our observations that some mechanism must be preventing the companion from dissociating the SiO molecules over the entire inner envelope of R Aqr.

**2. To monitor changes in the structure of the maser emission in time, and to compare the structure sampled at various phases in the Mira’s stellar cycle.**

The SiO maser emission towards R Aqr has been observed at four different epochs. These epochs correspond to phases  $\phi \approx 0.31, 0.78, 0.87,$  and  $0.04$  in the stellar pulsation cycle. Although the frequency and spacing of these observations was far from optimal, some valuable insights may still be gained from this multi-epoch approach. From this study, it is evident that the structure of the emission changes rapidly over the stellar cycle. The total intensity images show significant flux density

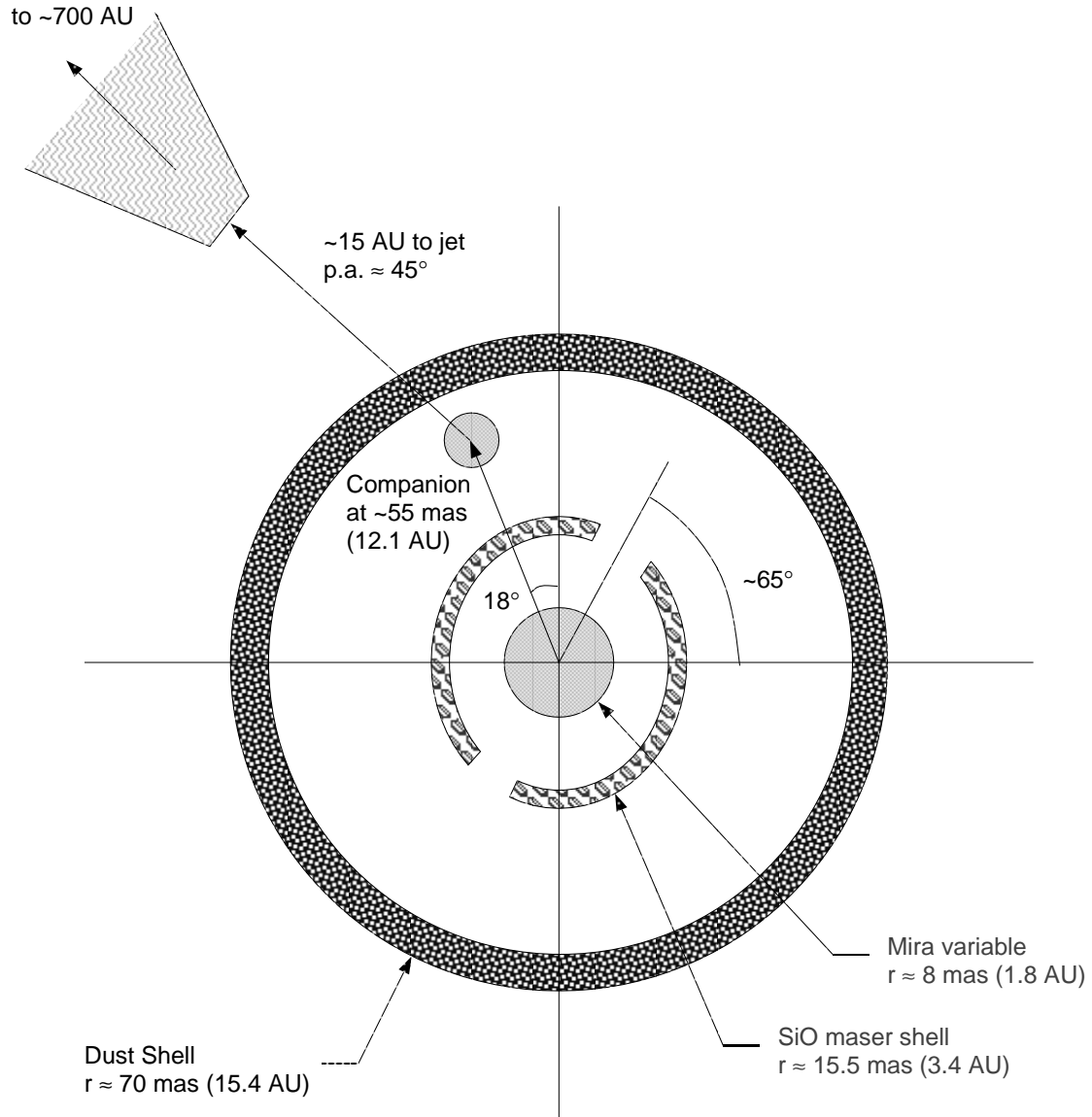


Figure 7.1: Diagram showing the R Aqr system from information derived in this work and the references cited in the text. The system is shown as it appears projected onto the sky. Distances are not to scale and the southern jet is not shown for the purpose of clarity.

variations over timescales as short as  $\sim 1$  month. In addition, there is very little similarity in the structure over the  $\sim 6$  month interval spanning Epochs 1 and 2. Although this time variability is evident in the spectra for each epoch, changes in the spatial structure of the emission would not be observed if it were not for the high-resolution imaging capability of the VLBA.

Due to the limited time sampling of the SiO emission in this experiment, these data are not able to verify the previously cited phase lag  $\sim 0.1\text{--}0.2$  (Martínez, Bujarrabal, and Alcolea 1988) between the visual stellar magnitude and the SiO maser flux density. However, we do find that the flux density for Epoch 1, observed during the post-maximum phase of the Mira, is significantly greater than the flux densities observed for Epochs 2, 3, and 4, taken after the Mira had gone through a stellar minimum ( $\phi = 0.5$ ) perhaps indicating a lag in the phase.

**3. To determine the proper motion of individual maser spots and the motion of the masing region as a whole. It is unknown whether the masers lie in a region of outflow or inflow and what effect the pulsations of the Mira have on this region.**

Through the multi-epoch observations presented in this dissertation, the first detection of circumstellar SiO maser proper motions has been made. The surprising result is that the masers are actually found to be falling inward at a velocity of  $\sim 4 \text{ km s}^{-1}$ . This overall contraction of the R Aqr SiO maser shell has been verified using the following three methods:

1. The computation of the proper motion vectors for individual features common to Epochs 2 and 4.
2. The calculation of pairwise separations over the three time periods separating Epochs 2, 3, and 4.
3. The least squares fitting of a circle to the Epoch 2, 3, and 4 data for those features common to all three epochs.

The infall of material within the circumstellar dust shell has been proposed by Hinkle, Hall, and Ridgway (1982). They suggested a scenario in which an outwardly propagating shock, driven by the stellar oscillation, passes through the extended atmosphere between premaximum and post-maximum phases ( $\phi \approx 0.8\text{--}0.1$ ). Once the shock has passed, the material in the extended atmosphere can fall inward under the influence of gravity from  $\phi \approx 0.1\text{--}0.8$ . The numerical work of Bowen (1988) demonstrates that the shock passage can occur later and that the infall can extend beyond phase 0.8 for the outer portions of the extended atmosphere. The observations presented in this thesis confirm that there is a period of material infall in the stellar

cycle. The circumstellar SiO maser emission towards R Aqr has been found to contract through phases 0.78, 0.87, and 0.04 at an infall speed which can be easily explained assuming only gravitational infall. The determined infall velocities are also consistent with the shock velocity of  $\sim 5 \text{ km s}^{-1}$  determined by Reid and Menten (1997) for the region outside  $\sim 2 R_*$ .

**4. To determine the polarization structure of the R Aquarii SiO maser emission, and to image the magnetic field in the stellar atmosphere close to the Mira.**

The circular and linear polarization morphology of the SiO maser emission towards R Aqr has been imaged for the first time. The mean fractional circular polarization for Epochs 1, 2, and 4 has been found to range from 3.8% to 4.3% with peak circular polarizations as high as  $\sim 30\%$ . The circular polarization for Epoch 3 was determined to be much higher than the other three epochs, with component polarizations ranging from 3% to 26% and a mean value of  $\sim 14.4\%$ . Assuming the model for polarized maser radiation of Elitzur (1996), a mean circular polarization of  $\sim 4\%$  implies a magnetic field strength  $B \sec \theta \approx 13 \text{ G}$  and a mean circular polarization of 14.4% yields a field strength  $B \sec \theta \approx 46 \text{ G}$ . If the model for circularly polarized emission of Nedoluha and Watson (1994) is assumed, no distinction can be made from these observations between magnetic fields on the order of several milliGauss or several Gauss.

In the context of the Elitzur (1996) model, the magnetic fields determined above yield Zeeman splittings of  $\Delta v_B \approx 0.01 \text{ km s}^{-1}$  and  $\Delta v_B \approx 0.04 \text{ km s}^{-1}$  for 13 G and 46 G respectively. Despite the implied magnetic fields, there are no obvious Zeeman pairs in the Stokes  $V$  images of the SiO emission towards R Aqr. This result is common in SiO polarization observations. The various filter mechanisms employed in the model from the group at the University of Illinois (e.g. gradients in the magnetic field or the velocity) have been used to explain this removal of one of the Zeeman components.

The linearly polarized emission from the SiO masers towards R Aqr has also been mapped and individual component polarizations computed. The levels obtained for linear polarization of R Aqr have been found to be consistent with VLBI observations of the isolated Mira variable TX Cam (Kemball and Diamond 1997), and single dish observations of R Aqr (Allen et al. 1989). The mean fractional linear polarization for the four epochs ranges from 20.8–25.0% with isolated features having peak values as large as  $\sim 83\%$ . The calculated component linear polarizations have the peculiar characteristic that the high flux density features have relatively low fractional linear polarization. This property has also been observed in VLBI observations of R Cas (McIntosh 1987; McIntosh et al. 1989) and in single dish observations of R Aqr (Allen et al. 1989; Hall et al. 1990). There are several proposed explanations

for this decreased fractional polarization including Faraday depolarization. There is little evidence in the data here to support any of the suggested possibilities for the depolarization. However, the fact that uniform linear polarization position angles are observed over large portions of the maser shell seems to argue against Faraday rotation or non-uniformities in the maser region as causes for the depolarization of high-intensity features.

As mentioned above, the linear polarization vectors have a uniform structure over large sections of the ring of emission. This property of the linearly polarized emission has also been observed for the isolated Mira TX Cam (Kemball and Diamond 1997). The position angle distributions for each epoch have been found to be bimodal with values which are roughly parallel or perpendicular to the local tangent to the maser shell. The polarization model of Elitzur (1996) predicts that for magnetic field directions within  $35^\circ$  of the line of sight, the maser emission is unpolarized. When  $\theta$  (the angle between the line of sight and the direction of the magnetic field) is greater than  $35^\circ$ , two possible orientations for the polarization direction  $\chi$  and the projected magnetic field direction  $\gamma_B$  are predicted. These orientations are: for  $\theta > 55^\circ$ ,  $\chi \perp \gamma_B$  and for  $\theta < 55^\circ$ ,  $\chi \parallel \gamma_B$ . The theory therefore implies that the magnetic field is roughly perpendicular to the shell in regions where the polarization is tangential and roughly tangential in regions where the polarization is radial.

**5. To monitor the variations of the polarization structure as a function of time, and to determine the time evolution of the circumstellar magnetic field.**

The time evolution of the polarization structure of R Aqr has been observed in the limited sampling provided by these observations. The polarization morphology has been found to change significantly over time periods as short as  $\sim 1$  month. The polarization distribution mapped in Epoch 1 bears little resemblance to that of Epoch 2 observed  $\sim 6$  months later. There is an apparent plane of symmetry in the linear polarization distribution exhibited in Epochs 2 and 3 which is aligned with the gap in the emission. This plane was used to divide the emission into northeastern (NE) components and southwestern (SW) components. Components on the NE side of the ring have predominantly radial polarization vectors while the SW portion of the ring is primarily tangential. Over the 63 day interval between Epochs 3 and 4, the NE portion of the shell shifts from predominantly radial to predominantly tangential polarization.

These shifts in the linear polarization structure imply large scale changes in the magnetic field geometry. The change in circular polarization by a factor of  $\sim 4$  over the 35 day time period from Epoch 2 to Epoch 3 suggests a large magnetic field strength increase, although this increase could be due to a change in the direction of the magnetic field relative to the line of sight ( $\sec \theta$  dependence). Barvainis, McIn-

tosh, and Predmore (1987) have shown that the magnetic field energy density should dominate the dynamics of the extended atmospheres of these objects. The increase in magnetic field strength indicated by the change in circular polarization from Epoch 2 to Epoch 3 should be observed in the proper motion measurements of the SiO masers towards R Aqr. No such evidence for magnetic field driven motion has been found in these observations.

## 7.2 Future Work

The prospects for future work in the field of high-frequency VLBI imaging are extremely promising. The addition of the 7 mm receivers to the VLBA has allowed observers to image the 43-GHz SiO maser emission towards late-type stars. These masers lie within  $\sim 2$ – $4$  stellar radii of the center of the star. Thus, SiO masers provide a unique probe of the physical characteristics in the dynamic region close to the stellar surface. The Coordinated Millimeter VLBI Array (CMVA) and the future installation of 3 mm receivers on the VLBA will extend this capability to even higher frequencies.

This dissertation has presented the results of a series of 43-GHz SiO maser observations towards the symbiotic Mira R Aqr. These observations were taken at several stages in the stellar pulsation cycle. The total intensity and polarization morphology of the emission has been found to change on timescales of  $\sim 1$  month. As mentioned above, the sampling for this project was less than ideal. One of the results of these observations is the conclusion that the optimum spacing for circumstellar SiO observations is  $\sim 2$  weeks. The ultimate goal of future observations should be to monitor the SiO maser emission over a complete stellar cycle at intervals of  $\sim 2$  weeks. This would provide important information regarding the time evolution of the circumstellar maser emission. In addition, such an experiment could verify the observed inward motion of the SiO masers as the stellar phase approaches 1.0 and could determine if there is any outward proper motion during some period in the Mira's stellar phase. The VLBA is currently in a state in which a monitoring program like the one described above is possible.

There are also interesting SiO maser projects which would not require the large amount of observing time necessary for the monitoring program described above. One such project would be to perform full polarization imaging of two different SiO transitions simultaneously with the VLBA. Through single dish polarization observations, McIntosh and Predmore (1993) found evidence that the maser emission from three different transitions ( $v = 1, J = 3 - 2$ , 129 GHz;  $v = 1, J = 2 - 1$ , 86 GHz;  $v = 1, J = 1 - 0$ , 43 GHz) of SiO originated in the same volume of gas. VLBI obser-

vations of the  $v = 1, J = 1 - 0$  and the  $v = 2, J = 1 - 0$  transitions by Miyoshi et al. (1994) have also demonstrated that the maser transitions are cospatial. This information provides important constraints on the pumping mechanisms and the polarization mechanisms involved in the production of maser radiation. The VLBA, with its full polarization imaging capability, can confirm that the masers are truly cospatial by combining the two techniques used to come to this conclusion. Such a project can be performed with the current VLBA, by observing the  $v = 1, J = 1 - 0$  43.122-GHz and the  $v = 2, J = 1 - 0$  42.821-GHz SiO maser transitions simultaneously in full polarization towards multiple late-type stars.

A significant reduction in fractional linear polarization with increased component flux density has been found in these observations of R Aqr, and in previous SiO maser studies. McIntosh and Predmore (1993) also find that the fractional linear polarization is also decreased as higher frequency SiO transitions are observed. Both of these unexpected properties of the linear polarization are unexplained in the current polarization models. The simultaneous full-polarization imaging of multiple transitions described above, should help to determine if this effect is common in these objects. In addition, the observations should provide additional constraints on the theoretical models for maser polarization.

# Bibliography

- Alcolea, J., V. Bujarrabal, and J. Gómez-González (1990). *Astronomy and Astrophysics* 231, 431.
- Allen, D. A. (1984). *Astrophysics and Space Sciences* 99, 101.
- Allen, D. A., P. J. Hall, R. P. Norris, E. R. Troup, R. M. Wark, and A. E. Wright (1989). *Monthly Notices of the Royal Astronomical Society* 236, 363.
- Baade, W. (1943). *Annual Report Director Mount Wilson Observatory 1942-1943*, 17.
- Baade, W. (1944). *Annual Report Director Mount Wilson Observatory 1943-1944*, 12.
- Baan, W. A., P. A. D. Wood, and A. D. Haschik (1982). *Astrophysical Journal* 260, L49.
- Ball, J. A., C. A. Gottlieb, A. E. Lilley, and H. E. Radford (1970). *Astrophysical Journal* 162, L203.
- Barcia, A., V. Bujarrabal, and J. Gómez-González (1985). *Astronomy and Astrophysics* 142, L9.
- Barvainis, R., G. McIntosh, and C. R. Predmore (1987). *Nature* 329, 613.
- Bloemhof, E. E., J. M. Moran, and M. J. Reid (1996). *Astrophysical Journal* 467, L117.
- Bloemhof, E. E., M. J. Reid, and J. M. Moran (1992). *Astrophysical Journal* 397, 500.
- Boboltz, D. A., P. J. Diamond, and A. J. Kemball (1997). submitted. *Astrophysical Journal*.
- Bowen, G. H. (1988). *Astrophysical Journal* 329, 299.
- Brown, L. F., D. H. Roberts, and J. F. C. Wardle (1989). *Astronomical Journal* 97, 1522.
- Brugel, E. W., J. A. Cardelli, P. Szkody, and G. Wallerstein (1984). *Publications of the Astronomical Society of the Pacific* 96, 78.

- Buhl, D., L. E. Snyder, F. J. Lovas, and D. R. Johnson (1974). *Astrophysical Journal* 192, L97.
- Burgarella, D. and F. Paresce (1991). *Astrophysical Journal* 370, 590.
- Burgarella, D. and F. Paresce (1992). *Astrophysical Journal* 389, L29.
- Burke, B. F. and F. Graham-Smith (1997). *An Introduction to Radio Astronomy*. Cambridge: Cambridge University Press.
- Burnham, R. (1978). *Burnham's Celestial Handbook*, pp. 631–639. New York: Dover.
- Cahn, J. H. and M. Elitzur (1979). *Astrophysical Journal* 231, 124.
- Cahn, J. H. and S. P. Wyatt (1978). *Astrophysical Journal* 221, 163.
- Chapman, J. M., R. J. Cohen, and D. J. Saika (1991). *Monthly Notices of the Royal Astronomical Society* 249, 227.
- Cheung, A. C., D. M. Rank, C. H. Townes, D. D. Thornton, and W. Welch (1969). *Nature* 221, 626.
- Cheung, A. C., D. M. Rank, C. H. Townes, D. D. Thornton, and W. J. Welch (1968). *Physical Review Letters* 21, 1701.
- Chruchwell, E., A. Witzel, W. Huchtmeier, I. Pauliny-Toth, J. Roland, and W. Seiber (1977). *Astronomy and Astrophysics* 54, 969.
- Clayton, M. L. and M. W. Feast (1969). *Monthly Notices of the Royal Astronomical Society* 146, 411.
- Cohen, N. L. and F. D. Ghigo (1980). *Astronomical Journal* 85, 451.
- Colomer, F., D. A. Graham, T. P. Kirchbaum, B. O. Rönnäng, P. de Vicente, A. Witzel, A. Barcia, A. Baudry, R. S. Booth, J. Gómez-González, J. Alcolea, and G. Daigne (1992). *Astronomy and Astrophysics* 254, L17.
- Condon, J. J. (1997). *Publications of the Astronomical Society of the Pacific* 109, 166.
- Conway, R. G. and P. P. Kronberg (1969). *Monthly Notices of the Royal Astronomical Society* 142, 11.
- Cooke, B. and M. Elitzur (1985). *Astrophysical Journal* 295, 175.
- Cornwell, T. and E. B. Fomalont (1989). Self-calibration. In R. A. Perley, F. R. Schwab, and A. H. Bridle (Eds.), *Synthesis Imaging in Radio Astronomy*, pp. 185–197. San Francisco: Astronomical Society of the Pacific. ASP Conference Series, Volume 6.
- Cotton, W. D. (1989). Spectral line techniques. In M. Felli and R. E. Spencer (Eds.), *Very Long Baseline Interferometry: Techniques and Applications*, pp. 275–287. Dordrecht: Kluwer.

- Cotton, W. D. (1993). *Astronomical Journal* 106, 1241.
- Cotton, W. D. (1995). Interferometers and coherence theory. In J. A. Zensus, P. J. Diamond, and P. J. Napier (Eds.), *Very Long Baseline Interferometry Techniques and Applications*, pp. 289–308. San Francisco: Astronomical Society of the Pacific. ASP Conference Series, Volume 82.
- Danchi, W. C., M. Bester, C. G. Degiacomi, L. J. Greenhill, and C. H. Townes (1994). *Astronomical Journal* 107, 1469.
- Deguchi, S. (1977). *Publications of the Astronomical Society of Japan* 29, 669.
- Deguchi, S. and T. Iguchi (1976). *Publications of the Astronomical Society of Japan* 28, 307.
- Deguchi, S. and W. D. Watson (1986). *Astrophysical Journal* 302, 750.
- Deguchi, S., W. D. Watson, and L. R. Western (1986). *Astrophysical Journal* 302, 108.
- Diamond, P. J. (1989). Spectral line techniques. In M. Felli and R. E. Spencer (Eds.), *Very Long Baseline Interferometry: Techniques and Applications*, pp. 231–259. Dordrecht: Kluwer.
- Diamond, P. J., A. J. Kemball, J. Benson, W. Junor, and V. Dhawan (1994). Continued Monitoring of Stellar SiO Masers. VLBA Proposal.
- Diamond, P. J., A. J. Kemball, W. Junor, A. Zensus, J. Benson, and V. Dhawan (1994). *Astrophysical Journal* 430, L61.
- Dos Santos, P. M. and J. R. D. Lepine (1979). *Nature* 278, 34.
- Dougherty, S. M., M. F. Bode, H. M. Lloyd, R. J. Davis, and S. P. Eyres (1995). *Monthly Notices of the Royal Astronomical Society* 272, 843.
- Dougherty, S. M., M. F. Bode, H. M. Lloyd, L. V. Morrison, S. P. Eyres, and R. J. Davis (1996). Proper Motions in the Core of the Symbiotic System R Aquarii. In A. R. Taylor and J. M. Paredes (Eds.), *Radio Emission from the Stars and the Sun*, ASP Conference Series, Volume 93, pp. 191–193. San Francisco: Astronomical Society of the Pacific.
- Elitzur, M. (1978). *Astronomy and Astrophysics* 62, 305.
- Elitzur, M. (1980). *Astrophysical Journal* 240, 553.
- Elitzur, M. (1990). *Astrophysical Journal* 363, 628.
- Elitzur, M. (1991). *Astrophysical Journal* 370, 407.
- Elitzur, M. (1992). *Astronomical Masers*. Dordrecht: Kluwer.
- Elitzur, M. (1993). *Astrophysical Journal* 416, 256.
- Elitzur, M. (1996). *Astrophysical Journal* 457, 415.

- Elitzur, M., P. Goldreich, and N. P. Scoville (1976). *Astrophysical Journal* 205, 384.
- Engels, D., J. Schmid-Burgk, and C. M. Walmsley (1986). *Astronomy and Astrophysics* 167, 129.
- Feast, M. W. (1963). *Monthly Notices of the Royal Astronomical Society* 125, 367.
- Feast, M. W., I. S. Glass, P. A. Whitelock, and R. M. Catchpole (1989). *Monthly Notices of the Royal Astronomical Society* 241, 375.
- Felli, M. and R. E. Spencer (Eds.) (1989). *Very Long Baseline Interferometry: Techniques and Applications*. Dordrecht: Kluwer.
- García-Barreto, J. A., B. F. Burke, M. J. Reid, J. M. Moran, A. D. Haschick, and R. T. Schilizzi (1988). *Astrophysical Journal* 326, 954.
- Geballe, T. R. and C. H. Townes (1974). *Astrophysical Journal* 191, L37.
- Genzel, R., J. M. Moran, M. J. Reid, and D. Downes (1981). *Astrophysical Journal* 244, 884.
- Girard, T. and L. Willson (1987). *Astronomy and Astrophysics* 183, 247.
- Goldreich, P., D. A. Keely, and J. Y. Kwan (1973). *Astrophysical Journal* 179, 111.
- Goldreich, P. and N. P. Scoville (1976). *Astrophysical Journal* 205, 144.
- Gray, M. D., R. J. Ivison, J. A. Yates, E. M. L. Humphreys, P. J. Hall, and D. Field (1995). *Monthly Notices of the Royal Astronomical Society* 277, L67.
- Greenhill, L. J., F. Colomer, J. M. Moran, D. C. Backer, W. C. Danchi, and M. Bester (1995). *Astrophysical Journal* 449, 365.
- Greenhill, L. J., J. M. Moran, M. J. Reid, C. R. Gwinn, K. M. Menten, A. Eckart, and H. Hirabayashi (1990). *Astrophysical Journal* 364, 513.
- Guilloteau, S., A. Omont, and R. Lucas (1987). *Astronomy and Astrophysics* 176, L24.
- Gwinn, C. R., J. M. Moran, and M. J. Reid (1992). *Astrophysical Journal* 393, 149.
- Habing, H. J. (1990). The evolution of red giants to white dwarfs, a review of the observational evidence. In M. O. Mennessier and A. Omont (Eds.), *From Miras to Planetary Nebulae: Which Path for Stellar Evolution*, pp. 16–40. Montpellier, France: Editions Frontieres.
- Hall, P. J., D. A. Allen, E. R. Troup, R. M. Wark, and A. E. Wright (1990). *Monthly Notices of the Royal Astronomical Society* 243, 480.
- Hall, P. J., A. E. Wright, E. R. Troup, R. M. Wark, and D. A. Allen (1990). *Monthly Notices of the Royal Astronomical Society* 247, 549.

- Harding, K. (1816). *Zs. Ap.* 1, 449.
- Harvey, P. M., K. P. Bechis, W. J. Wilson, and J. A. Ball (1974). *Astrophysical Journal Supplements* 27, 331.
- Hege, E. K., C. K. Allen, and W. J. Cocke (1991). *Astrophysical Journal* 381, 543.
- Herbig, G. (1980). *IAU Circular*, no. 3535.
- Hinkle, K. H., D. N. B. Hall, and S. T. Ridgway (1982). *Astrophysical Journal* 252, 697.
- Hinkle, K. H., T. D. Wilson, W. W. G. Scharlach, and F. C. Fekel (1989). *Astronomical Journal* 98, 1820.
- Hoffmeister, C., G. Richter, and W. Wenzel (1985). *Variable Stars*, pp. 55–68. Berlin: Springer-Verlag.
- Hollis, J. M., M. Kafatos, A. G. Michalitsianos, and H. McAlister (1985). *Astrophysical Journal* 289, 765.
- Hollis, J. M., M. Kafatos, A. G. Michalitsianos, R. J. Oliverson, and F. Yusef-Zadeh (1987). *Astrophysical Journal* 321, L55.
- Hollis, J. M., R. G. Lyon, J. E. Dorband, and W. A. Feibelman (1997). *Astrophysical Journal* 475, 231.
- Hollis, J. M. and A. G. Michalitsianos (1993). *Astrophysical Journal* 411, 235.
- Hollis, J. M., A. G. Michalitsianos, M. Kafatos, M. C. H. Wright, and W. J. Welch (1986). *Astrophysical Journal* 309, L53.
- Hollis, J. M., R. J. Oliverson, M. Kafatos, A. G. Michalitsianos, and R. M. Wagner (1991). *Astrophysical Journal* 377, 227.
- Hollis, J. M., R. J. Oliverson, and R. M. Wagner (1989). *Astrophysical Journal* 337, 795.
- Hollis, J. M., J. A. Pedelty, and R. G. Lyon (1997). *Astrophysical Journal* 482, L85.
- Hollis, J. M., R. M. Wagner, and R. J. Oliverson (1990). *Astrophysical Journal* 351, L17.
- Hollis, J. M., M. C. H. Wright, W. J. Welch, P. R. Jewell, H. E. Crull, M. Kafatos, and A. G. Michalitsianos (1990). *Astrophysical Journal* 361, 663.
- Hubble, E. P. (1940). *Annual Report Director Mount Wilson Observatory 1939-1940*, 19.
- Hubble, E. P. (1943). *Annual Report Director Mount Wilson Observatory 1942-1943*, 17.

- Iverson, R., E. Seaquist, and P. Hall (1994). *Monthly Notices of the Royal Astronomical Society* 269, 218.
- Iverson, R., E. Seaquist, and P. Hall (1995). *Astrophysics and Space Sciences* 224, 255.
- Jacobsen, T. S. and G. Wallerstein (1975). *Publications of the Astronomical Society of the Pacific* 87, 269.
- Jura, M. and S. G. Kleinmann (1992). *Astrophysical Journal Supplements* 79, 105.
- Kafatos, M., J. M. Hollis, and A. G. Michalitsianos (1983). *Astrophysical Journal* 267, L103.
- Kafatos, M., J. M. Hollis, F. Yusef-Zadeh, A. G. Michalitsianos, and M. Elitzur (1989). *Astrophysical Journal* 346, 991.
- Kafatos, M. and A. G. Michalitsianos (1982). *Nature* 298, 540.
- Kafatos, M., A. G. Michalitsianos, and J. M. Hollis (1986). *Astrophysical Journal Supplements* 62, 853.
- Kaifu, N., D. Buhl, and L. E. Snyder (1975). *Astrophysical Journal* 195, 359.
- Kemball, A. J. (1992). *Data Reduction Techniques for Very Long Baseline Interferometric Spectropolarimetry*. Ph. D. thesis, Rhodes University.
- Kemball, A. J. and P. J. Diamond (1993). VLBI Spectral Line Polarization Observations of the OH Masers in the Supergiant IRC+10420. In A. W. Clegg and G. E. Nedoluha (Eds.), *Astrophysical Masers*, pp. 369–372. Berlin: Springer-Verlag.
- Kemball, A. J. and P. J. Diamond (1997). *Astrophysical Journal* 481, L111.
- Kemball, A. J., P. J. Diamond, and W. D. Cotton (1995). *Astronomy and Astrophysics Supplements* 110, 383.
- Kemball, A. J., P. J. Diamond, and I. I. K. Pauliny-Toth (1996). *Astronomical Journal* 464, L55.
- Kenyon, S. J. (1986). *The Symbiotic Stars*, pp. 170–176. Cambridge: Cambridge University Press.
- Kenyon, S. J. (1992). Symbiotic binary stars. In Y. Kondo, R. Sisteró, and R. Polidan (Eds.), *IAU Symposium No. 151, Evolutionary Processes in Interacting Binary Stars*, pp. 137. Dordrecht: Kluwer.
- Knowles, S. H., C. H. Mayer, A. C. Cheung, D. M. Rank, and C. H. Townes (1969). *Science* 163, 1055.
- Kogan, L. (1996). NRAO AIPS Memo Series No. 92.
- Kwan, J. and N. Scoville (1974). *Astrophysical Journal* 194, L97.

- Lampland, C. O. (1923). *Publications of the American Astronomical Society* 4, 319.
- Lane, A. P. (1984). The spatial structure of silicon monoxide masers. In R. Fanti, K. Kellermann, and G. Setti (Eds.), *IAU Symposium No. 110, VLBI and Compact Radio Sources*, pp. 329–330. Dordrecht: Reidel Publishing Company.
- Langer, S. H. and W. D. Watson (1984). *Astrophysical Journal* 284, 751.
- Lehto, H. J. and D. R. H. Johnson (1992). *Nature* 355, 705.
- Lépine, J. R. D., A. M. LeSqueren, and E. Scalise (1978). *Astrophysical Journal* 225, 869.
- Martínez, A., V. Bujarrabal, and J. Alcolea (1988). *Astronomy and Astrophysics Supplements* 74, 273.
- Marvel, K. B. (1996). *The Circumstellar Environment of Evolved Stars as Revealed by Studies of Circumstellar Water Masers*. Ph. D. thesis, New Mexico State University.
- Mattei, J. A. (1996). Observations from the AAVSO International Database. private communication.
- Mattei, J. A. and J. Allen (1979). *Journal of the Royal Astronomical Society of Canada* 73, 173.
- Mauron, N., J. L. Nieto, J. P. Picat, G. Lelievre, and H. Sol (1985). *Astronomy and Astrophysics* 142, L13.
- McIntosh, G. C. (1987). *Polarization Properties of SiO Masers*. Ph. D. thesis, University of Massachusetts, Amherst.
- McIntosh, G. C. and C. R. Predmore (1993). *Astrophysical Journal* 404, L71.
- McIntosh, G. C., C. R. Predmore, J. M. Moran, L. J. Greenhill, A. E. E. Rogers, and R. Barvainis (1989). *Astrophysical Journal* 337, 934.
- McIntosh, G. C., C. R. Predmore, and N. A. Patel (1994). *Astrophysical Journal* 428, L29.
- Merrill, P. W. (1935). *Astrophysical Journal* 81, 312.
- Merrill, P. W. (1950). *Astrophysical Journal* 112, 514.
- Michalitsianos, A. G. and M. Kafatos (1982). *Astrophysical Journal* 262, L47.
- Michalitsianos, A. G. and M. Kafatos (1988). A review of the R Aquarii system. In J. Mikolajewska, M. Friedjung, S. Kenyon, and R. Viotti (Eds.), *IAU Colloquium No. 103, The Symbiotic Phenomenon*, pp. 235. Dordrecht: Kluwer.
- Miyoshi, M., K. Matsumoto, S. Kamenno, H. Takaba, and T. Iwata (1994). *Nature* 371, 395.

- Miyoshi, M., J. Moran, J. Herrnstein, L. Greenhill, N. Nakai, P. Diamond, and M. Inoue (1995). *Nature* 373, 127.
- Moran, J. M., J. A. Ball, C. R. Predmore, A. P. Lane, G. R. Huguenin, M. J. Reid, and S. S. Hansen (1979). *Astrophysical Journal* 231, L67.
- Nedoluha, G. E. and W. D. Watson (1990). *Astrophysical Journal* 354, 660.
- Nedoluha, G. E. and W. D. Watson (1994). *Astrophysical Journal* 423, 394.
- Nyman, L.-Å. and H. Olofsson (1986). *Astronomy and Astrophysics* 158, 67.
- Palma, A., S. Green, D. J. DeFrees, and A. D. McLean (1988). *Astrophysical Journal Supplements* 68, 287.
- Paresce, F., R. Albrecht, C. Barbieri, J. C. Blades, A. Boksenberg, P. Crane, J. M. Deharveng, M. J. Disney, P. Jakobsen, T. M. Kamperman, I. R. King, F. Macchetto, C. D. Mackay, G. Weigelt, D. Baxter, P. Greenfield, R. Jedrzejewski, A. Nota, and W. B. Sparks (1991). *Astrophysical Journal* 369, L67.
- Paresce, F., C. Burrows, and K. Horne (1988). *Astrophysical Journal* 329, 318.
- Paresce, F. and W. Hack (1994). *Astronomy and Astrophysics* 287, 154.
- Perley, R. A., F. R. Schwab, and A. H. Bridle (Eds.) (1989). *Synthesis Imaging in Radio Astronomy*. San Francisco: Astronomical Society of the Pacific. ASP Conference Series, Volume 6.
- Reid, M. J., A. D. Haschick, B. F. Burke, J. M. Moran, K. J. Johnston, and G. W. Swenson (1980). *Astrophysical Journal* 239, 89.
- Reid, M. J. and K. M. Menten (1990). *Astrophysical Journal* 360, L51.
- Reid, M. J. and K. M. Menten (1997). *Astrophysical Journal* 476, 327.
- Reid, M. J., M. H. Schneps, J. M. Moran, C. R. Gwinn, R. Genzel, D. Downes, and B. Rönnäng (1988). *Astrophysical Journal* 330, 809.
- Roberts, D. H., J. F. C. Wardle, and L. F. Brown (1994). *Astrophysical Journal* 427, 718.
- Rogers, A. E. E., H. F. Hinteregger, A. R. Whitney, C. C. Counselmann, I. I. Shapiro, J. J. Whitels, W. K. Klemperer, W. W. Warnock, T. A. Clark, L. K. Hutton, G. E. Marandino, B. O. Ronnang, O. E. H. Rydbeck, and A. E. Niell (1974). *Astrophysical Journal* 193, 293.
- Romney, J. D. (1995). Interferometers and coherence theory. In J. A. Zensus, P. J. Diamond, and P. J. Napier (Eds.), *Very Long Baseline Interferometry Techniques and Applications*, pp. 17–37. San Francisco: Astronomical Society of the Pacific. ASP Conference Series, Volume 82.
- Rydbeck, O. E. H., J. Ellder, and W. M. Irvine (1973). *Nature* 246, 466.

- Scalise, E. and J. R. D. Lépine (1978). *Astronomy and Astrophysics* 65, L7.
- Schwarz, H., L. Nyman, E. Seaquist, and R. Ivison (1995). *Astronomy and Astrophysics* 303, 833.
- Seaquist, E., R. Ivison, and P. Hall (1995). *Monthly Notices of the Royal Astronomical Society* 276, 867.
- Snyder, L. E. and D. Buhl (1969). *Astrophysical Journal* 155, L65.
- Snyder, L. E. and D. Buhl (1974). *Astrophysical Journal* 189, L31.
- Solf, J. (1992). *Astronomy and Astrophysics* 257, 228.
- Solf, J. and H. Ulrich (1985). *Astronomy and Astrophysics* 148, 274.
- Sopka, R. J., G. Herbig, M. Kafatos, and A. Michalitsianos (1982). *Astrophysical Journal* 258, L35.
- Spergel, D. N., J. L. Giuliani, and G. R. Knapp (1983). *Astrophysical Journal* 275, 330.
- Thaddeus, P., J. Mather, J. H. Davis, and G. N. Blair (1974). *Astrophysical Journal* 192, L33.
- Thompson, A. R., J. M. Moran, and G. W. Swenson (1986). *Interferometry and Synthesis in Radio Astronomy*. New York: John Wiley & Sons. (TMS).
- Turner, B. E. and B. Zuckerman (1973). *Bulletin of the American Astronomical Society* 5, 240.
- van Belle, G. T., H. M. Dyck, J. A. Benson, and M. G. Lacasse (1996). *Astronomical Journal* 112, 2147.
- Viotti, R., L. Piro, M. Friedjung, and A. Cassatella (1987). *Astrophysical Journal* 319, L7.
- VLBA-Management (1992). VLBA Locations Graphic. NRAO Internal Distribution.
- Wallerstein, G. (1986). *Publications of the Astronomical Society of the Pacific* 98, 118.
- Wallerstein, G. and J. L. Greenstein (1980). *Publications of the Astronomical Society of the Pacific* 92, 275.
- Wallin, B. K. and W. D. Watson (1995). *Astrophysical Journal* 445, 465.
- Wallin, B. K. and W. D. Watson (1997). *Astrophysical Journal* 481, 832.
- Wardle, J. F. C. and P. P. Kronberg (1974). *Astrophysical Journal* 194, 249.
- Weaver, H., D. R. W. Williams, N. H. Dieter, and W. T. Lum (1965). *Nature* 208, 29.

- Weidemann, V. and D. Schönberner (1990). Stellar evolution theory: up to and on the AGB. In M. O. Mennessier and A. Omont (Eds.), *From Miras to Planetary Nebulae: Which Path for Stellar Evolution*, pp. 3–15. Montpellier, France: Editions Frontieres.
- Weinreb, S., M. L. Meeks, J. C. Carter, A. H. Barrett, and A. E. E. Rogers (1965). *Nature* 208, 441.
- Western, L. R. and W. D. Watson (1984). *Astrophysical Journal* 285, 158.
- Whitelock, P. A. (1987). *Publications of the Astronomical Society of the Pacific* 99, 573.
- Whitelock, P. A., M. W. Feast, R. M. Catchpole, B. S. Carter, and G. Roberts (1983). *Monthly Notices of the Royal Astronomical Society* 203, 351.
- Whiteoak, J. B. and F. F. Gardener (1974). *Astrophysical Journal* 15, L211.
- Wilkinson, P. N. (1989). An Introduction to Closure Phase and Self-Calibration. In M. Felli and R. E. Spencer (Eds.), *Very Long Baseline Interferometry: Techniques and Applications*, pp. 69–93. Dordrecht: Kluwer.
- Willson, L. A., P. Garnavich, and J. A. Mattei (1981). *IAU Inform. Bulletin Variable Stars* 1961, 1.
- Wilson, W. J. and A. H. Barrett (1968). *Science* 161, 778.
- Wyatt, S. P. and J. H. Cahn (1983). *Astrophysical Journal* 275, 225.
- Zensus, J. A., P. J. Diamond, and P. J. Napier (Eds.) (1995). *Very Long Baseline Interferometry and the VLBA*. San Francisco: Astronomical Society of the Pacific. ASP Conference Series, Volume 82.
- Zuckerman, B. (1979). *Astrophysical Journal* 230, 442.

# Appendix A

## TOTAL INTENSITY CHANNEL MAPS FOR R AQUARI

This appendix contains the total intensity (Stokes  $I$ ) channel maps produced for each of the four epochs of observations of the  $v = 1, J = 1 - 0$  43-GHz SiO maser emission towards R Aqr. The maps were produced following the self-calibration and imaging procedures outlined in Chapters 2 and 3. The integrated Stokes  $I$  images shown in Chapter 3 were produced from these channel maps by summing the flux over the entire velocity range in each of the following image cubes.

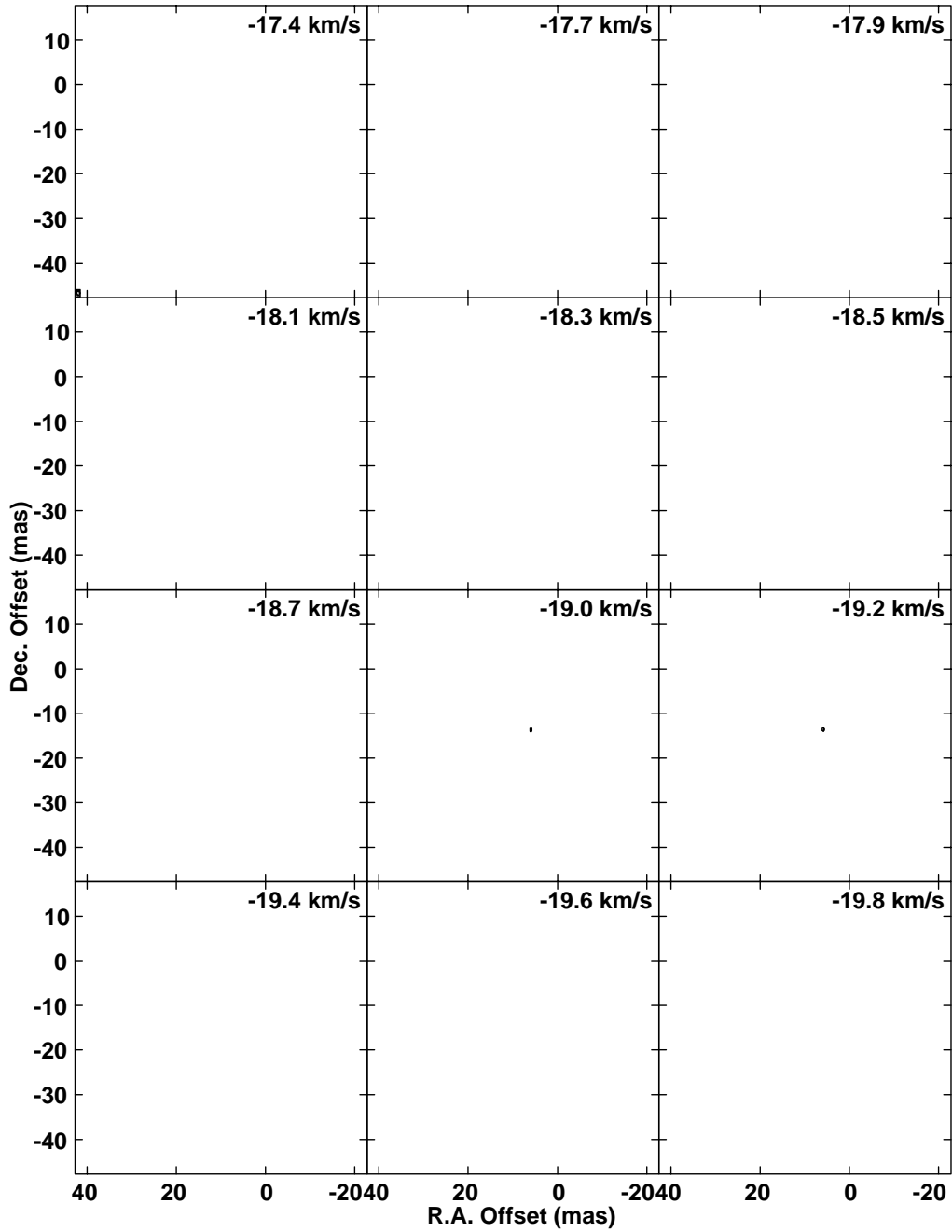


Figure A.1: Total intensity (Stokes  $I$ ) channel of the  $v = 1, J = 1 - 0$  43-GHz SiO maser emission towards R Aqr observed at Epoch 1. Contour levels are  $-15, -12, -9, -6, -3, -1.5, 1.5, 3, 6, 9, 12,$  and  $15\%$  of the peak flux density in the cube,  $32.8$  Jy/beam. The LSR velocity for each channel is stated in the upper right corner of each plane.

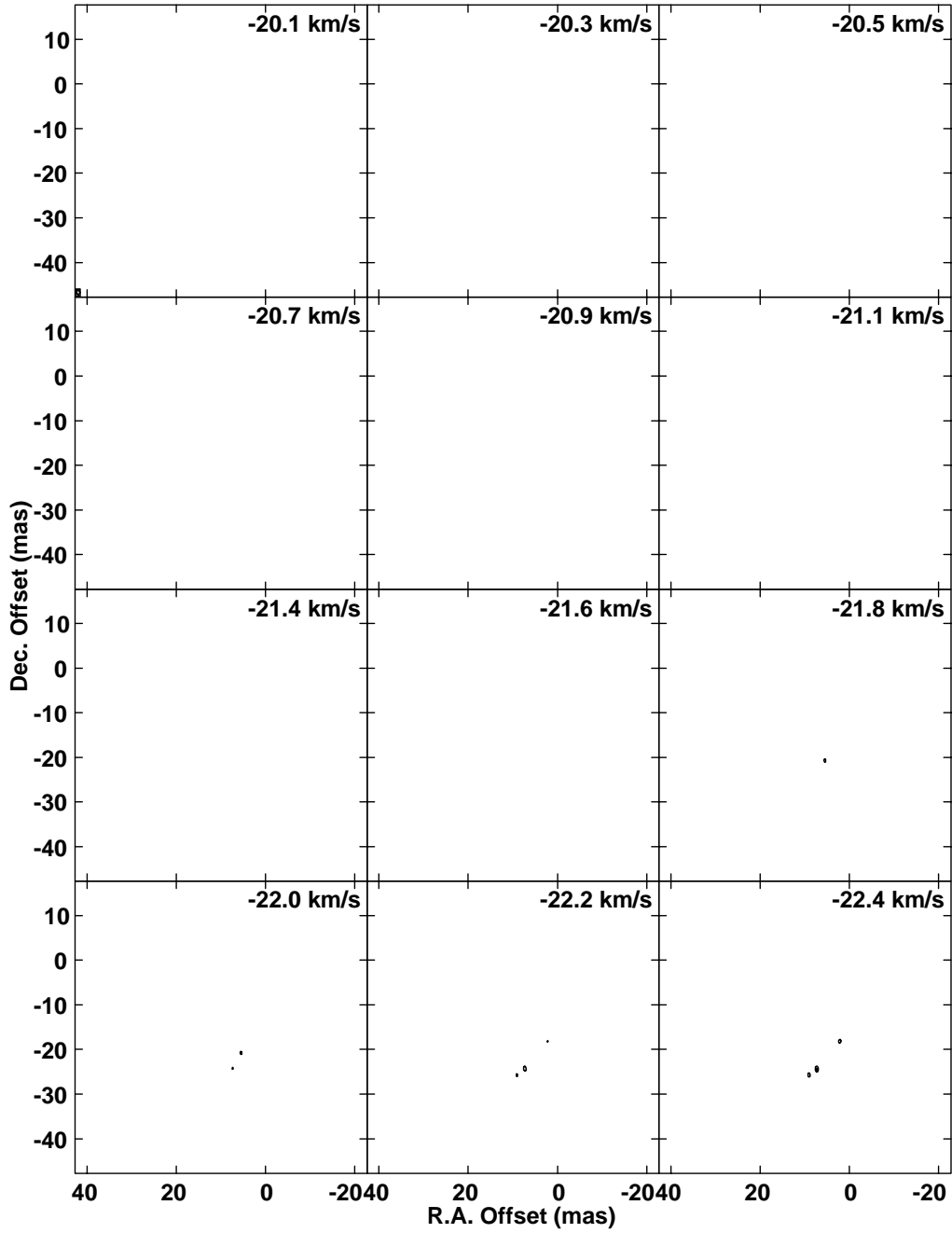


Figure A.1 continued.

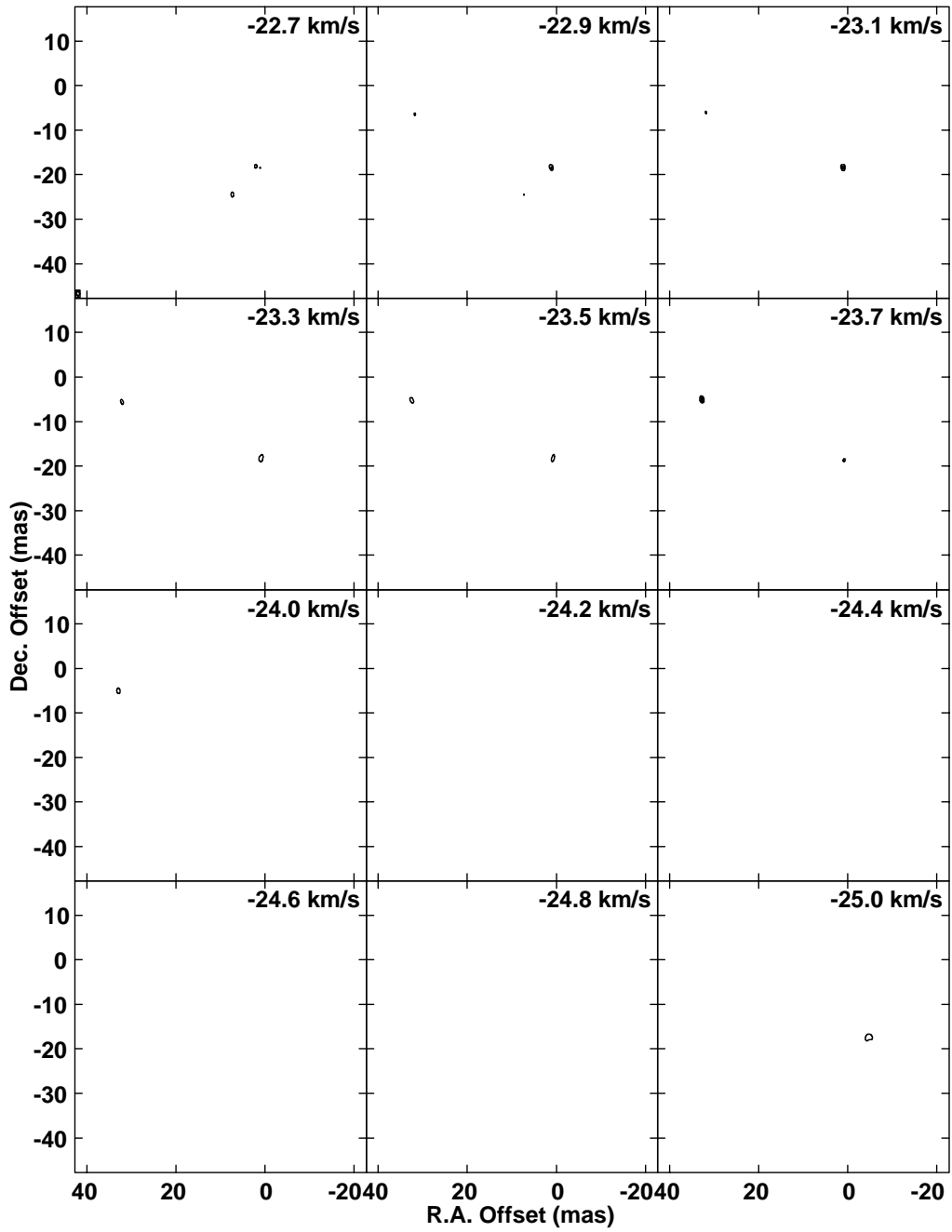


Figure A.1 continued.

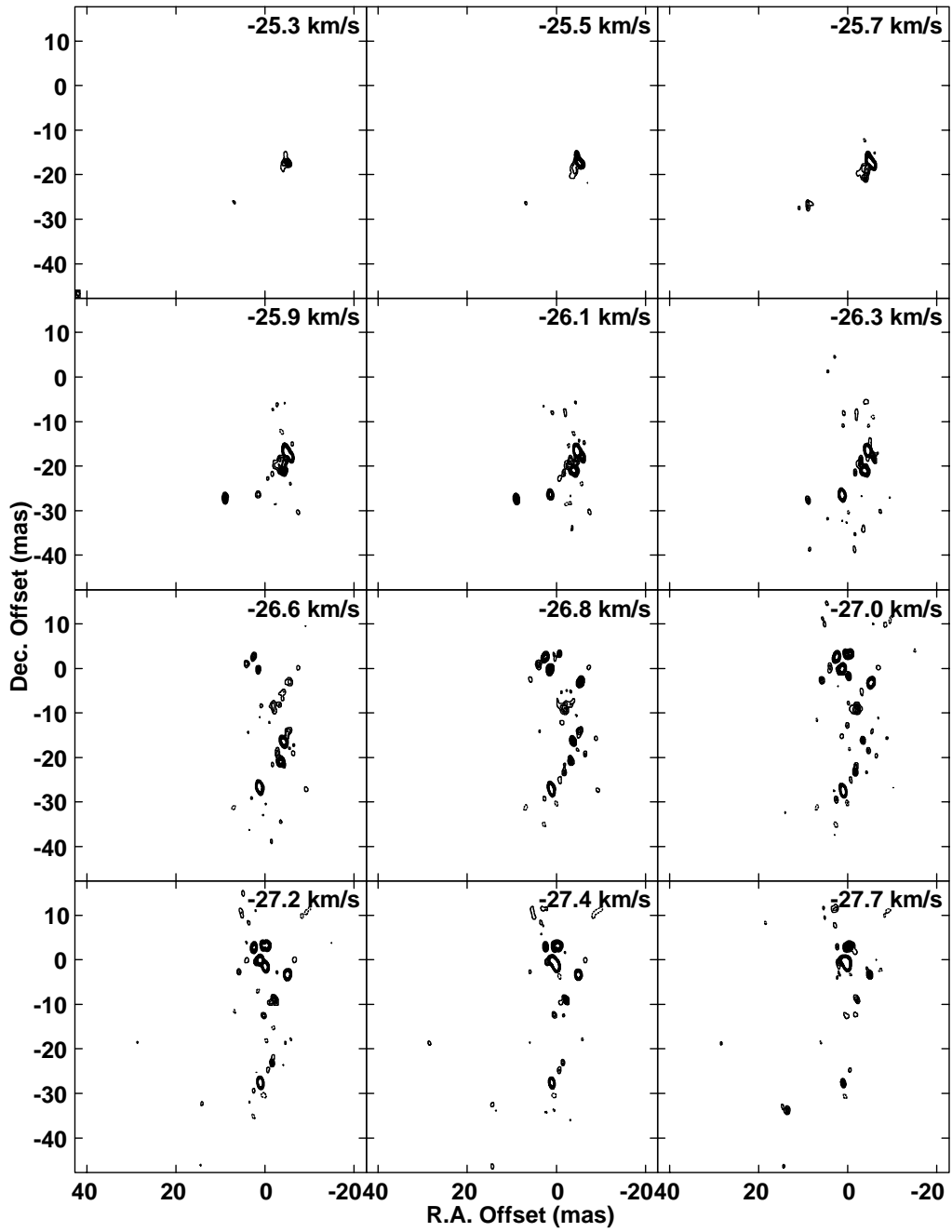


Figure A.1 continued.

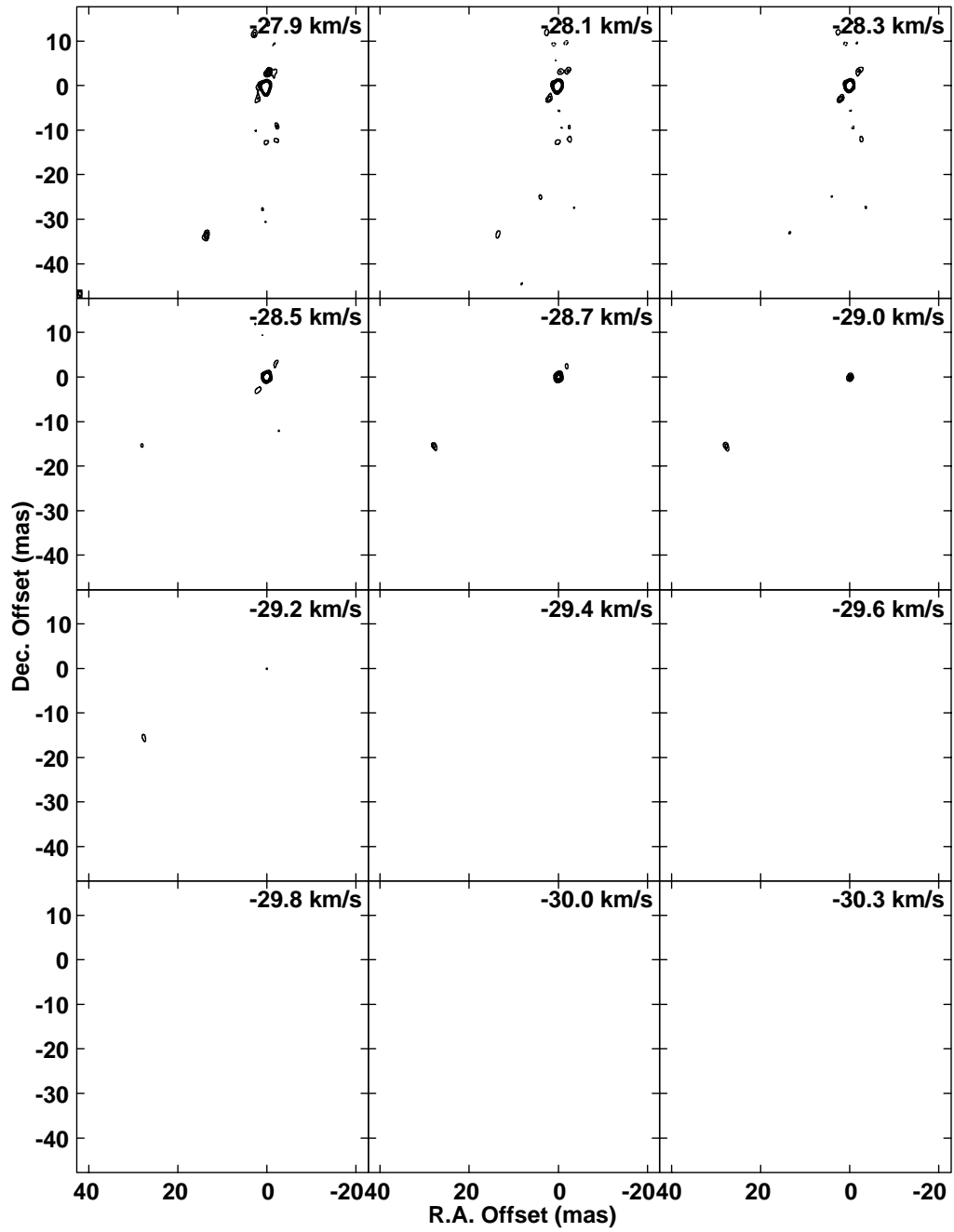


Figure A.1 continued.

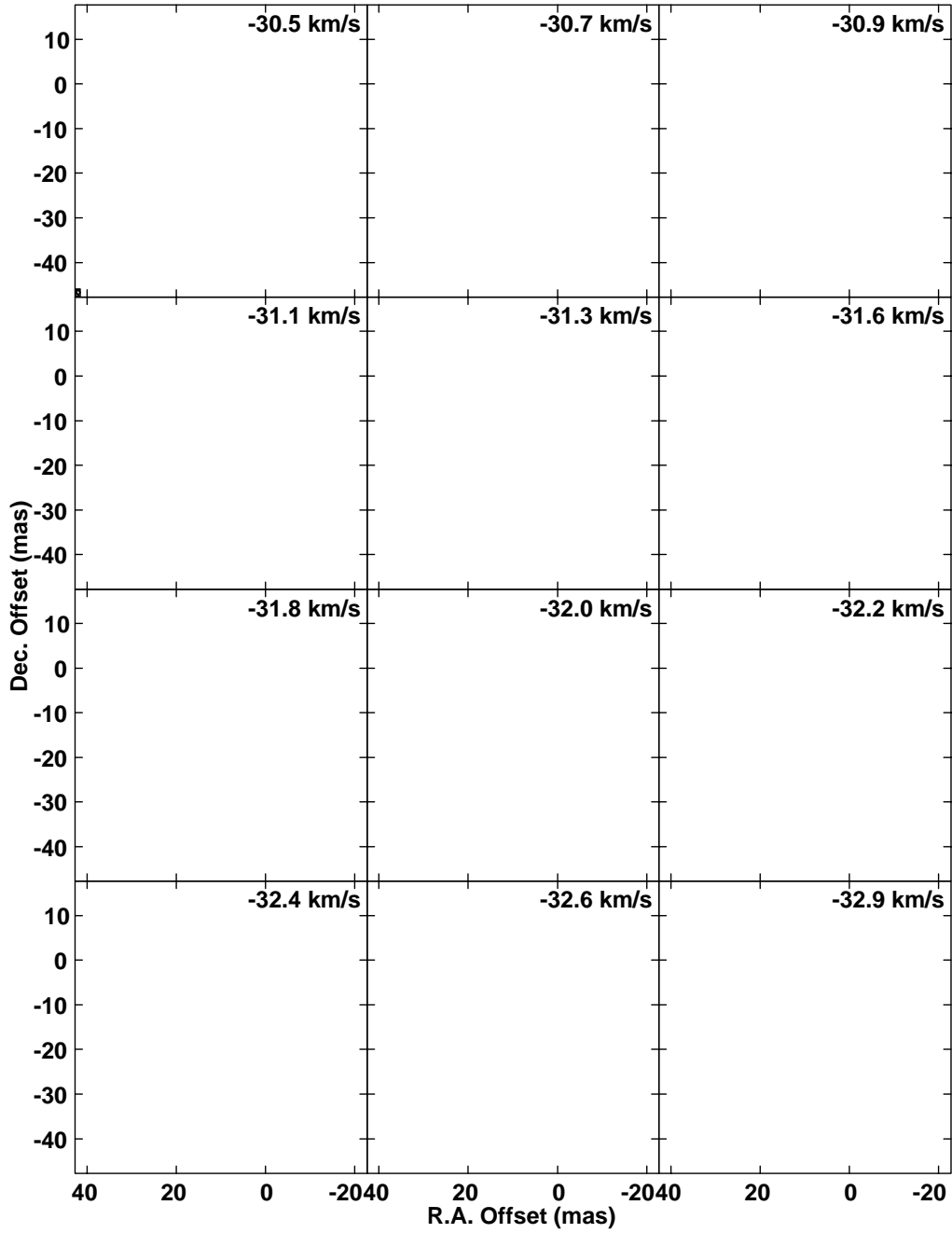


Figure A.1 continued.

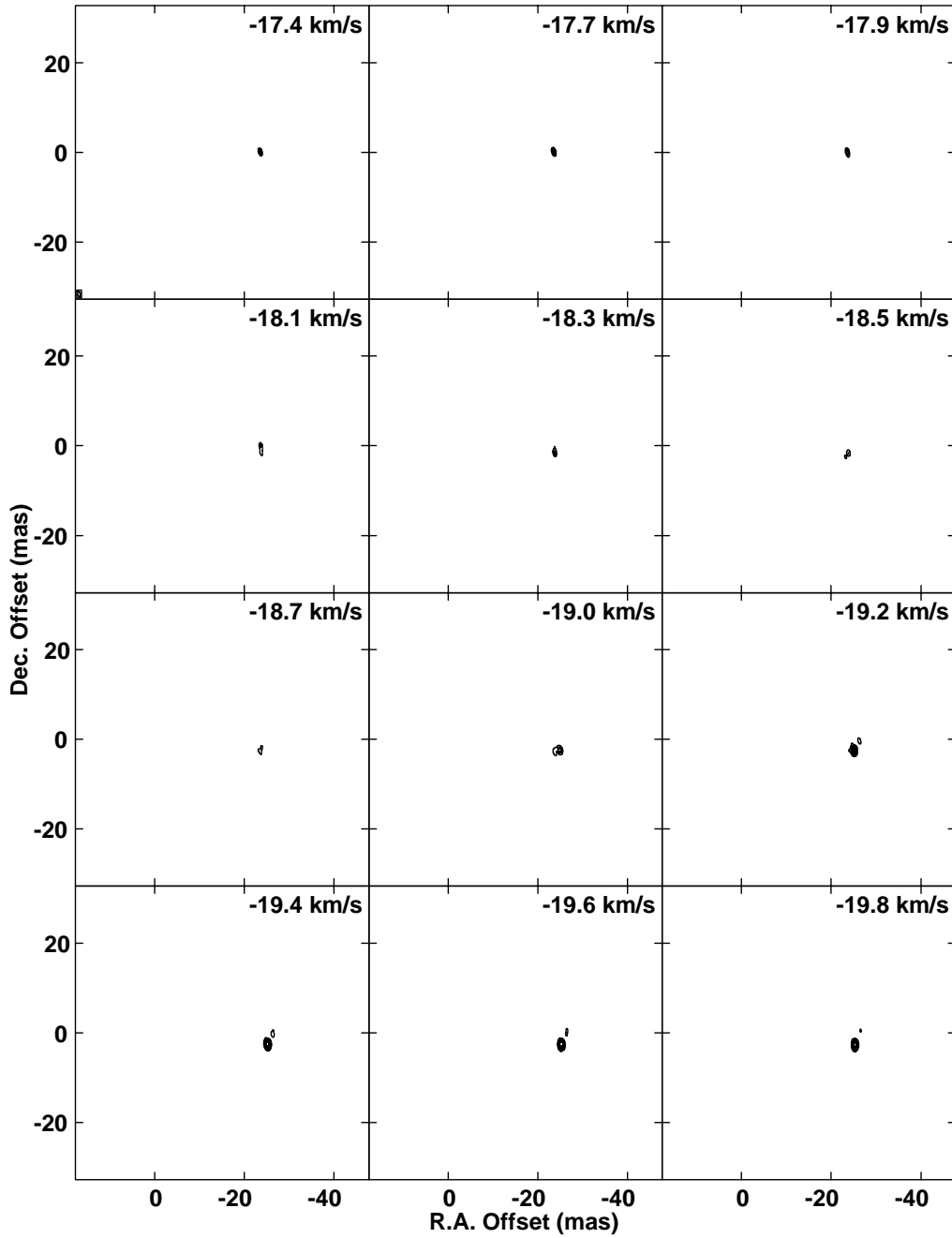


Figure A.2: Total intensity (Stokes  $I$ ) channel of the  $v = 1, J = 1 - 0$  43-GHz SiO maser emission towards R Aqr observed at Epoch 2. Contour levels are  $-20, -16, -12, -8, -4, -2, 2, 4, 8, 12, 16,$  and  $20\%$  of the peak flux density in the cube,  $9.8$  Jy/beam. The LSR velocity for each channel is stated in the upper right corner of each plane.

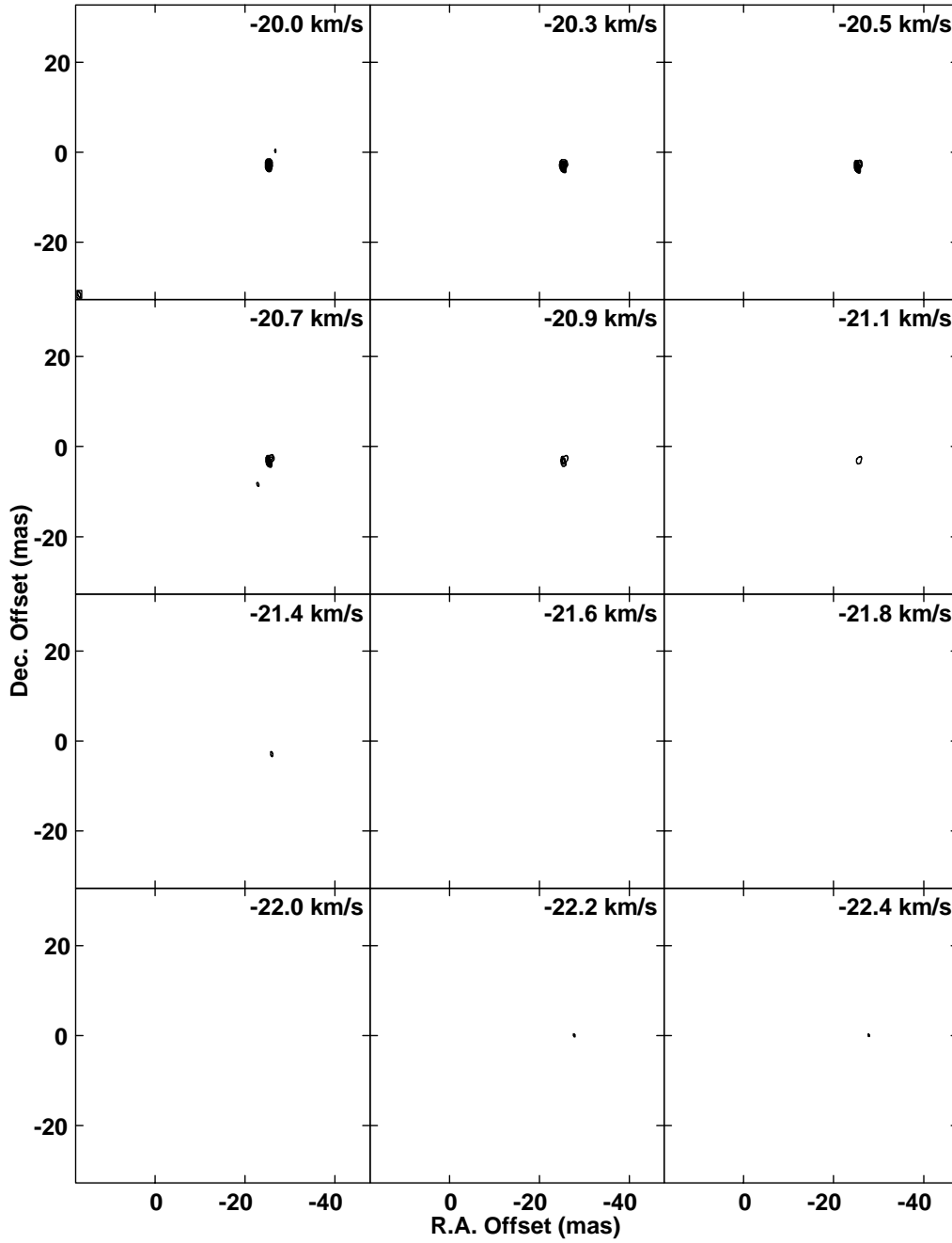


Figure A.2 continued.

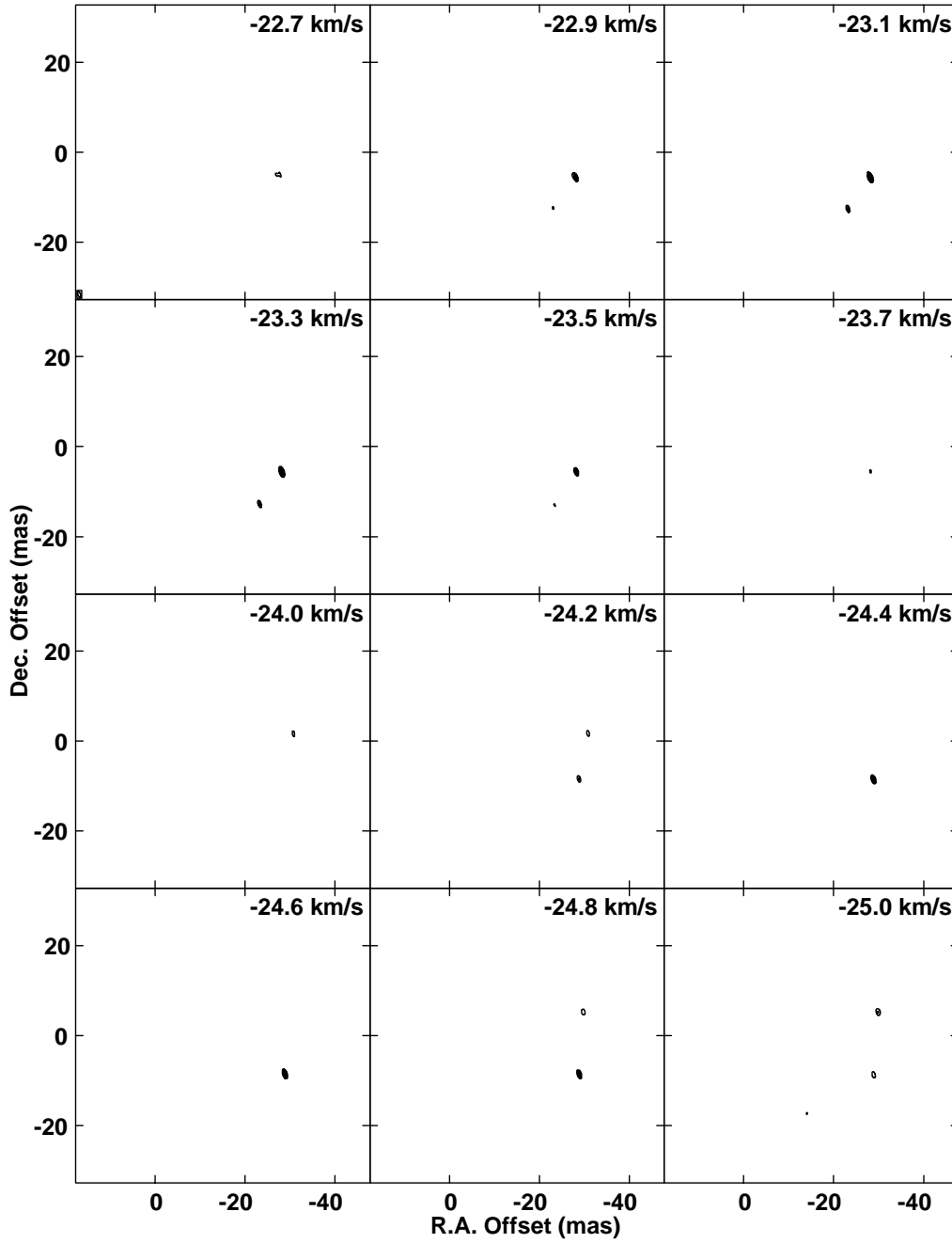


Figure A.2 continued.

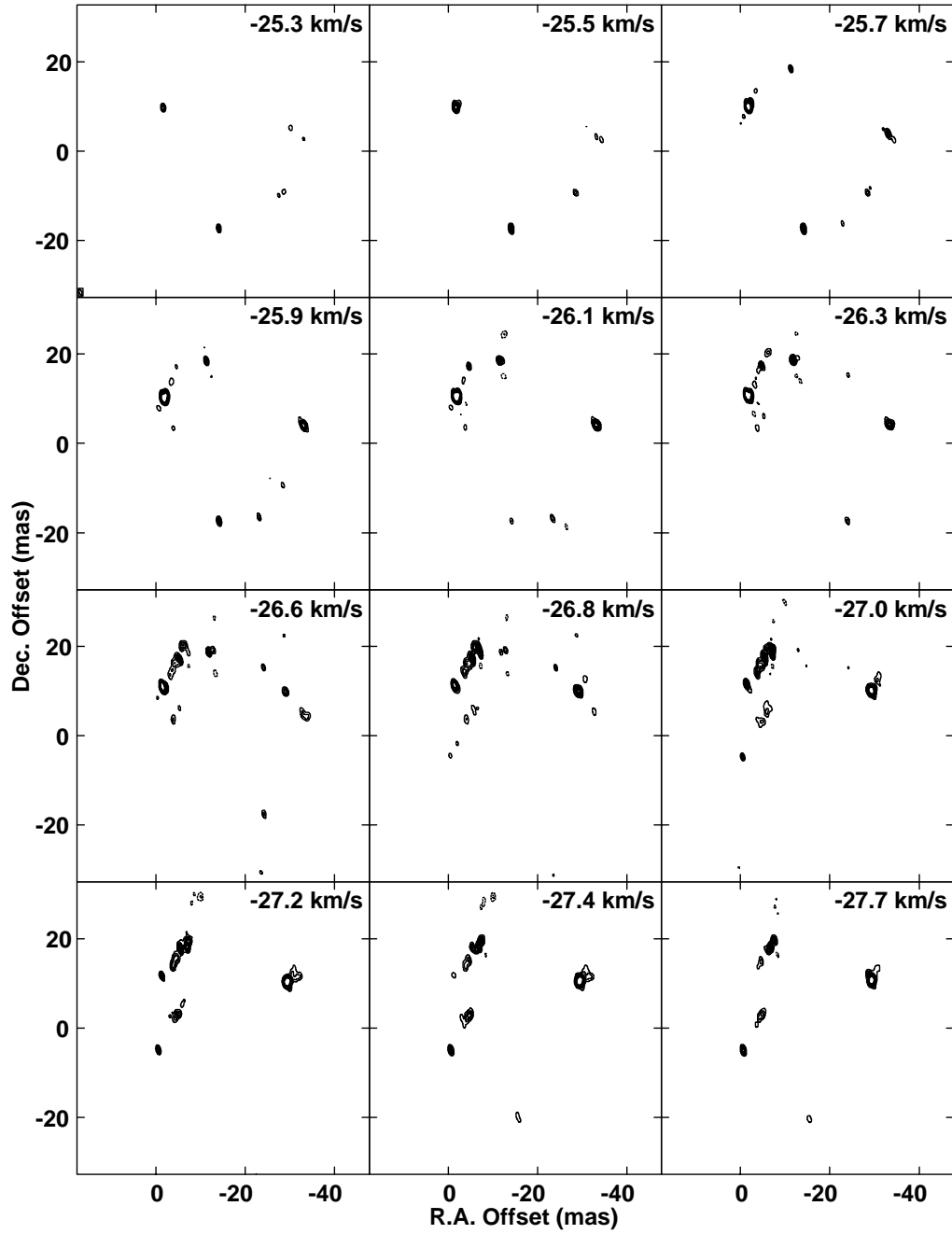


Figure A.2 continued.

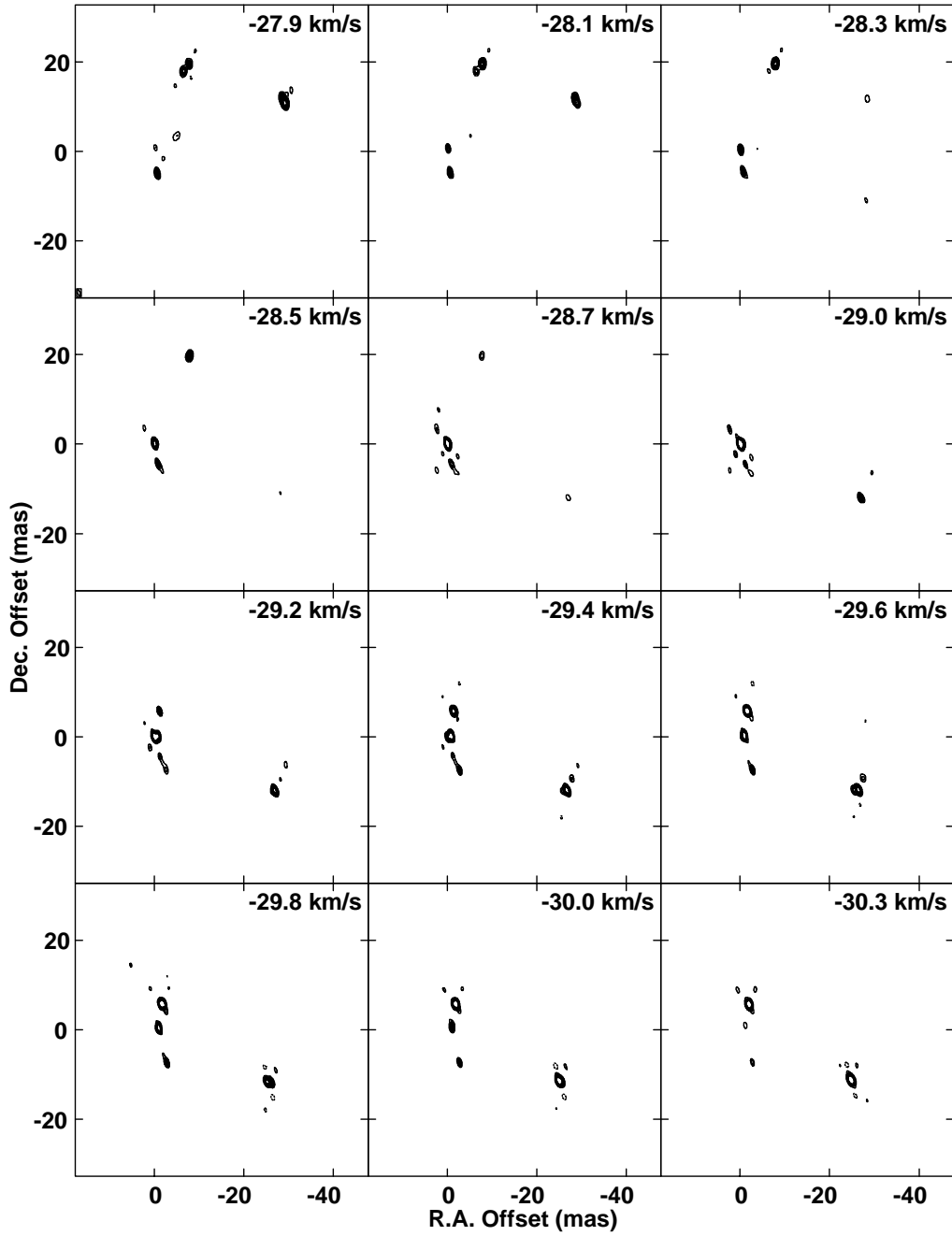


Figure A.2 continued.

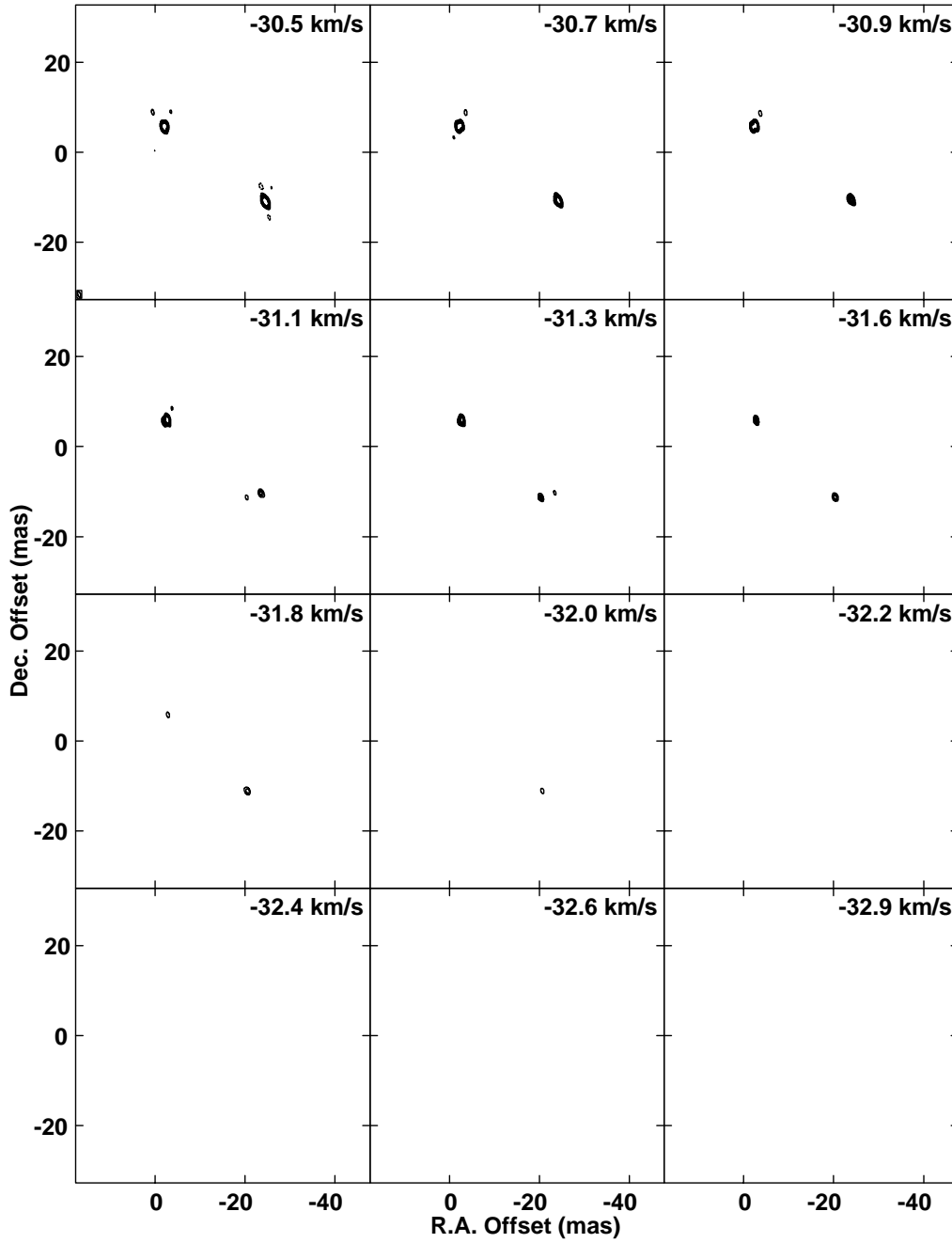


Figure A.2 continued.

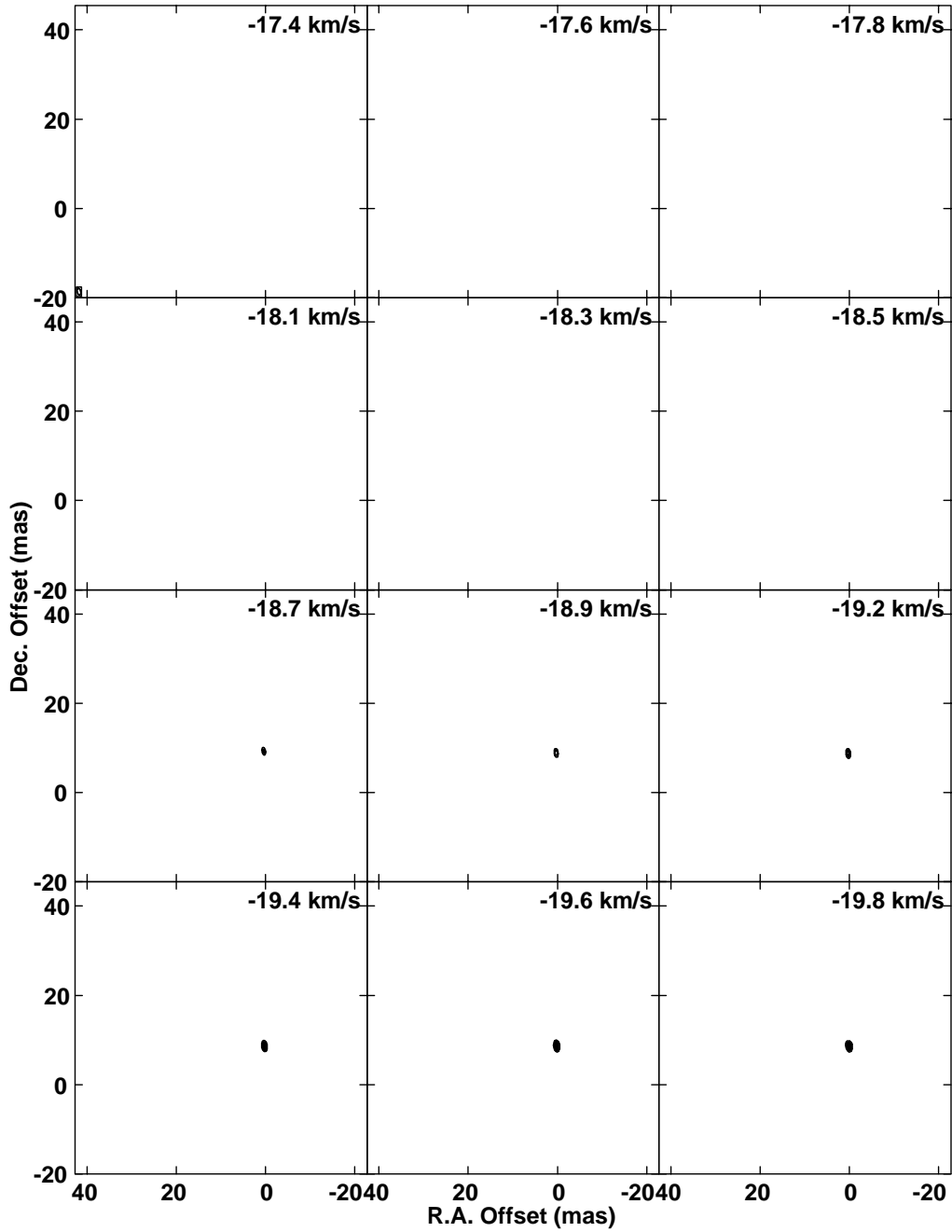


Figure A.3: Total intensity (Stokes  $I$ ) channel of the  $v = 1, J = 1 - 0$  43-GHz SiO maser emission towards R Aqr observed at Epoch 3. Contour levels are  $-40, -32, -24, -16, -8, -4, 4, 8, 16, 24, 32,$  and  $40\%$  of the peak flux density in the cube,  $14.8 \text{ Jy/beam}$ . The LSR velocity for each channel is stated in the upper right corner of each plane.

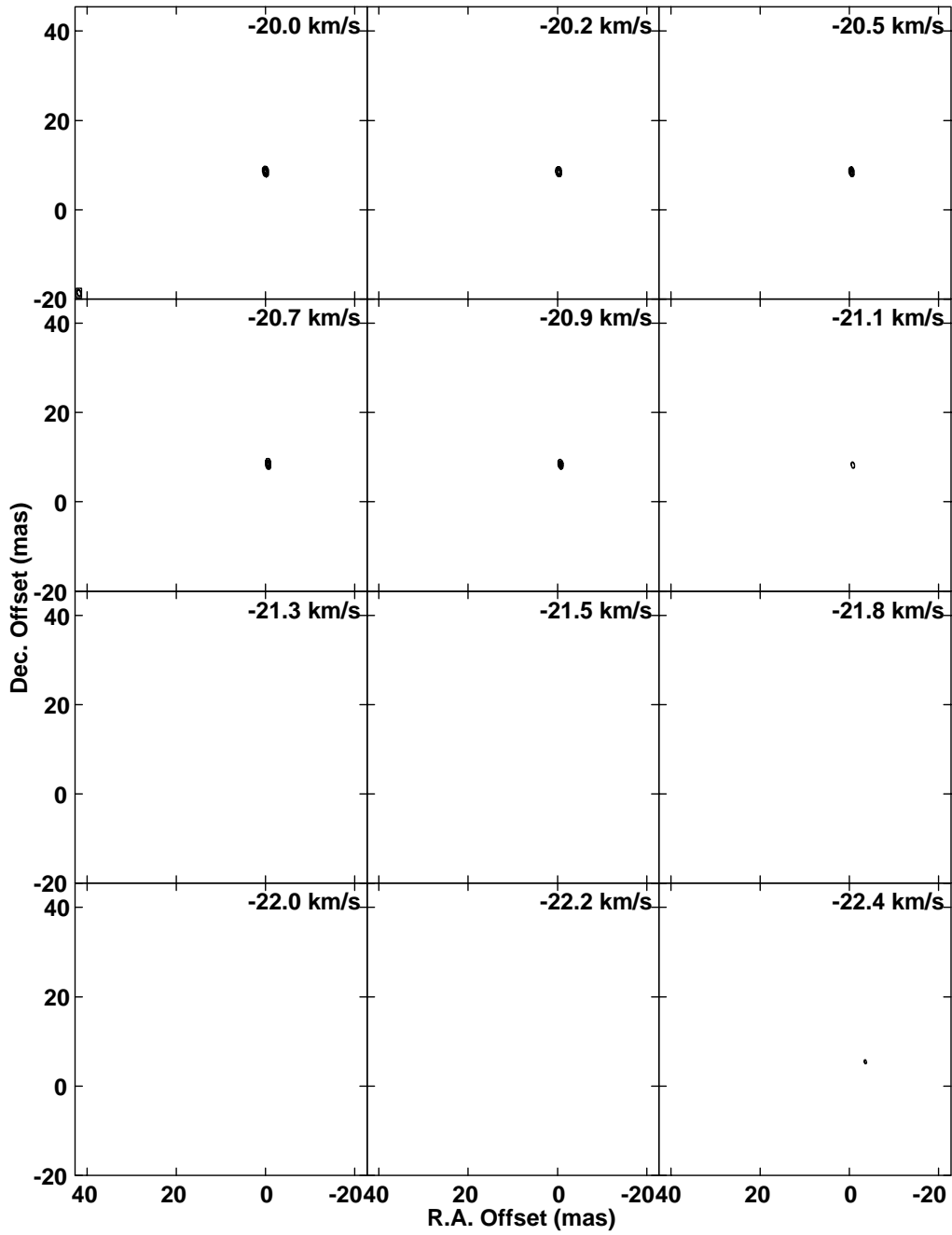


Figure A.3 continued.

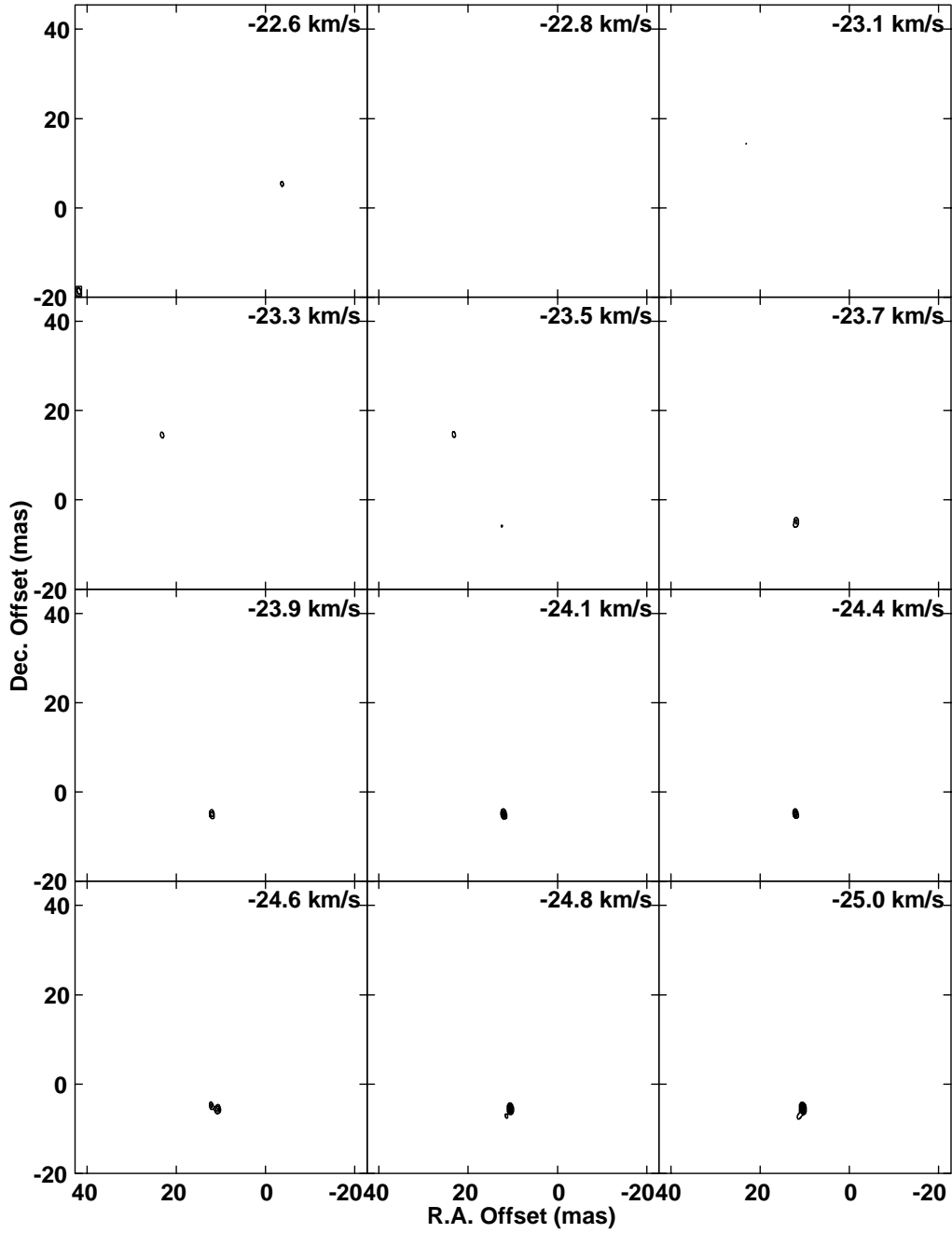


Figure A.3 continued.

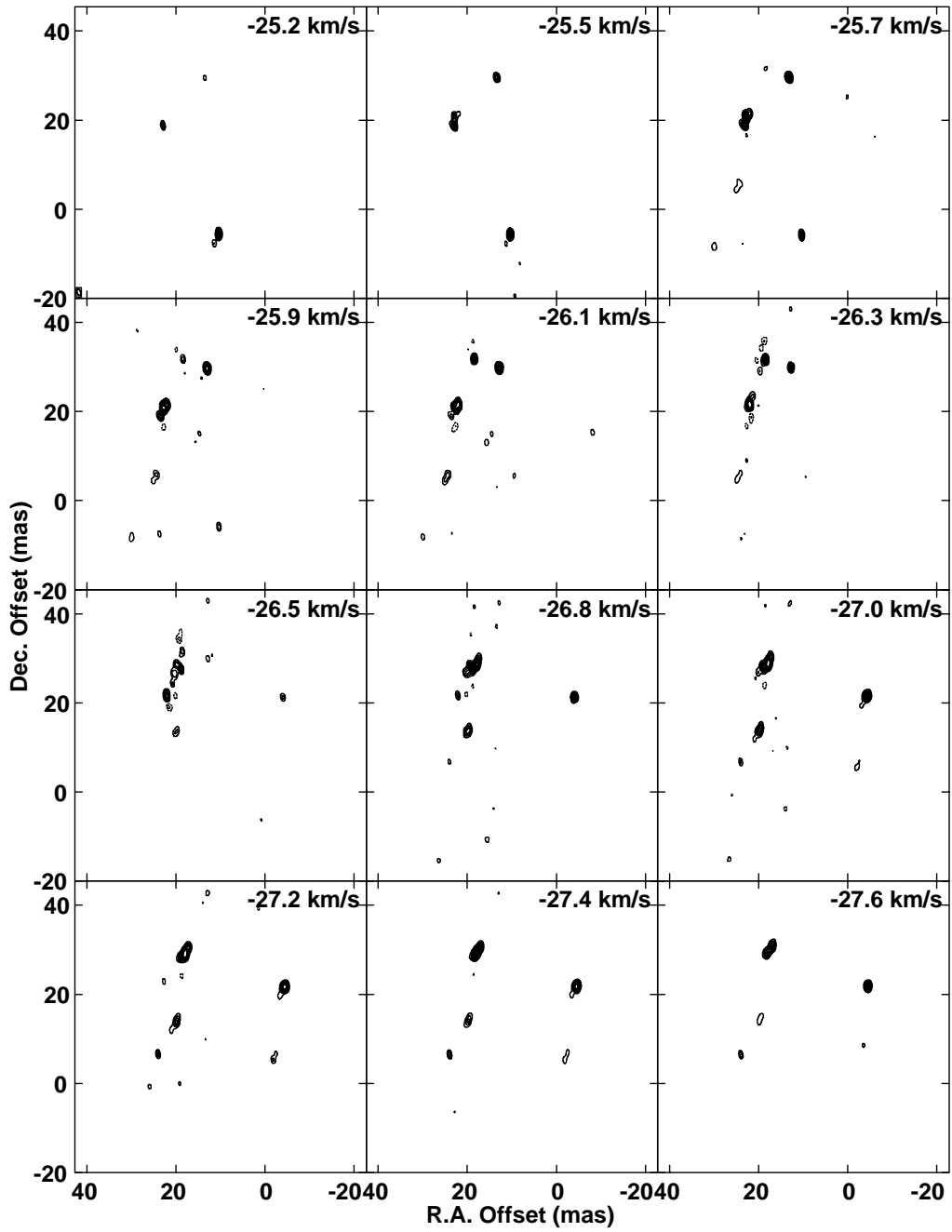


Figure A.3 continued.

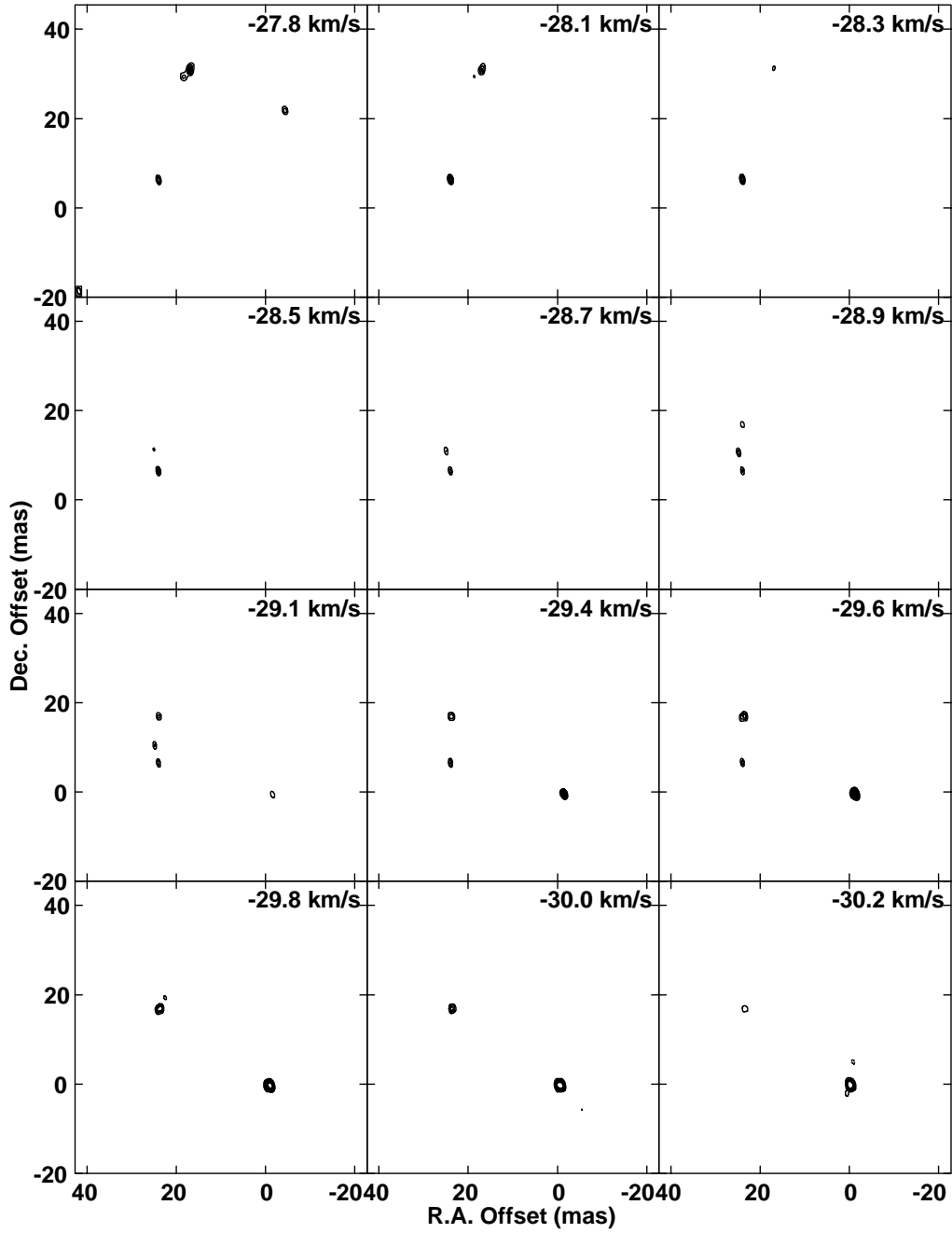


Figure A.3 continued.

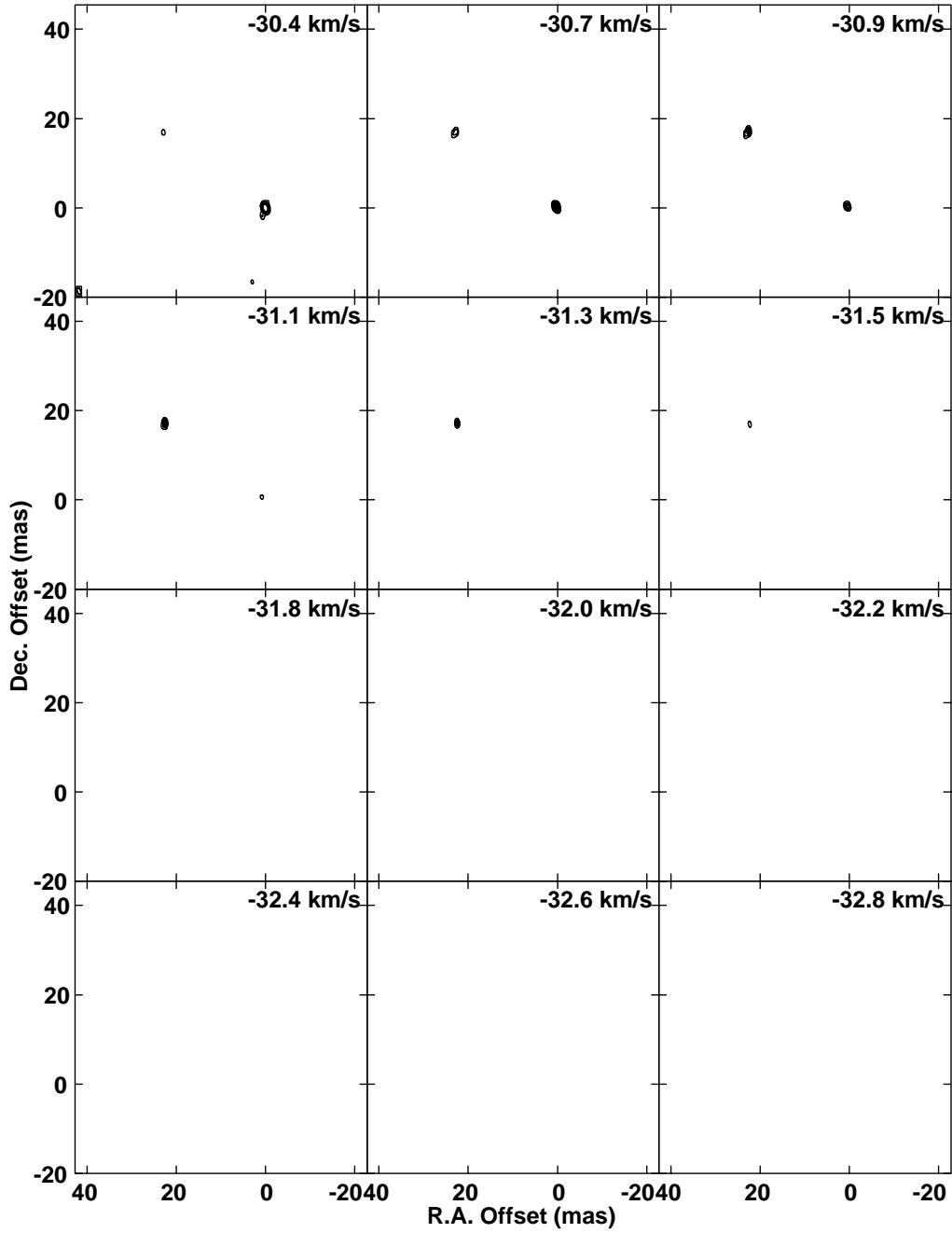


Figure A.3 continued.

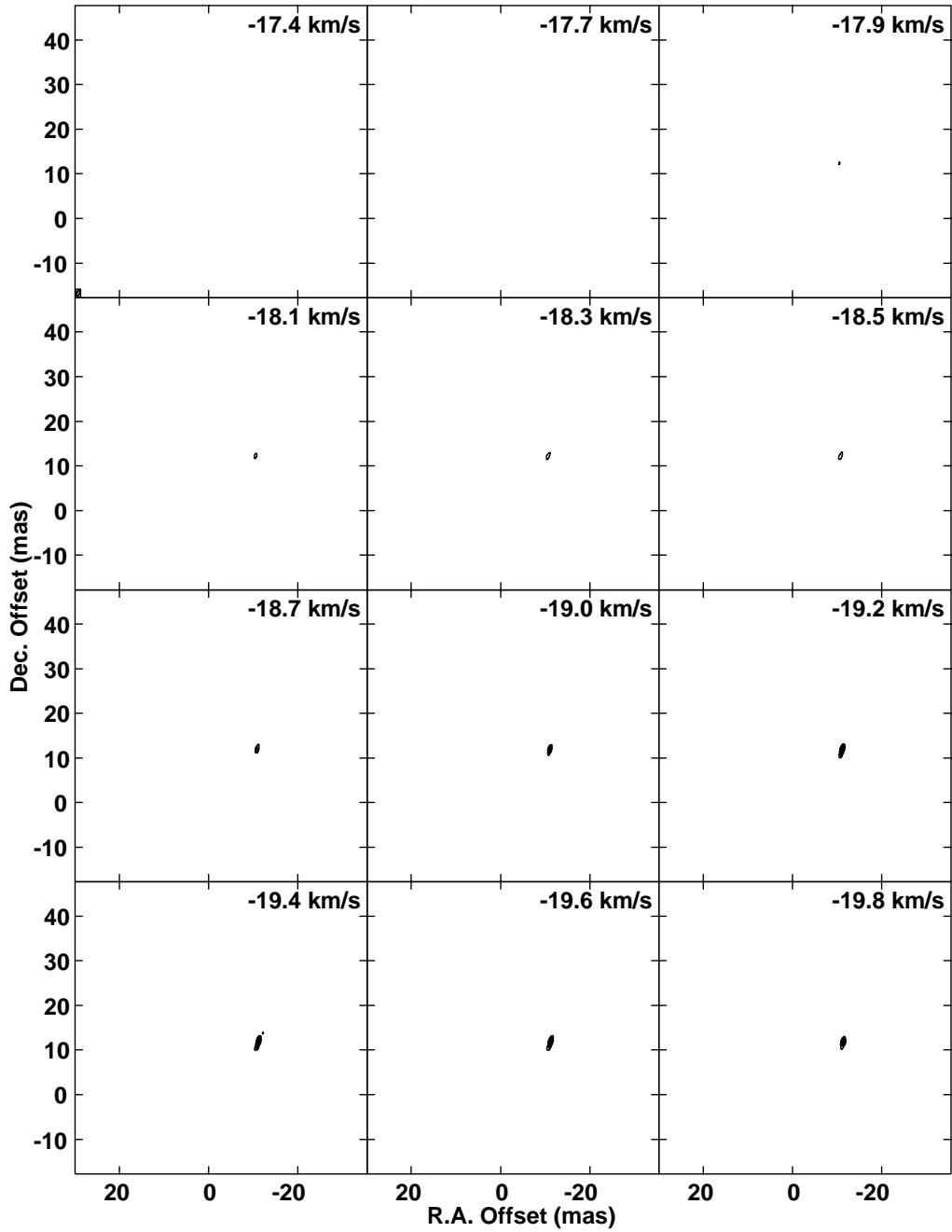


Figure A.4: Total intensity (Stokes  $I$ ) channel of the  $v = 1, J = 1 - 0$  43-GHz SiO maser emission towards R Aqr observed at Epoch 4. Contour levels are  $-20, -16, -12, -8, -4, -2, 2, 4, 8, 12, 16,$  and  $20\%$  of the peak flux density in the cube,  $20.5 \text{ Jy/beam}$ . The LSR velocity for each channel is stated in the upper right corner of each plane.

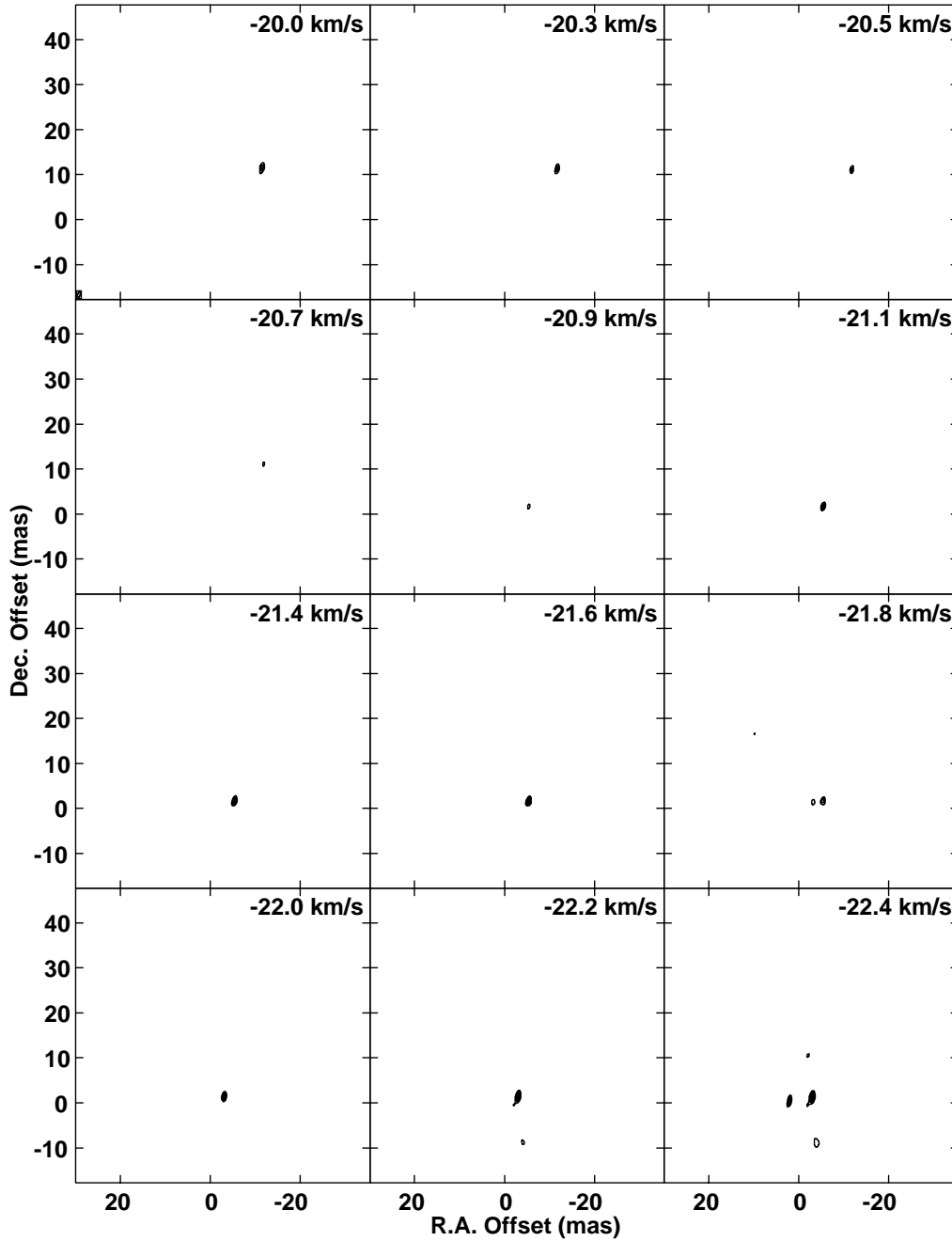


Figure A.4 continued.

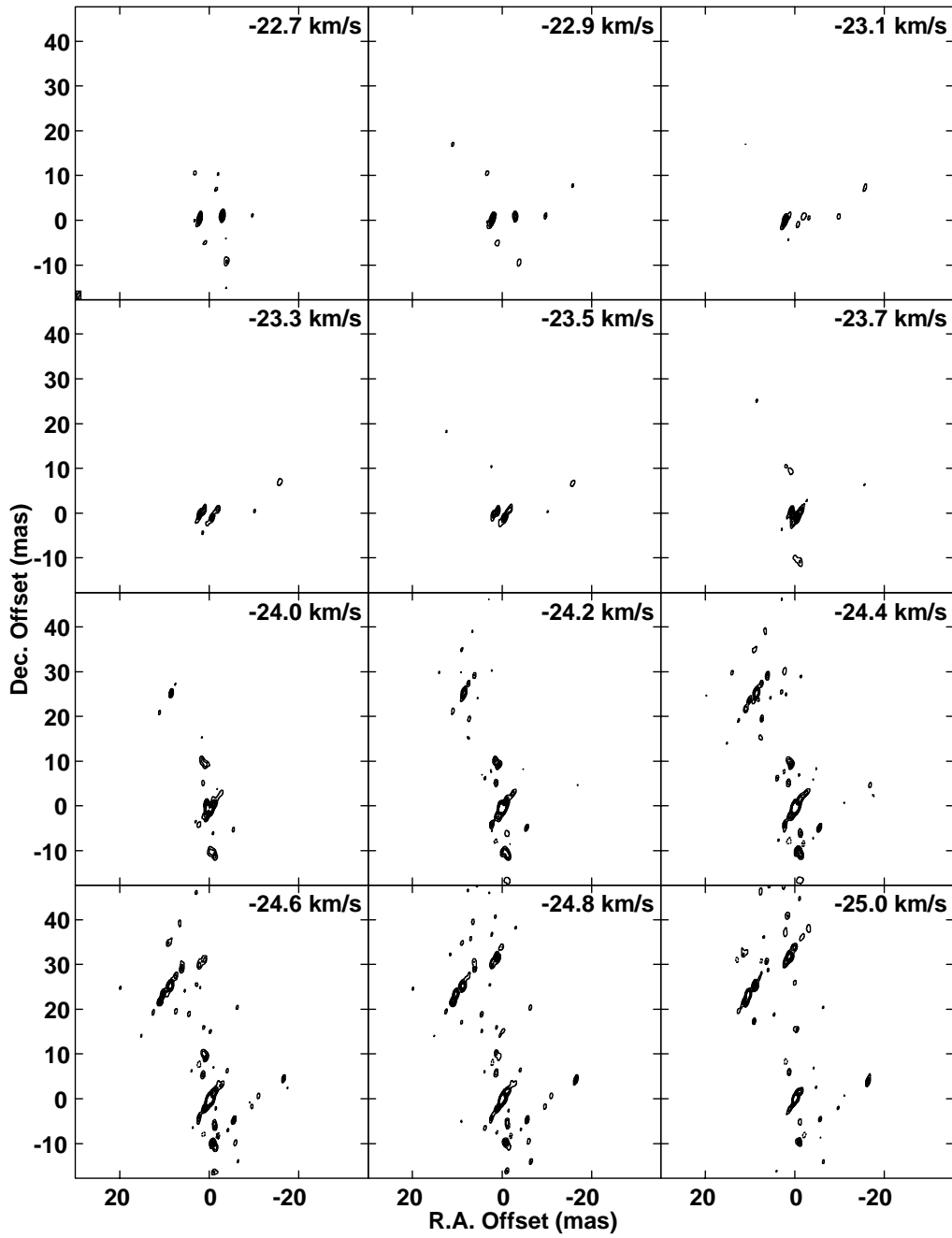


Figure A.4 continued.

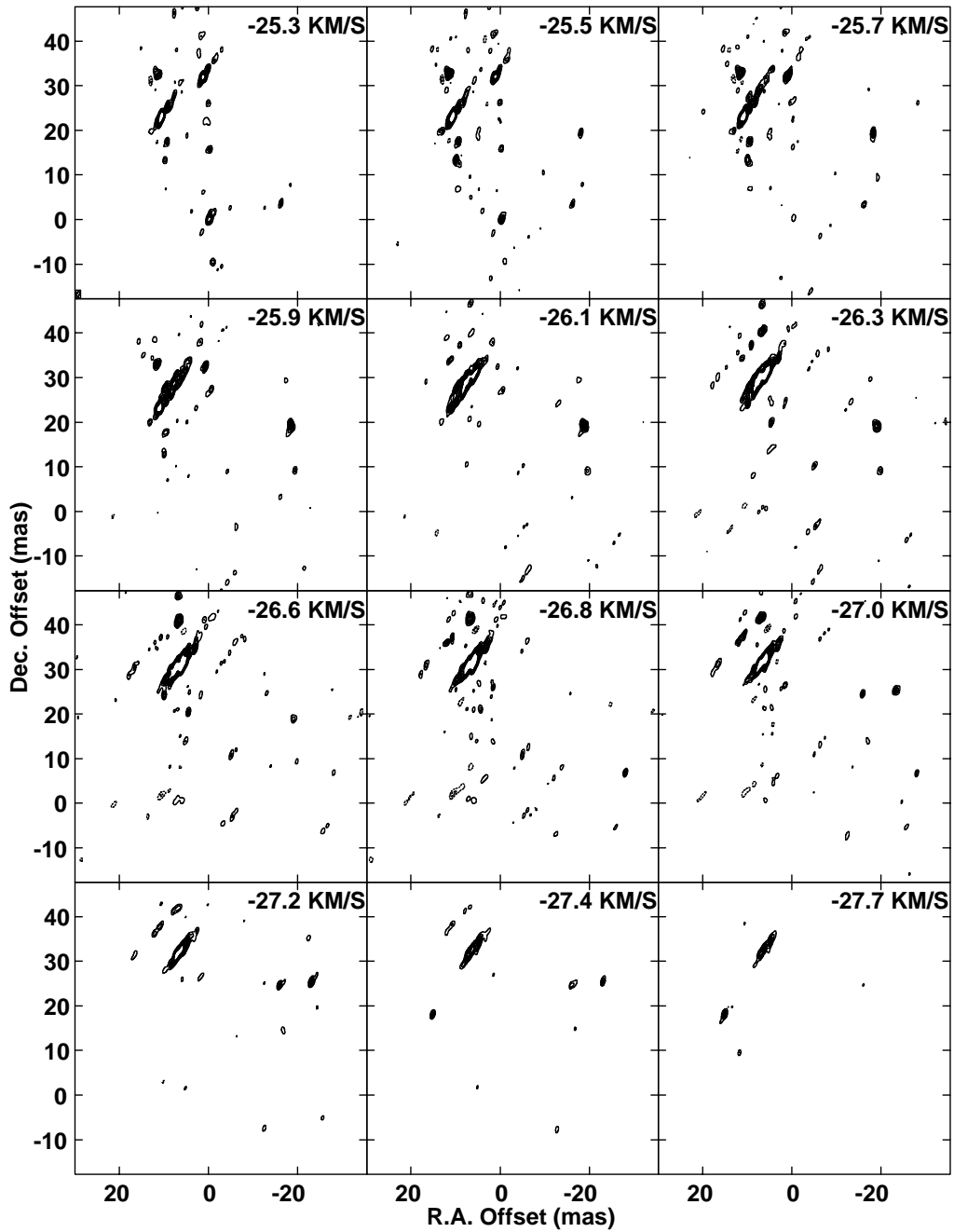


Figure A.4 continued.

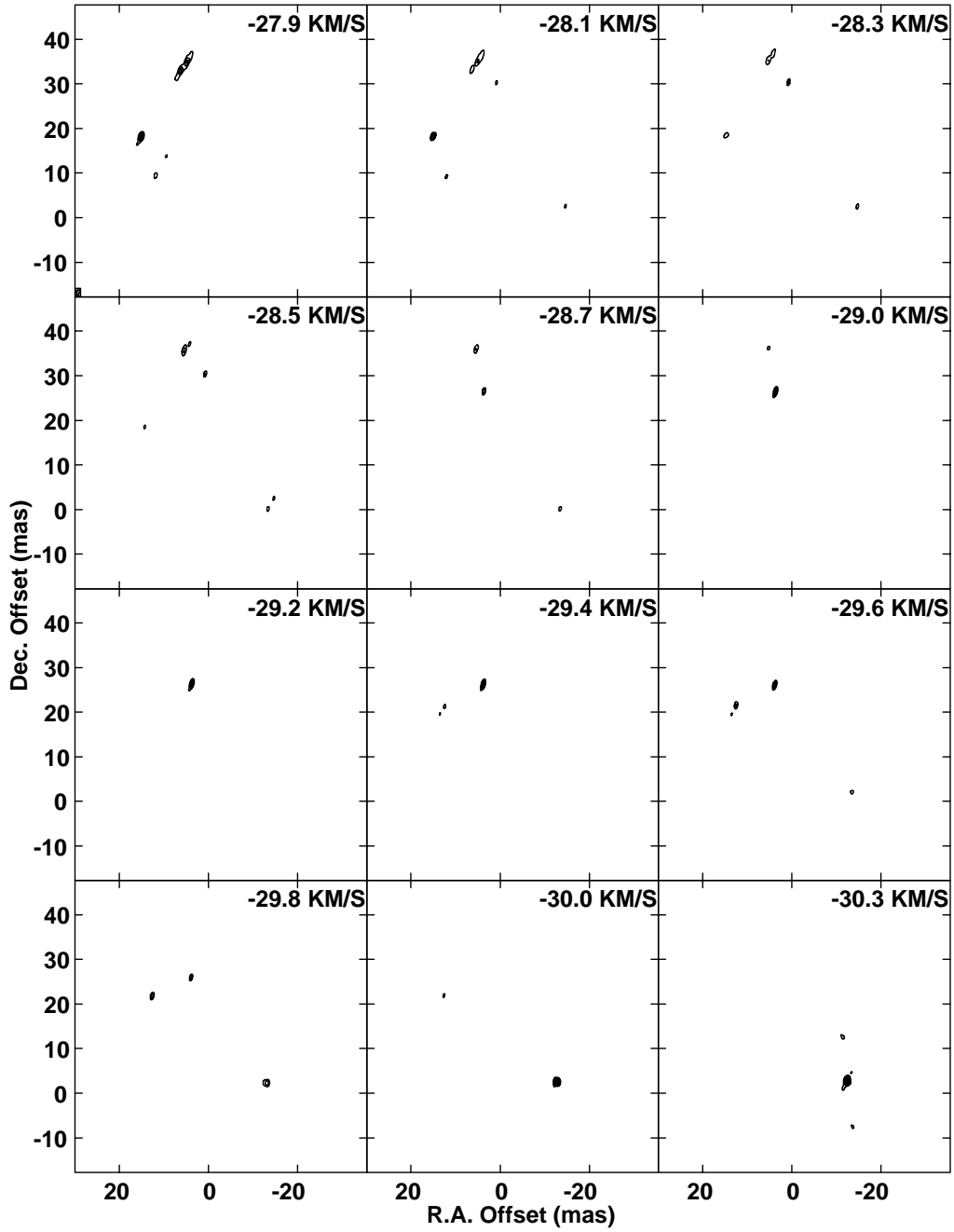


Figure A.4 continued.

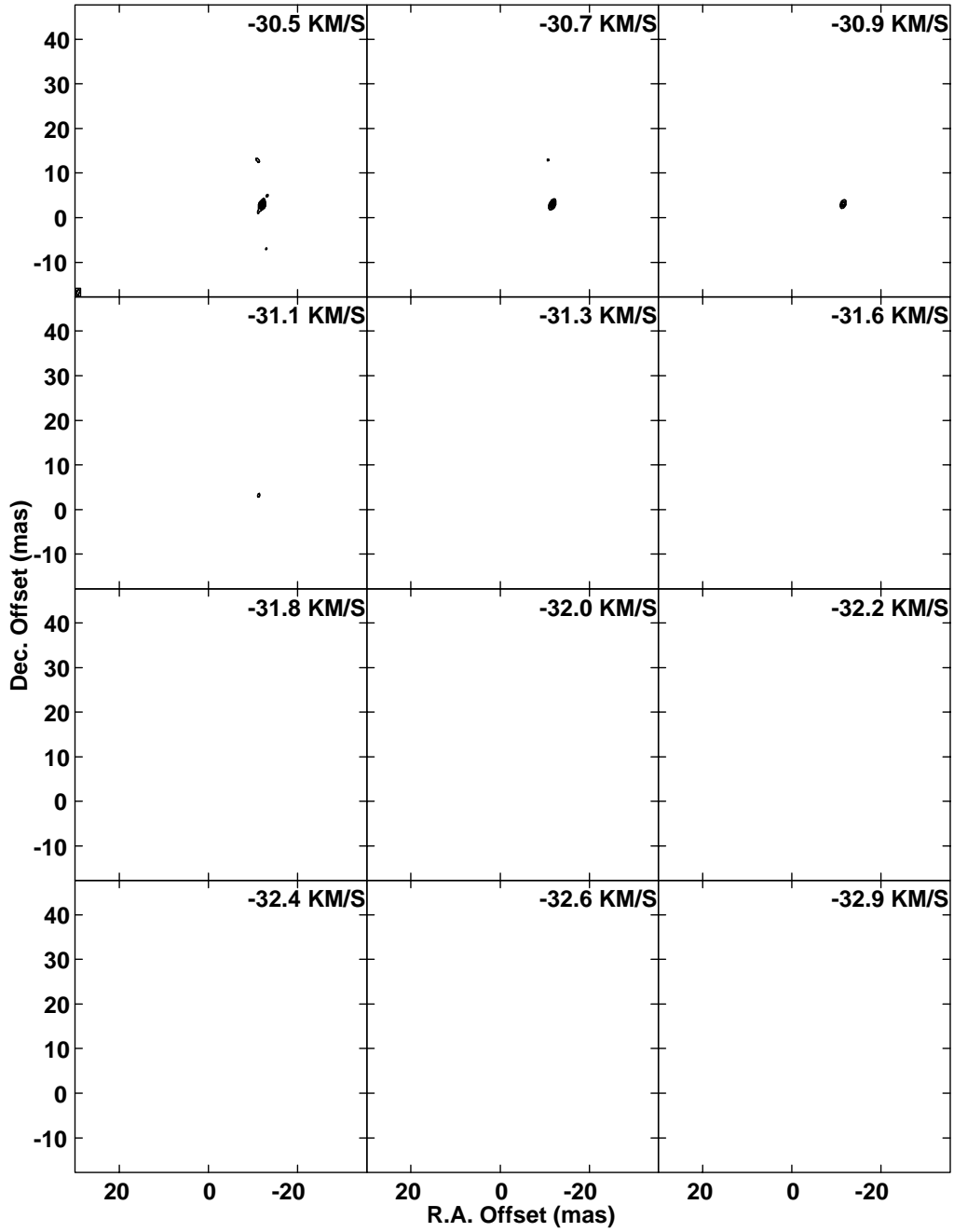


Figure A.4 continued.

# Appendix B

## COMPONENT LISTS FOR R AQUARI

This appendix contains the lists of components derived using the selection process described in § 5.3 for each of the four epochs of observations. Column 1 ( $v$ ) represents the LSR velocity of the component. Columns 2–5 ( $\alpha, \sigma_\alpha, \delta, \sigma_\delta$ ) list the offset in right ascension and declination of the component with respect to the reference feature for that particular epoch and the associated positional errors. Columns 6–13 ( $I, \sigma_I, Q, \sigma_Q, U, \sigma_U, V, \sigma_V$ ) represent the maximum flux in each of the four Stokes parameters for the component and their uncertainties. Columns 14 and 15 list the degree of circular polarization  $m_c$  and its associated error  $\sigma_c$  where zeroes indicate that the fractional polarization was below the rejection criteria  $u_c$  described in § 6.2. Columns 15–18 represent the fractional linear polarization  $m_l$ , its associated error  $\sigma_l$ , the linear polarization position angle  $\chi$ , and its associated uncertainty  $\sigma_\chi$ . Zeroes represent linear polarization values below the rejection criteria  $u_l$ . The fractional linear polarization has been corrected for bias as described in § 6.2.

Table B.1: List of components for Epoch 1

$v$ (km s <sup>-1</sup> )	$\alpha$ (mas)	$\sigma_\alpha$ (mas)	$\delta$ (mas)	$\sigma_\delta$ (mas)	$I$ (Jy)	$\sigma_I$ (Jy)	$Q$ (Jy)	$\sigma_Q$ (Jy)	$U$ (Jy)	$\sigma_U$ (Jy)	$V$ (Jy)	$\sigma_V$ (Jy)	$m_c$ (%)	$\sigma_c$ (%)	$m_l$ (%)	$\sigma_l$ (%)	$\chi$ (deg.)	$\sigma_\chi$ (deg.)
-28.917	27.491	0.026	-15.868	0.049	1.118	0.040	-0.051	0.009	0.016	0.008	0.008	0.009	0.0	0.0	4.7	0.8	169.3	4.3
-28.855	27.981	0.035	-15.292	0.066	1.113	0.101	-0.044	0.010	0.025	0.009	-0.011	0.018	0.0	0.0	4.5	1.0	163.2	5.2
-28.261	-2.577	0.041	-12.038	0.077	1.097	0.151	0.016	0.014	0.330	0.013	0.040	0.029	0.0	0.0	30.1	4.3	131.6	1.2
-28.245	2.336	0.040	-3.215	0.076	1.242	0.151	-0.085	0.014	0.115	0.013	0.036	0.030	0.0	0.0	11.5	1.8	151.2	2.7
-28.235	0.372	0.031	-0.187	0.059	26.626	0.151	-4.354	0.014	3.348	0.013	1.069	0.029	4.0	0.1	20.6	0.1	159.2	0.1
-28.233	2.625	0.040	11.962	0.075	1.182	0.151	-0.028	0.014	0.155	0.013	-0.024	0.029	0.0	0.0	13.3	2.0	138.1	2.5
-28.207	-2.142	0.040	3.374	0.075	1.332	0.138	0.043	0.014	0.089	0.013	0.017	0.029	0.0	0.0	7.4	1.2	120.1	4.0
-28.155	-0.113	0.008	0.048	0.014	29.087	0.151	2.147	0.014	6.514	0.013	0.962	0.030	3.3	0.1	23.6	0.1	123.9	0.1
-28.155	1.809	0.031	-2.687	0.059	1.312	0.151	-0.105	0.014	0.185	0.013	-0.026	0.030	0.0	0.0	16.2	2.1	147.8	1.9
-27.773	2.586	0.034	11.685	0.063	1.400	0.137	-0.043	0.011	0.056	0.011	0.016	0.030	0.0	0.0	5.0	0.9	151.8	4.5
-27.739	0.589	0.003	-0.455	0.005	32.329	0.179	-2.302	0.012	2.182	0.013	1.069	0.033	3.3	0.1	9.8	0.1	156.3	0.1
-27.547	0.323	0.033	-12.542	0.063	1.547	0.191	0.014	0.015	0.112	0.018	-0.030	0.035	0.0	0.0	7.2	1.5	129.4	3.8
-27.310	-0.484	0.027	3.190	0.050	10.123	0.208	-2.633	0.016	4.417	0.018	0.640	0.035	6.3	0.4	50.8	1.1	148.4	0.1
-27.265	0.375	0.012	3.133	0.023	7.879	0.208	-4.310	0.016	1.923	0.018	0.140	0.035	1.8	0.4	59.9	1.6	166.0	0.1
-27.206	-2.281	0.023	-9.046	0.043	3.329	0.208	-0.013	0.016	0.097	0.018	0.054	0.035	0.0	0.0	2.9	0.6	136.8	4.7
-27.197	-4.969	0.012	-3.400	0.023	12.909	0.208	-0.425	0.016	-3.455	0.018	0.279	0.035	2.2	0.3	27.0	0.5	39.5	0.1
-27.117	1.084	0.010	-0.065	0.018	12.699	0.208	-0.328	0.016	-0.106	0.018	0.223	0.035	1.8	0.3	2.7	0.1	7.0	1.5
-27.114	1.025	0.044	-27.560	0.083	30.144	0.208	7.345	0.016	3.296	0.018	0.225	0.035	0.7	0.1	26.7	0.2	100.1	0.1
-27.074	2.309	0.028	2.825	0.053	9.180	0.208	0.250	0.016	1.497	0.018	-0.617	0.035	-6.7	0.4	16.5	0.4	128.3	0.3
-27.064	-1.661	0.026	-23.168	0.048	3.308	0.208	-1.979	0.016	-1.326	0.018	0.091	0.035	2.8	1.1	72.0	4.6	14.9	0.2
-27.024	5.842	0.040	-2.651	0.076	1.909	0.208	0.010	0.016	0.262	0.018	-0.067	0.035	0.0	0.0	13.7	1.8	131.9	1.7
-26.971	2.761	0.022	2.377	0.041	6.390	0.208	0.623	0.016	1.076	0.018	-0.113	0.035	-1.8	0.6	19.5	0.7	118.0	0.4
-26.956	-1.953	0.045	-8.900	0.085	2.694	0.191	-0.013	0.018	0.012	0.018	0.063	0.035	0.0	0.0	0.0	0.0	0.0	0.0
-26.932	-5.529	0.024	-3.003	0.044	8.075	0.208	-0.204	0.016	-1.221	0.015	0.032	0.027	0.0	0.0	15.3	0.4	38.3	0.4
-26.889	1.617	0.013	-0.334	0.025	6.675	0.208	0.014	0.016	0.069	0.015	0.251	0.027	3.8	0.4	1.0	0.2	127.3	6.5
-26.521	1.366	0.021	-26.427	0.040	19.041	0.172	3.878	0.018	2.235	0.014	-0.049	0.024	-0.3	0.1	23.5	0.2	103.0	0.1
-26.429	-1.872	0.038	-8.038	0.072	1.649	0.148	0.028	0.018	-0.168	0.014	0.022	0.024	0.0	0.0	10.3	1.3	47.7	3.0
-26.326	-3.596	0.029	-20.925	0.055	7.864	0.172	-1.222	0.018	0.294	0.014	0.194	0.024	2.5	0.3	16.0	0.4	171.2	0.3
-26.229	-1.668	0.043	-21.537	0.081	1.371	0.148	0.014	0.018	-0.027	0.014	0.023	0.024	0.0	0.0	0.0	0.0	0.0	0.0
-26.114	-4.590	0.030	-16.659	0.057	27.227	0.148	-2.451	0.018	-6.946	0.014	0.198	0.024	0.7	0.1	27.1	0.2	33.3	0.1

Continued on next page.

Table B.1 continued.

$v$ (km s <sup>-1</sup> )	$\alpha$ (mas)	$\sigma_\alpha$ (mas)	$\delta$ (mas)	$\sigma_\delta$ (mas)	$I$ (Jy)	$\sigma_I$ (Jy)	$Q$ (Jy)	$\sigma_Q$ (Jy)	$U$ (Jy)	$\sigma_U$ (Jy)	$V$ (Jy)	$\sigma_V$ (Jy)	$m_c$ (%)	$\sigma_c$ (%)	$m_l$ (%)	$\sigma_l$ (%)	$\chi$ (deg.)	$\sigma_\chi$ (deg.)
-26.111	-7.400	0.042	-30.276	0.080	0.986	0.148	0.048	0.018	0.058	0.014	0.032	0.024	0.0	0.0	7.5	1.9	113.2	6.3
-26.072	8.966	0.028	-27.524	0.052	3.124	0.148	0.158	0.018	0.434	0.014	0.067	0.024	2.1	0.8	14.8	0.8	123.0	1.1
-25.831	8.893	0.028	-26.562	0.052	1.956	0.145	0.404	0.011	0.174	0.012	0.073	0.012	3.7	0.7	22.5	1.8	99.7	0.8
-25.373	6.800	0.017	-26.340	0.032	0.718	0.047	-0.023	0.008	0.015	0.009	-0.013	0.007	0.0	0.0	3.6	1.1	161.4	9.1
-25.095	13.481	0.017	-28.223	0.033	0.511	0.023	-0.040	0.011	0.094	0.009	0.012	0.008	0.0	0.0	19.9	2.0	144.5	3.0
-24.743	12.013	0.018	-27.000	0.034	0.459	0.017	0.126	0.011	0.034	0.009	0.020	0.009	4.4	2.0	28.4	2.6	95.6	2.0
-23.801	33.013	0.017	-4.894	0.032	0.912	0.016	-0.498	0.007	-0.487	0.010	-0.088	0.008	-9.6	0.9	76.4	1.6	20.2	0.4
-23.759	0.798	0.013	-18.690	0.025	0.696	0.016	-0.022	0.007	0.074	0.010	0.017	0.008	2.4	1.2	11.0	1.4	141.3	2.7
-23.735	32.652	0.008	-5.109	0.016	1.081	0.016	-0.499	0.010	-0.475	0.010	-0.182	0.008	-16.8	0.8	63.7	1.3	19.8	0.4
-23.055	1.070	0.008	-18.411	0.016	1.369	0.017	0.011	0.010	0.270	0.009	0.027	0.010	2.0	0.7	19.7	0.7	131.8	1.1
-22.889	1.859	0.012	-18.060	0.022	0.580	0.017	-0.012	0.008	0.054	0.007	0.011	0.009	0.0	0.0	9.4	1.2	139.3	4.1
-22.589	7.311	0.013	-24.423	0.024	1.135	0.017	0.037	0.008	0.257	0.007	0.045	0.010	4.0	0.9	22.9	0.7	128.9	0.9
-22.478	2.138	0.009	-18.147	0.017	0.780	0.017	-0.046	0.009	0.079	0.009	0.012	0.010	0.0	0.0	11.7	1.2	148.1	2.8
-22.374	9.081	0.033	-25.763	0.062	0.792	0.017	0.069	0.009	0.233	0.009	-0.023	0.010	-2.9	1.3	30.7	1.3	124.8	1.1
-22.147	7.333	0.016	-24.260	0.029	0.930	0.014	0.033	0.009	0.186	0.009	0.022	0.008	2.4	0.9	20.3	1.0	128.0	1.4
-21.887	5.485	0.009	-20.740	0.017	0.678	0.014	-0.016	0.010	0.162	0.009	0.036	0.008	5.3	1.2	24.0	1.4	135.8	1.8
-19.813	5.312	0.015	-13.375	0.028	0.522	0.013	0.025	0.008	0.068	0.014	0.032	0.007	6.1	1.3	13.7	2.6	122.9	3.5
-19.094	5.915	0.007	-13.677	0.014	0.725	0.015	-0.008	0.008	0.144	0.009	0.034	0.007	4.7	1.0	19.9	1.3	134.6	1.6

Table B.2: List of components for Epoch 2

$v$ (km s <sup>-1</sup> )	$\alpha$ (mas)	$\sigma_\alpha$ (mas)	$\delta$ (mas)	$\sigma_\delta$ (mas)	$I$ (Jy)	$\sigma_I$ (Jy)	$Q$ (Jy)	$\sigma_Q$ (Jy)	$U$ (Jy)	$\sigma_U$ (Jy)	$V$ (Jy)	$\sigma_V$ (Jy)	$m_c$ (%)	$\sigma_c$ (%)	$m_l$ (%)	$\sigma_l$ (%)	$\chi$ (deg.)	$\sigma_\chi$ (deg.)
-31.499	-20.458	0.016	-11.225	0.029	0.778	0.019	0.023	0.010	0.171	0.009	-0.010	0.010	0.0	0.0	22.1	1.3	143.2	1.7
-31.031	-2.712	0.008	5.951	0.016	4.966	0.040	0.182	0.010	-0.448	0.009	-0.051	0.010	-1.0	0.2	9.7	0.2	68.1	0.6
-30.981	-23.511	0.014	-10.461	0.025	1.186	0.025	0.084	0.009	0.285	0.009	-0.080	0.008	-6.7	0.7	25.0	0.9	138.8	0.9
-30.766	-23.988	0.011	-10.633	0.021	2.712	0.040	-0.483	0.010	0.769	0.009	-0.248	0.008	-9.1	0.3	33.5	0.6	163.1	0.3
-30.479	-2.030	0.005	5.615	0.008	5.556	0.072	-1.589	0.010	-0.631	0.009	-0.354	0.009	-6.4	0.2	30.8	0.4	22.8	0.2
-29.798	-1.859	0.009	5.769	0.016	4.527	0.072	-1.865	0.011	-0.868	0.011	-0.464	0.008	-10.2	0.2	45.4	0.8	24.5	0.2
-29.707	-2.745	0.032	-7.360	0.061	1.959	0.072	0.097	0.011	0.998	0.011	-0.022	0.009	-1.1	0.5	51.2	2.0	144.2	0.3
-29.617	-1.366	0.006	5.716	0.011	4.791	0.072	-0.949	0.011	0.215	0.011	-0.470	0.008	-9.8	0.2	20.3	0.4	185.6	0.3
-29.545	-0.968	0.014	0.267	0.026	5.557	0.072	0.815	0.011	0.643	0.011	-0.209	0.008	-3.8	0.2	18.7	0.3	121.1	0.3
-29.481	-26.479	0.007	-11.850	0.013	3.626	0.065	-0.889	0.011	-0.461	0.011	-0.042	0.008	-1.2	0.2	27.6	0.6	25.7	0.3
-29.299	-26.933	0.018	-12.002	0.034	3.466	0.050	-0.998	0.011	-0.599	0.009	-0.063	0.008	-1.8	0.2	33.6	0.6	27.5	0.2
-29.156	-0.675	0.012	0.139	0.022	3.505	0.065	0.433	0.009	0.258	0.011	-0.185	0.008	-5.3	0.2	14.4	0.4	117.4	0.6
-29.138	-1.237	0.029	-4.434	0.053	0.656	0.050	0.056	0.011	0.010	0.009	-0.008	0.008	0.0	0.0	8.5	1.8	107.1	4.6
-28.980	0.996	0.046	-2.268	0.086	0.546	0.037	0.128	0.011	-0.012	0.009	-0.048	0.008	-8.8	1.6	23.5	2.6	99.3	2.0
-28.934	-0.024	0.006	-0.007	0.011	9.885	0.050	2.645	0.011	0.204	0.009	-0.297	0.008	-3.0	0.1	26.8	0.2	104.2	0.1
-28.391	-0.755	0.009	-4.375	0.018	1.271	0.033	0.157	0.011	-0.063	0.010	-0.027	0.008	-2.1	0.6	13.3	0.9	91.1	1.7
-28.386	-8.105	0.021	19.892	0.039	1.971	0.029	-0.059	0.011	-0.243	0.009	-0.023	0.008	-1.2	0.4	12.7	0.5	50.2	1.2
-28.151	-0.234	0.032	0.649	0.059	1.081	0.047	0.222	0.010	0.051	0.010	-0.014	0.009	0.0	0.0	21.1	1.3	108.5	1.3
-28.149	-7.765	0.007	19.457	0.012	3.059	0.047	-0.195	0.011	-0.417	0.010	-0.060	0.009	-2.0	0.3	15.0	0.4	44.5	0.7
-27.944	-28.541	0.021	11.831	0.039	2.541	0.047	-0.710	0.010	0.527	0.010	-0.090	0.009	-3.5	0.4	34.8	0.8	173.7	0.3
-27.941	-6.537	0.025	17.923	0.046	1.543	0.047	0.027	0.010	-0.405	0.010	-0.026	0.009	-1.7	0.6	26.3	1.0	58.9	0.7
-27.753	-29.333	0.009	10.731	0.016	4.113	0.053	-0.109	0.010	0.530	0.010	-0.083	0.010	-2.0	0.2	13.2	0.3	152.8	0.5
-27.602	-0.618	0.023	-4.969	0.043	3.036	0.089	0.639	0.010	0.046	0.010	-0.075	0.010	-2.5	0.3	21.1	0.7	104.1	0.4
-27.432	-7.425	0.014	19.533	0.027	1.766	0.089	-0.188	0.010	-0.563	0.010	-0.031	0.010	-1.8	0.6	33.6	1.8	47.8	0.5
-27.427	-29.773	0.012	10.834	0.022	4.513	0.089	0.307	0.010	0.831	0.010	-0.099	0.010	-2.2	0.2	19.6	0.4	136.9	0.3
-27.410	-4.362	0.030	2.431	0.056	0.930	0.089	0.020	0.010	-0.015	0.010	-0.071	0.010	-7.6	1.3	0.0	0.0	0.0	0.0
-27.401	-4.911	0.034	3.098	0.064	1.161	0.089	0.024	0.010	-0.013	0.010	-0.028	0.010	-2.4	0.9	0.0	0.0	0.0	0.0
-27.381	-6.897	0.009	18.149	0.017	3.176	0.089	0.075	0.010	-1.167	0.010	-0.031	0.010	-1.0	0.3	36.8	1.1	58.8	0.2
-27.047	-29.000	0.021	10.016	0.039	3.630	0.086	-1.313	0.009	-0.123	0.008	-0.055	0.010	-1.5	0.3	36.3	0.9	14.7	0.2
-27.002	-1.419	0.017	11.546	0.032	2.604	0.086	0.254	0.009	-0.058	0.008	-0.127	0.010	-4.9	0.4	10.0	0.5	95.6	0.9

Continued on next page.

Table B.2 continued.

$v$ (km s <sup>-1</sup> )	$\alpha$ (mas)	$\sigma_\alpha$ (mas)	$\delta$ (mas)	$\sigma_\delta$ (mas)	$I$ (Jy)	$\sigma_I$ (Jy)	$Q$ (Jy)	$\sigma_Q$ (Jy)	$U$ (Jy)	$\sigma_U$ (Jy)	$V$ (Jy)	$\sigma_V$ (Jy)	$m_c$ (%)	$\sigma_c$ (%)	$m_l$ (%)	$\sigma_l$ (%)	$\chi$ (deg.)	$\sigma_\chi$ (deg.)
-26.941	-3.775	0.032	14.368	0.060	1.052	0.086	-0.007	0.009	-0.044	0.008	0.020	0.010	1.9	1.0	4.2	0.8	52.5	5.8
-26.856	-4.209	0.024	15.902	0.044	1.431	0.068	-0.014	0.009	-0.039	0.008	-0.040	0.010	-2.8	0.7	2.8	0.6	47.1	6.1
-26.624	-12.807	0.048	19.143	0.091	0.703	0.068	-0.362	0.009	0.076	0.008	0.032	0.010	4.6	1.5	52.6	5.2	186.1	0.6
-26.611	-24.076	0.052	15.269	0.098	0.571	0.068	-0.051	0.009	-0.419	0.008	-0.026	0.010	-4.6	1.8	73.9	8.9	53.5	0.6
-26.515	-3.923	0.038	3.580	0.072	0.566	0.068	0.024	0.013	-0.039	0.008	-0.009	0.010	0.0	0.0	7.9	1.9	72.8	7.4
-26.447	-11.761	0.044	18.665	0.083	1.639	0.083	-0.707	0.010	-0.576	0.010	-0.084	0.010	-5.1	0.7	55.6	2.9	31.6	0.3
-26.352	-4.721	0.043	17.230	0.080	0.880	0.083	-0.021	0.013	-0.266	0.010	-0.026	0.009	-3.0	1.1	30.3	3.1	54.7	1.4
-26.235	-33.594	0.028	4.131	0.053	1.967	0.083	0.184	0.010	0.035	0.010	-0.031	0.009	-1.6	0.5	9.5	0.6	107.4	1.5
-26.123	-3.228	0.035	13.197	0.066	0.468	0.058	0.055	0.009	0.015	0.008	-0.139	0.008	-29.7	4.1	12.0	2.4	109.6	4.1
-26.112	-2.223	0.005	10.739	0.010	4.317	0.083	0.383	0.013	0.049	0.010	-0.060	0.008	-1.4	0.2	8.9	0.3	105.6	0.7
-25.965	-32.996	0.009	4.059	0.017	2.638	0.083	-0.108	0.013	0.331	0.010	0.010	0.008	0.0	0.0	13.2	0.6	156.0	1.0
-25.964	-11.310	0.042	18.473	0.078	1.520	0.083	-0.520	0.013	-0.446	0.010	-0.030	0.008	-2.0	0.5	45.1	2.6	32.3	0.5
-25.889	-1.720	0.012	10.048	0.023	6.474	0.044	1.180	0.013	0.069	0.009	-0.192	0.009	-3.0	0.1	18.3	0.2	103.7	0.2
-25.673	-14.070	0.021	-17.485	0.040	2.039	0.044	-0.026	0.013	0.305	0.010	-0.153	0.009	-7.5	0.5	15.0	0.6	149.4	1.2
-25.652	-1.661	0.025	9.809	0.048	5.523	0.026	1.041	0.010	-0.127	0.010	-0.130	0.009	-2.4	0.2	19.0	0.2	98.5	0.3
-25.635	-28.414	0.033	-9.315	0.061	0.586	0.044	-0.060	0.013	0.188	0.009	-0.023	0.009	-3.9	1.6	33.6	3.0	155.9	1.8
-25.556	-14.239	0.013	-17.061	0.024	0.834	0.026	-0.029	0.010	0.279	0.009	-0.075	0.009	-9.0	1.1	33.6	1.5	150.0	1.0
-24.933	-28.893	0.029	-8.626	0.055	0.927	0.026	-0.139	0.010	0.173	0.010	-0.017	0.009	0.0	0.0	23.9	1.3	166.4	1.3
-24.499	-28.856	0.033	-8.529	0.062	1.372	0.015	-0.242	0.009	0.008	0.009	-0.028	0.009	-2.0	0.7	17.6	0.7	191.1	1.1
-23.211	-28.243	0.012	-5.739	0.023	0.981	0.015	-0.226	0.009	0.336	0.010	-0.044	0.009	-4.5	0.9	41.3	1.2	164.0	0.7
-20.910	-25.908	0.012	-2.628	0.022	0.554	0.013	-0.078	0.010	0.067	0.010	-0.021	0.010	-3.8	1.8	18.5	1.8	171.7	2.8
-20.382	-25.199	0.009	-3.190	0.016	2.470	0.020	-0.647	0.010	0.543	0.010	-0.113	0.009	-4.6	0.4	34.2	0.5	172.0	0.3
-19.643	-25.419	0.003	-2.371	0.006	2.431	0.015	-0.497	0.010	0.237	0.009	-0.032	0.010	-1.3	0.4	22.6	0.4	179.3	0.5
-19.285	-24.961	0.004	-2.641	0.007	2.282	0.013	-0.445	0.010	0.191	0.009	-0.098	0.010	-4.3	0.4	21.2	0.4	180.4	0.5
-18.368	-23.816	0.013	-1.566	0.024	0.599	0.012	-0.074	0.009	0.158	0.009	0.007	0.010	0.0	0.0	29.1	1.6	159.5	1.5
-17.718	-23.595	0.007	0.058	0.013	0.950	0.012	-0.109	0.010	0.146	0.010	0.018	0.011	0.0	0.0	19.2	1.1	165.4	1.6

Table B.3: List of components for Epoch 3

$v$ (km s <sup>-1</sup> )	$\alpha$ (mas)	$\sigma_\alpha$ (mas)	$\delta$ (mas)	$\sigma_\delta$ (mas)	$I$ (Jy)	$\sigma_I$ (Jy)	$Q$ (Jy)	$\sigma_Q$ (Jy)	$U$ (Jy)	$\sigma_U$ (Jy)	$V$ (Jy)	$\sigma_V$ (Jy)	$m_c$ (%)	$\sigma_c$ (%)	$m_l$ (%)	$\sigma_l$ (%)	$\chi$ (deg.)	$\sigma_\chi$ (deg.)
-31.091	22.489	0.023	17.229	0.046	3.126	0.076	-0.186	0.039	-0.021	0.057	-0.279	0.052	-8.9	1.7	5.8	1.2	23.2	8.7
-30.799	23.251	0.021	16.468	0.042	1.651	0.086	-0.058	0.040	-0.079	0.057	-0.260	0.060	-15.7	3.7	0.0	0.0	0.0	0.0
-30.761	22.782	0.056	16.930	0.113	1.754	0.180	-0.028	0.050	-0.057	0.051	-0.137	0.060	-7.8	3.5	0.0	0.0	0.0	0.0
-30.701	0.630	0.010	0.313	0.021	4.377	0.086	0.051	0.040	0.124	0.057	-1.042	0.060	-23.8	1.4	0.0	0.0	0.0	0.0
-30.270	-0.083	0.008	-0.145	0.016	11.609	0.224	-0.469	0.050	2.029	0.065	-2.599	0.065	-22.4	0.7	17.9	0.7	161.5	0.7
-30.093	-0.528	0.008	-0.228	0.017	8.108	0.196	-0.235	0.065	1.519	0.065	-2.004	0.075	-24.7	1.1	18.9	0.9	159.4	1.2
-29.871	-1.063	0.017	-0.310	0.034	9.664	0.224	-0.591	0.065	1.732	0.062	-2.306	0.075	-23.9	1.0	18.9	0.8	164.4	1.0
-29.814	23.487	0.048	16.954	0.097	2.617	0.224	-0.074	0.065	-0.258	0.065	-0.245	0.075	-9.4	3.0	10.0	2.6	57.0	6.9
-29.529	-1.534	0.017	-0.464	0.035	6.095	0.113	-0.537	0.044	1.300	0.057	-1.603	0.039	-26.3	0.8	23.1	1.0	166.2	0.9
-29.458	24.062	0.056	16.752	0.112	2.109	0.145	0.155	0.065	-0.775	0.057	-0.223	0.075	-10.6	3.6	37.4	3.7	70.7	2.3
-29.014	24.837	0.016	10.575	0.033	1.631	0.083	-0.149	0.047	-0.305	0.057	-0.027	0.039	0.0	0.0	20.6	3.5	52.0	4.1
-28.665	24.948	0.042	11.031	0.084	1.281	0.085	-0.033	0.053	-0.202	0.047	-0.040	0.044	0.0	0.0	15.5	3.7	60.4	7.4
-28.145	23.986	0.020	6.409	0.041	3.082	0.138	0.417	0.053	0.254	0.060	-0.222	0.067	-7.2	2.2	15.7	1.9	125.7	3.4
-28.118	23.999	0.059	6.625	0.119	2.144	0.213	0.357	0.074	0.273	0.053	-0.094	0.042	-4.4	2.0	20.8	3.7	128.7	3.9
-28.116	16.730	0.029	31.359	0.058	1.504	0.080	0.018	0.036	-0.091	0.034	-0.052	0.054	0.0	0.0	5.7	2.1	70.6	11.1
-27.872	18.287	0.031	29.433	0.063	1.816	0.106	-0.089	0.036	-0.192	0.039	-0.113	0.048	-6.2	2.7	11.5	2.2	52.6	4.9
-27.714	16.948	0.008	30.849	0.015	5.360	0.114	-0.681	0.036	-0.664	0.060	-1.355	0.067	-25.3	1.4	17.7	1.0	42.1	1.5
-27.655	19.915	0.066	14.015	0.132	1.270	0.114	0.049	0.036	-0.110	0.060	-0.055	0.067	0.0	0.0	0.0	0.0	0.0	0.0
-27.438	19.483	0.068	14.676	0.137	1.812	0.138	-0.238	0.043	-0.140	0.056	-0.139	0.039	-7.7	2.2	15.0	2.8	35.2	5.5
-27.305	-4.638	0.018	21.811	0.037	6.566	0.213	-0.523	0.043	2.553	0.060	-1.473	0.067	-22.4	1.3	39.7	1.6	160.8	0.5
-27.264	-1.915	0.040	5.361	0.080	1.577	0.196	-0.152	0.043	0.106	0.056	-0.145	0.041	-9.2	2.8	11.3	3.2	182.6	8.1
-27.142	17.864	0.010	29.123	0.020	10.956	0.213	-1.274	0.074	-2.242	0.060	-2.100	0.067	-19.2	0.7	23.5	0.7	50.2	0.8
-27.136	-4.104	0.056	21.442	0.113	6.190	0.280	-2.139	0.074	1.947	0.056	-1.297	0.053	-21.0	1.3	46.7	2.4	178.8	0.6
-26.958	20.086	0.025	13.435	0.050	3.148	0.213	-0.158	0.074	-0.604	0.053	-0.134	0.042	-4.3	1.4	19.7	2.2	57.7	3.3
-26.936	19.534	0.028	14.211	0.056	2.937	0.213	-0.110	0.074	-0.550	0.053	-0.430	0.042	-14.6	1.8	19.0	2.3	59.3	3.7
-26.716	18.954	0.024	27.807	0.049	7.956	0.280	-0.160	0.074	-0.097	0.053	-0.974	0.053	-12.2	0.8	2.2	0.8	35.6	9.1
-26.640	20.286	0.051	26.616	0.102	2.432	0.280	-0.106	0.061	-0.035	0.045	-0.352	0.053	-14.5	2.7	0.0	0.0	0.0	0.0
-26.232	22.028	0.045	21.599	0.090	9.151	0.280	0.274	0.061	0.436	0.066	-1.596	0.072	-17.4	1.0	5.6	0.7	138.9	3.5
-26.226	12.691	0.023	29.844	0.046	3.875	0.252	-3.167	0.056	-0.544	0.066	-0.617	0.067	-15.9	2.0	82.9	5.6	24.9	0.6
-26.191	18.382	0.036	31.789	0.072	4.623	0.252	-0.545	0.056	-0.787	0.066	-0.149	0.072	-3.2	1.6	20.7	1.8	47.6	1.8

Continued on next page.

Table B.3 continued.

$v$ (km s <sup>-1</sup> )	$\alpha$ (mas)	$\sigma_\alpha$ (mas)	$\delta$ (mas)	$\sigma_\delta$ (mas)	$I$ (Jy)	$\sigma_I$ (Jy)	$Q$ (Jy)	$\sigma_Q$ (Jy)	$U$ (Jy)	$\sigma_U$ (Jy)	$V$ (Jy)	$\sigma_V$ (Jy)	$m_c$ (%)	$\sigma_c$ (%)	$m_l$ (%)	$\sigma_l$ (%)	$\chi$ (deg.)	$\sigma_\chi$ (deg.)
-25.942	24.936	0.069	4.608	0.138	1.632	0.244	-0.127	0.056	0.056	0.066	-0.122	0.072	0.0	0.0	0.0	0.0	0.0	0.0
-25.933	24.321	0.042	5.803	0.084	1.882	0.244	0.068	0.056	0.059	0.066	-0.124	0.072	0.0	0.0	0.0	0.0	0.0	0.0
-25.914	23.458	0.053	19.027	0.107	3.842	0.244	0.038	0.056	0.174	0.066	-0.074	0.072	0.0	0.0	0.0	0.0	0.0	0.0
-25.910	12.950	0.026	29.679	0.052	6.048	0.244	-3.547	0.060	-0.768	0.066	-0.934	0.072	-15.4	1.3	60.0	2.6	26.1	0.5
-25.855	22.765	0.014	20.822	0.029	8.850	0.244	0.238	0.060	0.507	0.066	-1.188	0.072	-13.4	0.9	6.3	0.7	142.4	3.1
-25.776	13.339	0.040	29.634	0.081	5.166	0.204	-3.022	0.060	-0.631	0.054	-0.873	0.072	-16.9	1.5	59.7	2.6	25.9	0.5
-25.534	23.020	0.017	18.886	0.034	5.406	0.138	-1.224	0.060	0.654	0.054	-0.261	0.048	-4.8	0.9	25.6	1.3	185.9	1.1
-25.340	10.184	0.012	-5.403	0.024	3.634	0.130	-0.021	0.060	-0.133	0.054	-0.898	0.042	-24.7	1.5	0.0	0.0	0.0	0.0
-25.302	11.347	0.046	-7.664	0.093	1.345	0.130	0.041	0.060	-0.035	0.054	-0.125	0.042	-9.3	3.2	0.0	0.0	0.0	0.0
-25.189	10.482	0.012	-5.648	0.023	6.599	0.138	-0.080	0.060	-0.236	0.054	-1.033	0.058	-15.7	0.9	3.7	0.8	55.6	6.8
-24.927	11.210	0.032	-6.950	0.066	1.064	0.108	-0.070	0.050	-0.035	0.041	-0.065	0.057	0.0	0.0	0.0	0.0	0.0	0.0
-24.247	13.071	0.058	-7.322	0.117	0.469	0.078	0.098	0.047	-0.088	0.038	-0.075	0.058	0.0	0.0	0.0	0.0	0.0	0.0
-24.155	12.027	0.031	-4.906	0.063	2.730	0.078	0.313	0.057	-0.063	0.054	-0.459	0.058	-16.8	2.2	11.5	2.1	104.3	4.9
-23.576	12.456	0.086	-5.858	0.173	0.785	0.081	0.067	0.057	-0.036	0.054	-0.157	0.061	-20.0	8.0	0.0	0.0	0.0	0.0
-23.335	23.174	0.045	14.557	0.091	1.053	0.088	0.208	0.052	0.035	0.054	0.024	0.061	0.0	0.0	19.4	5.1	114.8	7.3
-22.567	-3.661	0.052	5.344	0.104	0.924	0.108	-0.050	0.043	0.180	0.054	-0.099	0.051	0.0	0.0	19.5	6.0	162.8	6.7
-20.626	-0.569	0.017	8.482	0.034	2.937	0.077	-0.230	0.075	1.221	0.060	-0.312	0.052	-10.6	1.8	42.2	2.3	160.3	1.7
-19.637	0.148	0.013	8.635	0.026	4.616	0.095	-0.522	0.054	1.221	0.051	-0.610	0.065	-13.2	1.4	28.7	1.3	166.6	1.2
-18.685	0.386	0.029	9.283	0.058	1.400	0.073	-0.129	0.035	0.047	0.032	-0.112	0.051	-8.0	3.7	9.5	2.5	190.0	6.8

Table B.4: List of components for Epoch 4

$v$ (km s <sup>-1</sup> )	$\alpha$ (mas)	$\sigma_\alpha$ (mas)	$\delta$ (mas)	$\sigma_\delta$ (mas)	$I$ (Jy)	$\sigma_I$ (Jy)	$Q$ (Jy)	$\sigma_Q$ (Jy)	$U$ (Jy)	$\sigma_U$ (Jy)	$V$ (Jy)	$\sigma_V$ (Jy)	$m_c$ (%)	$\sigma_c$ (%)	$m_l$ (%)	$\sigma_l$ (%)	$\chi$ (deg.)	$\sigma_\chi$ (deg.)
-30.784	-11.334	0.013	2.924	0.025	0.997	0.023	0.019	0.009	0.058	0.010	-0.007	0.009	0.0	0.0	6.0	1.0	155.9	4.3
-30.464	-11.983	0.003	2.941	0.007	1.936	0.023	0.030	0.011	0.246	0.010	-0.028	0.009	-1.4	0.5	12.8	0.5	161.5	1.3
-29.069	3.706	0.014	26.398	0.028	1.927	0.014	0.367	0.009	-0.101	0.011	0.058	0.009	3.0	0.5	19.7	0.5	112.3	0.8
-28.722	5.336	0.016	36.084	0.031	0.649	0.014	0.036	0.009	0.002	0.011	-0.009	0.009	0.0	0.0	5.3	1.3	121.6	8.7
-28.629	-13.423	0.014	0.220	0.028	0.413	0.014	0.142	0.012	0.168	0.011	-0.008	0.012	0.0	0.0	53.2	3.3	144.9	1.5
-28.351	-14.659	0.017	2.516	0.033	0.416	0.016	-0.012	0.012	0.133	0.011	-0.024	0.012	-5.8	2.9	32.0	2.9	167.6	2.6
-28.329	0.751	0.033	30.350	0.065	0.620	0.024	0.044	0.012	-0.050	0.009	-0.008	0.012	0.0	0.0	10.6	1.7	95.7	4.6
-28.312	4.207	0.012	36.468	0.024	0.623	0.016	0.033	0.009	-0.033	0.011	-0.010	0.008	0.0	0.0	7.3	1.6	97.5	6.2
-27.864	14.826	0.008	18.304	0.016	0.893	0.024	0.083	0.012	-0.218	0.011	-0.096	0.012	-10.8	1.4	26.1	1.4	85.4	1.5
-27.750	11.794	0.045	9.475	0.089	0.528	0.028	-0.017	0.008	0.050	0.011	0.011	0.009	0.0	0.0	9.8	2.1	174.4	4.5
-27.698	15.252	0.006	18.067	0.011	1.843	0.028	-0.031	0.009	-0.179	0.011	-0.112	0.009	-6.1	0.5	9.8	0.6	70.1	1.4
-27.368	-16.681	0.030	25.021	0.059	0.553	0.055	0.262	0.008	0.039	0.011	0.016	0.009	0.0	0.0	47.9	5.0	124.2	1.2
-27.189	-15.901	0.028	24.591	0.055	1.370	0.125	0.277	0.010	0.981	0.011	0.014	0.009	0.0	0.0	74.4	6.8	157.1	0.3
-27.133	11.890	0.030	36.430	0.060	1.062	0.125	0.010	0.010	-0.030	0.008	-0.075	0.008	-7.1	1.1	2.9	0.8	84.2	8.9
-26.940	5.902	0.003	32.553	0.006	11.435	0.130	0.399	0.010	-0.123	0.008	-0.276	0.011	-2.4	0.1	3.7	0.1	111.4	0.6
-26.873	10.820	0.043	37.317	0.085	1.274	0.130	0.019	0.010	0.010	0.009	0.021	0.011	0.0	0.0	0.0	0.0	0.0	0.0
-26.251	-19.100	0.032	18.886	0.064	1.834	0.104	0.028	0.010	0.321	0.011	0.006	0.010	0.0	0.0	17.6	1.2	162.5	0.9
-25.841	9.780	0.033	12.899	0.066	0.779	0.100	-0.015	0.012	-0.009	0.010	-0.025	0.012	-3.2	1.6	0.0	0.0	0.0	0.0
-25.775	-18.224	0.031	19.703	0.061	1.745	0.117	-0.743	0.010	0.819	0.010	-0.007	0.011	0.0	0.0	63.4	4.3	186.1	0.3
-25.724	13.063	0.033	19.922	0.065	0.925	0.117	0.017	0.010	0.016	0.011	-0.067	0.011	-7.2	1.5	0.0	0.0	0.0	0.0
-25.705	9.545	0.010	24.996	0.019	3.258	0.117	0.016	0.010	0.034	0.010	-0.169	0.011	-5.2	0.4	1.1	0.3	152.4	7.6
-25.661	0.106	0.043	26.325	0.085	0.703	0.117	-0.015	0.010	0.012	0.010	-0.014	0.011	0.0	0.0	0.0	0.0	0.0	0.0
-25.626	-16.212	0.036	3.423	0.070	0.852	0.117	0.076	0.010	0.304	0.010	0.006	0.011	0.0	0.0	36.8	5.2	158.0	0.9
-25.624	11.820	0.027	32.938	0.053	1.823	0.117	-0.016	0.011	0.012	0.012	-0.022	0.012	0.0	0.0	0.0	0.0	0.0	0.0
-25.608	0.707	0.037	32.265	0.074	3.468	0.117	0.019	0.010	0.230	0.011	-0.090	0.011	-2.6	0.3	6.6	0.4	162.6	1.2
-25.511	9.875	0.039	13.407	0.078	1.566	0.117	-0.021	0.011	0.021	0.012	-0.017	0.012	0.0	0.0	0.0	0.0	0.0	0.0
-25.449	10.597	0.003	23.103	0.006	15.193	0.117	-0.493	0.013	0.156	0.012	-0.177	0.012	-1.2	0.1	3.4	0.1	201.2	0.7
-25.393	11.224	0.048	32.525	0.094	1.698	0.117	0.021	0.013	0.006	0.012	-0.027	0.012	-1.6	0.7	0.0	0.0	0.0	0.0
-25.373	9.307	0.033	17.435	0.065	1.580	0.117	-0.025	0.013	0.015	0.012	-0.024	0.012	-1.5	0.8	0.0	0.0	0.0	0.0
-25.146	1.242	0.011	31.840	0.021	6.112	0.111	0.033	0.013	-0.050	0.012	-0.026	0.012	-0.4	0.2	1.0	0.2	91.7	6.1
-25.006	-0.805	0.036	-9.563	0.070	1.020	0.111	0.027	0.013	-0.008	0.012	-0.023	0.012	0.0	0.0	0.0	0.0	0.0	0.0

Continued on next page.

Table B.4 continued.

$v$ (km s <sup>-1</sup> )	$\alpha$ (mas)	$\sigma_\alpha$ (mas)	$\delta$ (mas)	$\sigma_\delta$ (mas)	$I$ (Jy)	$\sigma_I$ (Jy)	$Q$ (Jy)	$\sigma_Q$ (Jy)	$U$ (Jy)	$\sigma_U$ (Jy)	$V$ (Jy)	$\sigma_V$ (Jy)	$m_c$ (%)	$\sigma_c$ (%)	$m_l$ (%)	$\sigma_l$ (%)	$\chi$ (deg.)	$\sigma_\chi$ (deg.)
-24.990	9.066	0.016	25.299	0.032	2.876	0.121	0.014	0.013	0.019	0.012	-0.041	0.012	-1.4	0.4	0.0	0.0	0.0	0.0
-24.910	10.882	0.030	21.826	0.059	3.225	0.121	0.032	0.013	0.015	0.011	-0.071	0.010	-2.2	0.3	1.0	0.4	132.6	9.2
-24.788	-0.669	0.019	0.063	0.037	2.749	0.117	0.331	0.011	-0.070	0.012	-0.125	0.013	-4.5	0.5	12.3	0.7	114.0	1.0
-24.774	10.339	0.027	23.359	0.054	4.984	0.121	0.015	0.010	0.025	0.011	-0.058	0.010	-1.2	0.2	0.5	0.2	149.5	10.1
-24.698	0.012	0.007	-0.011	0.014	10.471	0.121	0.526	0.013	-0.193	0.012	-0.133	0.013	-1.3	0.1	5.3	0.1	109.9	0.6
-24.554	-5.532	0.031	-4.790	0.062	0.994	0.121	0.069	0.010	-0.014	0.011	0.015	0.013	0.0	0.0	7.0	1.3	114.3	4.5
-24.525	6.131	0.039	29.172	0.078	1.027	0.121	0.018	0.010	0.028	0.011	0.013	0.013	0.0	0.0	0.0	0.0	0.0	0.0
-24.452	8.564	0.015	25.160	0.030	6.607	0.121	0.030	0.013	-0.024	0.011	0.025	0.013	0.0	0.0	0.6	0.2	100.7	8.8
-24.424	2.274	0.035	-4.193	0.069	1.051	0.121	0.042	0.010	0.019	0.011	0.025	0.013	0.0	0.0	4.3	1.1	132.2	6.7
-24.413	7.531	0.040	27.285	0.079	0.787	0.121	0.016	0.009	-0.019	0.011	0.019	0.013	0.0	0.0	0.0	0.0	0.0	0.0
-24.286	1.432	0.037	10.092	0.074	1.037	0.098	0.035	0.010	0.011	0.011	-0.035	0.013	-3.4	1.3	3.4	1.0	128.7	8.5
-24.194	0.823	0.037	9.230	0.074	1.295	0.097	0.094	0.009	-0.015	0.011	-0.035	0.013	-2.7	1.0	7.3	0.9	115.5	3.3
-24.170	-0.275	0.006	-0.887	0.012	5.391	0.097	0.475	0.009	0.070	0.011	-0.073	0.013	-1.4	0.2	8.9	0.2	124.2	0.7
-24.136	0.402	0.005	-0.703	0.010	5.039	0.097	0.411	0.009	-0.114	0.011	-0.080	0.010	-1.6	0.2	8.5	0.2	112.2	0.7
-24.134	-1.232	0.021	-10.917	0.041	1.201	0.097	0.074	0.009	-0.009	0.011	0.025	0.013	0.0	0.0	6.2	0.9	116.5	4.2
-24.049	-0.336	0.014	-10.228	0.027	1.091	0.059	0.076	0.009	-0.016	0.009	-0.041	0.013	-3.8	1.2	7.1	0.9	114.1	3.3
-23.659	-0.550	0.032	-0.918	0.063	3.278	0.019	0.226	0.008	-0.006	0.009	-0.090	0.008	-2.7	0.2	6.9	0.2	119.2	1.1
-23.356	-1.801	0.006	0.798	0.012	0.932	0.019	0.115	0.009	-0.005	0.009	-0.034	0.008	-3.6	0.9	12.3	1.0	118.8	2.2
-22.973	-15.800	0.031	7.640	0.062	0.424	0.021	0.057	0.008	0.155	0.008	-0.021	0.008	-5.0	1.9	38.9	2.7	154.9	1.4
-22.966	2.084	0.027	0.346	0.053	2.654	0.023	0.159	0.008	-0.136	0.008	-0.024	0.010	-0.9	0.4	7.9	0.3	99.7	1.1
-22.915	2.129	0.006	-0.093	0.012	1.949	0.022	0.179	0.009	-0.179	0.009	-0.064	0.007	-3.3	0.4	13.0	0.5	97.5	1.0
-22.892	-9.694	0.018	1.001	0.035	0.517	0.021	0.281	0.008	0.048	0.008	-0.008	0.008	0.0	0.0	55.1	2.7	124.8	0.8
-22.768	0.959	0.024	-5.034	0.047	0.530	0.022	0.020	0.009	0.005	0.009	-0.012	0.008	0.0	0.0	0.0	0.0	0.0	0.0
-22.758	-3.087	0.010	0.623	0.020	1.237	0.021	0.386	0.008	0.045	0.008	-0.109	0.008	-8.8	0.7	31.4	0.8	123.3	0.6
-22.414	-2.916	0.012	1.455	0.024	2.608	0.023	0.782	0.010	0.008	0.009	-0.053	0.010	-2.0	0.4	30.0	0.5	120.3	0.3
-22.315	-3.120	0.015	0.952	0.030	1.242	0.023	0.446	0.010	0.040	0.009	-0.065	0.010	-5.2	0.8	36.0	1.0	122.6	0.6
-21.372	-5.401	0.029	1.668	0.057	1.149	0.015	0.598	0.010	0.056	0.010	-0.040	0.009	-3.5	0.8	52.3	1.1	122.7	0.5
-20.189	-11.690	0.015	11.658	0.031	0.817	0.015	0.248	0.011	0.316	0.010	0.051	0.009	6.2	1.1	49.2	1.6	145.9	0.8
-19.451	-10.862	0.011	10.754	0.021	0.752	0.029	0.254	0.010	0.405	0.009	0.033	0.011	4.4	1.5	63.6	2.7	149.0	0.6
-19.400	-11.207	0.003	11.970	0.007	2.558	0.029	0.782	0.010	1.574	0.009	0.280	0.011	10.9	0.4	68.7	0.9	151.8	0.2
-18.565	-10.677	0.011	11.876	0.022	0.544	0.017	0.111	0.009	0.207	0.010	0.008	0.011	0.0	0.0	43.1	2.2	150.9	1.1